



Universiteit  
Leiden

The Netherlands

## The electrochemical reduction of dioxygen and hydrogen peroxide by molecular copper catalysts

Langerman, M.

### Citation

Langerman, M. (2021, October 12). *The electrochemical reduction of dioxygen and hydrogen peroxide by molecular copper catalysts*. Retrieved from <https://hdl.handle.net/1887/3217072>

Version: Publisher's Version

License: [Licence agreement concerning inclusion of doctoral thesis in the Institutional Repository of the University of Leiden](#)

Downloaded from: <https://hdl.handle.net/1887/3217072>

**Note:** To cite this publication please use the final published version (if applicable).

# The electrochemical reduction of dioxygen and hydrogen peroxide by molecular copper catalysts

Proefschrift

ter verkrijging van

de graad van doctor aan de Universiteit Leiden,

op gezag van rector magnificus prof.dr.ir. H. Bijl,

volgens besluit van het college voor promoties

te verdedigen op dinsdag 12 oktober 2021

klokke 13:45 uur

door

**Michiel Langerman**

geboren te Maastricht

in 1991

# Promotiescommissie

## **Promotoren**

Dr. D. G. H. Hetterscheid

Prof.dr E. Bouwman

## **Overige commissieleden**

Prof.dr. H. S. Overkleeft (voorzitter)

Prof.dr. M. T. M. Koper (secretaris)

Prof.dr. S. A. Bonnet

Prof.dr. J. Mayer (Yale University)

Dr. S. C. Marinescu (University of Southern California)

Financial support was provided by the European Research Council and the Leiden Institute of Chemistry of Leiden University.

Print: Ipskamp Drukkers B.V., Enschede

ISBN: 978-94-6421-487-1





# Table of Contents

---

<b>Chapter 1</b>	Introduction to the role of molecular copper complexes as catalysts for the oxygen reduction reaction	<b>7</b>
<b>Chapter 2</b>	Fast oxygen reduction catalysed by a copper(II) tris(2-pyridylmethyl)amine complex via a stepwise mechanism	<b>25</b>
<b>Chapter 3</b>	Mechanistic study of the activation and the electrocatalytic reduction of hydrogen peroxide by Cu-tmpa in neutral aqueous solution	<b>39</b>
<b>Chapter 4</b>	Dioxygen reduction in acetonitrile: the influence of acid strength on the catalytic reaction	<b>57</b>
<b>Chapter 5</b>	On the scaling relation between the reduction potential of copper catalysts and the turnover frequency for the oxygen and hydrogen peroxide reduction reactions	<b>87</b>
<b>Chapter 6</b>	Summary and outlook	<b>109</b>
<b>Appendices</b>	A — Supplementary Information for Chapter 2	<b>115</b>
	B — Supplementary Information for Chapter 3	<b>129</b>
	C — Supplementary Information for Chapter 4	<b>133</b>
	D — Supplementary Information for Chapter 5	<b>145</b>
<b>Samenvatting en toekomstperspectieven</b>		<b>155</b>
<b>Curriculum Vitae</b>		<b>163</b>
<b>List of Publications</b>		<b>165</b>
<b>Acknowledgements</b>		<b>167</b>

---



# Chapter 1

---

Introduction to the role of molecular copper complexes as catalysts for the oxygen reduction reaction



## 1.1. Renewable energy and electrochemistry

Despite indications that the year-on-year growth of global greenhouse gas emissions has slowed down over the last 5 years, the atmospheric CO<sub>2</sub> levels keeps rising steadily.<sup>[1]</sup> As a result global temperatures are expected to rise by as much as 2 °C by the second half of the 21<sup>st</sup> century, with lasting effects on the global climate.<sup>[2-3]</sup> This will have dire consequences for a large part of humanity, especially for those living in low lying coastal areas due to rising sea levels,<sup>[4-5]</sup> and in (near-) equatorial regions as a result of reduced precipitation in conjunction with an increase of extreme weather events.<sup>[6]</sup> Furthermore, despite efforts to reduce or limit power consumption at a regional level, a significant increase (50%) in global energy demand is expected by 2050.<sup>[7-8]</sup> This is projected to be largely the result of improvements in living conditions in Asia and the accompanied increase in energy demand. This signifies the importance of shifting to renewable energy sources to replace current fossil fuel energy sources and meet future energy demands in a short timeframe, to prevent future energy demand being fulfilled by traditional fossil fuel energy sources.

Renewable energy sources such as wind and solar energy will play an important part in this energy transition. With the use of photovoltaic solar cells, the abundant solar energy reaching Earth can be directly converted into electricity. The ease of scalability and the great affordability of this form of renewable energy makes it the prime candidate for sustainable energy generation. Increased generation of electrical energy will require significant electrification of transportation and industry via electrochemistry,<sup>[9]</sup> as chemical feedstocks from fossil fuels will be significantly diminished. Additionally, the use of solar energy and, to a lesser degree, wind energy results in an increased intermittency of the power generation, influenced by the day-night cycle and seasonality of solar intensity.<sup>[7, 10-11]</sup> This requires a way to quickly and efficiently store energy for use during periods of reduced electricity generation. Although battery technology has taken enormous strides in the last decade, especially in the automotive sector,<sup>[12-13]</sup> large scale energy storage would ideally be done in the form of chemical energy. The storage of electricity in batteries is not easily scalable due to a linear increase in material cost with increasing capacity, while conversion to chemical energy can be done catalytically. Chemical energy can be stored in several different forms, such as methane, methanol, and dihydrogen; compounds that can be electrochemically converted to generate electricity, or vice versa. While not the most energy dense chemical, dihydrogen is one of the primary candidates as a renewable energy carrier, as only H<sub>2</sub>, O<sub>2</sub> and H<sub>2</sub>O are involved as chemicals, resulting in an environmentally friendly process without harmful waste. Additionally, hydrogen gas can readily be produced from water via the water splitting reaction, a process known since the 1839, when the first electrochemical cell was used to electrolyse water.<sup>[14]</sup>

However, several technological challenges remain to be resolved in order to efficiently scale up and allow for the widespread adoption of electrolyzers and fuel cells.<sup>[15-16]</sup> The most significant challenges are posed by the catalysts, electrode materials and certain energy inefficiencies in the involved electrochemical reactions.

## 1.2. The electrochemical oxygen reduction reaction

The oxygen reduction reaction (ORR) is one of the main efficiency-limiting catalytic reactions affecting the performance of fuel cells. The ORR is the driving-force behind the oxidation of fuels in different types of fuel cells, whether they are proton-exchange membrane fuel cells (PEMFC) or solid-oxide fuel cells (SOFC). In these fuel cells, dihydrogen (or another fuel, such as methane) is oxidized at the anode, resulting in the formation of protons and electrons, with the electrons generating an electrical current through an external circuit. These then reach the cathode, where they facilitate the reduction of dioxygen to water (Figure 1.1).

The theoretical maximum potential generated by such a hydrogen fuel cell is 1.23 V, as this is the standard reduction potential of  $O_2$  (Scheme 1.1). However, limitations in the design of the fuel cell and the catalytic reactions themselves result in significant potential losses, thus limiting the efficiency of the fuel cell. While the hydrogen oxidation reaction (HOR) at the anode can be efficiently catalysed close the  $H^+/H_2$  equilibrium by platinum catalysts with minimal overpotential losses, the ORR at the cathode is a significantly more complex multi-electron and multi-proton reaction involving several different reaction intermediates. Dispersed platinum nanoparticles on carbon (Pt/C) are currently used as ORR catalysts for application in fuel cells, but require high-catalyst loadings and suffer from poor long-term stability.<sup>[17-18]</sup> Additionally, the

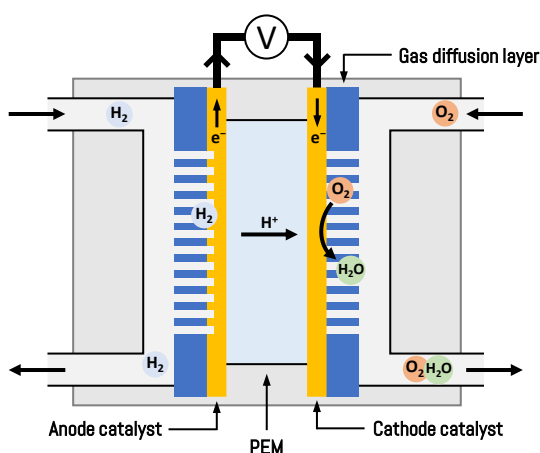


**Figure 1.1.** Simplified schematic representation of a PEM hydrogen fuel cell.

current state-of-the-art Pt ORR catalysts operate at overpotentials of more than 0.4 V.<sup>[19-20]</sup> Thus, in contrast to the HOR, the ORR is one of the major contributing factors to the loss of efficiency due to sluggish reaction kinetics and the large overpotential required to reduce dioxygen to water.



**Scheme 1.1.** The two half-reactions responsible for generating electricity from hydrogen oxidation in a hydrogen fuel cell.

While there is significant interest in developing efficient Pt-free catalysts for the HOR to reduce the cost of fuel cells, the most significant gains in efficiency and price can be made through the development of better ORR catalysts, to both reduce the overpotential losses or find alternatives to the expensive Pt-based ORR catalysts. Several issues have to be overcome when developing new catalysts for the ORR. According to the Sabatier principle, the binding of the intermediate to the catalyst should be of intermediate strength, not too strong and not too weak, for optimal catalysis to occur.<sup>[18, 21]</sup> However, for the ORR the binding strength of the metal catalyst to the intermediate OOH and OH species are very similar. Metals that destabilize the O-O bond of the metal-bound OOH intermediate by strengthening the M-OOH bond also show strong M-OH binding, which negatively impacts the reaction kinetics. This results in a specific optimum binding strength, where the optimal catalysts are guided by these scaling relationships. Nørskov *et al.* showed that Pt has the optimal binding strength with oxygen species, and thus has the best ORR activity and lowest overpotential of all transition metal catalysts.<sup>[19]</sup> Many different alloys have been investigated as ORR catalysts since, but these still adhere to the scaling relations, hindering the development of more efficient heterogeneous metal catalysts.<sup>[20, 22-23]</sup> To overcome the scaling relations associated with the ORR, catalysts would have to be developed that avoid the formation of the M-OOH intermediate. Alternatively, catalysts that are able to stabilize certain intermediates over others may lead to a more efficient catalytic reaction. This can be achieved by using three-dimensional catalysts, such as molecular catalysts, where a second coordination sphere around the metal centre can influence the stabilization of specific reaction intermediates.

### 1.3. Oxygen activation and reduction in natural systems

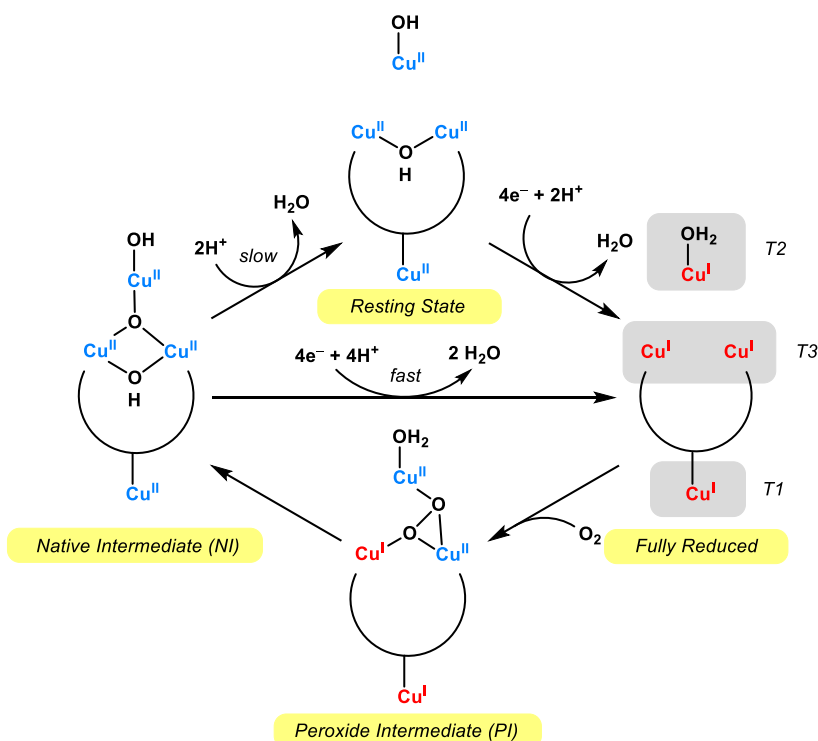
The active sites of enzymes are the perfect example of a three-dimensional catalyst. In these active sites substrates and reaction intermediates are stabilized or destabilized by interactions with amino acid moieties in the binding pocket, thereby tuning the

activation energies such that a catalytic reaction is optimized for a challenging cellular environment. Copper plays an important role in oxidoreductases, a family of redox-active metalloproteins responsible for catalysing reactions that involve electron transfer, where copper is the second most abundant metal after iron for these enzymes.<sup>[17, 24-25]</sup> Examples of these copper-containing enzymes include lytic polysaccharide monooxygenases (LPMOs),<sup>[26-31]</sup> particulate methane monooxygenase (pMMO),<sup>[32-33]</sup> and multi-copper oxidases (MCO) such as tyrosinase, catechol oxidase and laccase.<sup>[34-36]</sup> These enzymes activate and reduce dioxygen in order to oxidize a substrate, forming water in the process. The active sites of these copper-containing enzymes are classified in several types, based on their geometric and electronic structure.<sup>[34]</sup> Type 1 (“blue copper”) centres contain a single copper ion in a trigonal-pyramidal or trigonal-bipyramidal geometry. Type 2 copper centres contain a single copper centre in a square-planar geometry. Finally, type 3 (dinuclear) copper centres contain two antiferromagnetically coupled trigonal-planar or trigonal-bipyramidal Cu centres bridged by a hydroxide ion in the resting state. Additionally, cytochrome c oxidase contains a mixed-metal dinuclear active site containing both a Cu ( $\text{Cu}_B$ ) centre in a trigonal-pyramidal geometry and an Fe (heme  $a_3$ ) centre. This enzyme catalyses the four-electron reduction of  $\text{O}_2$  to  $\text{H}_2\text{O}$  in order to drive its proton pumping activity. In recent years a number of molecular models to mimic the cytochrome c oxidase catalytic centre have been created.<sup>[37-38]</sup>

One MCO that has drawn significant interest in the context of the oxygen reduction reaction is Laccase, a multicopper enzyme capable of fully reducing  $\text{O}_2$  to  $\text{H}_2\text{O}$ .<sup>[34-35]</sup> In Laccase, the reduction of  $\text{O}_2$  acts as the driving force for the oxidation of a wide range of phenolic substrates in plants, bacteria and fungi. The ORR in Laccase takes place at a trinuclear copper site, consisting of a type 2 (T2) copper centre and a type 3 (T3) copper centre, containing two copper ions. A third type (T1) copper site is present closer to the outside surface of the enzyme and is responsible for substrate oxidation. Electron transfer takes place over a distance of 14 Å between this T1 centre and trinuclear T2/3 cluster in the active site responsible for the ORR. The square-planar T2 copper centre contains two histidine ligands, while the tetrahedral T3 copper centres each have three histidine ligands and are bridged by a hydroxide group in the resting state, resulting in antiferromagnetic coupling between the two T3 copper ions. During the catalytic cycle for the reduction of  $\text{O}_2$  by Laccase, the oxidized resting state, where all four copper ions are in a 2+ oxidation state, is first fully reduced via electrons supplied via the T1 copper site (Scheme 1.2).<sup>[39-40]</sup> Upon reacting with dioxygen, a peroxide intermediate (PI) is formed, wherein peroxide is bridged between the three T2/T3 copper ions in the active site. After further electron-transfer steps, the O-O bond is cleaved, resulting in the native intermediate (NI) structure. Elimination of water from the NI state will regain the

resting state, or can preferentially lead straight to the fully reduced state if substrate oxidation is taking place, which allows for further electron transfer via the T1 site to the trinuclear centre.

Laccase has been used as a catalyst for the electrochemical ORR by immobilizing the enzyme on an electrode.<sup>[41-47]</sup> These electrochemical studies revealed that Laccase is able to catalyse the reduction of dioxygen close to the ORR equilibrium potential, with a minimal overpotential of around 0.1 V. While this shows the thermodynamic efficiency of Laccase as an ORR catalyst, low current densities are achieved due to the large bulk of the enzyme leading to a low number of active sites per electrode surface area. While there have been successful attempts at increasing current density by incorporating Laccase into hydrogels or carbon aerogels, resulting in enzyme multilayers, slow electron transport limits the efficiency of such systems.<sup>[42-43, 48]</sup> Whereas enzymes are important benchmarks for the electrocatalytic ORR, their practical application is limited due to the limited stability of the enzymes and the aforementioned low current densities, in comparison to heterogenous and molecular catalysts.

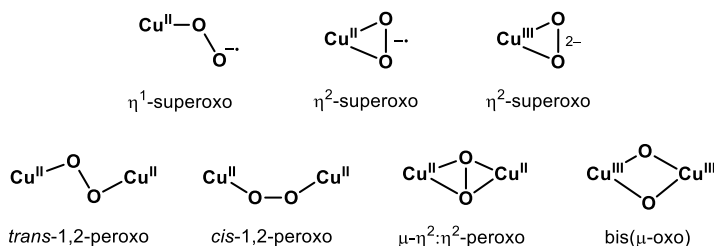


**Scheme 1.2.** Simplified schematic representation of the catalytic ORR mechanism of Laccase, showing only the main intermediates that have been detected via spectroscopic methods.<sup>[39-40]</sup>

## 1.4. Molecular copper catalysts

Molecular complexes offer an opportunity to incorporate a ligand structure similar to those found in enzymes, while avoiding some of the efficiency-limiting downsides associated with the use of enzymes as electrocatalysts. Additionally, the reactivity of molecular complexes can be tuned by straightforward ligand modifications. The design of molecular catalysts is not only inspired by the active sites of enzymes, but molecular complexes often also serve as synthetic mimics for these active sites. Spectroscopic information of these model compounds is used to study the geometry, electronic structure, and the reactivity towards the binding of substrates to the metal centres to elucidate the reactions taking place in the active sites of enzymes.

The interaction of dioxygen and copper ions plays an important role in copper-containing enzymes that are able to reduce  $O_2$ , and molecular compounds have been used to investigate these interactions. To study the formation of copper-dioxygen adducts, the reactivity of a wide range of  $Cu^I$  complexes with  $O_2$  has been investigated.<sup>[49-53]</sup> Several different binding modes of  $O_2$  to copper centres have been identified (Scheme 1.3).<sup>[54]</sup> The pyridylalkylamine copper complex  $[Cu(tmpa)(L)]^+$  ( $Cu$ -tmpa; tmpa = tris(2-pyridylmethyl)amine),  $L$  = solvent molecule) is one of the earliest examples for which the formation of a copper-dioxygen adduct was proven using a combination of spectroscopic techniques.<sup>[55-56]</sup> Using low temperature UV-vis absorption measurements and x-ray crystallography, Karlin *et al.* showed that the reaction between  $[Cu^I(tmpa)(L)]^+$  and  $O_2$  resulted in the formation of a dinuclear  $Cu_2-O_2$  species. Follow-up studies using stopped-flow kinetic studies revealed that the formation of a short-lived copper(II)-superoxide complex precedes the formation of a *trans*- $\mu$ -1,2-peroxo complex.<sup>[57-59]</sup> Exceedingly fast kinetics of the reaction between  $Cu^I$  and  $O_2$  in aprotic solvents were measured.<sup>[59]</sup> Following this report, a variety of different alkylamine and pyridylalkylamine complexes have been studied.<sup>[50, 60-66]</sup> The generalized reaction pathway that was determined for reaction of these copper complexes with dioxygen follows the initial formation of a mononuclear  $Cu^{II}-O_2^{\bullet-}$  adduct, followed by a dimerization step resulting in the formation of a bridged  $O_2^{2-}$  species.

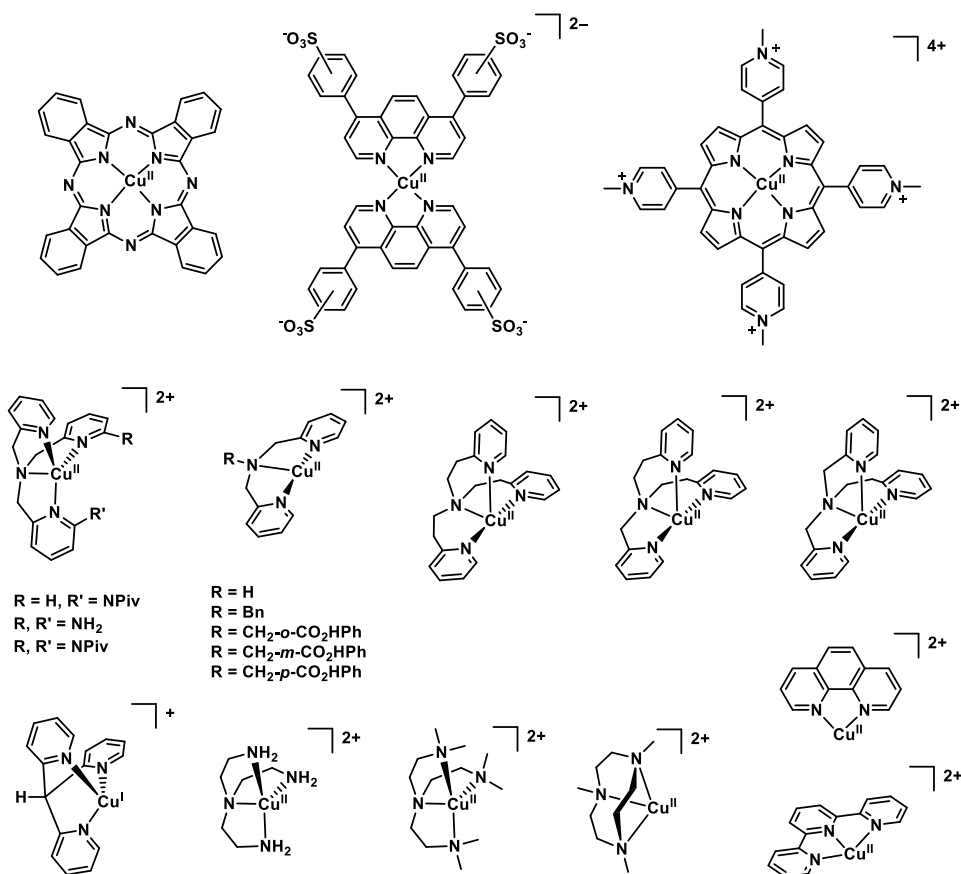


Scheme 1.3. Binding modes of dioxygen to copper.<sup>[49]</sup>

Prior to the use of model copper complexes for the elucidation of reaction mechanisms of active sites in enzymes, copper complexes had already been studied as novel catalysts for the electrochemical reduction of O<sub>2</sub>.<sup>[67-69]</sup> This was driven by the discovery by Jasinski of a cobalt phthalocyanine complexes as a molecular catalyst for the ORR.<sup>[70]</sup> Some of the earliest in-depth efforts to study the electrocatalytic reduction of O<sub>2</sub> by molecular copper complexes were performed by Anson *et al.*<sup>[71-75]</sup> They showed that (substituted) phenanthroline copper complexes adsorbed on the surface of a graphitic electrode were able to catalyse the electrochemical ORR.<sup>[71-72]</sup> Additionally, it was shown that a change in the coordination geometry took place upon reduction of the copper complex, from a square-pyramidal Cu<sup>II</sup> to a tetrahedral Cu<sup>I</sup> complex, even when absorbed on the electrode surface.<sup>[71]</sup> Further research was performed on the electrocatalytic ORR by substituted phenanthroline copper complexes,<sup>[76]</sup> including on phenanthroline copper complexes covalently bonded to the carbon electrode, which revealed a possible Cu<sub>2</sub>O<sub>2</sub> intermediate during the ORR.<sup>[77]</sup>

In the last decade the first biomimetic copper complexes have been investigated for their ORR activity, both using sacrificial chemical reductants and as electrocatalysts (Scheme 1.4).<sup>[38, 78-93]</sup> Work by Karlin and Fukuzumi showed that Cu-tmpa is able to catalyse the ORR in acetone using ferrocene (Fc) as a reductant.<sup>[78]</sup> It was observed that the peroxo dimer  $[\{Cu^{II}(tmpa)\}_2(O_2)]^{2+}$  is formed once all the perchloric acid is consumed by the catalytic reaction. Upon addition of more acid, this peroxo complex was also shown to be able to reduce dioxygen. Similar results were obtained for a substituted pyridylalkylamine complex  $[Cu(PV-tmpa)(L)]^{2+}$ , containing a pivalamido moiety on the ortho position of one of the pyridine arms.<sup>[83]</sup> However, upon addition of the acid to the peroxo complex, its corresponding UV-Vis absorption band immediately disappeared. This was followed by a slower increase of the Fc<sup>+</sup> absorption band, showing that catalytic reduction was taking place. This suggests that the monomeric Cu<sup>II</sup>-OOH was formed upon addition of the acid, from which further reduction to H<sub>2</sub>O proceeded. It was shown that the catalytic ORR rate constant of  $[Cu(PV-tmpa)(L)]^{2+}$  was significantly larger than that of Cu-tmpa. However, differences in the ability of the acetate ion to coordinate to the copper centres between these two different complexes played an important role, and the use of non-coordinating acids could have a significant effect upon the relative rate constants. For the related  $[Cu(tepa)]^{2+}$  (tepa = tris[2-(2-pyridyl)ethyl]-amine) complex, it was shown that formation of a dinuclear copper peroxo intermediate is not a prerequisite to facilitate the 2-electron reduction of O<sub>2</sub> to H<sub>2</sub>O<sub>2</sub>, as this species was not observed.<sup>[81]</sup>

The ORR by Cu-tmpa in aqueous buffered solutions was also investigated using electrochemical methods by Gewirth *et al.*<sup>[84-85]</sup> Cu-tmpa and several other pyridylalkylamine complexes were incorporated into a carbon black (Vulcan XC-72) ink



**Scheme 1.4.** Schematic drawing of mononuclear copper complexes that have been reported to reduce dioxygen, either in the presence of chemical reductants or under electrochemical conditions.<sup>[67-69, 71-93]</sup> Counterions and coordinating solvent molecules are omitted for clarity.

and dropcasted on a glassy carbon electrode. Comparison of the different pyridylalkylamine copper complexes showed minimal differences between catalysts in the onset of the ORR and the limiting currents above pH 4 during hydrodynamic voltammetry measurements using rotating ring-disk electrodes.<sup>[85]</sup> At pH 4 and below, more significant differences were observed, with only Cu-tmpa maintaining its 4-electron ORR performance. However, based on experiments where Cu-tmpa was used as a homogenous ORR catalyst in solution, it was shown that Cu-tmpa is not stable in electrolyte solutions with a pH below 4, even under non-catalytic conditions.<sup>[87]</sup> This raises questions concerning the nature of the catalysts that is present in heterogenized form under acidic conditions.

It was suggested that Cu-tmpa dimerizes upon reduction in the presence of dioxygen, based on an apparent shift in the onset potential of the ORR under rotating



conditions of the rotating ring disk electrode (RRDE),<sup>[84]</sup> and the previously discussed studies on Cu-tmpa in organic solvents. However, the current at a given fixed potential always decreases proportional to the decrease in catalyst concentration under conditions where substrate is not limiting. This will result in a shift of the “apparent onset” of the catalytic reaction to lower potentials as a function of decreasing catalyst concentration, if a fixed current density is used as a reference to determine the onset potential. Furthermore, the catalytic onset potential is generally an ill-defined property.<sup>[94]</sup> Indeed, the same data showed that the half-wave potential of the catalytic curve did not appear to shift as a function of catalyst loading, which is a more appropriate property to observe possible changes in electrocatalytic mechanisms.

A dinuclear copper complex containing two 3,5-diamino-1,2,4-triazole (dat) ligands (Cu-dat) has been considered a benchmark for molecular electrocatalytic ORR performance. In molecular form both copper centres are spaced similarly to the T3 copper centres present in Laccase.<sup>[95]</sup> Gewirth *et al.* reported an ORR onset at 0.86 V vs. RHE at pH 13 which is the lowest reported overpotential for any copper catalyst.<sup>[96]</sup> However, the species that was used in this study was formed by mixing a 2:1 ratio of ligand to Cu<sup>II</sup> salt with carbon black, followed by dropcasting onto a glassy carbon electrode. This procedure did not correspond to the ratios used in the studies to investigate the structure of Cu-dat species.<sup>[95]</sup> Our group has recently shown that the catalytic activity of the Cu-dat compound is largely the result of the formation of amorphous Cu<sup>0</sup> and Cu<sup>I</sup> depositions on the electrode surface, and can therefore not be ascribed to the molecular structure of the complex.<sup>[97]</sup> These findings showcase some of the issues that arise when analysing molecular (electro)catalyst and the difficulty in transferring and applying results obtained under different experimental conditions to an electrocatalytic system.

## 1.5. Benchmarking the performance of homogeneous electrocatalysts using electrochemical methods

With the increased interest in molecular electrocatalysts for small molecule conversion (H<sub>2</sub>, O<sub>2</sub>, H<sub>2</sub>O, CO<sub>2</sub>) for renewable energy applications, it is necessary to have a robust framework to elucidate catalytic mechanisms and quantify the performance of molecular catalysts to allow comparisons between different catalysts. This has been an important topic in the field and has been highlighted in many publications in the last decade.<sup>[98-107]</sup> Molecular electrocatalysts have been studied under a wide range of experimental conditions, utilizing different solvents, solution pH, and supporting electrode materials.<sup>[108-110]</sup> The specific conditions in which molecular homogeneous electrocatalysts are evaluated using electrochemical techniques are often dictated by the solubility or stability of the catalyst under the chosen conditions. Thus, many

molecular electrocatalysts are evaluated in organic solvents, such as MeCN or DMF. Yet, in the context of renewable energy applications, water solubility is considered an important property in the development of new molecular catalysts, as is the catalyst performance under aqueous conditions.<sup>[111-117]</sup> Evaluating the efficiency of a catalyst does not only require the determination of the kinetic performance in the form of catalytic rate constants or turnover frequencies, but also of the thermodynamic performance in the form of the catalytic onset potential or the overpotential relative to the equilibrium potential of the catalysed reaction. However, as mentioned in the previous section, the definition of the onset potential can be rather arbitrary or even not defined at all. These factors can hinder the benchmarking of electrocatalysts and makes comparisons between catalysts difficult.

Efforts have been made to standardize and rationalize the definition of the onset and overpotentials for molecular electrocatalysts.<sup>[94, 118-120]</sup> The determination of the overpotential is relatively straightforward under ideal conditions, in which a voltammogram shows an S-shaped catalytic curve and the limiting plateau current is available. Here, the preferred measure of the catalytic potential for the determination of the overpotential is the catalytic half-wave potential ( $E_{cat/2}$ ). This is the potential at which half the limiting or peak catalytic current is observed. In turn, the overpotential is defined as the difference between the equilibrium potential of the given reaction and the catalytic half-wave potential. Using the  $E_{cat/2}$  as the measure for the catalytic potential results in smaller deviations when the catalytic systems behave less ideal.<sup>[94]</sup> However, in the case of fast ORR electrocatalysts, mass transport limitations in  $O_2$  can result in peak shaped catalytic currents that strongly deviate from an ideal S-shape, and where the mass transport independent plateau current is never reached. In these situations, the catalytic peak current can be reached before the redox potential of the catalytic species. Thus, an accurate description of  $E_{cat/2}$  can only be obtained by using very high scan rates or by increasing the ratio of substrate to catalyst.<sup>[107]</sup> In such cases the redox equilibrium potential ( $E_{1/2}$ ) of the catalytic species or a well-defined onset potential at the start of the catalytic wave would be a better descriptor to determine the overpotential.

While the equilibrium potential of the catalysed reaction is well-established in aqueous solutions, this can be more challenging in non-aqueous solutions, where the  $H^+/H_2$  reduction potential is not always known, or acid  $pK_a$ 's have not been determined. Several methods have been described to determine the overpotential in non-aqueous solutions.<sup>[119-120]</sup> Recently, Roberts and Bullock reported a method to directly measure the equilibrium potentials of the  $H^+/H_2$  couple in a given solvent without the need for the  $pK_a$  of the acid or the standard reduction potential  $E_H^0$  in the particular solvent.<sup>[121]</sup> This was followed by the determination of the standard reduction potential of  $O_2$  in

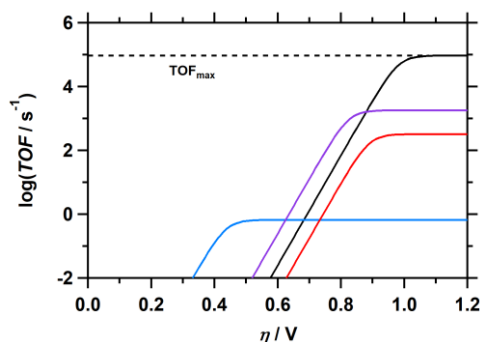


**Figure 1.2.** Simulated logTOF– $\eta$  plot, showing the catalytic performance as a function of applied overpotential of several catalysts, each with a different  $\text{TOF}_{\text{max}}$  and catalytic overpotential.

acetonitrile and DMF using the same method by Mayer *et al.*<sup>[122]</sup>

Another development is the introduction of the foot-of-the-wave analysis (FOWA) pioneered by Savéant and Costentin,<sup>[123]</sup> which couples kinetic performance to the thermodynamic catalytic potential. As previously mentioned, side-phenomena such as substrate depletion and catalyst deactivation can result in significant deviation from the S shaped catalytic wave under purely kinetic conditions. This would result in underestimation of the observed rate constant. However, the FOWA can be used to analyse reactions where these side phenomena occur, as the catalytic current at the foot of the catalytic wave is considered to be purely kinetic in nature, without interference from side phenomena. Thus, the ideal or maximum rate constant can be derived from the foot of the catalytic wave. FOWA expressions for more complicated multi-electron multistep molecular electrocatalytic systems have also been proposed.<sup>[98-100, 102, 124-125]</sup> It has to be noted that while FOWA is a very powerful tool, it is also very sensitive to the choice of the potential window used for the FOWA determination.<sup>[124]</sup> The FOWA will be further discussed in Chapter 2. Maximum turnover frequencies ( $\text{TOF}_{\text{max}}$ ) derived from the FOWA can be used to construct a log(TOF)– $\eta$  plot, where the log(TOF) is plotted as a function of the applied overpotential (Figure 1.2). While the  $\text{TOF}_{\text{max}}$  of a catalyst is often never reached under experimental conditions, and will therefore be larger than the observed rate constants or TOFs, it can be useful in comparisons between catalysts. When multiple catalysts are compared in such a graph, overpotential zones can be identified in which particular catalysts show superior catalytic performance. It also highlights the trade-off between overpotential and the maximum catalytic rates of a catalyst. Therefore, these log(TOF)– $\eta$  plots, also called molecular Tafel Plots, can be a useful tool for comparing the catalytic performance of molecular electrocatalysts relative to the applied overpotential.<sup>[105-106, 126-127]</sup>

## 1.6. Aim of research

The focus of the research described in this thesis is placed on the elucidation of electrocatalytic mechanisms of the ORR by homogeneous copper complexes. As discussed in the previous sections, a large knowledge base exists on the reaction of dioxygen with molecular  $\text{Cu}^{\text{I}}$  coordination complexes. Cu-tmpa is one of the most-studied catalysts for the chemical and electrochemical reduction of dioxygen, and is used as a reference for many other similar copper complexes. However, significant issues remain in translating mechanistic insights observed during chemical reduction to electrochemical systems, and vice versa, whereby heterogenized catalytic species have erroneously been ascribed a certain molecular character. An important question regarding Cu-tmpa is whether a dinuclear intermediate is required for the reduction of dioxygen under electrocatalytic conditions or whether this species is only present under non-catalytic conditions, something for which conflicting data was reported in previous electrochemical and non-electrochemical studies of the ORR. The limited understanding of the catalytic mechanism hinders the rational design of improved copper catalysts. Thus, we set out to elucidate the mechanism of the electrocatalytic ORR by Cu-tmpa under different conditions using a range of electrochemical techniques.

In Chapter 2, the mechanism of the electrochemical ORR by homogeneous Cu-tmpa in a neutral aqueous solution is discussed. The product distribution of the catalytic reaction as a function of the applied potential was determined using RRDE techniques. This revealed the formation of  $\text{H}_2\text{O}_2$  as an intermediate product during the overall four electron reduction towards  $\text{H}_2\text{O}$ . Additionally, the catalytic performance was quantified, revealing one of the fastest reported rate constants for the ORR by a molecular catalyst. Finally, we show that a mononuclear species is responsible for the reduction of dioxygen, both in the FOWA potential window and at higher applied overpotentials. These results strengthen the notion that a dinuclear copper species is not required for fast oxygen reduction and illustrate the difficulties of transferring observations made under non-electrocatalytic conditions to an electrochemical system.

As it was shown that  $\text{H}_2\text{O}_2$  plays an important role in the catalytic mechanism of the ORR, the research described in Chapter 3 builds upon the results of the previous chapter and elaborates on the reduction of hydrogen peroxide by Cu-tmpa in a neutral aqueous electrolyte solution. By comparing the catalytic performance between deuterated and non-deuterated solutions, a kinetic isotope effect (KIE) was determined. This revealed that the catalytic mechanism for the reduction of  $\text{H}_2\text{O}_2$  follows a Fenton-like reaction pathway, wherein the formation of a copper(II) hydroxyl species and a free hydroxyl radical are involved in the rate-determining step. This shows

similarities with the mechanisms suggested for the active sites of several monocopper enzymes that show reactivity towards dioxygen and hydrogen peroxide.

The results described in Chapter 2 raised the question on whether the choice of solvent or proton source could be the main determinant for the catalytic mechanism, in relation to previous Cu-O<sub>2</sub> reactivity studies reported previously. In Chapter 4, it is shown that use of the strongly coordinating acetonitrile as an aprotic solvent slows down the electrocatalytic reduction of dioxygen by Cu-tmpa by several orders of magnitude. Using the previously discussed method to directly measure the equilibrium potential of the H<sup>+</sup>/H<sub>2</sub> couple, a slightly lower overpotential was observed compared to neutral aqueous solution. In contrast to previous suggestions, we show that even when the catalytic ORR is slowed down to a significant degree in acetonitrile, a mononuclear reaction mechanism is involved. This holds true in the presence of both coordinating and non-coordinating proton donors. Thus, we confirm that dimerization does not play a role in the electrocatalytic ORR by Cu-tmpa in water or acetonitrile under these conditions.

In Chapter 5, the electrocatalytic performance of several pyridylalkylamine copper complexes for the ORR and the reduction of hydrogen peroxide is discussed. The effect of changes in the ligand structure by varying ligand arm lengths on the redox chemistry and catalytic rates were investigated. Scaling relations were observed between the redox potentials of the catalysts and the maximum catalytic rate constants determined via FOWA, for both the reduction of dioxygen and hydrogen peroxide. This also coincides with a positive shift of the onset and  $E_{\text{cat}/2}$  potentials corresponding with an increase in redox potential, thus resulting a significant reduction of the ORR overpotential compared to Cu-tmpa.

## 1.7. References

- [1] P. Friedlingstein, et al., *Earth Syst. Sci. Data* **2020**, 12, 3269-3340.
- [2] IPCC, **2014**: *Climate Change 2014: Synthesis Report. Contribution of Working Groups I, II and III to the Fifth Assessment Report of the Intergovernmental Panel on Climate Change*, [Core Writing Team, Rajendra K. Pachauri, Leo Meyer (Eds.)]. IPCC, Geneva, Switzerland.
- [3] IPCC, **2018**: *Global Warming of 1.5°C. An IPCC Special Report on the impacts of global warming of 1.5°C above pre-industrial levels and related global greenhouse gas emission pathways, in the context of strengthening the global response to the threat of climate change, sustainable development, and efforts to eradicate poverty*, [V. Masson-Delmotte, P. Zhai, H.-O. Pörtner, D. Roberts, J. Skea, P.R. Shukla, A. Pirani, W. Moufouma-Okia, C. Péan, R. Pidcock, S. Connors, J.B.R. Matthews, Y. Chen, X. Zhou, M.I. Gomis, E. Lonnoy, T. Maycock, M. Tignor, T. Waterfield (Eds.)]. In Press.
- [4] M. I. Voudoukas, L. Mentaschi, E. Voukouvalas, M. Verlaan, L. Feyen, *Earth's Future* **2017**, 5, 304-323.
- [5] R. S. Nerem, B. D. Beckley, J. T. Fasullo, B. D. Hamlington, D. Masters, G. T. Mitchum, *Proc. Natl. Acad. Sci.* **2018**, 115, 2022-2025.
- [6] T. Weber, A. Haensler, D. Rechid, S. Pfeifer, B. Eggert, D. Jacob, *Earth's Future* **2018**, 6, 643-655.
- [7] A. S. Brouwer, M. van den Broek, A. Seebregts, A. Faaij, *Renew. Sustain. Energy Rev* **2014**, 33, 443-466.
- [8] IEA, **2020**: *World Energy Outlook 2020*, IEA, Paris, France. Retrieved from: <https://www.iea.org/reports/world-energy-outlook-2020>.

- [9] M. Yan, Y. Kawamata, P. S. Baran, *Chem. Rev.* **2017**, *117*, 13230-13319.
- [10] M. Yekini Suberu, M. Wazir Mustafa, N. Bashir, *Renew. Sustain. Energy Rev* **2014**, *35*, 499-514.
- [11] O. Gröger, H. A. Gasteiger, J.-P. Suchsland, *J. Electrochem. Soc.* **2015**, *162*, A2605-A2622.
- [12] A. Masias, J. Marcicki, W. A. Paxton, *ACS Energy Letters* **2021**, *6*, 621-630.
- [13] M. Marinaro, D. Bresser, E. Beyer, P. Faguy, K. Hosoi, H. Li, J. Sakovica, K. Amine, M. Wohlfahrt-Mehrens, S. Passerini, *J. Power Sources* **2020**, *459*, 228073.
- [14] W. R. Grove, *Philosophical Magazine Series 3* **1839**, *14*, 127-130.
- [15] Z. P. Cano, D. Banham, S. Ye, A. Hintennach, J. Lu, M. Fowler, Z. Chen, *Nat. Energy* **2018**, *3*, 279-289.
- [16] M. Bernt, A. Hartig-Weiß, M. F. Tovini, H. A. El-Sayed, C. Schramm, J. Schröter, C. Gebauer, H. A. Gasteiger, *Chem. Ing. Tech.* **2020**, *92*, 31-39.
- [17] E. Torres, M. Ayala, in *Comprehensive Inorganic Chemistry II (Second Edition)* (Eds.: Jan Reedijk, Kenneth Poepelmeier), Elsevier, Amsterdam, **2013**, pp. 685-735.
- [18] A. J. Medford, A. Vojvodic, J. S. Hummelshøj, J. Voss, F. Abild-Pedersen, F. Studt, T. Bligaard, A. Nilsson, J. K. Nørskov, *J. Catal.* **2015**, *328*, 36-42.
- [19] J. K. Nørskov, J. Rossmeisl, A. Logadottir, L. Lindqvist, J. R. Kitchin, T. Bligaard, H. Jónsson, *J. Phys. Chem. B* **2004**, *108*, 17886-17892.
- [20] N. M. Marković, T. J. Schmidt, V. Stamenković, P. N. Ross, *Fuel Cells* **2001**, *1*, 105-116.
- [21] A. B. Laursen, A. S. Varela, F. Dionigi, H. Fanchiu, C. Miller, O. L. Trinhammer, J. Rossmeisl, S. Dahl, *J. Chem. Educ.* **2012**, *89*, 1595-1599.
- [22] V. Stamenkovic, B. S. Mun, K. J. J. Mayrhofer, P. N. Ross, N. M. Markovic, J. Rossmeisl, J. Greeley, J. K. Nørskov, *Angew. Chem. Int. Ed.* **2006**, *45*, 2897-2901.
- [23] Greeley, J. E. L. Stephens, A. S. Bondarenko, T. P. Johansson, H. A. Hansen, T. F. Jaramillo, Rossmeisl, J. Chorkendorff, J. K. Nørskov, *Nat Chem* **2009**, *1*, 552-556.
- [24] K. J. Waldron, J. C. Rutherford, D. Ford, N. J. Robinson, *Nature* **2009**, *460*, 823-830.
- [25] C. Andreini, I. Bertini, G. Cavallaro, G. L. Holliday, J. M. Thornton, *JBIC Journal of Biological Inorganic Chemistry* **2008**, *13*, 1205-1218.
- [26] G. Vaaje-Kolstad, B. Westereng, S. J. Horn, Z. Liu, H. Zhai, M. Sørli, V. G. H. Eijsink, *Science* **2010**, *330*, 219-222.
- [27] G. Vaaje-Kolstad, Z. Forsberg, J. S. M. Loose, B. Bissaro, V. G. H. Eijsink, *Curr. Opin. Struct. Biol.* **2017**, *44*, 67-76.
- [28] K. E. H. Frandsen, et al., *Nat. Chem. Biol.* **2016**, *12*, 298-303.
- [29] G. R. Hemsworth, B. Henrissat, G. J. Davies, P. H. Walton, *Nat. Chem. Biol.* **2014**, *10*, 122-126.
- [30] B. Wang, P. H. Walton, C. Rovira, *ACS Catal.* **2019**, *9*, 4958-4969.
- [31] B. Wang, Z. Wang, G. J. Davies, P. H. Walton, C. Rovira, *ACS Catal.* **2020**, *10*, 12760-12769.
- [32] L. Ciano, G. J. Davies, W. B. Tolman, P. H. Walton, *Nat. Catal.* **2018**, *1*, 571-577.
- [33] M. O. Ross, F. MacMillan, J. Wang, A. Nisthal, T. J. Lawton, B. D. Olafson, S. L. Mayo, A. C. Rosenzweig, B. M. Hoffman, *Science* **2019**, *364*, 566-570.
- [34] E. I. Solomon, U. M. Sundaram, T. E. Machonkin, *Chem. Rev.* **1996**, *96*, 2563-2606.
- [35] E. I. Solomon, P. Chen, M. Metz, S.-K. Lee, A. E. Palmer, *Angew. Chem. Int. Ed.* **2001**, *40*, 4570-4590.
- [36] A. M. Mayer, R. C. Staples, *Phytochemistry* **2002**, *60*, 551-565.
- [37] J. P. Collman, N. K. Devaraj, R. A. Decréau, Y. Yang, Y.-L. Yan, W. Ebina, T. A. Eberspacher, C. E. D. Chidsey, *Science* **2007**, *315*, 1565-1568.
- [38] S. Chatterjee, K. Sengupta, S. Hematian, K. D. Karlin, A. Dey, *J. Am. Chem. Soc.* **2015**, *137*, 12897-12905.
- [39] S. M. Jones, E. I. Solomon, *Cell. Mol. Life Sci.* **2015**, *72*, 869-883.
- [40] L. Rulišek, U. Ryde, *Coord. Chem. Rev.* **2013**, *257*, 445-458.
- [41] S. C. Barton, H.-H. Kim, G. Binyamin, Y. Zhang, A. Heller, *J. Am. Chem. Soc.* **2001**, *123*, 5802-5803.
- [42] V. Soukharev, N. Mano, A. Heller, *J. Am. Chem. Soc.* **2004**, *126*, 8368-8369.
- [43] N. Mano, V. Soukharev, A. Heller, *J. Phys. Chem. B* **2006**, *110*, 11180-11187.
- [44] C. F. Blanford, R. S. Heath, F. A. Armstrong, *Chem. Commun.* **2007**, 1710-1712.
- [45] J. A. Cracknell, K. A. Vincent, F. A. Armstrong, *Chem. Rev.* **2008**, *108*, 2439-2461.
- [46] C. F. Blanford, C. E. Foster, R. S. Heath, F. A. Armstrong, *Faraday Discuss.* **2009**, *140*, 319-335.
- [47] M. S. Thorum, C. A. Anderson, J. J. Hatch, A. S. Campbell, N. M. Marshall, S. C. Zimmerman, Y. Lu, A. A.

- Gewirth, *J. Phys. Chem. Lett.* **2010**, *1*, 2251-2254.
- [48] S. Tsujimura, Y. Kamitaka, K. Kano, *Fuel Cells* **2007**, *7*, 463-469.
- [49] E. A. Lewis, W. B. Tolman, *Chem. Rev.* **2004**, *104*, 1047-1076.
- [50] J. A. Halfen, S. Mahapatra, E. C. Wilkinson, S. Kaderli, V. G. Young, L. Que, A. D. Zuberbühler, W. B. Tolman, *Science* **1996**, *271*, 1397-1400.
- [51] L. M. Mirica, X. Ottenwaelder, T. D. P. Stack, *Chem. Rev.* **2004**, *104*, 1013-1046.
- [52] I. Pecht, M. Anbar, *J. Chem. Soc. A* **1968**, 1902-1904.
- [53] A. L. Crumbliss, L. J. Gestaut, *J. Coord. Chem.* **1976**, *5*, 109-111.
- [54] C. E. Elwell, N. L. Gagnon, B. D. Neisen, D. Dhar, A. D. Spaeth, G. M. Yee, W. B. Tolman, *Chem. Rev.* **2017**, *117*, 2059-2107.
- [55] R. R. Jacobson, Z. Tyeklar, A. Farooq, K. D. Karlin, S. Liu, J. Zubieta, *J. Am. Chem. Soc.* **1988**, *110*, 3690-3692.
- [56] M. J. Baldwin, P. K. Ross, J. E. Pate, Z. Tyeklar, K. D. Karlin, E. I. Solomon, *J. Am. Chem. Soc.* **1991**, *113*, 8671-8679.
- [57] K. D. Karlin, N. Wei, B. Jung, S. Kaderli, P. Niklaus, A. D. Zuberbuehler, *J. Am. Chem. Soc.* **1993**, *115*, 9506-9514.
- [58] K. D. Karlin, S. Kaderli, A. D. Zuberbühler, *Acc. Chem. Res.* **1997**, *30*, 139-147.
- [59] C. X. Zhang, S. Kaderli, M. Costas, E.-i. Kim, Y.-M. Neuhold, K. D. Karlin, A. D. Zuberbühler, *Inorg. Chem.* **2003**, *42*, 1807-1824.
- [60] M. Schatz, et al., *Inorg. Chem.* **2001**, *40*, 2312-2322.
- [61] H. R. Lucas, L. Li, A. A. N. Sarjeant, M. A. Vance, E. I. Solomon, K. D. Karlin, *J. Am. Chem. Soc.* **2009**, *131*, 3230-3245.
- [62] H. R. Lucas, G. J. Meyer, K. D. Karlin, *J. Am. Chem. Soc.* **2010**, *132*, 12927-12940.
- [63] P. Comba, C. Haaf, S. Helmle, K. D. Karlin, S. Pandian, A. Waleska, *Inorg. Chem.* **2012**, *51*, 2841-2851.
- [64] M. T. Kieber-Emmons, J. W. Ginsbach, P. K. Wick, H. R. Lucas, M. E. Helton, B. Lucchese, M. Suzuki, A. D. Zuberbühler, K. D. Karlin, E. I. Solomon, *Angew. Chem. Int. Ed.* **2014**, *53*, 4935-4939.
- [65] I. Garcia-Bosch, R. E. Cowley, D. E. Díaz, M. A. Siegler, W. Nam, E. I. Solomon, K. D. Karlin, *Chem. Eur. J.* **2016**, *22*, 5133-5137.
- [66] I. López, R. Cao, D. A. Quist, K. D. Karlin, N. Le Poul, *Chem. Eur. J.* **2017**, *23*, 18314-18319.
- [67] V. E. Kazarinov, M. R. Tarasevich, K. A. Radyushkina, V. N. Andreev, *J. Electroanal. Chem.* **1979**, *100*, 225-232.
- [68] M. R. Tarasevich, K. A. Radyushkina, *Russ. Chem. Rev.* **1980**, *49*, 718-730.
- [69] P. Vasudevan, Santosh, N. Mann, S. Tyagi, *Transit Met Chem* **1990**, *15*, 81-90.
- [70] R. Jasinski, *Nature* **1964**, *201*, 1212-1213.
- [71] J. Zhang, F. C. Anson, *J. Electroanal. Chem.* **1992**, *341*, 323-341.
- [72] K. Shigehara, F. C. Anson, *J. Electroanal. Chem.* **1982**, *132*, 107-118.
- [73] J. Zhang, F. C. Anson, *J. Electroanal. Chem.* **1993**, *348*, 81-97.
- [74] J. Zhang, F. C. Anson, *Electrochim. Acta* **1993**, *38*, 2423-2429.
- [75] Y. Lei, F. C. Anson, *Inorg. Chem.* **1994**, *33*, 5003-5009.
- [76] C. C. L. McCrory, X. Ottenwaelder, T. D. P. Stack, C. E. D. Chidsey, *J. Phys. Chem. A* **2007**, *111*, 12641-12650.
- [77] C. C. L. McCrory, A. Devadoss, X. Ottenwaelder, R. D. Lowe, T. D. P. Stack, C. E. D. Chidsey, *J. Am. Chem. Soc.* **2011**, *133*, 3696-3699.
- [78] S. Fukuzumi, H. Kotani, H. R. Lucas, K. Doi, T. Suenobu, R. L. Peterson, K. D. Karlin, *J. Am. Chem. Soc.* **2010**, *132*, 6874-6875.
- [79] S. Fukuzumi, L. Tahsini, Y.-M. Lee, K. Ohkubo, W. Nam, K. D. Karlin, *J. Am. Chem. Soc.* **2012**, *134*, 7025-7035.
- [80] L. Tahsini, H. Kotani, Y. M. Lee, J. Cho, W. Nam, K. D. Karlin, S. Fukuzumi, *Chem. Eur. J.* **2012**, *18*, 1084-1093.
- [81] D. Das, Y.-M. Lee, K. Ohkubo, W. Nam, K. D. Karlin, S. Fukuzumi, *J. Am. Chem. Soc.* **2013**, *135*, 2825-2834.
- [82] D. Das, Y.-M. Lee, K. Ohkubo, W. Nam, K. D. Karlin, S. Fukuzumi, *J. Am. Chem. Soc.* **2013**, *135*, 4018-4026.
- [83] S. Kakuda, R. L. Peterson, K. Ohkubo, K. D. Karlin, S. Fukuzumi, *J. Am. Chem. Soc.* **2013**, *135*, 6513-6522.
- [84] M. A. Thorseth, C. S. Letko, T. B. Rauchfuss, A. A. Gewirth, *Inorg. Chem.* **2011**, *50*, 6158-6162.
- [85] M. A. Thorseth, C. S. Letko, E. C. M. Tse, T. B. Rauchfuss, A. A. Gewirth, *Inorg. Chem.* **2013**, *52*, 628-634.
- [86] E. C. M. Tse, D. Schilter, D. L. Gray, T. B. Rauchfuss, A. A. Gewirth, *Inorg. Chem.* **2014**, *53*, 8505-8516.
- [87] M. Asahi, S.-i. Yamazaki, S. Itoh, T. Ioroi, *Electrochim. Acta* **2016**, *211*, 193-198.

- [88] S. Fukuzumi, Y.-M. Lee, W. Nam, *ChemCatChem* **2018**, *10*, 9-28.
- [89] M. Asahi, S.-i. Yamazaki, S. Itoh, T. Ioroi, *Dalton Trans.* **2014**, *43*, 10705-10709.
- [90] M. Asahi, S.-i. Yamazaki, Y. Morimoto, S. Itoh, T. Ioroi, *Inorg. Chim. Acta* **2018**, *471*, 91-98.
- [91] Q. He, T. Mugadza, G. Hwang, T. Nyokong, *Int. J. Electrochem. Sci* **2012**, *7*, 7045-7064.
- [92] M. A. Thorseth, C. E. Tornow, E. C. M. Tse, A. A. Gewirth, *Coord. Chem. Rev.* **2013**, *257*, 130-139.
- [93] N. W. G. Smits, B. van Dijk, I. de Bruin, S. L. T. Groeneveld, M. A. Siegler, D. G. H. Hetterscheid, *Inorg. Chem.* **2020**, *59*, 16398-16409.
- [94] A. M. Appel, M. L. Helm, *ACS Catal.* **2014**, *4*, 630-633.
- [95] E. Aznar, S. Ferrer, J. Borrás, F. Lloret, M. Liu-González, H. Rodríguez-Prieto, S. García-Granda, *Eur. J. Inorg. Chem.* **2006**, *2006*, 5115-5125.
- [96] M. S. Thorum, J. Yadav, A. A. Gewirth, *Angew. Chem. Int. Ed.* **2009**, *48*, 165-167.
- [97] B. van Dijk, J. P. Hofmann, D. G. H. Hetterscheid, *Phys. Chem. Chem. Phys.* **2018**, *20*, 19625-19634.
- [98] V. Artero, J.-M. Saveant, *Energy Environ. Sci.* **2014**, *7*, 3808-3814.
- [99] C. Costentin, J.-M. Savéant, *ChemElectroChem* **2014**, *1*, 1226-1236.
- [100] C. Costentin, G. Passard, J.-M. Savéant, *J. Am. Chem. Soc.* **2015**, *137*, 5461-5467.
- [101] T. Bligaard, R. M. Bullock, C. T. Campbell, J. G. Chen, B. C. Gates, R. J. Gorte, C. W. Jones, W. D. Jones, J. R. Kitchin, S. L. Scott, *ACS Catal.* **2016**, *6*, 2590-2602.
- [102] R. Matheu, S. Neudeck, F. Meyer, X. Sala, A. Llobet, *ChemSusChem* **2016**, *9*, 3361-3369.
- [103] Y. Matsubara, *ACS Energy Letters* **2019**, *4*, 1999-2004.
- [104] K. J. Lee, N. Elgrishi, B. Kandemir, J. L. Dempsey, *Nat. Rev. Chem.* **2017**, *1*, 0039.
- [105] C. Costentin, J.-M. Savéant, *J. Am. Chem. Soc.* **2017**, *139*, 8245-8250.
- [106] J.-M. Saveant, *ChemElectroChem* **2016**, *3*, 1967-1977.
- [107] E. S. Rountree, B. D. McCarthy, T. T. Eisenhart, J. L. Dempsey, *Inorg. Chem.* **2014**, *53*, 9983-10002.
- [108] V. S. Thoi, Y. Sun, J. R. Long, C. J. Chang, *Chem. Soc. Rev.* **2013**, *42*, 2388-2400.
- [109] M. L. Pegis, C. F. Wise, D. J. Martin, J. M. Mayer, *Chem. Rev.* **2018**, *118*, 2340-2391.
- [110] J.-M. Savéant, *Chem. Rev.* **2008**, *108*, 2348-2378.
- [111] Q. Yin, J. M. Tan, C. Besson, Y. V. Geletii, D. G. Musaev, A. E. Kuznetsov, Z. Luo, K. I. Hardcastle, C. L. Hill, *Science* **2010**, *328*, 342-345.
- [112] S. M. Barnett, K. I. Goldberg, J. M. Mayer, *Nat Chem* **2012**, *4*, 498-502.
- [113] B. D. Matson, C. T. Carver, A. Von Ruden, J. Y. Yang, S. Raugei, J. M. Mayer, *Chem. Commun.* **2012**, *48*, 11100-11102.
- [114] C. Liu, H. Lei, Z. Zhang, F. Chen, R. Cao, *Chem. Commun.* **2017**, *53*, 3189-3192.
- [115] L.-L. Zhou, T. Fang, J.-P. Cao, Z.-H. Zhu, X.-T. Su, S.-Z. Zhan, *J. Power Sources* **2015**, *273*, 298-304.
- [116] J. J. Walsh, G. Neri, C. L. Smith, A. J. Cowan, *Organometallics* **2019**, *38*, 1224-1229.
- [117] Y. Han, Y. Wu, W. Lai, R. Cao, *Inorg. Chem.* **2015**, *54*, 5604-5613.
- [118] A. D. Wilson, R. H. Newell, M. J. McNevin, J. T. Muckerman, M. Rakowski DuBois, D. L. DuBois, *J. Am. Chem. Soc.* **2006**, *128*, 358-366.
- [119] G. A. N. Felton, R. S. Glass, D. L. Lichtenberger, D. H. Evans, *Inorg. Chem.* **2006**, *45*, 9181-9184.
- [120] V. Fourmond, P.-A. Jacques, M. Fontecave, V. Artero, *Inorg. Chem.* **2010**, *49*, 10338-10347.
- [121] J. A. S. Roberts, R. M. Bullock, *Inorg. Chem.* **2013**, *52*, 3823-3835.
- [122] M. L. Pegis, J. A. S. Roberts, D. J. Wasylenko, E. A. Mader, A. M. Appel, J. M. Mayer, *Inorg. Chem.* **2015**, *54*, 11883-11888.
- [123] C. Costentin, S. Drouet, M. Robert, J.-M. Savéant, *J. Am. Chem. Soc.* **2012**, *134*, 11235-11242.
- [124] V. C. C. Wang, B. A. Johnson, *ACS Catal.* **2019**, *9*, 7109-7123.
- [125] C. Costentin, D. G. Nocera, C. N. Brodsky, *Proc. Natl. Acad. Sci.* **2017**, *114*, 11303-11308.
- [126] C. Costentin, J.-M. Savéant, *Nat. Rev. Chem.* **2017**, *1*, 0087.
- [127] I. Azcarate, C. Costentin, M. Robert, J.-M. Savéant, *J. Phys. Chem. C* **2016**, *120*, 28951-28960.





## Chapter 2

---

### Fast oxygen reduction catalysed by a copper(II) tris(2-pyridylmethyl)amine complex via a stepwise mechanism

*Catalytic pathways for the reduction of dioxygen can either lead to the formation of water or peroxide as the reaction product. We demonstrate that the electrocatalytic reduction of  $O_2$  by the pyridylalkylamine copper complex  $[Cu(tmpa)(L)]^{2+}$  in neutral aqueous solution follows a stepwise  $4e^-/4H^+$  pathway, in which  $H_2O_2$  is formed as a detectable intermediate and subsequently reduced to  $H_2O$  in a separate catalytic reaction. These homogeneous catalytic reactions are shown to be first order in catalyst. Coordination of  $O_2$  to  $Cu^I$  is found to be the rate determining step in the formation of the peroxide intermediate. Furthermore, the electrochemical study of the reaction kinetics reveals a high turnover frequency of  $1.5 \times 10^5 \text{ s}^{-1}$ , the highest reported for any molecular copper catalyst.*

Adapted from M. Langerman, D. G. H. Hetterscheid, *Angew. Chem. Int. Ed.* **2019**, 58, 12974-12978.

## 2.1. Introduction

With the shift in the energy landscape from fossil fuels towards sustainable sources of energy, storage and conversion of fuels such as hydrogen is expected to play an important role. It is therefore important that efficient fuel cells are available to minimize energy loss during fuel-to-energy interconversion. However, the cathodic oxygen reduction reaction (ORR) is a significant limiting factor in the efficiency of fuel cells.<sup>[1-2]</sup> In nature, multicopper oxidases such as laccase are known to catalyse the four-electron reduction of O<sub>2</sub> to H<sub>2</sub>O efficiently.<sup>[3]</sup> Immobilization of Laccase on electrodes has shown that the ORR can be performed close to the thermodynamic equilibrium potential of water.<sup>[4-9]</sup> In the effort to create synthetic mimics of these copper enzymes, a wide range of model copper systems have been studied for their oxygen activation reactivity.<sup>[9-13]</sup> While some early examples of copper complexes have been studied for their activity towards the ORR,<sup>[14-18]</sup> only in the last decade have the first molecular copper model catalysts been evaluated for their ORR activity, either by means of sacrificial reductants or via electrochemical studies.<sup>[19-24]</sup> [Cu(tmpa)(L)]<sup>2+</sup> (tmpa = tris(2-pyridylmethyl)amine), L = solvent) and many derivatives of the pyridylalkylamine template have been studied as a mimic for active sites in redox active metalloenzymes for its non-planar and flexible coordination sphere and its reactivity towards dioxygen.<sup>[13, 25-27]</sup> The dioxygen binding chemistry of Cu-tmpa has been thoroughly studied by Karlin *et al.*<sup>[28-30]</sup> It was shown that in a range of solvents, the binding of dioxygen to [Cu(tmpa)]<sup>+</sup> leads to fast formation of an end-on Cu<sup>II</sup> superoxo complex, followed by a slower dimerization step to form a dinuclear copper peroxo complex. Additionally, Fukuzumi and Karlin have studied the ORR activity of Cu-tmpa in acetone, using decamethylferrocene as a sacrificial reductant, which involves a dinuclear intermediate.<sup>[19, 22]</sup> Recently, it was shown that heterogenized Cu-tmpa, and several derivatives, adsorbed on carbon black catalyse the electrochemical ORR in aqueous buffer solutions.<sup>[21, 31]</sup> Additionally, the electrochemical ORR activity of homogenous Cu-tmpa dissolved in aqueous solution has been investigated, as well as pH effects on the redox chemistry.<sup>[32-33]</sup> However, thus far catalytic rates have not been reported and the mechanism wherein ORR occurs has not been elucidated.

The field of homogeneous electrocatalysis for the conversion of small molecules (O<sub>2</sub>, CO<sub>2</sub>, H<sub>2</sub>O, H<sub>2</sub>, *etc.*) is expanding rapidly, and great strides have been made to develop new methods to be able to study their reaction kinetics and to allow for benchmarking of different catalysts.<sup>[34-37]</sup> Foot-of-the-wave analysis (FOWA) has become an important tool to determine the catalytic performance of homogeneous electrocatalysts, as it allows for the determination of rate constants under limiting conditions.<sup>[34, 37-42]</sup> Using these methods, we have quantified the fast electrocatalytic ORR by homogeneous Cu-tmpa in neutral aqueous solution. Additionally, a comprehensive study of the product

formation using R(R)DE techniques has provided important new insight into the electrocatalytic ORR mechanism, and shows that catalysis occurs via a stepwise mechanism at a single copper centre.

## 2.2. Results and Discussion

The redox and catalytic behaviour of Cu-tmpa in a phosphate buffer (PB) solution at pH 7, containing 100 mM phosphate salts ( $\text{NaH}_2\text{PO}_4$  and  $\text{Na}_2\text{HPO}_4$ ), was investigated. Cyclic voltammograms (CVs) of Cu-tmpa were recorded using a Glassy Carbon (GC) working electrode ( $A = 0.0707 \text{ cm}^2$ ). In the presence of 1 atm argon, a well-defined reversible  $\text{Cu}^{\text{I}}/\text{Cu}^{\text{II}}$  redox couple is visible at  $E_{1/2} = 0.21 \text{ V}$  vs. RHE, shown in Figure 2.1. In the presence of 1 atm  $\text{O}_2$ , a peak-shaped catalytic wave appears with an onset potential at 0.5 V vs. RHE. This peak-shaped catalytic wave is characteristic for cases of substrate depletion, demonstrating the fast catalysis by Cu-tmpa. The homogeneity of the catalyst was established by electrochemical quartz crystal microbalance (EQCM) experiments, both under non-catalytic and catalytic conditions (Appendix A.2).<sup>[43-46]</sup>

Determination of the relationship between the catalytic current and the catalyst concentration would provide useful insight towards the possible mechanism for the ORR. Due to the low solubility of  $\text{O}_2$  in most solvents, aqueous or otherwise, either very high  $\text{O}_2$  pressures or low catalyst concentrations must be used to avoid the  $\text{O}_2$  mass-transport limitation. By measuring CVs in the presence of 1 atm  $\text{O}_2$  at low catalyst concentrations (0.1–1.0  $\mu\text{M}$  Cu-tmpa), a linear first-order dependence of the catalytic current on the catalyst concentration was observed (Figure A.5).

To determine product selectivity and the electron-transfer number of the catalyst in neutral aqueous solution, rotating (ring-)disk electrode (R(R)DE) voltammetry was used. Previous hydrodynamic studies on the electrocatalytic ORR performance of Cu-tmpa have been carried out using a Vulcan supported surface deposit of Cu-tmpa<sup>[21, 31]</sup>, or only evaluated the behaviour of Cu-tmpa in aqueous solution under non-catalytic conditions.<sup>[33]</sup> While R(R)DE voltammetry is most often used to study heterogeneous catalytic reactions, it can be used to study homogeneous catalytic reactions under certain conditions. One of the main difficulties with the use of the R(R)DE methods for homogeneous catalysts is that both the product and substrate are present in the liquid phase. For complex multi-electron multi-step catalytic reactions (ECE, or ECEC') such as the ORR, this can result in significant deviations from the behaviour dictated by the Koutecky-Levich (KL) equation, which governs the behaviour of reactions with one diffusing species. In such cases, slow catalysis will result in non-ideal behaviour of the measured limiting currents as a function of the rotation rate, and deviations from linearity will be observed in KL-plots. However, for fast catalytic reactions, the limiting current corresponds to the electron transfer number ( $n$ ) of the catalytic reaction.<sup>[47]</sup> In

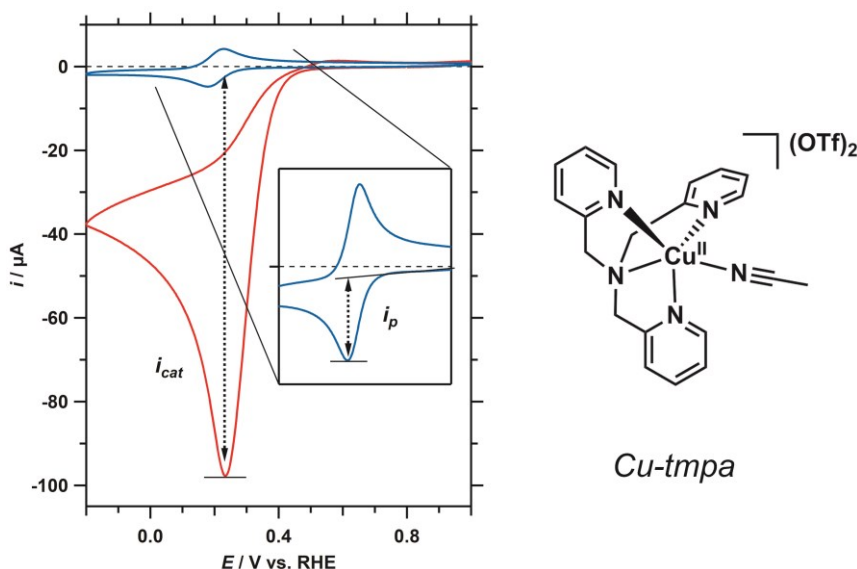


**Figure 2.1.** CVs of Cu-tmpa (0.32 mM) in the presence of 1 atm Ar (blue, zoom in inset) or 1 atm O<sub>2</sub> (red).  $E_{cat/2} = 0.31$  V vs. RHE. Conditions: pH 7 PB ([PO<sub>4</sub>] = 100 mM), 1 atm O<sub>2</sub>, 293 K, 100 mV s<sup>-1</sup> scan rate.

effect, sufficiently fast molecular catalysts (where  $k \gg$  rotation rate) can be considered to behave as heterogeneous within this time frame. Indeed, this is exactly what is observed in the case of Cu-tmpa. Figure 2.2a shows a clear positive shift in the ORR onset potential to 0.5 V vs. RHE in the presence of Cu-tmpa compared to the bare GC electrode. KL analysis was performed on the mass-transport limiting current ( $I_L$ ) obtained at different rotation rates (Figure 2.2b/c). Indeed, good linearity is achieved in the KL-plot, similar to that of a Pt disk electrode. This shows that  $n$  is constant as a function of rotation rate under these conditions. The number of electrons involved in the homogeneous ORR catalysed by Cu-tmpa was determined to be 3.9 (see Appendix A.5), which shows the high selectivity towards the 4-electron reduction of dioxygen. This selectivity is in agreement with the heterogenized carbon black supported Cu-tmpa system.<sup>[21]</sup>

For product determination on the Pt ring electrode, it is important to account for any contributions from reduced catalytic intermediate species towards the observed ring current, as these species could also be oxidized at the ring. A small oxidative ring current can be seen from 0.5 to 0.1 V vs RHE during catalysis, which decreases as the mass-transport limited current is reached (Figure 2.2a, red trace). The observed ring current during the ORR in the presence of Cu-tmpa is negligible when compared to the GC electrode, which itself is well-known to catalyse the 2-electron reduction of O<sub>2</sub> to H<sub>2</sub>O<sub>2</sub>. To exclude the possibility that the observed ring current during ORR is caused by

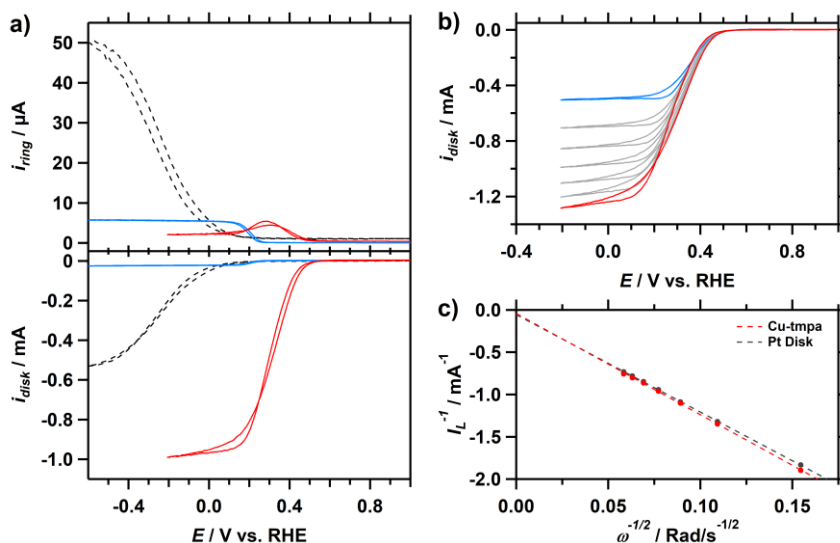


**Figure 2.2.** a) RRDE CVs of bare GC (dotted line) under 1 atm O<sub>2</sub> and Cu-tmpa (0.3 mM) under 1 atm Ar (blue) and 1 atm O<sub>2</sub> (red) at 1600 RPM. b) Disk current of Cu-tmpa (0.3 mM) under 1 atm O<sub>2</sub> at different rotation rates from 400 RPM (blue line) to 2800 RPM (red line); 400 RPM increments. c) Koutecky-Levich plot of the inverse limiting current ( $i_L^{-1}$ ) at -0.2 V (vs. RHE.) as a function of the inverse square root of the rotation rate. Conditions: pH 7 PB ([PO<sub>4</sub>] = 100 mM), 293 K, Pt ring at 1.2 V vs. RHE, 50 mV s<sup>-1</sup> scan rate.

the oxidation of a (partially) reduced catalytic species, the fixed potential applied to the Pt ring was set below the onset potential of H<sub>2</sub>O<sub>2</sub> oxidation on Pt. Decreasing the fixed potential on the ring from 1.2 to 0.8 V vs. RHE, which is still higher than the Cu<sup>I</sup>/Cu<sup>II</sup> redox couple, eliminated the oxidation event taking place on the Pt ring (Figure A.8b). This potential dependence indicates that the observed ring current is due to oxidation of H<sub>2</sub>O<sub>2</sub>. In addition, the ring current actually significantly increases upon a 300 times decrease in catalyst concentration (Figure A.9). This increase would not be possible if the species that is oxidized by Pt would be a Cu<sub>x</sub>-O<sub>2</sub> intermediate. This shows that the oxidative event on the ring can be attributed to H<sub>2</sub>O<sub>2</sub> oxidation.

Quantification of the percentage H<sub>2</sub>O<sub>2</sub> (%H<sub>2</sub>O<sub>2</sub>) produced during ORR was achieved using Eq. 2.1, using the disk current ( $i_{disk}$ ), ring current ( $i_{ring}$ ), and the collection efficiency of H<sub>2</sub>O<sub>2</sub> of the Pt ring ( $N_{H2O2}$ ). %H<sub>2</sub>O<sub>2</sub> was determined from chronoamperometric measurements at a range of potentials below 0.5 V vs. RHE for Cu-tmpa concentrations of 0.3 mM and 1.0  $\mu$ M (Appendix A.7). At the onset of the catalytic activity, significant amounts of H<sub>2</sub>O<sub>2</sub> are detected, both for catalyst concentrations of 0.3 mM (ca. 75%) and 1.0  $\mu$ M (ca. 90%) (Figure 2.3). A plateau of %H<sub>2</sub>O<sub>2</sub> is clearly visible at the catalytic onset at the lower concentration, while this is less pronounced at higher catalyst concentration. These percentages decrease with decreasing potential and upon

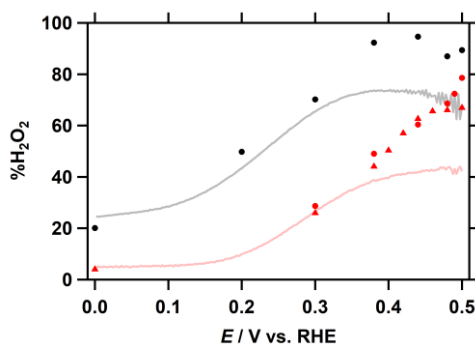


**Figure 2.3.** %H<sub>2</sub>O<sub>2</sub> obtained from RRDE CA (dots and triangles) and LSV (lines, 50 mV s<sup>-1</sup>) measurements as a function of applied potential at a rotation rate of 1600 RPM with 0.3 mM (red), and 1.0 μM (black) Cu-tmpa. Conditions: pH 7 PB ([PO<sub>4</sub>] = 100 mM), 293 K, Pt ring at 1.2 V vs. RHE.

reaching the limiting current potential regime the %H<sub>2</sub>O<sub>2</sub> stabilizes at 4% and 20% at 0.0 V vs. RHE for 0.3 mM and 1.0 μM Cu-tmpa, respectively. However, below 0.1 V a contribution of the GC electrode towards H<sub>2</sub>O<sub>2</sub> production cannot be excluded. These results show that a catalytic reaction that leads to the formation H<sub>2</sub>O<sub>2</sub> is active over the entire catalytic potential window.

$$\%H_2O_2 = \frac{2 \times (i_{ring}/N_{H2O2})}{i_{disk} + (i_{ring}/N_{H2O2})} \times 100 \quad (2.1)$$

Conversion of  $i_{disk}$  measured during RDE experiments to the kinetic current density ( $j_k$ ) allows for the evaluation of Tafel slopes of the ORR in the potential region where the current is not mass-transport limited. By plotting the applied potential as a function of the logarithm of  $j_k$  a Tafel plot can be constructed (Figure 2.4). As we are dealing with a homogeneous multi-electron, multistep catalytic reaction with several diffusing species, care should be taken not to over-interpret the Tafel slopes, or derive specific e<sup>-</sup>/(H<sup>+</sup>) transfer steps from the Tafel slope values. In the presence of O<sub>2</sub>, a clear change of Tafel slope from is seen around 0.38 V vs. RHE, while in the presence of H<sub>2</sub>O<sub>2</sub> under the exact same conditions no change in slope is observed. The observed slope change during ORR indicates that a different process becomes rate-determining. The potential at which this occurs closely matches the potential where half the limiting current is observed and is below the onset potential (ca. 0.45 V) of H<sub>2</sub>O<sub>2</sub> reduction by Cu-tmpa (Figure A.14). The Tafel slope observed for the reduction of H<sub>2</sub>O<sub>2</sub> by Cu-tmpa is very similar to the -136 mV/dec slope between 0.38 V and 0.20 V during the ORR, which indicates that the same step in the mechanism is rate-determining in this regime. Tafel slopes derived from measurements performed at low (1.0 μM) catalyst concentration show the same behaviour as at higher Cu-tmpa concentration (Figure A.15).

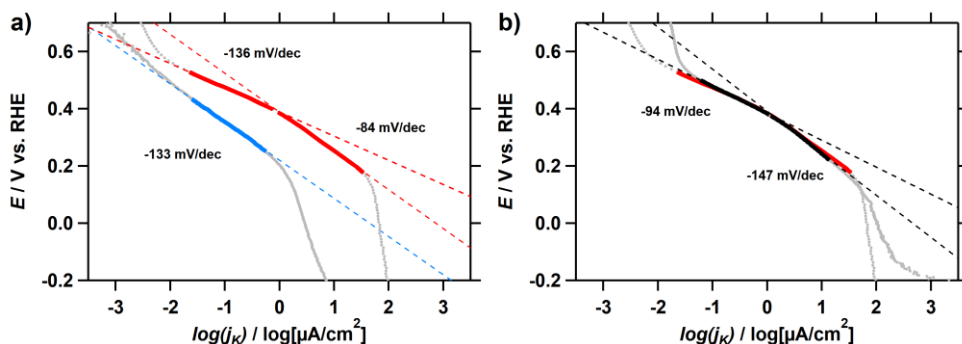


**Figure 2.4. a)** Plot of Tafel slopes derived from RRDE CV at 1600 RPM in the presence of 0.3 mM Cu-tmpa and 1 atm  $O_2$  (red lines) or 1.1 mM  $H_2O_2$  (blue line). **b)** Tafel slopes in the presence of 0.3 mM (red lines) and 1.0  $\mu M$  (black lines) Cu-tmpa under 1 atm  $O_2$ . Conditions: pH 7 PB ( $[PO_4] = 100$  mM), 293 K, 50 mV  $s^{-1}$  scan rate.

Turnover frequencies (TOFs,  $s^{-1}$ ) were obtained from electrochemical measurements; either by direct determination using the catalytic current enhancement,<sup>[35]</sup> or by applying the foot-of-the-wave analysis (FOWA).<sup>[34, 37-39]</sup> At the onset of the catalytic wave the catalytic reaction is assumed to be under kinetic conditions. As such, FOWA is not affected by side phenomena such as substrate consumption, catalyst deactivation, or product inhibition. It is therefore especially useful for the ORR, where substrate consumption plays an important role. If more reliable kinetic conditions can be achieved during catalysis, the observed first order rate constant  $k_{obs}$  (or TOF) for the ORR can be directly determined from the catalytic current enhancement ( $i_{cat}/i_p$ ) by applying Eq. 2.2.

$$\frac{i_{cat}}{i_p} = 2.24n \sqrt{\frac{RT}{Fv}} k_{obs} \quad (2.2)$$

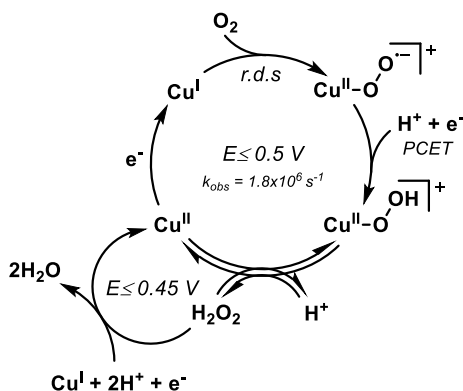
Here  $i_{cat}$  and  $i_p$  refer to the maximum catalytic current and the peak reductive current of the  $Cu^{(II/I)}$  redox couple, respectively (Figure 2.1).<sup>[35]</sup> From the current enhancement derived at low catalyst concentration (0.1–1.0  $\mu M$ ), a TOF of  $1.5 \times 10^5 \pm 0.2 \times 10^5 s^{-1}$  was obtained (Appendix A.9, Figure A.15). It is important to note that this TOF is associated with the overall 4e catalytic reaction. However, as shown by the RRDE measurements and Tafel slope analysis, there are two different rate-determining catalytic regimes. Interestingly, FOWA can be employed to determine the  $k_{obs}$  (or  $TOF_{max}$ ) associated with the partial reduction of  $O_2$  to  $H_2O_2$ , as FOWA only uses the foot of the catalytic wave where  $H_2O_2$  reduction rates are still negligible. The  $TOF_{max}$  for Cu-tmpa in pH 7 phosphate buffer in the presence of 1 atm  $O_2$  was found to be  $1.8 \times 10^6 \pm 0.6 \times 10^6 s^{-1}$ .



It has been firmly established by stopped-flow experiments that oxygen binding to  $[\text{Cu}^{\text{I}}(\text{tmpa})]^+$  proceeds via a fast equilibrium to initially produce  $[\text{Cu}^{\text{II}}(\text{O}_2^{\bullet-})(\text{tmpa})]^+$  as a detectable intermediate.<sup>[29]</sup> This species subsequently forms the  $[\{\text{Cu}^{\text{II}}(\text{tmpa})\}_2(\mu\text{-O}_2)]^{2+}$  dimer in a reaction that is consistently slower than the initial oxygen binding over a wide temperature and solvent range. If catalysis were to proceed via such a dimeric species, it should lead to a second order dependence in Cu-tmpa. Instead, the observed linearity in the FOWA region is in agreement with a catalytic first order relationship in catalyst (see Appendix A.9),<sup>[38]</sup> and is in good agreement with the first order catalyst concentration dependence discussed previously. That catalysis can indeed occur at a single site copper species was demonstrated previously using a site isolated immobilized copper phenanthroline system, albeit with a very low catalytic conversion to  $\text{H}_2\text{O}_2$ .<sup>[20]</sup>

The  $\text{TOF}_{\text{max}}$  associated with the first  $2\text{e}^-/2\text{H}^+$  reduction step to  $\text{H}_2\text{O}_2$  is the same, within the error margin, as the TOFs (also determined by FOWA) of the fastest iron porphyrin complexes ( $2.2 \times 10^6 \text{ s}^{-1}$ ) recently reported by Mayer *et al.*, which are the fastest homogeneous ORR catalysts in acetonitrile reported to date.<sup>[23, 48]</sup> When accounting for the oxygen solubility difference using  $\text{TOF} = k_{\text{O}_2}[\text{O}_2]$ , where  $[\text{O}_2] \approx 1.1 \text{ mM}$  in water ( $[\text{PO}_4] = 100 \text{ mM}$ ) under 1 atm  $\text{O}_2$ , the obtained second-order rate constant  $k_{\text{O}_2} = 1.6 \times 10^9 (\pm 0.5 \times 10^9) \text{ M}^{-1} \text{ s}^{-1}$  is an order of magnitude faster than the aforementioned iron porphyrins. This  $k_{\text{O}_2}$  is comparable to the second order rate constant of  $\text{O}_2$  binding,  $k_{\text{O}_2} = 1.3 \times 10^9 \text{ M}^{-1} \text{ s}^{-1}$ , found for  $\text{Cu}^{\text{I}}\text{-tmpa}$  in THF, which represents the fastest  $k_{\text{O}_2}$  among copper complexes and hemes; both synthetic and natural.<sup>[30]</sup>

The  $\%\text{H}_2\text{O}_2$  quantification and analysis of Tafel slopes derived from RRDE measurements provide a strong indication that the ORR goes through a stepwise mechanism (see Scheme 2.1). Herein  $\text{O}_2$  is first reduced to  $\text{H}_2\text{O}_2$ , which in turn is further reduced to  $\text{H}_2\text{O}$  upon reaching the required potential. In this case the overall reaction will still yield a catalytic electron transfer number close to 4 in the  $\text{O}_2$  mass-transport limited regime, as was established by KL and RRDE analysis. The onset potential of  $\text{H}_2\text{O}_2$  reduction by Cu-tmpa is around 0.45 V vs. RHE, roughly 50 mV lower than that of  $\text{O}_2$  reduction. The difference between onset potentials is small, which explains why  $\%\text{H}_2\text{O}_2$  quickly lowers upon decreasing the potential. At low catalyst concentration a catalyst diffusion effect is observed and  $\%\text{H}_2\text{O}_2$  is stable over a larger potential range before decreasing. This is expected as oxygen is a competitive inhibitor of  $\text{H}_2\text{O}_2$  reduction. Peroxide will accumulate more at low catalyst concentrations, whereas it is more rapidly reduced at higher catalyst loadings while maintaining the same amounts of oxygen in solution. As both the ORR Tafel slope below 0.38 V and the Tafel slope for  $\text{H}_2\text{O}_2$  reduction by Cu-tmpa are the same, it gives a strong indication the reduction of



**Scheme 2.1.** Proposed stepwise mechanism for the electrocatalytic ORR by Cu-tmpa in neutral aqueous solution. For clarity, the tmpa ligand is not depicted. PCET = proton-coupled electron transfer.

$\text{H}_2\text{O}_2$  to  $\text{H}_2\text{O}$  is rate determining in this potential window during the ORR. When FOWA is applied to determine the rate constant of the partial reduction of  $\text{O}_2$  to  $\text{H}_2\text{O}_2$ , linearity of the catalytic current is only observed when applying the FOWA expression corresponding to a first order catalytic system (see Appendix A.9). This shows that the partial reduction of  $\text{O}_2$  to  $\text{H}_2\text{O}_2$  is also first order in catalyst. The initial quantitative accumulation of hydrogen peroxide, the kink in the Tafel slope and its independence on the Cu-tmpa concentration, and the first order rate dependence in Cu-tmpa throughout point to two separate catalytic cycles, wherein  $\text{H}_2\text{O}_2$  is readily replaced in the coordination sphere of copper (see Scheme 2.1).

## 2.3. Conclusion

Our findings contrast the previously proposed dinuclear mechanism for the ORR by Cu-tmpa using sacrificial reductants in acetone, where fast  $\text{O}_2$  binding resulting in a copper superoxo species was followed by a slower dimerization step.<sup>[19]</sup> Under aqueous electrochemical conditions, fast electron transfer and high proton mobility resulting in a fast PCET step most likely favours the formation of the hydroperoxo complex over dimerization.

To conclude, the electrocatalytic ORR activity of Cu-tmpa in neutral aqueous solution was quantified, revealing very fast kinetics and high TOFs. The rate constants reported here are the first rate constants reported for the electrochemical reduction of  $\text{O}_2$  by a homogeneous copper complex. Application of the FOWA revealed that the TOF associated with the partial reduction of  $\text{O}_2$  is very close to the  $\text{O}_2$  binding constant with Cu-tmpa. This suggests that coordination of dioxygen to  $\text{Cu}^{\text{I}}$  is the rate determining step in the formation of peroxide. Additionally, we have shown that in aqueous solution the

ORR occurs at a single Cu-tmpa centre through a stepwise type mechanism, in which O<sub>2</sub> first undergoes 2-electron reduction to H<sub>2</sub>O<sub>2</sub>, followed by 2-electron reduction of H<sub>2</sub>O<sub>2</sub> to H<sub>2</sub>O. This stepwise mechanism was first mentioned as one of the possible mechanisms for Cu-tmpa by Asahi *et al.*, based on the ability of Cu-tmpa to catalyse the H<sub>2</sub>O<sub>2</sub> reduction.<sup>[32]</sup> However, until now there has been no direct evidence on whether a stepwise reaction actually takes place during ORR. This work provides new insight the oxygen reduction reaction mediated by copper, and opens new possibilities towards the electrochemical synthesis of hydrogen peroxide relevant to energy conversion reactions, given that peroxide is an excellent candidate as a renewable fuel.

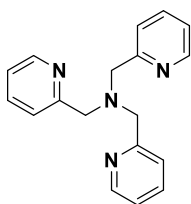
## 2.4. Experimental

### 2.4.1. General

Di-(2-picolyl)amine, 2-pyridinecarboxaldehyde, and sodium triacetoxyborohydride were obtained from Sigma Aldrich. Cu(OTf)<sub>2</sub> was obtained from Alfa Aesar. THF and CH<sub>3</sub>CN were obtained from Sigma-Aldrich and dried using a PureSolve 400 solvent dispenser. Filtration and isolation of the complex was done using Whatman<sup>®</sup> RC60 membrane filters. Aqueous electrolyte solutions were prepared using NaH<sub>2</sub>PO<sub>4</sub> (Suprapur<sup>®</sup>, Merck), Na<sub>2</sub>HPO<sub>4</sub> (Suprapur<sup>®</sup>, Merck), Na<sub>2</sub>SO<sub>4</sub> (Suprapur<sup>®</sup>, Merck), and NaOH (TraceSelect ≥ 99.9995%, Fluka). Elemental analysis was performed by Mikroanalytisches Laboratorium Kolbe. Milli-Q Ultrapure grade water was used for all electrochemical experiments and for the preparation of all aqueous electrolyte solutions. Alumina suspensions (1.0, 0.3, and 0.05 μm) were obtained from Buehler. pH measurements were done using a Hanna Instruments HI 4222 pH meter which was calibrated using IUPAC standard buffers.

### 2.4.2. Synthesis

#### 2.4.2.1. Synthesis of tris(2-pyridylmethyl)amine – tmpa

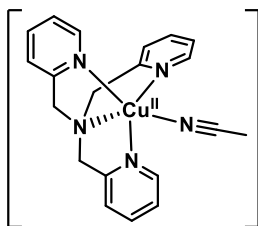


A modified literature procedure was used for the synthesis of tmpa.<sup>[49-50]</sup> Di-(2-picolyl)amine (4.0 mmol, 797 mg) and 2-pyridinecarboxaldehyde (4.0 mmol, 428 mg) were dissolved in dry THF (20 mL) under N<sub>2</sub> atmosphere. NaBH(OAc)<sub>3</sub> was added to the solution, followed by the addition of acetic acid (4.0 mmol, 0.229 mL). The reaction was stirred for 3 days at room temperature. The

reaction was quenched with sat. NaHCO<sub>3</sub> (10 mL). The mixture was extracted with EtOAc and the organic layer was washed with sat. NaHCO<sub>3</sub> (10 mL). The solvent was removed by rotary, and the product was dissolved in CHCl<sub>3</sub>. The solution was dried with MgSO<sub>4</sub> and filtered over a glass frit. Following removal of the solvent by rotary

evaporation, the product was obtained as off-white crystalline solid. Yield: 60% (2.40 mmol, 697 mg). ESI-MS:  $^1\text{H}$  NMR (400 MHz, Methanol- $d_4$ )  $\delta$  8.43 (ddd,  $J = 5.0, 1.9, 0.9$  Hz, 2H), 7.79 (td,  $J = 7.7, 1.8$  Hz, 2H), 7.68 (dt,  $J = 7.9, 1.1$  Hz, 2H), 7.27 (ddd,  $J = 7.6, 4.9, 1.3$  Hz, 2H), 3.85 (s, 4H). ESI MS  $m/z$  (calc): 291.2 (291.2,  $[\text{M} + \text{H}]^+$ ).

#### 2.4.2.2. Synthesis of $[\text{Cu}(\text{tmpa})(\text{CH}_3\text{CN})](\text{OTf})_2$ – Cu-tmpa



$\text{Cu}(\text{OTf})_2$  (0.60 mmol, 218 mg) and tmpa (0.60 mmol, 173 mg) were dissolved in dry  $\text{CH}_3\text{CN}$  (20 mL) under  $\text{N}_2$  atmosphere. A bright blue solution immediately formed, and the solution was allowed to stir for 1 hour.  $\text{Et}_2\text{O}$  (40 mL) was slowly added to the solution, and the complex was allowed to crystallize overnight at  $-18^\circ\text{C}$ . The crystals were filtered off and washed with  $\text{Et}_2\text{O}$ .

After dissolving the crystals in  $\text{CH}_3\text{CN}$ , the crystallization step was repeated to obtain the complex as blue crystals. Yield: 69% (0.41 mmol, 285 mg). ESI MS  $m/z$  (calc): 502.1 (502.0,  $[\text{M} - \text{CH}_3\text{CN} - \text{OTf}]^+$ ). Elemental analysis calcd (%) for  $\text{C}_{20}\text{H}_{18}\text{CuF}_6\text{N}_4\text{O}_6\text{S}_2 + 0.7 \text{CH}_3\text{CN} + 0.9 \text{H}_2\text{O}$ : C 36.88, H 3.17, N 9.45; found: C 37.09, H 3.42, N 9.24.

#### 2.4.3. Electrochemical measurements

Autolab PGSTAT 12, 204, and 128N potentiostats in combination with Autolab NOVA software were used for all measurements. All electrochemical measurements apart from RRDE and EQCM experiments were performed in a custom-build glass 10 mL single-compartment cell with a three-electrode setup. All glassware used during the electrochemical measurements were regularly cleaned to remove impurities by overnight submersion in an aqueous 0.5 M  $\text{H}_2\text{SO}_4$  solution containing 1 mg/mL  $\text{KMnO}_4$ , followed by removal of excess  $\text{KMnO}_4$  from the glassware with diluted  $\text{H}_2\text{SO}_4$  and  $\text{H}_2\text{O}_2$ . Finally, the glassware was subsequently rinsed five times and boiled two times in Milli-Q water. Prior to each experiment the glassware was boiled once in Milli-Q water. Glassy carbon (GC) was used as the working electrode and either a Teflon encapsulated GC rod ( $A = 0.0707 \text{ cm}^2$ , type 1, Alfa Aesar), or a PEEK encapsulated GC ( $A = 0.0707 \text{ cm}^2$ , Metrohm) were used in a submerged setup. Before every experiment the GC electrodes were manually polished with 1.0, 0.3, and 0.05  $\mu\text{m}$  alumina suspensions on Buehler cloth polishing pads, for 5 minutes respectively, followed by sonication in Milli-Q water for 15 minutes. A gold wire was used as the counter electrode and was flame annealed and rinsed with Milli-Q water before each experiment. As a reference electrode a Pt mesh was used as the reversible hydrogen electrode (RHE) in the same buffer solution as the working electrode, connected via a Luggin capillary, and continuously sparged with  $\text{H}_2$  gas. All gasses used during electrochemical measurements,  $\text{H}_2$ ,  $\text{O}_2$ , and Argon

(5.0 grade), were supplied by Linde. Oxygen-free electrolyte solutions were prepared by sparging the cell for 30 minutes with argon, after which a 1 atm argon atmosphere was maintained. Oxygen-saturated electrolyte solutions were obtained by sparging the cell for 20 minutes with O<sub>2</sub>, after which a 1 atm O<sub>2</sub> atmosphere was maintained.

## 2.5. References

- [1] H. A. Gasteiger, S. S. Kocha, B. Sompalli, F. T. Wagner, *Appl. Catal. B* **2005**, *56*, 9-35.
- [2] O. Gröger, H. A. Gasteiger, J.-P. Suchsland, *J. Electrochem. Soc.* **2015**, *162*, A2605-A2622.
- [3] E. I. Solomon, U. M. Sundaram, T. E. Machonkin, *Chem. Rev.* **1996**, *96*, 2563-2606.
- [4] V. Soukharev, N. Mano, A. Heller, *J. Am. Chem. Soc.* **2004**, *126*, 8368-8369.
- [5] N. Mano, V. Soukharev, A. Heller, *J. Phys. Chem. B* **2006**, *110*, 11180-11187.
- [6] C. F. Blanford, R. S. Heath, F. A. Armstrong, *Chem. Commun.* **2007**, 1710-1712.
- [7] J. A. Cracknell, K. A. Vincent, F. A. Armstrong, *Chem. Rev.* **2008**, *108*, 2439-2461.
- [8] C. F. Blanford, C. E. Foster, R. S. Heath, F. A. Armstrong, *Faraday Discuss.* **2009**, *140*, 319-335.
- [9] C. E. Elwell, N. L. Gagnon, B. D. Neisen, D. Dhar, A. D. Spaeth, G. M. Yee, W. B. Tolman, *Chem. Rev.* **2017**, *117*, 2059-2107.
- [10] E. A. Lewis, W. B. Tolman, *Chem. Rev.* **2004**, *104*, 1047-1076.
- [11] J. Serrano-Plana, I. Garcia-Bosch, A. Company, M. Costas, *Acc. Chem. Res.* **2015**, *48*, 2397-2406.
- [12] S. Hong, Y.-M. Lee, K. Ray, W. Nam, *Coord. Chem. Rev.* **2017**, *334*, 25-42.
- [13] L. M. Mirica, X. Ottenwaelder, T. D. P. Stack, *Chem. Rev.* **2004**, *104*, 1013-1046.
- [14] P. Vasudevan, Santosh, N. Mann, S. Tyagi, *Transit Met Chem* **1990**, *15*, 81-90.
- [15] J. Zhang, F. C. Anson, *J. Electroanal. Chem.* **1992**, *341*, 323-341.
- [16] J. Zhang, F. C. Anson, *J. Electroanal. Chem.* **1993**, *348*, 81-97.
- [17] J. Zhang, F. C. Anson, *Electrochim. Acta* **1993**, *38*, 2423-2429.
- [18] C. C. L. McCrory, X. Ottenwaelder, T. D. P. Stack, C. E. D. Chidsey, *J. Phys. Chem. A* **2007**, *111*, 12641-12650.
- [19] S. Fukuzumi, H. Kotani, H. R. Lucas, K. Doi, T. Suenobu, R. L. Peterson, K. D. Karlin, *J. Am. Chem. Soc.* **2010**, *132*, 6874-6875.
- [20] C. C. L. McCrory, A. Devadoss, X. Ottenwaelder, R. D. Lowe, T. D. P. Stack, C. E. D. Chidsey, *J. Am. Chem. Soc.* **2011**, *133*, 3696-3699.
- [21] M. A. Thorseth, C. S. Letko, E. C. M. Tse, T. B. Rauchfuss, A. A. Gewirth, *Inorg. Chem.* **2013**, *52*, 628-634.
- [22] S. Kakuda, R. L. Peterson, K. Ohkubo, K. D. Karlin, S. Fukuzumi, *J. Am. Chem. Soc.* **2013**, *135*, 6513-6522.
- [23] M. L. Pegis, C. F. Wise, D. J. Martin, J. M. Mayer, *Chem. Rev.* **2018**, *118*, 2340-2391.
- [24] S. Fukuzumi, Y.-M. Lee, W. Nam, *ChemCatChem* **2018**, *10*, 9-28.
- [25] K. D. Karlin, J. C. Hayes, S. Juen, J. P. Hutchinson, J. Zubieta, *Inorg. Chem.* **1982**, *21*, 4106-4108.
- [26] K. D. Karlin, S. Kaderli, A. D. Zuberbühler, *Acc. Chem. Res.* **1997**, *30*, 139-147.
- [27] A. Wada, Y. Honda, S. Yamaguchi, S. Nagatomo, T. Kitagawa, K. Jitsukawa, H. Masuda, *Inorg. Chem.* **2004**, *43*, 5725-5735.
- [28] K. D. Karlin, N. Wei, B. Jung, S. Kaderli, P. Niklaus, A. D. Zuberbuehler, *J. Am. Chem. Soc.* **1993**, *115*, 9506-9514.
- [29] C. X. Zhang, S. Kaderli, M. Costas, E.-i. Kim, Y.-M. Neuhold, K. D. Karlin, A. D. Zuberbühler, *Inorg. Chem.* **2003**, *42*, 1807-1824.
- [30] H. C. Fry, D. V. Scaltrito, K. D. Karlin, G. J. Meyer, *J. Am. Chem. Soc.* **2003**, *125*, 11866-11871.
- [31] M. A. Thorseth, C. S. Letko, T. B. Rauchfuss, A. A. Gewirth, *Inorg. Chem.* **2011**, *50*, 6158-6162.
- [32] M. Asahi, S.-i. Yamazaki, S. Itoh, T. Ioroi, *Dalton Trans.* **2014**, *43*, 10705-10709.
- [33] M. Asahi, S.-i. Yamazaki, S. Itoh, T. Ioroi, *Electrochim. Acta* **2016**, *211*, 193-198.
- [34] C. Costentin, S. Drouet, M. Robert, J.-M. Savéant, *J. Am. Chem. Soc.* **2012**, *134*, 11235-11242.
- [35] R. M. Bullock, A. M. Appel, M. L. Helm, *Chem. Commun.* **2014**, *50*, 3125-3143.
- [36] A. M. Appel, M. L. Helm, *ACS Catal.* **2014**, *4*, 630-633.
- [37] E. S. Rountree, B. D. McCarthy, T. T. Eisenhart, J. L. Dempsey, *Inorg. Chem.* **2014**, *53*, 9983-10002.

- [38] C. Costentin, J.-M. Savéant, *ChemElectroChem* **2014**, *1*, 1226-1236.
- [39] D. J. Wasylenko, C. Rodríguez, M. L. Pegis, J. M. Mayer, *J. Am. Chem. Soc.* **2014**, *136*, 12544-12547.
- [40] D. J. Martin, B. D. McCarthy, E. S. Rountree, J. L. Dempsey, *Dalton Trans.* **2016**, *45*, 9970-9976.
- [41] C. Costentin, D. G. Nocera, C. N. Brodsky, *Proc. Natl. Acad. Sci.* **2017**, *114*, 11303-11308.
- [42] C. Costentin, J.-M. Savéant, *J. Am. Chem. Soc.* **2017**, *139*, 8245-8250.
- [43] N. D. Schley, J. D. Blakemore, N. K. Subbaiyan, C. D. Incarvito, F. D'Souza, R. H. Crabtree, G. W. Brudvig, *J. Am. Chem. Soc.* **2011**, *133*, 10473-10481.
- [44] D. G. H. Hetterscheid, C. J. M. van der Ham, O. Diaz-Morales, M. W. G. M. Verhoeven, A. Longo, D. Banerjee, J. W. Niemantsverdriet, J. N. H. Reek, M. C. Feiters, *Phys. Chem. Chem. Phys.* **2016**, *18*, 10931-10940.
- [45] D. G. H. Hetterscheid, *Chem. Commun.* **2017**, *53*, 10622-10631.
- [46] B. van Dijk, J. P. Hofmann, D. G. H. Hetterscheid, *Phys. Chem. Chem. Phys.* **2018**, *20*, 19625-19634.
- [47] P. A. Malachuk, L. S. Marcoux, R. N. Adams, *J. Phys. Chem.* **1966**, *70*, 4068-4070.
- [48] M. L. Pegis, B. A. McKeown, N. Kumar, K. Lang, D. J. Wasylenko, X. P. Zhang, S. Raagei, J. M. Mayer, *ACS Cent. Sci.* **2016**, *2*, 850-856.
- [49] J. Wang, C. Li, Q. Zhou, W. Wang, Y. Hou, B. Zhang, X. Wang, *Dalton Trans.* **2016**, *45*, 5439-5443.
- [50] A. Podgoršek, M. Zupan, J. Iskra, *Angew. Chem. Int. Ed.* **2009**, *48*, 8424-8450.



## Chapter 3

---

### Mechanistic study of the activation and the electrocatalytic reduction of hydrogen peroxide by Cu-tmpa in neutral aqueous solution

*Hydrogen peroxide plays an important role as an intermediate and product in the reduction of dioxygen by copper enzymes and mononuclear copper complexes. The copper(II) tris(2-pyridylmethyl)amine complex (Cu-tmpa) has been shown to produce  $H_2O_2$  as an intermediate during the electrochemical 4-electron reduction of  $O_2$ . We investigated the electrochemical hydrogen peroxide reduction reaction (HPRR) by Cu-tmpa in a neutral aqueous solution. The catalytic rate constant of the reaction was shown to be one order of magnitude lower than the reduction of dioxygen. A significant solvent kinetic isotope effect (KIE) of 1.4 to 1.7 was determined for the reduction of  $H_2O_2$ , pointing to a Fenton-like reaction pathway as the likely catalytic mechanism, involving a single copper site that produces an intermediate copper(II) hydroxyl species and a free hydroxyl radical anion in the process.*

Adapted from M. Langerman, D. G. H. Hetterscheid, *ChemElectroChem* **2021**, 8, 2783.



### 3.1. Introduction

The formation, decomposition, and reduction of  $\text{H}_2\text{O}_2$  plays an important role in many (bio)chemical processes, such as oxidation reactions,<sup>[1-4]</sup> fuel cell chemistry,<sup>[5-8]</sup> and enzymatic reactions. Many peroxidases and catalases scavenge and disproportionate  $\text{H}_2\text{O}_2$  into  $\text{O}_2$  and  $\text{H}_2\text{O}$  to prevent formation of reactive oxygen species (ROS) that induce damage to their hosts.<sup>[9-10]</sup> In the context of elucidating the oxidative catalytic reactions taking place at the active sites of these enzymes, often containing copper, iron, or manganese ions, many synthetic mimic catalysts have been synthesized and studied intensively.<sup>[11-15]</sup>

Of particular interest are lytic polysaccharide monooxygenases (LPMOs), a family of copper-containing enzymes that are able to degrade lignocellulosic biomass.<sup>[16-20]</sup> Over the last decade, since the discovery of the LPMO family of enzymes, significant scientific effort has been put into the determination of the structure and active site of LPMOs. It was revealed that all LPMOs contain a type II copper centre as their active site in a  $\text{Cu}^{\text{II}}$  resting state, with little variation in the primary coordination sphere for the different LPMOs.<sup>[18, 21]</sup> The primary coordination sphere is formed by the coordination of three N ligands in a T-shaped geometry around the copper centre, with the whole primary coordination sphere conforming to either a tetrahedral or trigonal-bipyramidal geometry. The N ligands comprise a monodentate histidine and a bidentate histidine, coordinating with both the imidazole and backbone nitrogen coordinating to the copper centre, the so-called histidine brace. Polysaccharides are cleaved by LPMOs through an oxidative mechanism, and it was shown that both  $\text{O}_2$  and  $\text{H}_2\text{O}_2$  can act as the oxidant. Additionally, in the absence of polysaccharide substrate,  $\text{H}_2\text{O}_2$  is produced by the enzyme in the presence of  $\text{O}_2$ . This behaviour shows similarities to that of Cu-tmpa (tmpa = tris(2-pyridylmethyl)amine), which can both reduce  $\text{O}_2$  and  $\text{H}_2\text{O}_2$ , while also producing  $\text{H}_2\text{O}_2$  as a detectable intermediate during the catalytic cycle. Density functional theory (DFT) calculations of LPMO systems have shown that the most likely catalytic species responsible for the cleavage of polysaccharides is a copper oxyl radical ( $\text{Cu}^{\text{II}}\text{-O}^{\bullet}$ ) species. Several different routes have been suggested for the catalytic pathway.<sup>[22]</sup> Fenton chemistry plays an important role in many of these processes, and it has been shown that Fenton-like reactions can take place between  $\text{Cu}^{\text{I}}$  complexes and  $\text{H}_2\text{O}_2$ , resulting in the homolytic cleavage of the O-O bond.<sup>[23-24]</sup>

Another enzyme that shows similarities to both the LPMOs and Cu-tmpa, is the particulate methane monooxygenase (pMMO), which activates and reduces dioxygen in order to oxidize methane to methanol. Many conflicting suggestions have been proposed on the nature of the  $\text{Cu}_B$  active site in pMMO, which was either considered a mononuclear or dinuclear copper centre,<sup>[21, 25-29]</sup> but recent experimental work points towards a catalytic centre containing a mononuclear copper ion in a square pyramidal

geometry and includes a histidine brace similar to the LPMOs.<sup>[30]</sup>

How hydrogen peroxide is formed and activated is a very important research question, taking into account potential applications of this chemistry. In traditional polymer electrolyte membrane (PEM) fuel cells, formation of  $\text{H}_2\text{O}_2$  is considered undesirable as it leads to both catalyst poisoning and damaging of the proton exchange membrane.<sup>[5, 31-34]</sup> However, more recently hydrogen peroxide has also been suggested as an alternative sustainable fuel or oxidant in fuel cells, owing to the broad range of standard equilibrium potentials associated with  $\text{H}_2\text{O}_2$ .<sup>[8, 35-38]</sup> Currently, the bulk of  $\text{H}_2\text{O}_2$  is synthesized through the anthraquinone process, which uses several different catalysts (Pd or Ni), creates significant amount of waste products, and requires expensive separation steps in order to obtain concentrated  $\text{H}_2\text{O}_2$ .<sup>[39]</sup> As such, despite the use of  $\text{H}_2\text{O}_2$  as a sustainable oxidant in many chemical reaction, it's production is not sustainable.<sup>[3, 40]</sup> Indeed, electrochemical synthesis by selective 2-electron reduction of  $\text{O}_2$  at low overpotentials would be a more desirable approach to obtain  $\text{H}_2\text{O}_2$ .

Understanding how hydrogen peroxide is activated and reduced at copper sites and what drives the 4-electron versus the 2-electron selectivity for the reduction of  $\text{O}_2$  by copper catalysts is essential for the design of new catalysts for the oxygen reduction reaction, and the electrochemical production of  $\text{H}_2\text{O}_2$ . Here, we report our findings on the electrocatalytic behaviour of Cu-tmpa towards the hydrogen peroxide reduction reaction (HPRR) under neutral aqueous conditions, resulting in solvent kinetic isotope effects (KIE), rate orders, and catalytic rate constants. Based on this, we propose a catalytic mechanism for the Cu-tmpa catalysed HPRR.

## 3.2. Results and discussion

### 3.2.1. Electrocatalytic reduction of hydrogen peroxide by Cu-tmpa

The electrochemical behaviour of Cu-tmpa towards the ORR was extensively discussed in the previous chapter, where it was shown that the reduction of  $\text{H}_2\text{O}_2$  to  $\text{H}_2\text{O}$  is an essential part of the catalytic cycle to achieve the four-electron reduction of  $\text{O}_2$  to  $\text{H}_2\text{O}$ . Thus, the electrocatalytic reduction of  $\text{H}_2\text{O}_2$  by Cu-tmpa in a phosphate buffer (PB) solution of pH 7, containing 100 mM phosphate salts ( $\text{NaH}_2\text{PO}_4$  and  $\text{Na}_2\text{HPO}_4$ ), was investigated in detail and the results are discussed in this chapter. In Figure 3.1a, a CV measured in the aforementioned solution in the presence of 1.1 mM  $\text{H}_2\text{O}_2$  shows a peak-shaped catalytic wave. The catalytic half-wave potential ( $E_{\text{cat}/2}$ ) of this catalytic wave is situated at 0.34 V vs. RHE, which is close to the values for the ORR of 0.31 V (Chapter 2) to 0.33 V (this work) vs. RHE observed under stationary conditions. For both the HPRR and the ORR a catalytic peak potential of 0.26 V was found. Additionally, a

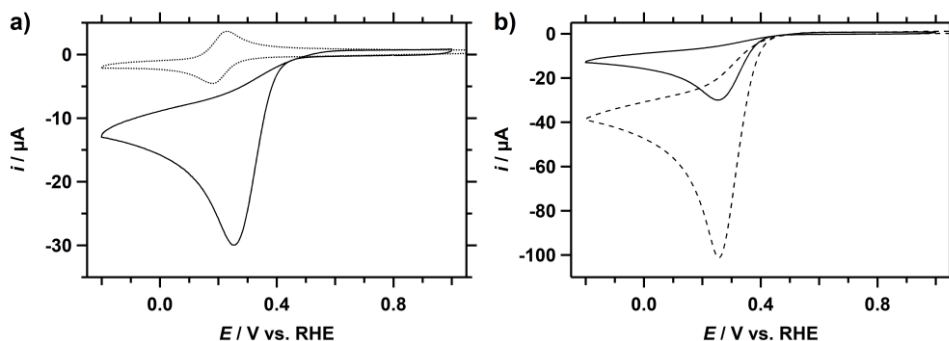


**Figure 3.1 a)** CVs of Cu-tmpa (0.30 mM) in the presence of 1 atm Ar (dotted) or 1.1 mM H<sub>2</sub>O<sub>2</sub> (solid).  $E_{cat/2}$  = 0.34 V vs. RHE. **b)** Comparison of CVs of 1.1 mM H<sub>2</sub>O<sub>2</sub> (solid) and 1 atm O<sub>2</sub> (dashed) reduction by Cu-tmpa (0.30 mM). Conditions: pH 7 PB ([PO<sub>4</sub>] = 100 mM), 293 K, 100 mV s<sup>-1</sup> scan rate, 0.0707 cm<sup>2</sup> electrode surface area.

comparison of the CVs of the electrochemical reduction of H<sub>2</sub>O<sub>2</sub> and O<sub>2</sub> reveals that the peak catalytic current ( $i_{cat}$ ) for the HPRR (30 μA) is less than a third of that of ORR (100 μA), as shown in Figure 3.1b. While a lower  $i_{cat}$  can be an indication of a slower catalytic reaction, this only holds true if the substrate and catalytic mechanism are the same when comparing between CV measurements. This is clearly not the case for the ORR and HPRR, and the large difference in peak catalytic current can be explained by the difference in catalytic electron transfer number  $n$  of the reaction and the diffusion coefficient  $D$  of the substrate. Thus, considering the different electron transfer number for the ORR ( $n = 4$ ) and the HPRR ( $n = 2$ ), a  $D_{O_2}$  of  $2 \times 10^{-5}$  cm<sup>2</sup> s<sup>-1</sup>, and a  $D_{H_2O_2}$  of  $0.6$ – $1.4 \times 10^{-5}$  cm<sup>2</sup> s<sup>-1</sup>,<sup>[41-42]</sup> an expected ratio between the respective peak catalytic currents ( $i_{cat,H_2O_2}/i_{cat,O_2}$ ) can be determined. If the HPRR is limited in H<sub>2</sub>O<sub>2</sub> concentration, as was the case for O<sub>2</sub> during the ORR for this catalyst, and  $i_{cat}$  is therefore not determined by the catalytic rate constant or catalyst concentration, a  $i_{cat,H_2O_2}/i_{cat,O_2}$  ratio in the range of 0.27 to 0.42 is expected. The  $i_{cat,H_2O_2}/i_{cat,O_2}$  derived from the CVs in Figure 3.1b falls within the calculated ratio, indicating that the HPRR is also limited in substrate concentration at 1.1 mM H<sub>2</sub>O<sub>2</sub> and a Cu-tmpa concentration of 0.3 mM.

### 3.2.2. Catalyst concentration dependence

The relationship between the catalytic current and the catalyst concentration was investigated by determining the peak catalytic current at a low catalyst concentration range (1.0–2.5 μM), in the presence of 1.1 mM H<sub>2</sub>O<sub>2</sub>. While the GC electrode showed no activity towards the reduction of H<sub>2</sub>O<sub>2</sub>, background correction was applied to the CV to remove contributions in the range of 0.5 to 1 μA from the GC double layer. The resulting linear sweep voltammograms (LSV) are shown in Figure 3.2a. For each Cu-tmpa concentration, the peak current is visible around 0.23 V vs. RHE, with an  $E_{cat/2}$  at

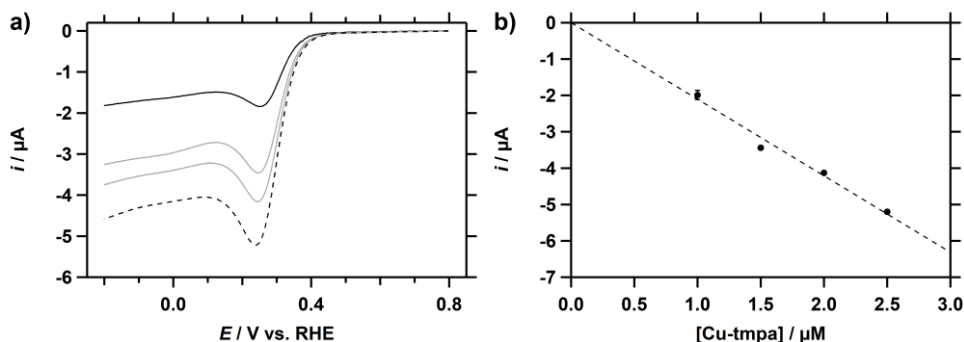


**Figure 3.2 a)** Background corrected linear sweep voltammograms (LSV) of the reduction of  $\text{H}_2\text{O}_2$  (1.1 mM) for different concentrations of Cu-tmpa; 1.0 (solid black)/1.5/2.0/2.5 (dashed)  $\mu\text{M}$ . **b)** The peak catalytic current  $i_{\text{cat}}$  taken at 0.23 V vs. RHE plotted against the catalyst concentration. Conditions: pH 7 PB ( $[\text{PO}_4] = 100 \text{ mM}$ ), 293 K,  $100 \text{ mV s}^{-1}$  scan rate.

0.31 V. Both potentials have shifted closer to the redox potential of the catalyst compared to the  $E_{\text{cat}}$  and  $E_{\text{cat}/2}$  observed at high catalyst concentration, which is expected when substrate diffusion limitations play a lesser role during catalysis. For the HPRR, a linear relationship is observed between the  $i_{\text{cat}}$  and the Cu-tmpa concentration (Figure 3.2b), as was also shown for the Cu-tmpa catalysed ORR. A plot of  $\log(i_{\text{cat}})$  as a function of the logarithm of the catalyst concentration has a slope of 1.05 ( $R^2 = 0.96$ ), confirming the first-order nature of the catalytic reaction (Figure B.1). Additionally, the same experiment performed at higher  $\text{H}_2\text{O}_2$  concentration of 10 mM over a Cu-tmpa concentration range from 1 to 10  $\mu\text{M}$  showed the same first-order dependence in catalyst concentration (see Figure B.2).

### 3.2.3. Relationship between hydrogen peroxide concentration and catalytic activity.

As opposed to  $\text{O}_2$ , it is far more straightforward to increase the concentration of  $\text{H}_2\text{O}_2$  in the solution to study the relationship between the substrate concentration and the catalytic reaction. CVs were measured in a PB pH 7 electrolyte solution containing Cu-tmpa and different  $\text{H}_2\text{O}_2$  concentrations ranging from 1.1 to 30 mM. These CVs show the familiar peak shaped catalytic wave around 0.25 V vs. RHE (Figure 3.3a), but from a  $\text{H}_2\text{O}_2$  concentration of 20 mM and upwards a shoulder or second reduction event appears below 0.1 V in the CV, and becomes clearly visible at 30 mM. Expanding the concentration range to 100 mM shows that the peak current of this second catalytic wave keeps increasing with the increasing  $\text{H}_2\text{O}_2$  concentration, while the peak current of the first catalytic stays the same. Moreover, the potential at which the peak catalytic current of this reduction is reached also shifts more negatively with increasing concentration. Another observation is that an oxidation event appears in the positive

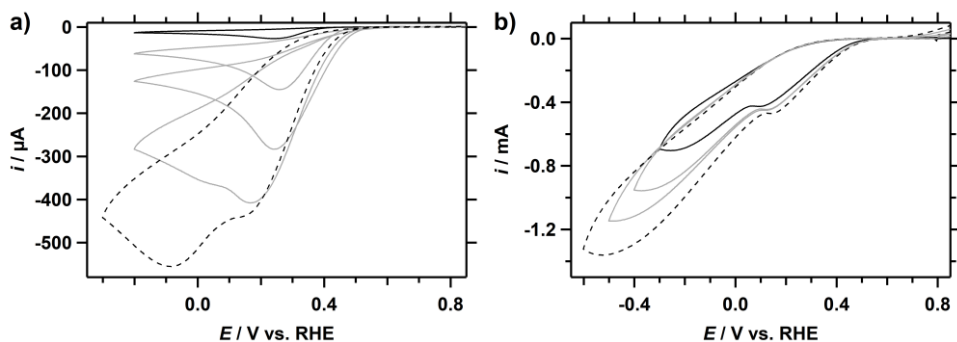


**Figure 3.3.** CVs of the reduction of  $\text{H}_2\text{O}_2$  in the presence of 0.3 mM Cu-tmpa for a range of  $\text{H}_2\text{O}_2$  concentrations under 1 atm Ar; **a)** 1.1 (solid black)/5.0/10/20/30 (dashed) mM, **b)** 40 (solid black)/60/80/100 (dashed) mM. Conditions: pH 7 PB ( $[\text{PO}_4] = 100 \text{ mM}$ ), 293 K,  $100 \text{ mV s}^{-1}$  scan rate.

potential window above 0.6 V vs. RHE at  $\text{H}_2\text{O}_2$  concentrations of 40 mM and higher (Figure B.3a). Although this oxidation could be the result of scanning to a lower potential, both the 30 and 40 mM  $\text{H}_2\text{O}_2$  measurements have the same potential window, yet this oxidation is only present in the CVs corresponding to the solution containing 40 mM  $\text{H}_2\text{O}_2$  and higher. Therefore, it is more likely that the observed oxidation is related to the increased peroxide concentration. The onset of this catalytic oxidation is close to the standard reduction potential for the oxidation of  $\text{H}_2\text{O}_2$  to  $\text{O}_2$  ( $E^0 = 0.695 \text{ V vs. RHE}$ ), making the 2-electron oxidation of  $\text{H}_2\text{O}_2$  the most likely candidate for the observed  $\text{H}_2\text{O}_2$ -concentration dependent oxidation. The GC electrode is not able to activate  $\text{H}_2\text{O}_2$  in neutral solution at these low potentials, as it was only shown to catalyse the oxidation above 1.4 V vs. RHE in a PB pH 7.4 buffer (though at 1.0 mM  $\text{H}_2\text{O}_2$ ),<sup>[43]</sup> while under basic conditions ( $> \text{pH } 10$ ) oxidation was observed above 0.9 V vs. RHE while rotating (250 mM  $\text{H}_2\text{O}_2$ ).<sup>[44]</sup> To confirm this, CVs were measured with a GC electrode in a PB pH 7 electrolyte solutions containing  $\text{H}_2\text{O}_2$  concentrations ranging from 1.5 to 500 mM (Figure B.3b). No anodic currents were observed in the absence of Cu-tmpa, showing the involvement of the copper complex in apparent oxidation of  $\text{H}_2\text{O}_2$ .

A plot of the peak catalytic current  $i_{\text{cat}}$  derived from the obtained CVs versus the  $\text{H}_2\text{O}_2$  concentration, reveals two different regimes where reduction of hydrogen peroxide takes place (Figure 3.4a). A linear relationship between  $i_{\text{cat}}$  and the concentration is apparent at low concentrations of  $\text{H}_2\text{O}_2$ , but above 30 mM the catalytic current of the first reductive wave is no longer dependent on the substrate concentration. When the second catalytic wave at lower potential is considered, it clearly shows that the corresponding  $i_{\text{cat},2}$  still has a mostly linear dependency on  $\text{H}_2\text{O}_2$  concentration (Figure 3.4b), although a slight deviation from an ideal linear relationship

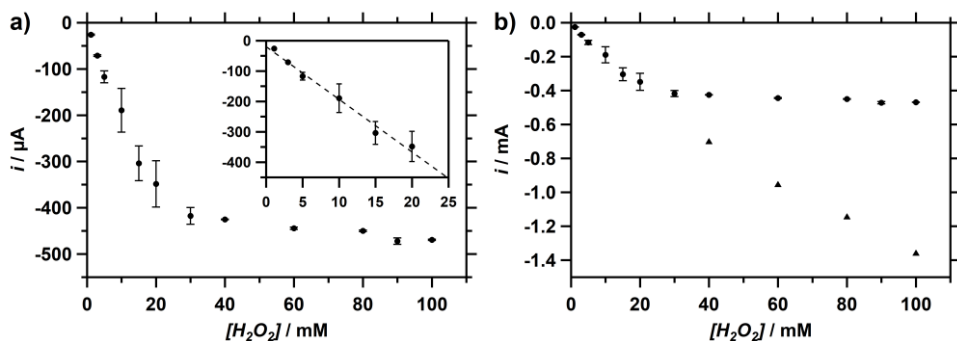


**Figure 3.4.** **a)** Catalytic current as a function of  $\text{H}_2\text{O}_2$  concentration in the presence of 0.3 mM Cu-tmpa, showing a  $[\text{H}_2\text{O}_2]$  dependent (zoom in inset) and independent regime. **b)** An expanded view including the  $i_{\text{cat}}$  values of the 2<sup>nd</sup> catalytic reduction (triangles). Conditions: pH 7 PB ( $[\text{PO}_4] = 100 \text{ mM}$ ), 293 K, 100 mV  $\text{s}^{-1}$  scan rate.

is visible at higher concentrations. These results show that the reduction reaction of  $\text{H}_2\text{O}_2$  to water is both first-order in  $\text{H}_2\text{O}_2$  and Cu-tmpa.

The existence of two distinct catalytic waves can be related to the buffer capacity of the electrolyte solution at pH 7. As the hydrogen peroxide concentration is approaching that of phosphate buffer in the electrolyte solution at these higher concentrations, the buffering ability of the solution can become compromised. This would result in significantly increased pH gradient close to the electrode surface. Thus, the appearance of a second catalytic reduction at a lower potential is likely the result of a shift in proton source for the reduction of  $\text{H}_2\text{O}_2$  to  $\text{H}_2\text{O}$ , possibly from  $\text{H}_2\text{O}$  or even  $\text{H}_2\text{O}_2$  itself, as the  $\text{pK}_a$  of hydrogen peroxide is 11.75 in water.

### 3.2.4. Kinetic isotope effect studies of the peroxide reduction reaction

To get more insight into the rate-determining step in the mechanism of the electrocatalytic reduction of  $\text{H}_2\text{O}_2$ , solvent kinetic isotope effects (KIE) were determined. Cyclic voltammograms were measured in a 0.1 M phosphate buffer (pH 7) solution containing 0.3 mM Cu-tmpa. Both deuterated and non-deuterated phosphate buffers contained the same concentration and ratio of phosphate salts (0.1 M). The  $\text{pH}^*$ , defined as the apparent pH directly determined from a  $\text{H}_2\text{O}$  calibrated pH meter in a  $\text{D}_2\text{O}$  solution, of the deuterated solution was determined to be 7.13. Using Eq. 3.1 to convert the  $\text{pH}^*$  to the pH,<sup>[45]</sup> this  $\text{pH}^*$  value corresponds to a pH of 7.03. This agrees well with the pH of 7.01 that was measured for the non-deuterated electrolyte solution. The pD can in turn be calculated using Eq. 3.2, resulting in a pD of 7.58.

$$\text{pH} = 0.929 \times \text{pH}^* + 0.41 \quad (3.1)$$

$$\text{pD} = \text{pH}^* + 0.45 \quad (3.2)$$

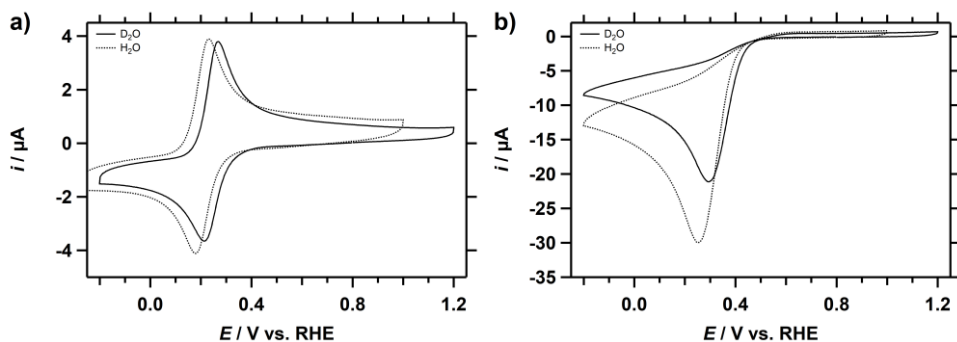


**Figure 3.5. a)** CVs of 0.3 mM Cu-tmpa under 1 atm Ar in a deuterated (solid) and non-deuterated (dotted) PB electrolyte solution. **b)** CVs of the catalytic reduction of  $\text{H}_2\text{O}_2$  (1.1 mM under 1 atm Ar) by Cu-tmpa in a deuterated (solid) and non-deuterated (dotted) PB electrolyte solution. Conditions: pH 7 PB ( $[\text{PO}_4] = 100$  mM), 293 K,  $100 \text{ mV s}^{-1}$  scan rate.

In the presence of 1 atm argon, and in the absence of hydrogen peroxide, the  $E_{1/2}$  of the Cu-tmpa redox couple is positively shifted by 37 mV in the deuterated phosphate buffer compared to the non-deuterated phosphate buffer (Figure 3.5a). Saturating the deuterated electrolyte solution in the RHE compartment with  $\text{H}_2$  instead of  $\text{D}_2$  is the likely cause of this, the observed potential shift being similar to the difference in equilibrium potential  $E^\circ$  for the  $\text{H}^+/\text{H}_2$  and  $\text{D}^+/\text{D}_2$  couples.<sup>[46-47]</sup> Upon the addition of 1.1 mM  $\text{H}_2\text{O}_2$  to the electrolyte solutions, a clear difference in catalytic rates can be observed between the deuterated and non-deuterated electrolyte solutions (Figure 3.5b). As with the redox couple in the absence of substrate, the  $E_{\text{cat}/2}$  of the catalytic wave is positively shifted by 37 mV in the deuterated solution. More striking is the decrease of the peak catalytic current  $i_{\text{cat}}$  in the deuterated solution, from 30 to 20  $\mu\text{A}$ .

Conversely, when the catalytic activity of Cu-tmpa towards the ORR in deuterated PB (pH 7) electrolyte solution in the presence of 1 atm  $\text{O}_2$  is investigated by cyclic voltammetry (Figure 3.6), the catalytic half-wave potential  $E_{\text{cat}/2}$  is again shifted positively by 37 mV. The difference of the  $i_{\text{cat}}$  between the deuterated solution and the non-deuterated solution is only 5  $\mu\text{A}$ , which is insignificant compared to the difference observed for the  $\text{H}_2\text{O}_2$  reduction. This is in line with the observations that the electrocatalytic ORR by Cu-tmpa is severely rate-limited in the mass-transport of  $\text{O}_2$  at a Cu-tmpa concentration of 0.3 mM,<sup>[48]</sup> and suggests that this is the case in both non-deuterated and deuterated electrolyte solutions.

The KIE is defined as the ratio between the catalytic rate constants in aqueous and deuterated solutions. The electrocatalytic rate constant is directly proportional to the catalytic current enhancement, e.g. the squared ratio of  $i_{\text{cat}}$  over  $i_p$ , where the  $i_p$  is the peak reductive current of the  $\text{Cu}^{\text{II/I}}$  redox couple. Thus, the KIE can be determined by applying Eq. 3.3 to the values obtained from the CVs under both conditions.

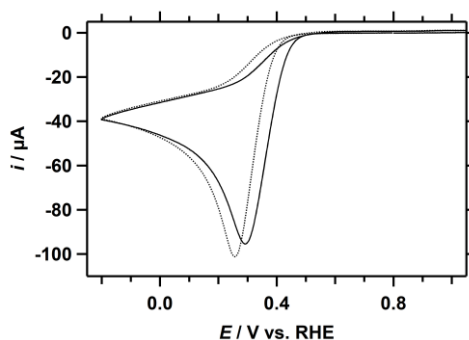


**Figure 3.6.** CVs of the catalytic reduction of O<sub>2</sub> (1 atm) by Cu-tpma (0.3 mM) in a deuterated (solid) and non-deuterated (dotted) PB electrolyte solution. Conditions: pH 7 PB ([PO<sub>4</sub>] = 100 mM), 293 K, 100 mV s<sup>-1</sup> scan rate.

$$KIE = \frac{k_{obs,H}}{k_{obs,D}} \propto \frac{(i_{cat}/i_p)_H^2}{(i_{cat}/i_p)_D^2} \quad (3.3)$$

This resulted in a solvent KIE value of 1.65 for the reduction of hydrogen peroxide, which indicates that breaking of an O–H bond is involved in the rate-determining step of the catalytic reaction. While the determined KIE value is not particularly large, it is in the range of KIEs that are associated with homolytic cleavage of the O–O bond of the Cu<sup>II</sup>-OOH, in conjunction with a proton transfer.<sup>[49–51]</sup> However, it was shown in section 3.2.1 and 3.2.3 that the HPRR by Cu-tpma is mass-transport limited in H<sub>2</sub>O<sub>2</sub> under the experimental conditions used here, which may underestimate the KIE obtained from  $i_{cat}$  derived from the CVs in Figure 3.5b. Directly deriving the rate constants under non mass-transport limiting conditions, will result in a more accurate determination of the KIE.

### 3.2.5. Reaction kinetics and FOWA of the HPRR

While a quick analysis of cyclic voltammograms of the ORR and HPRR by Cu-tpma (Figure 3.1b) already reveals that HPRR by Cu-tpma is significantly slower than ORR under the same catalytic conditions and substrate concentrations, the rate constants of the reaction can be determined via foot-of-the-wave analysis (FOWA) or by direct determination using the catalytic current enhancement. Using the FOWA method to determine rate constants, only the beginning of the catalytic wave is used, a region which is not affected by substrate consumption, catalyst deactivation, product inhibition or other side phenomena. In this way the ideal or maximum turnover frequency associated with the catalytic reaction can be determined.<sup>[52–55]</sup> A detailed description of the FOWA is available in Appendix A.9.

For the FOWA, a CV was measured in triplicate in a PB (pH 7) electrolyte solution



containing 0.3 mM Cu-tmpa and 1.1 mM H<sub>2</sub>O<sub>2</sub>, using a freshly polished GC electrode. The resulting CVs are shown in Figure B.4a. From these CVs, plots of the current enhancement  $i_c/i_p$  vs.  $\exp[-F/RT(E - E_{1/2})]$  were constructed (Figure B.4c). Here,  $i_c$  is the current associated with the catalytic HPOR reaction at the applied potential  $E$  and  $i_p$  is the peak cathodic current associated with the Cu<sup>II/I</sup> redox couple of Cu-tmpa. In the foot-of-the-wave region, a linear fit (Figure B.4e;  $R^2 > 0.98$ ) was applied between the onset of the HPOR and the potential at which  $i_c/i_p$  is at least larger than 1.6, i.e. the potential where the catalytic current is 60% larger than the peak cathodic current of the Cu<sup>II/I</sup> redox couple. The catalytic onset is defined as  $i_c/i_{\text{redox}} \geq 2$ , where  $i_{\text{redox}}$  is the current associated with the reduction of the catalyst measured at the applied potential  $E$ , in the absence of H<sub>2</sub>O<sub>2</sub>. From the slope of the linear fit, the TOF<sub>max</sub> for the HPOR by Cu-tmpa in pH 7 phosphate buffer solution containing 1.1 mM H<sub>2</sub>O<sub>2</sub> was determined to be  $2.1 \times 10^5 \pm 0.1 \times 10^5 \text{ s}^{-1}$ . This is one order of magnitude (9 times) less than was reported for the ORR in Chapter 2 (Figure 3.7a). Using the same approach, the TOF<sub>max</sub> for the HPOR in the deuterated pH 7 phosphate buffer solution was determined to be  $1.5 \times 10^5 \pm 0.1 \times 10^5 \text{ s}^{-1}$ . A comparison of the TOF<sub>max</sub> of the HPOR in H<sub>2</sub>O and D<sub>2</sub>O is shown in Figure 3.7b and confirms that the Cu-tmpa catalysed HPOR is indeed slower in D<sub>2</sub>O. By applying Eq. 3.3, where TOF<sub>max</sub> was used as the  $k_{\text{obs}}$ , a KIE of  $1.37 \pm 0.14$  was calculated.

$$\frac{i_{\text{cat}}}{i_p} = 2.24n \sqrt{\frac{RT}{Fv}} k_{\text{obs}} \quad (3.4)$$

$$i_p = 0.446nFSC_{\text{cat}}^0 \sqrt{\frac{Fv}{RT}} D_{\text{cat}} \quad (3.5)$$

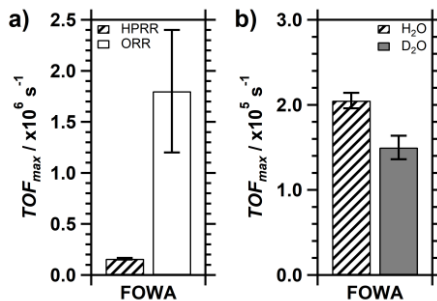


**Figure 3.7. a)** Comparison between the TOF<sub>max</sub> of Cu-tmpa for the HPOR (1.1 mM H<sub>2</sub>O<sub>2</sub> under 1 atm Ar) and the ORR (1 atm O<sub>2</sub>) as determined by FOWA. **b)** Comparison between the TOF<sub>max</sub> of the HPOR in H<sub>2</sub>O and D<sub>2</sub>O. Conditions: pH 7 PB ([PO<sub>4</sub>] = 100 mM), 293 K, 100 mV s<sup>-1</sup> scan rate.

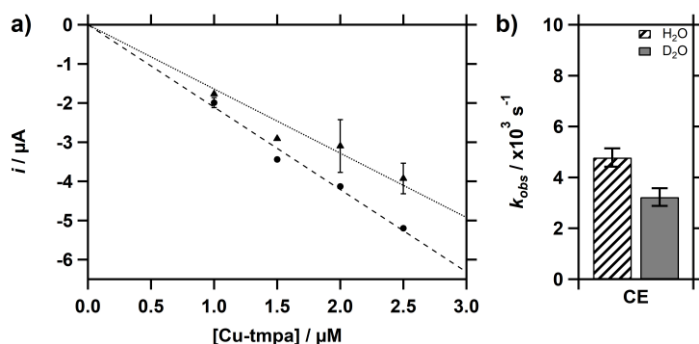


**Figure 3.8.** a) The peak catalytic current  $i_{cat}$  plotted against the Cu-tmpa concentration in a deuterated (triangles) and non-deuterated (circles) PB electrolyte solution containing 1.1 mM  $H_2O_2$  under 1 atm Ar. b) Comparison for the  $k_{obs}$  derived from the current enhancement (CE) between the hydrogen peroxide reduction in  $H_2O$  and  $D_2O$ . Conditions: pH 7 PB ( $[PO_4] = 100$  mM), 293 K, 100  $mV s^{-1}$  scan rate.

A more direct approach to obtain a rate constant can be achieved by using the catalytic current enhancement  $i_{cat}/i_p$  and applying Eq. 3.4, where  $R$ ,  $T$  and  $F$  are known constants,  $\nu$  is the scan rate (V/s), and  $n$  is the number of electrons transferred during the catalytic reaction. The current enhancement was determined from the background-corrected peak catalytic current  $i_{cat}$  at low catalyst concentration (1.0–2.5  $\mu M$ ) in the presence of 1.1 mM  $H_2O_2$ , as discussed in section 3.2.2. No redox current is visible above the double layer current at these low catalyst concentrations. Therefore, for each catalyst concentration the  $i_p$  was calculated using the diffusion coefficient of Cu-tmpa ( $D = 4.9 \times 10^{-6} cm^2 s^{-1}$ ) by applying the Randles-Sevcik equation (Eq. 3.5). This resulted in a  $k_{obs}$  of  $4.8 \times 10^3 \pm 0.4 \times 10^3 s^{-1}$  (Figure 3.8). Repeating the same experiments in deuterated electrolyte solutions resulted in a  $k_{obs}$  of  $3.2 \times 10^3 \pm 0.4 \times 10^3 s^{-1}$ . Equation 3.3 was applied to these catalytic rate constants giving a KIE of  $1.48 \pm 0.17$ , showing that at both low and high catalyst concentration, and under both substrate limited and non-limiting conditions, a significant kinetic isotope effect is observed.

### 3.2.6. Discussion

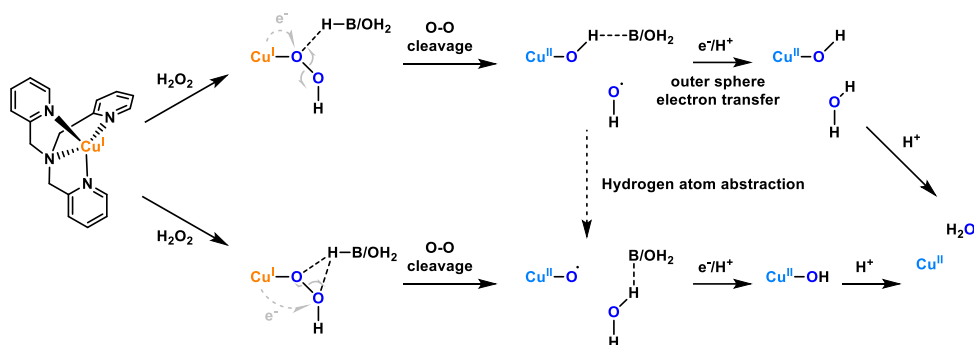
As demonstrated, the electrocatalytic HPRR by Cu-tmpa is a first-order reaction in both the catalyst and the hydrogen peroxide substrate. Using FOWA, the  $TOF_{max}$  for the reduction of  $H_2O_2$  was shown to be one order of magnitude lower than that of the 2-electron reduction of  $O_2$  to  $H_2O_2$ , consistent with the analysis of the Tafel slopes for ORR and HPRR reported in Chapter 2. The HPRR  $k_{obs}$  ( $4.8 \times 10^3 s^{-1}$ ) that was determined at low catalyst concentration was significantly lower than the FOWA-derived  $TOF_{max}$  ( $2.1 \times 10^5 s^{-1}$ ) at higher catalyst concentration. Such a  $k_{obs} < TOF_{max}$  is expected due to previously mentioned deviations from an ideal catalytic system.

However, the difference between the  $k_{obs}$  and the  $TOF_{max}$  of the HPRR is significantly

larger (2.5 times) than the difference between the  $k_{\text{obs}}$  ( $1.5 \times 10^5 \text{ s}^{-1}$ ) and  $\text{TOF}_{\text{max}}$  ( $1.8 \times 10^6 \text{ s}^{-1}$ ) of the ORR that we have previously reported. A few factors can explain this difference. Firstly, during the ORR the partial 2-electron reduction of  $\text{O}_2$  to  $\text{H}_2\text{O}_2$  and the 2-electron reduction of  $\text{H}_2\text{O}_2$  both contribute to the peak catalytic current, each with a different catalytic rate. Thus, the intermediate  $\text{H}_2\text{O}_2$  is generated in situ near the electrode surface, thereby minimizing the effect of mass-transport of  $\text{H}_2\text{O}_2$  to the electrode on the subsequent 2-electron reduction to  $\text{H}_2\text{O}$ . Given that the diffusion constant of  $\text{H}_2\text{O}_2$  ( $0.6\text{--}1.4 \times 10^{-5} \text{ cm}^2 \text{ s}^{-1}$ ) is significantly lower than that of  $\text{O}_2$  ( $2.0 \times 10^{-5} \text{ cm}^2 \text{ s}^{-1}$ ), this would enhance the catalytic current associated with the reduction of  $\text{H}_2\text{O}_2$ , contributing to a higher overall  $k_{\text{obs}}$  for the 4-electron ORR as determined via the current enhancement (CE)  $i_{\text{cat}}/i_{\text{p}}$ . This would result in a smaller difference between the  $k_{\text{obs}}$  and  $\text{TOF}_{\text{max}}$  for the ORR, where the latter is derived from the partial 2-electron reduction of  $\text{O}_2$ . Conversely, for the HPRR both the FOWA and CE rate constants are associated with the same 2-electron reduction of  $\text{H}_2\text{O}_2$ . During the HPRR diffusion of  $\text{H}_2\text{O}_2$  to the electrode does play a role and does not benefit of an increased catalytic rate due to in situ generation of the substrate that resulted in a smaller difference between the  $k_{\text{obs}}$  and  $\text{TOF}_{\text{max}}$  for the ORR.

For the ORR, part of this can be explained by the fact that the full 4-electron reduction takes place at the potential where  $k_{\text{obs}}$  is determined for the ORR, while for the FOWA only the partial 2-electron ORR was considered. During the 4-electron reduction of  $\text{O}_2$ , the intermediate  $\text{H}_2\text{O}_2$  is generated in situ near the electrode surface, thereby minimizing the effect of mass-transport of  $\text{H}_2\text{O}_2$  to the electrode on the subsequent 2-electron reduction to  $\text{H}_2\text{O}$ . This would enhance the catalytic current associated with the reduction of  $\text{H}_2\text{O}_2$ , contributing to a higher apparent  $k_{\text{obs}}$  for the 4-electron ORR as determined via current enhancement, as both the partial reduction of  $\text{O}_2$  and the reduction of  $\text{H}_2\text{O}_2$  contribute to the overall catalytic reaction rate. Conversely, for the HPRR both the FOWA and CE rate constants are associated with the same catalytic reaction, specifically the 2-electron reduction of  $\text{H}_2\text{O}_2$ . Thus, a smaller difference between the  $\text{TOF}_{\text{max}}$  and  $k_{\text{obs}}$  would be observed for the ORR than for the HPRR.

Furthermore, in the case of the HPRR, one of the contributing factors to the observed deviation from the ideal behaviour can be related to catalysts decomposition or deposition. Indeed, prolonged cycling during CV measurements shows a significant change in shape of the catalytic events (Appendix B4, Figure B.5), followed by increased activity after mixing and saturating the solution with argon, something that was not observed for the ORR. During ORR, the reduction of  $\text{H}_2\text{O}_2$  is only expected under conditions wherein the overall reduction reaction is nearly mass transport limited in  $\text{O}_2$ . Under such conditions one would not expect to find a large deviation from the ideal



**Scheme 3.1.** Possible electrocatalytic HPRR pathways in the presence of Cu-tmpa, showing a pathway that proceeds via a Cu hydroxyl and free hydroxyl radical (top), or via copper oxyl radical (bottom). In copper monooxygenases, the possibility of an HAA step has been proposed, enabled by the stabilizing effect of the binding pocket on the hydroxyl radical (see text).

catalytic activity due to catalyst degradation, if one considers that catalyst deactivation is linked to the reduction of  $\text{H}_2\text{O}_2$  and not to the 2-electron reduction of  $\text{O}_2$ .

The mechanism for  $\text{H}_2\text{O}_2$  reduction on copper has been proposed to go through a Fenton-type mechanism, based on research on copper monooxygenases or on bio-inspired copper complexes as monooxygenase mimics.<sup>[23-24]</sup> In this mechanism, it is proposed that the O-O bond of hydrogen peroxide is split homolytically. This can either result in a copper oxyl radical ( $\text{Cu-O}^{\bullet}$ ) and a free hydroxyl ion ( $\text{HO}^-$ ), or a copper hydroxyl species ( $\text{Cu-OH}$ ) and a free hydroxyl radical anion ( $\text{HO}^{\bullet-}$ ). For LPMO, it has been found by computational methods that the latter route is more favourable.<sup>[56]</sup> Additionally, it was shown that the hydroxyl radical was stabilized in the enzyme binding pocket of the active site, preventing damage caused by free radical species. This allowed for a hydrogen atom abstraction (HAA) by the hydroxyl radical from the copper bound hydroxyl group, resulting in  $\text{Cu-O}^{\bullet}$  and a water molecule.<sup>[24]</sup> These possible catalytic pathways are schematically shown in Scheme 3.1, which also includes an outer sphere electron-transfer PCET step as an alternative for the HAA.<sup>[57-58]</sup> In an electrochemical system, where electron transfer is very fast, and no free radical-stabilizing binding pocket is available, outer sphere electron transfer mediated by the solvent and/or phosphate ions should be considered.

The solvent kinetic isotope effect of 1.4–1.7 for the HPRR catalysed by Cu-tmpa indicates that bond breaking of an O-H bond is involved in the rate-determining step of the catalytic reaction. The relatively low KIE would suggest a weak O-H bond with little covalent character is involved. Solvent KIEs in the same range were observed for an Fe(III)-hydroperoxide porphyrin model for the active site of heme oxygenase.<sup>[50-51, 59]</sup> Based on computational methods, the solvent KIE was proposed to be associated with

a concerted, stepwise mechanism of proton transfer from the  $\text{H}_2\text{O}/\text{H}_3\text{O}^+$  and solvent O-O bond breaking, while involving a rearrangement of the formed hydroxyl radical anion. Such a mechanism would align closer with the top route shown in Scheme 3.1. The resulting free hydroxyl radical anion would also explain the observed instability of the complex under catalytic conditions, as it could react with the tmpa ligand. Further research using hydroxyl radical scavengers would be required to give more insight in whether this is indeed the case.<sup>[60]</sup>

### 3.3. Conclusion

The catalytic performance was investigated of Cu-tmpa for the electrocatalytic reduction of  $\text{H}_2\text{O}_2$  in pH 7 phosphate buffered neutral aqueous solution. It was confirmed that the reduction of  $\text{H}_2\text{O}_2$  is significantly slower than  $\text{O}_2$  reduction, with rate constants being 10 ( $\text{TOF}_{\text{max}}$ ) to 30 ( $k_{\text{obs}}$ ) times lower. As is the case for the ORR, the HPRR displayed a first-order dependence on the catalyst concentration, showing that only a single copper site is involved in the catalytic reaction, which fits well with the reported literature on iron- and copper-catalysed  $\text{H}_2\text{O}_2$  reduction in enzymes. Additionally, the reaction shows a first-order dependence on the  $\text{H}_2\text{O}_2$  concentration as well, up until the buffering capacity of the 0.1 M PB buffer is compromised. The effect on the catalytic performance by using  $\text{D}_2\text{O}$  as the solvent was studied, and resulted in a solvent KIE between 1.4–1.7 for the HPRR. However, while this does confirm that a hydrogen or proton transfer is involved in the rate-determining step of the catalytic reaction, the magnitude of the KIE alone does not allow us to pinpoint the exact mechanistic route for the HPRR. Yet, when combining what is known about copper monooxygenases with the obtained solvent KIE and the apparent instability of the Cu-tmpa under catalytic HPRR conditions, the pathway in which free hydroxyl radical anions are formed seems the most likely candidate at this point.

### 3.4. Experimental

#### 3.4.1. General

Aqueous electrolyte solutions were prepared using  $\text{NaH}_2\text{PO}_4$  (Suprapur®, Merck) and  $\text{Na}_2\text{HPO}_4$  (Suprapur®, Merck).  $[\text{Cu}(\text{tmpa})(\text{CH}_3\text{CN})](\text{OTf})_2$  was synthesized as described in Chapter 2. Milli-Q Ultrapure grade water was used for all electrochemical experiments and for the preparation of all aqueous electrolyte solutions.  $\text{D}_2\text{O}$  for the kinetic isotope experiments was obtained from Sigma-Aldrich (99.9 atom% D).  $\text{H}_2\text{O}_2$  was obtained from Sigma-Aldrich ( $\geq 30\%$ , for ultratrace analysis), and the exact concentration was determined via permanganate titration. Alumina suspensions (1.0, 0.3, and 0.05  $\mu\text{m}$ ) were obtained from Buehler. pH measurements were done using a Hanna Instruments

HI 4222 pH meter which was calibrated by five-point calibration using IUPAC standard buffers. All gasses used during electrochemical measurements,  $H_2$ ,  $O_2$ , and argon (each 5.0 grade), were supplied by Linde.

### 3.4.2. Electrochemical measurements

All electrochemical experiments were performed in a custom-built 10 mL single-compartment glass cell with a three-electrode setup. The measurements were performed using Autolab PGSTAT 12, 204, and 128N potentiostats, operated by the Autolab NOVA 2 software. The working electrodes were glassy carbon (GC) disks, either a GC rod ( $A = 0.071 \text{ cm}^2$ , type 1, Alfa Aesar) in hanging meniscus configuration, or a PEEK encapsulated GC disk ( $A = 0.071 \text{ cm}^2$ , Metrohm) submerged in the solution. Unless otherwise stated, the GC electrodes were manually polished before each catalytic measurement for 5 mins with 1.0, 0.3, and  $0.05 \mu\text{m}$  alumina suspensions on Buehler cloth polishing pads, or with a Struers LaboPol-30 polishing machine using  $1.0 \mu\text{m}$  diamond and  $0.04 \mu\text{m}$  silica suspension on polishing cloths (Dur-type) for 1 min each. This was followed by sonication of the electrode in Milli-Q purified water for 10–15 minutes. A gold wire was used as a counter electrode and was flame annealed and rinsed with Milli-Q purified water. The reference electrode was a reversible hydrogen electrode (RHE) made from a Pt mesh submerged in same electrolyte solution as the main cell compartment, connected via a Luggin capillary, and continuously sparged with  $H_2$  gas. Oxygen-free electrolyte solutions were prepared by saturating the cell for 20 to 30 minutes with Ar, after which an atmosphere of 1 atm Ar was maintained. Oxygen-saturated electrolyte solutions were obtained by saturating the cell for 20 minutes with  $O_2$ , after which a 1 atm  $O_2$  atmosphere was maintained.

All glassware was regularly cleaned by submersion in an aqueous oxidizing solution containing 0.5 M  $H_2SO_4$  and 1 mg/mL (6.3 mM)  $KMnO_4$  overnight. This is followed by removal of excess  $KMnO_4$  and  $MnO_2$  from the glassware with diluted  $H_2SO_4$  and  $H_2O_2$ , followed by rinsing the glassware three times with water and boiling twice submerged in Milli-Q purified water.

### 3.4.3. Electrochemical measurements in $D_2O$

In preparation of the measurements in  $D_2O$ , all glassware was cleaned following the procedure described previously. Additionally, the glassware was dried in an oven at  $140^\circ\text{C}$  for 2 days. The GC working electrode was polished as previously described, followed by sonication in  $D_2O$  instead of  $H_2O$ . After each polishing cycle and before every measurement, the GC electrode was submerged in the deuterated electrolyte solution for at least 2 minutes. Both the counter and reference electrode were flame annealed and rinsed with  $D_2O$  before the experiment. The electrolyte solutions were prepared by

weighing the required phosphate salts ( $\text{NaH}_2\text{PO}_4$  and  $\text{Na}_2\text{HPO}_4$ ), which were stored under vacuum in a desiccator containing aluminosilicate drying pearls, in a 100 mL volumetric flask. The volumetric flask was filled to 100 mL with  $\text{D}_2\text{O}$ . The apparent  $\text{pH}^*$  was measured using a calibrated pH meter (mentioned in section 3.4.2) filled with non-deuterated electrolyte solution. Both the main cell compartment and the Luggin compartment containing the RHE electrode were filled with the same deuterated PB solution. Catalyst solutions were obtained by first drying Cu-tmpa on a Schlenk-line overnight, before weighing the required amount. This was followed by preparation of concentrated stock solutions of Cu-tmpa (30.0 mM) in  $\text{D}_2\text{O}$  for use in the electrochemical experiments.  $\text{H}_2\text{O}_2$  (10.0 M in  $\text{H}_2\text{O}$ ) was used as is, as the maximum proton content during the electrochemical measurements would not exceed 0.01%.

### 3.5. References

- [1] G. Grigoropoulou, J. H. Clark, J. A. Elings, *Green Chem.* **2003**, *5*, 1-7.
- [2] R. Noyori, M. Aoki, K. Sato, *Chem. Commun.* **2003**, 1977-1986.
- [3] A. Goti, F. Cardona, in *Green Chemical Reactions* (Eds.: Pietro Tundo, Vittorio Esposito), Springer Netherlands, Dordrecht, **2008**, pp. 191-212.
- [4] A. Podgoršek, M. Zupan, J. Iskra, *Angew. Chem. Int. Ed.* **2009**, *48*, 8424-8450.
- [5] V. Prabhakaran, C. G. Arges, V. Ramani, *Proc. Natl. Acad. Sci.* **2012**, *109*, 1029-1034.
- [6] D. E. Curtin, R. D. Lousenberg, T. J. Henry, P. C. Tangeman, M. E. Tisack, *J. Power Sources* **2004**, *131*, 41-48.
- [7] Y. Wang, K. S. Chen, J. Mishler, S. C. Cho, X. C. Adroher, *Appl. Energy* **2011**, *88*, 981-1007.
- [8] L. An, T. Zhao, X. Yan, X. Zhou, P. Tan, *Sci. Bull.* **2015**, *60*, 55-64.
- [9] K. Asada, *Physiol. Plant.* **1992**, *85*, 235-241.
- [10] E. Nagababu, F. J. Chrest, J. M. Rifkind, *Biochim. Biophys. Acta, Gen. Subj.* **2003**, *1620*, 211-217.
- [11] D. Maiti, A. A. Narducci Sarjeant, K. D. Karlin, *Inorg. Chem.* **2008**, *47*, 8736-8747.
- [12] A. Ghosh, D. A. Mitchell, A. Chanda, A. D. Ryabov, D. L. Popescu, E. C. Upham, G. J. Collins, T. J. Collins, *J. Am. Chem. Soc.* **2008**, *130*, 15116-15126.
- [13] B. J. Day, *Biochem. Pharmacol.* **2009**, *77*, 285-296.
- [14] A. Tovmasyan, et al., *Free Radical Biol. Med.* **2015**, *86*, 308-321.
- [15] S. Signorella, C. Palopoli, G. Ledesma, *Coord. Chem. Rev.* **2018**, *365*, 75-102.
- [16] G. Vaaje-Kolstad, B. Westereng, S. J. Horn, Z. Liu, H. Zhai, M. Sørli, V. G. H. Eijsink, *Science* **2010**, *330*, 219-222.
- [17] S. J. Horn, G. Vaaje-Kolstad, B. Westereng, V. G. Eijsink, *Biotechnol. Biofuels* **2012**, *5*, 45-45.
- [18] G. Vaaje-Kolstad, Z. Forsberg, J. S. M. Loose, B. Bissaro, V. G. H. Eijsink, *Curr. Opin. Struct. Biol.* **2017**, *44*, 67-76.
- [19] G. R. Hemsworth, E. M. Johnston, G. J. Davies, P. H. Walton, *Trends Biotechnol.* **2015**, *33*, 747-761.
- [20] F. Calderaro, M. Keser, M. Akeroyd, L. E. Bevers, V. G. H. Eijsink, A. Várnai, M. A. van den Berg, *Biotechnol. Biofuels* **2020**, *13*, 195.
- [21] L. Ciano, G. J. Davies, W. B. Tolman, P. H. Walton, *Nat. Catal.* **2018**, *1*, 571-577.
- [22] J. A. Hangasky, M. A. Marletta, *Biochemistry* **2018**, *57*, 3191-3199.
- [23] S. Kim, J. W. Ginsbach, J. Y. Lee, R. L. Peterson, J. J. Liu, M. A. Siegler, A. A. Sarjeant, E. I. Solomon, K. D. Karlin, *J. Am. Chem. Soc.* **2015**, *137*, 2867-2874.
- [24] B. Wang, P. H. Walton, C. Rovira, *ACS Catal.* **2019**, *9*, 4958-4969.
- [25] R. L. Lieberman, A. C. Rosenzweig, *Nature* **2005**, *434*, 177-182.
- [26] R. A. Himes, K. D. Karlin, *Curr. Opin. Chem. Biol.* **2009**, *13*, 119-131.
- [27] S. M. Smith, S. Rawat, J. Telsner, B. M. Hoffman, T. L. Stemmler, A. C. Rosenzweig, *Biochemistry* **2011**, *50*, 10231-10240.

- [28] L. Cao, O. Caldararu, A. C. Rosenzweig, U. Ryde, *Angew. Chem. Int. Ed.* **2018**, *57*, 162-166.
- [29] M. Miyanishi, T. Abe, Y. Hori, Y. Shiota, K. Yoshizawa, *Inorg. Chem.* **2019**, *58*, 12280-12288.
- [30] M. O. Ross, F. MacMillan, J. Wang, A. Nisthal, T. J. Lawton, B. D. Olafson, S. L. Mayo, A. C. Rosenzweig, B. M. Hoffman, *Science* **2019**, *364*, 566-570.
- [31] W. Liu, D. Zuckerbrod, *J. Electrochem. Soc.* **2005**, *152*, A1165.
- [32] T. Kinumoto, M. Inaba, Y. Nakayama, K. Ogata, R. Umabayashi, A. Tasaka, Y. Iriyama, T. Abe, Z. Ogumi, *J. Power Sources* **2006**, *158*, 1222-1228.
- [33] M. Inaba, T. Kinumoto, M. Kiriake, R. Umabayashi, A. Tasaka, Z. Ogumi, *Electrochim. Acta* **2006**, *51*, 5746-5753.
- [34] K. Hongsirikarn, X. Mo, J. G. Goodwin, S. Creager, *J. Power Sources* **2011**, *196*, 3060-3072.
- [35] S. Fukuzumi, Y. Yamada, K. D. Karlin, *Electrochim. Acta* **2012**, *82*, 493-511.
- [36] L. An, T. S. Zhao, X. L. Zhou, L. Wei, X. H. Yan, *RSC Adv.* **2014**, *4*, 65031-65034.
- [37] E. Miglbauer, P. J. Wójcik, E. D. Głowacki, *Chem. Commun.* **2018**, *54*, 11873-11876.
- [38] Y. Yang, Y. Xue, F. Huang, H. Zhang, K. Tao, R. Zhang, Q. Shen, H. Chang, *ACS Appl. Energy Mater.* **2018**, *1*, 5328-5335.
- [39] J. M. Campos-Martin, G. Blanco-Brieva, J. L. G. Fierro, *Angew. Chem. Int. Ed.* **2006**, *45*, 6962-6984.
- [40] R. Hage, A. Lienke, *Angew. Chem. Int. Ed.* **2006**, *45*, 206-222.
- [41] S. A. M. van Stroe-Biezen, F. M. Everaerts, L. J. J. Janssen, R. A. Tacke, *Anal. Chim. Acta* **1993**, *273*, 553-560.
- [42] S. B. Hall, E. A. Khudaish, A. L. Hart, *Electrochim. Acta* **1999**, *44*, 2455-2462.
- [43] K. Aoki, M. Ishida, K. Tokuda, K. Hasebe, *J. Electroanal. Chem.* **1988**, *251*, 63-71.
- [44] P. Westbroek, E. Temmerman, *J. Electroanal. Chem.* **2000**, *482*, 40-47.
- [45] A. Krężel, W. Bal, *J. Inorg. Biochem.* **2004**, *98*, 161-166.
- [46] M. M. Ghoneim, S. Clouser, E. Yeager, *J. Electrochem. Soc.* **1985**, *132*, 1160-1162.
- [47] J. Xu, W. Huang, R. L. McCreery, *J. Electroanal. Chem.* **1996**, *410*, 235-242.
- [48] M. Langerman, D. G. H. Hetterscheid, *Angew. Chem. Int. Ed.* **2019**, *58*, 12974-12978.
- [49] E. Gopinath, T. C. Bruice, *J. Am. Chem. Soc.* **1991**, *113*, 4657-4665.
- [50] R. Davydov, T. Matsui, H. Fujii, M. Ikeda-Saito, B. M. Hoffman, *J. Am. Chem. Soc.* **2003**, *125*, 16208-16209.
- [51] D. Kumar, S. P. de Visser, S. Shaik, *J. Am. Chem. Soc.* **2005**, *127*, 8204-8213.
- [52] C. Costentin, S. Drouet, M. Robert, J.-M. Savéant, *J. Am. Chem. Soc.* **2012**, *134*, 11235-11242.
- [53] D. J. Wasylenko, C. Rodríguez, M. L. Pegis, J. M. Mayer, *J. Am. Chem. Soc.* **2014**, *136*, 12544-12547.
- [54] C. Costentin, J.-M. Savéant, *ChemElectroChem* **2014**, *1*, 1226-1236.
- [55] E. S. Rountree, B. D. McCarthy, T. T. Eisenhart, J. L. Dempsey, *Inorg. Chem.* **2014**, *53*, 9983-10002.
- [56] B. Wang, E. M. Johnston, P. Li, S. Shaik, G. J. Davies, P. H. Walton, C. Rovira, *ACS Catal.* **2018**, *8*, 1346-1351.
- [57] N. Ramaswamy, S. Mukerjee, *J. Phys. Chem. C* **2011**, *115*, 18015-18026.
- [58] I. Kenkel, et al., *J. Am. Chem. Soc.* **2017**, *139*, 1472-1484.
- [59] P. K. Sharma, R. Kevorkiants, S. P. de Visser, D. Kumar, S. Shaik, *Angew. Chem. Int. Ed.* **2004**, *43*, 1129-1132.
- [60] A. C. Maier, E. H. Iglebaek, M. Jonsson, *ChemCatChem* **2019**, *11*, 5435-5438.





# Chapter 4

---

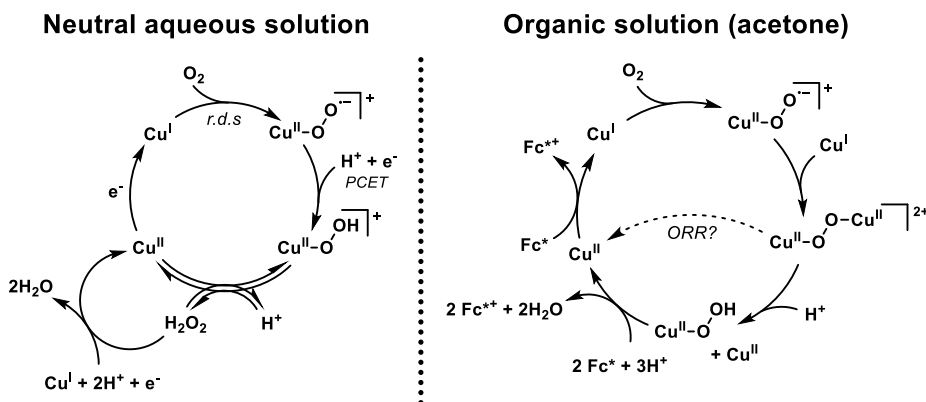
## Dioxygen reduction in acetonitrile: the influence of acid strength on the catalytic reaction

*The pyridylalkylamine copper complex  $[\text{Cu}(\text{tmpa})(\text{L})]^{2+}$  has previously been proposed to reduce dioxygen via a dinuclear resting state, based on experiments in organic aprotic solvents using chemical reductants. Conversely, a mononuclear reaction mechanism was observed under electrochemical conditions in a neutral aqueous solution. We have investigated the electrochemical oxygen and hydrogen peroxide reduction reaction catalysed by  $[\text{Cu}(\text{tmpa})(\text{L})]^{2+}$  in acetonitrile, using several different acids over a range of  $pK_a$ . We demonstrate that strong acids lead to the loss of redox reversibility and to the destabilization of the copper complex under non-catalytic conditions. Under milder conditions, the electrochemical oxygen reduction reaction (ORR) was shown to proceed via a mononuclear catalytic intermediate, similar to what we have previously observed in water. However, in acetonitrile the catalytic rate constants of the ORR are dramatically lower by a factor  $10^5$ , which is caused by the unfavourable equilibrium of formation of  $[\text{Cu}^{\text{II}}(\text{O}_2^{\bullet-})(\text{tmpa})]^+$  in acetonitrile. This results in higher catalytic rates for the reduction of hydrogen peroxide than for the ORR.*

## 4.1. Introduction

For the electrocatalytic oxygen reduction reaction (ORR) by  $[\text{Cu}(\text{tmpa})(\text{L})]^{2+}$  ( $\text{L}$  = solvent molecule; abbreviated as Cu-tmpa) in aqueous solution it was shown in Chapter 2 that the formation and reduction of  $\text{H}_2\text{O}_2$  play an important role in the catalytic mechanism.<sup>[1]</sup> Yet, the very high catalytic rates observed for these reactions and the abundance of protons in the aqueous environment preclude clear identification of reaction intermediates. The reaction of Cu-tmpa and other pyridylalkylamine copper complexes with  $\text{O}_2$  in non-aqueous solutions has been studied intensively by Karlin and others.<sup>[2-7]</sup> Several intermediate species in the reaction between  $\text{Cu}^{\text{I}}$  complexes and  $\text{O}_2$  have been identified.<sup>[8-10]</sup> This wealth of available knowledge concerning the nature of reaction intermediates and their reaction kinetics may help shed light on the catalytic pathway of the ORR by homogeneous electrocatalysts. Thus far however, such studies have not been performed on the electrocatalytic reduction of  $\text{O}_2$  by Cu-tmpa or related copper complexes in organic solvents. The main focus in many publications on the subject of the ORR by these copper complexes has been on the  $\text{O}_2$  reduction in acetone mediated by ferrocene (Fc) as a reducing agent, as opposed to electrocatalytic reduction.<sup>[11-15]</sup> It was shown that the dinuclear peroxido complex  $[\{\text{Cu}^{\text{II}}(\text{tmpa})\}_2(\mu\text{-O}_2)]^{2+}$  is formed as a resting state upon the addition of  $\text{O}_2$  to the  $\text{Cu}^{\text{I}}$ -tmpa compound, and that from this resting state dioxygen reduction can take place after addition of a proton source. Whether this dinuclear peroxido complex is responsible for the catalysis is unclear. For a similar complex with a pivalamido functional group attached to one of the pyridine arms,  $[\text{Cu}(\text{PV-tmpa})(\text{L})]^{2+}$ , it was shown that a mononuclear Cu-OOH species is formed upon addition of acid to a solution containing the dinuclear species, from which the catalytic cycle proceeds.<sup>[14]</sup> Thus, this shows that  $\text{O}_2$  bridging between two Cu centres is perhaps not essential for the breaking of the O–O bond. Similarly, the related complex  $[\text{Cu}(\text{tepa})]^{2+}$  (tepa = tris[2-(2-pyridyl)ethyl]-amine) does not form a dinuclear species at all in the presence of  $\text{O}_2$  and ferrocene in acetone, but is able to perform the 2-electron reduction of  $\text{O}_2$  to  $\text{H}_2\text{O}_2$  upon addition of  $\text{HClO}_4$ .<sup>[15]</sup> The proposed catalytic mechanisms for the electrochemical ORR in water and the ORR in acetone using sacrificial reductants are shown in Scheme 4.1.

We have shown in Chapter 2 that mechanistic details are not necessarily transferable from one system to the other, either due to differences between chemical and electrochemical reduction, such as much faster electrochemical electron transfer, the nature of the solvent, or the acidity of the protons involved in the catalytic mechanism. Therefore, an important next step would be to study the electrocatalytic ORR by Cu-tmpa in non-aqueous solutions, where the precise specification of all catalytic species under resting conditions is known, to help bridge the gap in knowledge between our electrochemical studies in water and the stoichiometric studies by Karlin



**Scheme 4.1.** Different catalytic mechanisms have been proposed for the reduction of O<sub>2</sub> by Cu-tmpa in neutral aqueous solution (electrocatalytic, Chapter 2),<sup>[1]</sup> and in acetone (ferrocene-mediated).<sup>[2, 11, 14]</sup> The tmpa ligand is excluded from the scheme for clarity.

*et al.* in organic solvents. Here, we report the electrochemical behaviour of Cu-tmpa in acetonitrile (MeCN), using several acids with a range of different pK<sub>a</sub> values as proton donors. Additionally, the electrocatalytic performance of Cu-tmpa for the ORR and the hydrogen peroxide reduction reaction (HPRR) will be discussed, including the overpotential observed in a buffered electrolyte solution.

## 4.2. Results

### 4.2.1. Behaviour of Cu-tmpa in an MeCN electrolyte solution in the absence of acid

The redox behaviour of Cu-tmpa in an acetonitrile solution containing the supporting electrolyte NBu<sub>4</sub>PF<sub>6</sub> (100 mM) was investigated in the absence of acids. Cyclic voltammograms (CVs) of Cu-tmpa in this solution were recorded using a Glassy Carbon (GC) working electrode ( $A = 0.0707 \text{ cm}^2$ ). When the solution is saturated with argon, a well-defined reversible Cu<sup>II/I</sup> redox couple is observed at  $E_{1/2} = -0.41 \text{ mV}$  vs. Fc<sup>+</sup>/Fc with a peak-to-peak separation ( $\Delta E_p$ ) of 59 mV, shown in Figure 4.1a. This corresponds well to the previously reported half-wave potential for this complex in acetonitrile.<sup>[16]</sup> Upon saturation of the solution with 1 atm O<sub>2</sub>, the initial reduction of Cu<sup>II</sup> to Cu<sup>I</sup> is still observed (Figure 4.1b). However, an additional reduction takes place when the applied potential is lower than  $-0.80 \text{ V}$ . At the same time, the oxidative current associated with the oxidation of Cu<sup>I</sup> to Cu<sup>II</sup> is significantly lower than the same oxidative peak measured in the presence of 1 atm argon. Subsequent CV cycles in the same potential window (up to  $-1.1 \text{ V}$ ) also show a decrease of the Cu<sup>II/I</sup> reduction peak and an increase in of the  $\Delta E_p$  from 56 mV in the first scan to 88 mV (Figure 4.1c). The oxidation at  $-0.35 \text{ V}$  reappears

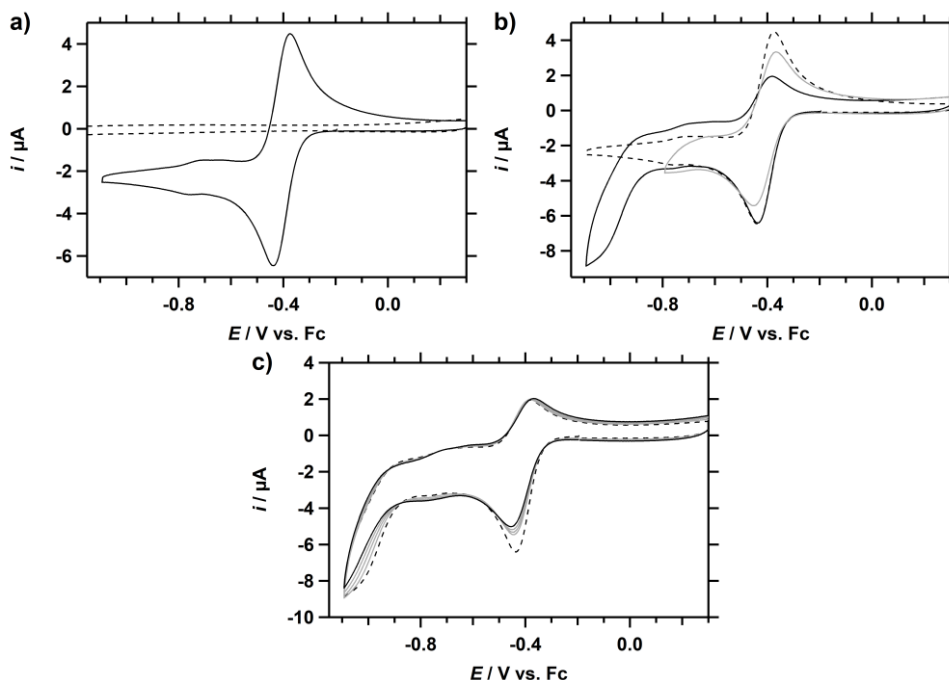


**Figure 4.1.** **a)** Cyclic voltammogram of Cu-tmpa (0.3 mM) in the absence of acid, including GC blank measurement (dashed), under 1 atm Ar. **b)** CVs of Cu-tmpa in the presence of 1 atm  $O_2$  with varying potential windows. The redox couple in the presence of Ar is shown for comparison (dashed). **c)** CVs showing the redox behaviour in the presence of oxygen over 5 cycles; first scan (dashed trace) and last scan (solid trace). Conditions:  $NBu_4PF_6$  (100 mM) in MeCN,  $100 \text{ mV s}^{-1}$ , 293 K.

when this measurement is repeated while limiting the lower limit of the potential window to  $-0.75 \text{ V}$  (Figure 4.1b, grey trace). However, the  $\Delta E_p$  remains at 88 mV and is stable over several scans.

#### 4.2.2. On the topic of equilibrium potentials in non-aqueous solutions and homoconjugation of acids and conjugate bases

Much research has been performed on electrocatalytic reactions for small molecule conversion catalysed by transition metal complexes in non-aqueous electrolyte solutions, particularly MeCN and DMF, often for solubility reasons.<sup>[17-20]</sup> However, comparing the catalytic performance of different molecular electrocatalysts in different non-aqueous media using a range of different proton sources may pose a significant challenge. Thermodynamics of the catalytic reactions of interest vary wildly with differing conditions and are more challenging to probe than in aqueous solutions, where reactions can more easily be referenced to the  $H_2/H^+$  couple, regardless of different acids, bases, or supporting electrolytes being used. To be able to determine

**Table 4.1.** Acid strength ( $pK_a$ ) and homoconjugation formation constants ( $K_f$ ) in MeCN of the acids used in this work.

Acid	$pK_a$	$\log(K_f)$
HOAc	23.5 <sup>[26-27]</sup>	3.9 <sup>[27]</sup>
HNEt <sub>3</sub> <sup>+</sup>	18.8 <sup>[21]</sup>	n/a
HTFA	12.7 <sup>[26-27]</sup>	3.9 <sup>[27]</sup>
HDMF <sup>+</sup>	6.1 <sup>[27]</sup>	1.6 <sup>[17]</sup>

the overpotential of the ORR in organic media, the equilibrium potential of the reaction has to be known for the given conditions. Recent work by Roberts and Bullock,<sup>[21]</sup> and Pegis, Appel and Mayer<sup>[22]</sup> has been key in providing a reliable method for determination of the equilibrium potential of the HER and in determining the standard potential of O<sub>2</sub>/H<sub>2</sub>O in MeCN and DMF, thus enabling more reliable and meaningful comparisons of the performance of catalysts towards the ORR.

However, the standard potentials for the catalytic reactions only apply when both the acid (HA or HB<sup>+</sup>) and its base (A<sup>-</sup> or B) are present in the solution in equal amounts, as different ratios can cause significant shifts in the equilibrium potential of the studied reactions. This is especially relevant as there will be a significant decrease in [HA] and concurrent increase in [A<sup>-</sup>] during the catalytic reaction, resulting in shift of the equilibrium potential as the catalytic reaction progresses. This requires the use of a buffered electrolyte for the determination of the overpotential, with equal concentrations of HA and A<sup>-</sup>. One complicating factor connected to the use of such a buffered electrolyte solution is the occurrence of homoconjugation. Homoconjugation occurs when the base A<sup>-</sup> (or B) reacts with the acid HA (or HB<sup>+</sup>), resulting in the formation of the conjugate species HA<sub>2</sub><sup>-</sup> (or HB<sub>2</sub><sup>+</sup>). Thus, upon homoconjugation of the acid and the conjugate base, the effective concentration of available protons in the form of free HA is reduced. However, it does not affect the equilibrium potential, as the ratio of available [HA] to [A<sup>-</sup>] does not change. The extend of this effect is dependent on the homoconjugation constant ( $K_f$ ), which varies with different acids. The  $K_f$  values of the acids relevant to this work are shown in Table 4.1. It has been reported that triethylamine does not undergo homoconjugation.<sup>[23-25]</sup>

#### 4.2.3. Stability and electrochemical behaviour of Cu-tmpa in the presence of different organic acids

To study the electrochemical activity of Cu-tmpa in acetonitrile, several different organic acids were used, namely triethylammonium (HNEt<sub>3</sub><sup>+</sup>), acetic acid (HOAc), trifluoroacetic acid (HTFA), and dimethylformamidium (HDMF<sup>+</sup>). These acids find

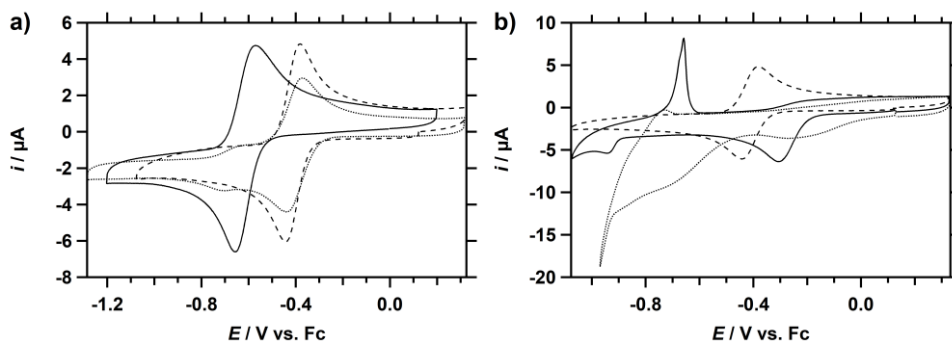


**Figure 4.2.** CVs of Cu-tmpa (0.3 mM) in a solution with (a) 50 mM HNEt<sub>3</sub>PF<sub>6</sub> (solid) and 20 mM HOAc (dotted), and (b) 20 mM (HDMF)OTf (solid) and 20 mM TFA (dotted), under 1 atm Ar. For reference, a CV of the complex in absence of acid (dashed trace) is shown in both. Conditions: NBu<sub>4</sub>PF<sub>6</sub> (100 mM) in MeCN, 100 mV s<sup>-1</sup>, 293 K.

common use in homogeneous electrocatalysis as proton sources for HER and ORR and were chosen for their range of  $pK_a$  values in MeCN, as shown in Table 4.1. As the strength of the aforementioned acids span a wide range of  $pK_a$ , from very strong acid (HDMF)OTf to the very weakly acidic HNEt<sub>3</sub>PF<sub>6</sub>, the stability of Cu-tmpa in the presence of the selected acids was studied using both cyclic voltammetry and UV-vis absorption measurements (see Appendix C.9). Unless otherwise stated, all electrochemical measurements were performed in MeCN containing NBu<sub>4</sub>PF<sub>6</sub> (0.1 M) as supporting electrolyte and the potential is reported versus the Fc<sup>+</sup>/Fc redox couple.

The CV of Cu-tmpa in 50 mM HNEt<sub>3</sub>PF<sub>6</sub> saturated with 1 atm argon showed a reversible redox couple at -0.61 V (Figure 4.2). In an electrolyte solution containing HOAc (20 mM) a reversible redox couple is observed at -0.40 V, which is very close to the  $E_{1/2}$  of the complex in the absence of acid. In the presence of either of these acids, the CV was shown to be very stable over multiple cycles. However, electrochemical stability was not observed in solutions containing HTFA or HDMF<sup>+</sup>. In the presence of HTFA, only the reduction of Cu<sup>II</sup> to Cu<sup>I</sup> is observed at -0.30 V, but the associated oxidation peak is absent. Scanning below -0.9 V reveals a small reduction event, while a sharp oxidative stripping peak appears on the forward scan of the CV. This behaviour is consistent with the deposition of metallic Cu<sup>0</sup> on the electrode surface. With (HDMF)OTf the voltammogram is even less-defined, showing a broad first reduction starting below 0 V, followed by second broad reduction event below -0.5 V. Below  $E = -0.9$  V a sharp reduction is observed, which is indicative of proton reduction.

Although the voltammograms of the full potential window are shown in Figure 4.2, limiting the potential windows of the measurements to -0.5 V did not lead to the re-appearance of the Cu<sup>II/I</sup> oxidation peak, whether in a solution containing HTFA or (HDMF)OTf. Considering this lack of reversible redox couple, or as is the case with

(HDMF)OTf, the lack of clearly defined reduction and oxidation events that could be assigned to Cu-tmpa even under non-catalytic conditions, use of these acids was not further studied. In water, it was found that below pH 4 the stability of Cu-tmpa decreased, thought to be due to demetallation of a Cu<sup>II</sup>-tmpa or Cu<sup>I</sup>-tmpa complex, while the complex is stable under strongly alkaline conditions.<sup>[26]</sup> Protonation of the pyridine moieties at low pH is a likely cause for the observed instability of Cu-tmpa, both in water and organic solvents.

#### 4.2.4. Comparison of catalytic activity between unbuffered and buffered acid conditions

##### 4.2.4.1. Acetic acid

The redox and catalytic behaviour of Cu-tmpa was investigated by performing cyclic voltammetry measurements in a NBu<sub>4</sub>PF<sub>6</sub> electrolyte solution containing HOAc or a buffered HOAc/OAc<sup>-</sup> acid-conjugate base mixture, using a glassy carbon electrode. The resulting CVs are shown in Figure 4.3a. The Cu<sup>II/I</sup> redox couple with  $E_{1/2} = -0.40$  V has a  $\Delta E_p$  of 66 mV in the electrolyte solution containing 20 mM HOAc saturated with 1 atm argon. Additionally, a small redox event is visible at  $-0.68$  V. In the solution containing the acid-conjugate base pair HOAc/OAc<sup>-</sup> (each 20 mM), the redox couple is shifted to a more negative potential, with  $E_{1/2} = -0.73$  V and a larger  $\Delta E_p$  of 78 mV. However, only a single redox couple is observed under these conditions as opposed to the two distinct redox couples observed in HOAc. Coordination of acetate to Cu<sup>II</sup> is responsible for the shift of the redox couple to a more negative couple, with the increased electron density resulting in a complex that is harder to reduce. Acetate coordination was also confirmed by UV-vis measurements of the absorption of Cu-tmpa in the presence of

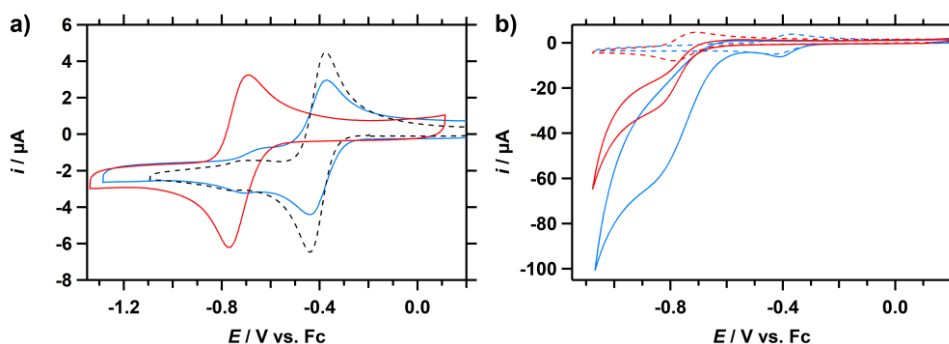


**Figure 4.3.** CV of Cu-tmpa (0.3 mM) under 1 atm Ar **(a)** and under 1 atm O<sub>2</sub> **(b)**, in the presence of 20 mM HOAc (blue) or 20 mM HOAc/OAc<sup>-</sup> (each 20 mM; red). For reference, a CV of the complex in absence of acid under 1 atm Ar (dashed trace) is shown on the left. Conditions: NBu<sub>4</sub>PF<sub>6</sub> (100 mM) in MeCN, 100 mV s<sup>-1</sup>, 293 K.



HOAc/OAc<sup>-</sup> (20 mM), based on the appearance of a sharp LMCT absorption peak around 300 nm and a blueshift of the d-d band, as can be seen in Figure C.12c (Appendix C.9).

Cu-tmpa shows very different catalytic characteristics under both conditions. When the solutions are saturated with O<sub>2</sub> a catalytic wave is observed in both cases (Figure 4.3b), however a lower catalytic current is observed for the buffered system. This is unsurprising, as homoconjugation lowers the amount of free acid in the solution compared to the situation where no conjugated base is present. With HOAc, the reduction from Cu<sup>II</sup> to Cu<sup>I</sup> is still distinctly visible, and the onset potential of the catalytic reaction is 220 mV below the peak reduction potential ( $E_{pc}$ ) of -0.44 V in the absence of oxygen. Here, the catalytic onset potential is defined as the potential where the current is 1  $\mu$ A higher than the current in the absence of the substrate. In the solution containing the acid-conjugate base pair, the reduction of Cu<sup>II</sup> and the onset of catalysis overlap, and the catalytic half-wave potential ( $E_{cat/2}$ ) of -0.77 V coincides closely with  $E_{pc}$  (-0.77 V). This is more easily visualized after performing a background correction of significant GC activity towards the ORR under these conditions. The resulting linear sweep voltammograms (LSVs) are shown in Figure C.4 (Appendix C.3). The background corrected LSVs show a peak catalytic current ( $i_{cat}$ ) of 56  $\mu$ A in the solution containing HOAc, while the  $i_{cat}$  in the buffered solution is almost halved to 29  $\mu$ A.

To get more insight into the catalytic pathway and the product that is formed, the reduction of H<sub>2</sub>O<sub>2</sub> by Cu-tmpa was investigated. One key difference between the conditions in which the ORR and HPORR were performed is the presence of 30 mM of H<sub>2</sub>O during the HPORR, as H<sub>2</sub>O<sub>2</sub> was added in the form of a 30% solution in water. CVs of the complex in both unbuffered and buffered electrolyte solution are shown in Figure 4.4. As was the case for the ORR, the onset of H<sub>2</sub>O<sub>2</sub> reduction in the presence of HOAc

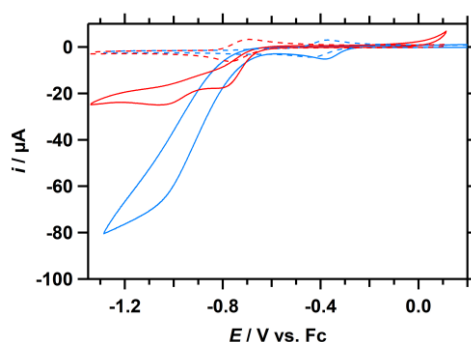


**Figure 4.4.** CV of Cu-tmpa (0.3 mM) under 1 atm Ar (dotted lines) and with 8.1 mM H<sub>2</sub>O<sub>2</sub> under 1 atm Ar (solid lines), in the presence of 20 mM HOAc (blue) or HOAc/OAc<sup>-</sup> (each 20 mM; red). Conditions: NBu<sub>4</sub>PF<sub>6</sub> (100 mM) in MeCN, [H<sub>2</sub>O] = 30 mM, 100 mV s<sup>-1</sup>, 293 K.

only starts after the complex has been reduced to  $\text{Cu}^{\text{I}}$ . However, the onset potential of the HPFR is shifted by  $-100$  mV versus the onset of the ORR. For the solution containing HOAc a single catalytic wave is observed, while for the buffered system a double S-shaped catalytic curve is visible with a much lower current, which again can be explained by a lowered availability of acidic protons compared to the electrolyte solution containing only HOAc, due to homoconjugation. However, the previously mentioned coordination of acetate may have an even greater influence on the HPFR in the buffered acetate system, resulting in a reduction of the catalytic activity compared to the unbuffered system.

#### 4.2.4.2. Triethylammonium

Similarly, the use of protonated triethylamine as the proton donor for the ORR was investigated. Cyclic voltammograms were recorded in a  $\text{NBu}_4\text{PF}_6$  electrolyte solution containing  $\text{HNET}_3^+$  (in the form of  $\text{HNET}_3\text{PF}_6$ ) or a buffered  $\text{HNET}_3^+/\text{NET}_3$  acid-conjugate base mixture and are shown in Figure 4.5. In the presence of argon, the  $E_{1/2}$  of the Cu-tpma redox couple in the solution containing  $\text{HNET}_3^+$  is  $-0.61$  V. Seemingly, Cu-tpma has a well-defined single redox couple, although the somewhat large  $\Delta E_p$  of 88 mV indicates a degree of irreversibility. On the other hand, in the solution containing the  $\text{HNET}_3^+/\text{NET}_3$  acid-conjugate base pair, two distinct reductions are observed. One has a cathodic peak potential ( $E_{pc}$ ) centred at  $-0.50$  V (marked by #) and the second at  $-0.70$  V (marked by  $\Delta$ ). These are paired with a broadened oxidation wave, which is caused by two overlapping redox couples. This is more evident when looking at a differential-pulse voltammogram (DPV) measured in the same solution (Figure C.3, Appendix C.2). In the DPV, a smaller oxidative peak is visible at a more negative potential, shifted by  $-0.20$  V from the main oxidative peak. This is the same difference in potential as observed for

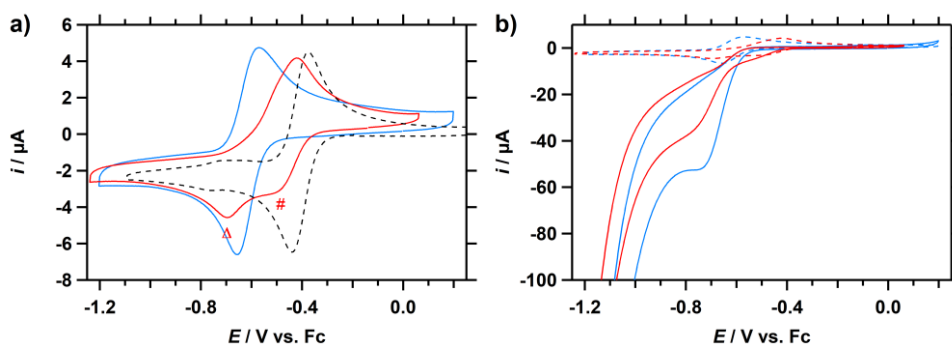


**Figure 4.5.** CVs of Cu-tpma (0.3 mM) under 1 atm Ar **(a)** and under 1 atm  $\text{O}_2$  **(b)**, in the presence of 50 mM  $\text{HNET}_3\text{PF}_6$  (blue) or  $\text{HNET}_3\text{PF}_6/\text{NET}_3$  (each 50 mM; red). For reference, a CV of the complex in absence of acid under 1 atm Ar (dashed trace) is shown on in **(a)**. Conditions:  $\text{NBu}_4\text{PF}_6$  (100 mM) in MeCN,  $100\text{ mV s}^{-1}$ , 293 K.

the  $E_{pc}$  of the two reductive peaks. The  $E_{1/2}$  of the main redox event is  $-0.462$  V and has a  $\Delta E_p$  of 81 mV. In the UV-vis absorption spectra, only a small 25 nm blueshift is observed for the d-d transition upon addition of  $\text{HNEt}_3^+$  or  $\text{HNEt}_3^+/\text{NEt}_3$  which could be indicating protonation of one of the coordinated nitrogen atoms of the tmpa ligand (see Figure C.12e/g, Appendix C.9). The behaviour of Cu-tmpa under these conditions is opposite to what was observed in presence of HOAc and  $\text{HOAc}/\text{OAc}^-$ , where the redox couple was shifted to more negative potentials in the buffered electrolyte solution due to the presence of acetate, while no shift was observed in the solution with only HOAc. In section 4.2.6 we show that the redox potential in the presence of  $\text{HNEt}_3^+$  is both dependent on acid concentration and time, showing that the behaviour of Cu-tmpa under these conditions is far from straightforward.

In the presence of 1 atm  $\text{O}_2$ , a catalytic response is observed in CV for both buffered and unbuffered electrolyte solutions containing 0.3 mM Cu-tmpa (Figure 4.5b). The catalytic onset in the unbuffered solution ( $-0.56$  V) coincides with the redox potential of Cu-tmpa under argon. In the buffered solution the catalytic onset coincides with the previously discussed second redox event at  $-0.70$  V (Figure 4.5a;  $\Delta$ ) that is observed in the same buffered solution under argon. As was observed with HOAc, Cu-tmpa shows a higher maximum current and a somewhat earlier onset in the unbuffered electrolyte solution, compared to that observed in the buffered electrolyte solution. The background corrected LSVs show an  $i_{cat}$  of 53  $\mu\text{A}$  in the solution containing  $\text{HNEt}_3^+$  (Figure C.4a), while the  $i_{cat}$  in the buffered  $\text{HNEt}_3^+/\text{NEt}_3$  electrolyte solution is about a third lower at 35  $\mu\text{A}$  (Figure C.4b).

The CVs of the catalytic response upon the addition of  $\text{H}_2\text{O}_2$  to the electrolyte solutions containing 0.3 mM Cu-tmpa are shown in Figure 4.6. While similar peak catalytic currents are reached for both buffered and unbuffered solutions, some

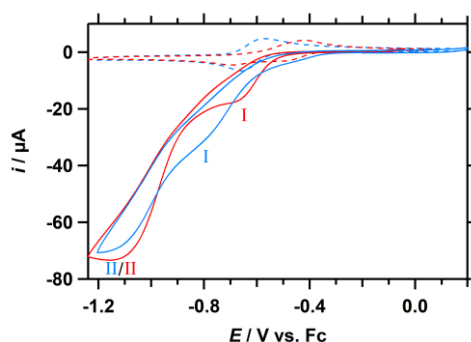


**Figure 4.6.** CVs of Cu-tmpa under 1 atm Ar (dashed lines) and with 8.1 mM  $\text{H}_2\text{O}_2$  under 1 atm Ar (solid lines), in the presence of 50 mM  $\text{HNEt}_3\text{PF}_6$  (blue) or  $\text{HNEt}_3\text{PF}_6/\text{NEt}_3$  (each 50 mM; red). Conditions:  $\text{NBu}_4\text{PF}_6$  (100 mM) in MeCN,  $[\text{H}_2\text{O}] = 30$  mM,  $100$  mV  $\text{s}^{-1}$ , 293 K.

**Table 4.2.** Overview of the electrochemical properties of Cu-tmpa and its catalytic activity toward the ORR under different conditions.

	$E_{pc}$ (V)	$E_{1/2}$ (V)	$\Delta E_p$ (mV)	$E_{onset, ORR}$	$E_{cat/2}$	$i_{cat}$ ( $\mu A$ )
No acid	-0.44	-0.41	59	-	-	-
HNEt <sub>3</sub> PF <sub>6</sub>	-0.66	-0.61	88	-0.56	-0.65	53
HNEt <sub>3</sub> PF <sub>6</sub> /NEt <sub>3</sub>	-0.50 <sup>a</sup> , -0.70 <sup>b</sup>	-0.46	81	-0.52	-0.68	35
HOAc	-0.44	-0.40	66	-0.56	-0.73	56
HOAc/NBu <sub>4</sub> OAc	-0.77	-0.73	78	-0.70	-0.77	29

<sup>a</sup>  $E_{pc}$  of the first reduction. <sup>b</sup>  $E_{pc}$  of the second reduction.  $E_{onset}$  is defined as the potential where the catalytic current  $i_{cat}$  is 1  $\mu A$  higher than  $i_p$  under argon. Potential V vs. Fc<sup>+</sup>/Fc

**Table 4.3.** Overview of the electrochemical properties of Cu-tmpa related to the catalytic reduction of H<sub>2</sub>O<sub>2</sub> under different conditions.

	$E_{onset, HP RR}$	$E_{cat/2}$	$i_{cat}$ ( $\mu A$ )
HNEt <sub>3</sub> PF <sub>6</sub>	-0.35	-0.59	40 <sup>a</sup> , 71
HNEt <sub>3</sub> PF <sub>6</sub> /NEt <sub>3</sub>	-0.56	-0.60	19 <sup>b</sup> , 72
HOAc	-0.66	-0.88	77
HOAc/OAcNBu <sub>4</sub>	-0.68	-0.72	18 <sup>a</sup> , 25

<sup>a</sup> catalytic current measured at -0.80 V. <sup>b</sup> Catalytic current measured at -0.75 V.  $E_{onset}$  is defined as the potential where current  $i_{cat}$  is 1  $\mu A$  higher than  $i_p$  under argon.

differences can be observed. In both cases, the catalytic wave seems to consist of two different waves (I and II), but in the buffered solution the initial “peak” current (I) is reached at a higher potential and lower current, while for the unbuffered system a higher current is reached and more overlap between the first (I) and second (II) wave is observed, which precludes the formation of a current plateau for the first wave.

The electrochemical properties of Cu-tmpa in the presence of argon, O<sub>2</sub>, and H<sub>2</sub>O<sub>2</sub> for the different acid and acid-conjugate base systems, with equal concentrations of HA (or HB<sup>+</sup>) and A<sup>-</sup> (or B), have been summarized in Table 4.2 and Table 4.3.

#### 4.2.5. OCP values for the determination of H<sub>2</sub>/H<sup>+</sup> and the overpotential for the ORR in non-aqueous solutions

After it was established that of the four acids that were investigated only HNEt<sub>3</sub><sup>+</sup> and HOAc are viable acids for use in combination with Cu-tmpa under electrochemical conditions, the open-circuit potentials (OCPs) for these acidic solutions and buffered 1:1 acid-conjugate base solutions were determined. The OCP can be used as a direct measure of the equilibrium potential of the H<sup>+</sup>/H<sub>2</sub> couple in organic solvent, which is especially useful in solvents where no robust pK<sub>a</sub> scale is available and the standard

potential of the  $H^+/H_2$  is not known.<sup>[21]</sup> In combination with the catalytic half-wave potential, the OCP can be used to determine overpotential and compare them with results obtained in different media.

The OCPs were measured using a platinum wire and averaged over a 60 second window in a 100 mM  $NBu_4PF_6$  electrolyte solution saturated with  $H_2$ , containing the desired acid or acid-conjugate base mixture, and referenced versus  $Fc^+/Fc$ . The resulting OCP values are summarized in Table 4.4. Buffering of the  $HNEt_3^+$  solution resulted in the largest OCP shift of -297 mV, while buffering of the HOAc containing solution resulted in a positive shift of 162 mV. To determine the effect of water in the acetonitrile solutions on the OCP, the OCP values were also determined for the same solutions containing 0.10 M  $H_2O$ . Adding water to acetonitrile solutions containing either only the acid or a 1:1 acid-conjugate base mixture does not have a large effect on the OCP, at most only shifting the potential by +29 mV in the case of the 1:1 HOAc/OAc<sup>-</sup> mixture. This also indicates that the in-situ generation of conjugate base during the electrocatalytic reaction will have a larger effect on local potential and pH than the generation of water during the same reaction.

To validate the experimental setup and the method that was used to determine the OCP, the values for the buffered  $HNEt_3^+/NEt_3$  system were compared to the OCP values of  $HNEt_3^+$  (used as a  $BF_4^-$  salt) in MeCN as reported in the literature,<sup>[21]</sup> which is in agreement with the OCP value reported in Table 4.4. For HOAc/OAc<sup>-</sup> an OCP value of -1.207 V was measured, which would correspond to a standard reduction potential of  $H^+$  ( $E_{H^+}^0$ ) of 0.159 V vs.  $Fc^+/Fc$ , after applying the Nernst equation on the measured OCP potential (Eq. 4.1). This is far removed from the previously established  $E_{H^+}^0$  in MeCN (0.028 V vs.  $Fc^+/Fc$ )<sup>[21]</sup>, which indicates that the conditions during our OCP measurements for HOAc/OAc<sup>-</sup> were not sufficiently controlled to obtain accurate values for the OCP.

$$E_{H^+}^0 = E_{OCP} + \frac{RT}{F} \ln(K_a) \quad (4.1)$$

$$\eta = E_{OCP} - E_{cat/2} + (E_{O_2}^0 - E_{H^+}^0) \quad (4.2)$$

$$\eta = (E_{O_2}^0 - 0.0592pK_a) - E_{cat/2} \quad (4.3)$$

Two different methods were applied to determine the overpotential ( $\eta$ ) of the ORR in the buffered electrolyte solutions, by using the OCP potential (Eq. 4.2), or by applying the Nernst equation (Eq. 4.3). Here,  $E_{cat/2}$  is the catalytic half-wave potential of the ORR by Cu-tmpa (Table 4.2), the standard reduction potential for the 4-electron reduction of  $O_2$  in MeCN ( $E_{O_2}^0 = 1.21$  V vs.  $Fc^+/Fc$ ) was reported by Pegis *et al.*,<sup>[27]</sup> and the standard reduction potential of  $H^+$  in MeCN ( $E_{H^+}^0 = -0.028$  V vs.  $Fc^+/Fc$ ) was reported by Roberts *et al.*<sup>[21]</sup> As shown in Table 4.4, good agreement is achieved between both methods for

**Table 4.4.** Overview of the open-circuit potentials obtained in solutions containing  $\text{HNEt}_3^+$ , HOAc, or their respective acid-conjugate base 1:1 mixture.

Conditions		$E_{\text{OCP}}$ (V vs. $\text{Fc}^+/\text{Fc}$ )	$\eta_{\text{OCP}}$ (V)	$\eta_{\text{Nernst}}$ (V)
$\text{HNEt}_3\text{PF}_6$ (50 mM)	No added water	-0.851	0.77	0.78
	$[\text{H}_2\text{O}] = 0.10 \text{ M}$	-0.825		
1:1 $\text{HNEt}_3\text{PF}_6/\text{NEt}_3$ (both 50 mM)	No added water	-1.148	0.80	0.59
	$[\text{H}_2\text{O}] = 0.10 \text{ M}$	-1.132		
HOAc (20 mM)	No added water	-1.011	0.80	0.59
	$[\text{H}_2\text{O}] = 0.10 \text{ M}$	-1.017		
1:1 HOAc/ $\text{NBu}_4\text{OAc}$ (both 20 mM)	No added water	-1.207	0.80	0.59
	$[\text{H}_2\text{O}] = 0.10 \text{ M}$	-1.178		

Conditions:  $\text{NBu}_4\text{PF}_6$  (100 mM) in MeCN, 1 atm  $\text{H}_2$ , 293 K.

the  $\text{HNEt}_3^+/\text{NEt}_3$  system. However, a significant difference in results is obtained for HOAc/ $\text{OAc}^+$  as was expected based on the calculated  $E_{\text{H}}^0$ . While this was not further investigated, it could indicate a concentration effect in combination with influence of HOAc/ $\text{OAc}^+$  homoconjugation on the OCP value.

#### 4.2.6. Acid concentration and time-dependence studies

Under non-catalytic conditions, a double redox event was observed in CVs of Cu-tpmpa in the presence of HOAc. Similar behaviour was also observed for solutions containing  $\text{HNEt}_3\text{PF}_6$  when an acid concentration below 50 mM was used. To investigate if the magnitude of the redox couples is dependent on the acid concentration in the electrolyte, CVs of electrolyte solutions containing 0.3 mM Cu-tpmpa and acid in a range

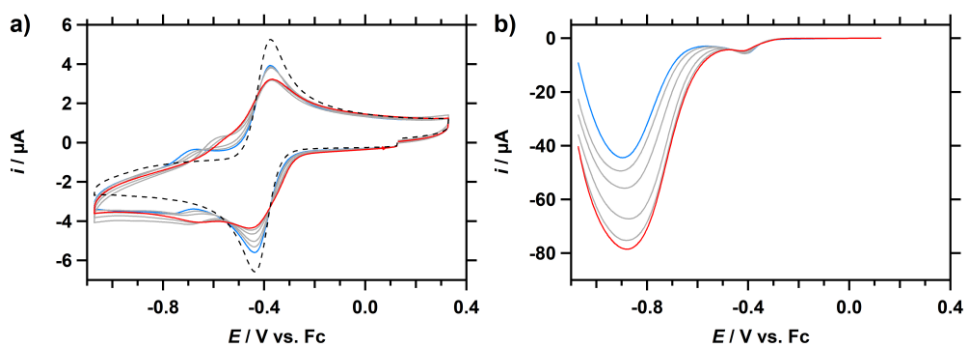


**Figure 4.7.** (a) CVs of Cu-tpmpa (0.3 mM) in the presence of 1 atm Ar for different concentrations of HOAc, ranging from 5 mM (blue trace) to 100 mM (red trace), including a CV in the absence of acid (dashed trace). (b) Background-corrected LSVs of the ORR catalysed by Cu-tpmpa over the same range of HOAc concentrations. Conditions:  $\text{NBu}_4\text{PF}_6$  (100 mM) in MeCN, 100  $\text{mV s}^{-1}$ , 293 K.

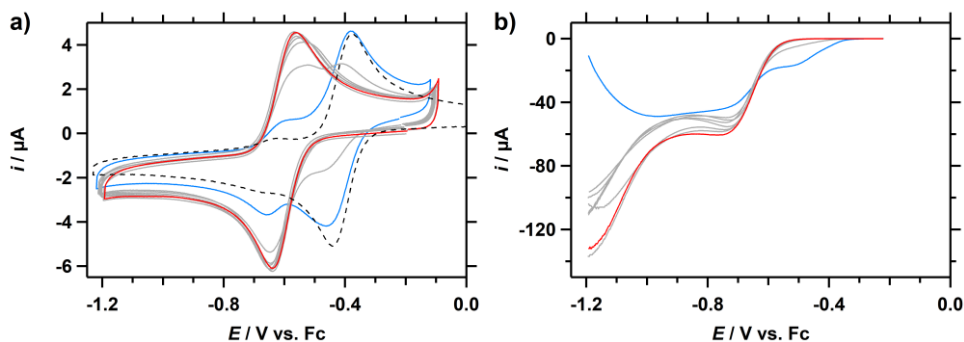


**Figure 4.8.** (a) CVs of Cu-tmpa (0.3 mM) in the presence of 1 atm Ar for different concentrations of HNEt<sub>3</sub><sup>+</sup>, ranging from 10 mM (blue trace) to 100 mM (red trace), including a CV in the absence of acid (dashed trace). (b) Background-corrected LSV of the ORR by Cu-tmpa over the same range of HNEt<sub>3</sub><sup>+</sup> concentrations. Conditions: NBu<sub>4</sub>PF<sub>6</sub> (100 mM) in MeCN, 100 mV s<sup>-1</sup>, 293 K.

of concentrations between 5 and 100 mM were recorded, for both 1 atm Ar and O<sub>2</sub> (Figure 4.7). The main redox couple at -0.4 V shows a decreasing redox current with increasing acid concentration. At the same time, the second redox event becomes more pronounced yet also moves from -0.7 V to -0.6 V. The addition of the first 5 mM HOAc already results in a clear decrease of the oxidative and reductive current of the main redox couple and the appearance of the smaller second smaller redox couple mentioned before. Further increase of acid concentration does not seem to result in a linear decrease of the redox current. The effect of acid concentration is more pronounced for the ORR activity, as shown in Figure 4.7b. Here, the catalytic current increases linearly with the increased concentration (Figure C.4). However, one has to consider that this may be merely an effect of the proton concentration on catalysis, and not specifically on the concentration of catalytic species that can be associated with the increasing current response from the second redox couple (see Appendix C.4).

The same approach was taken to study the effect of the concentration of HNEt<sub>3</sub>PF<sub>6</sub> on the redox chemistry and the catalytic ORR activity of Cu-tmpa. The resulting CVs over a range of acid concentration between 5 and 100 mM are shown in Figure 4.8. While the previously mentioned redox couple at -0.61 V is present at acid concentrations higher than 20 mM, at lower concentrations the most prominent redox couple of Cu-tmpa has the same redox potential as that of the complex in the absence of acid. However, several repeated CV measurements of Cu-tmpa in an electrolyte solution containing 50 mM HNEt<sub>3</sub>PF<sub>6</sub> showed small fluctuations in the position and magnitude of the redox couple. This was initially thought to be caused by different water content in the solutions that were used in these experiments, but upon further investigation a time-based element was identified as a probable cause. To confirm this, every 5 minutes a CV was measured of an electrolyte solution containing 0.3 mM Cu-

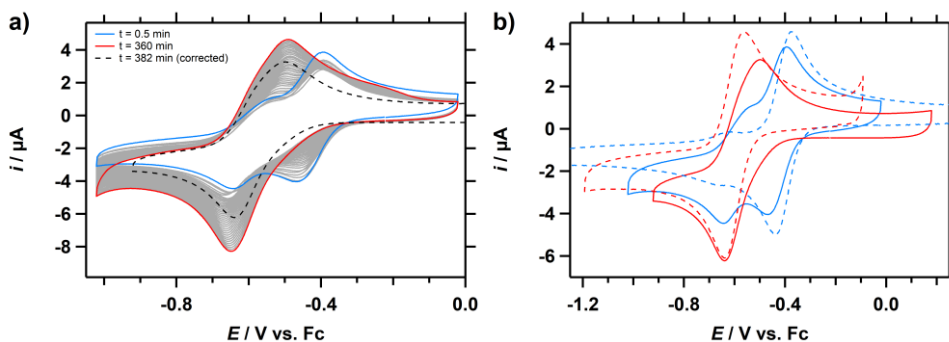


**Figure 4.9.** (a) CVs of Cu-tmpa (0.3 mM) in the presence of 50 mM  $\text{HNEt}_3\text{PF}_6$  under 1 atm Ar, measured at 5 min time intervals after addition of the acid (b) A comparison of CVs of 0.3 mM Cu-tmpa in the absence of acid (dashed blue trace), at  $t = 0.5 \text{ min}$  after addition of 50 mM  $\text{HNEt}_3^+$  (blue trace), at  $t = 382 \text{ min}$  after addition of 50 mM  $\text{HNEt}_3^+$  (red trace), and in a solution containing 100 mM  $\text{HNEt}_3^+$  (dashed red trace). Conditions:  $\text{NBu}_4\text{PF}_6$  (100 mM) in MeCN,  $100 \text{ mV s}^{-1}$ , 293 K.

tmpa and 50 mM  $\text{HNEt}_3\text{PF}_6$  under 1 atm of Ar. The resulting CVs are shown in Figure 4.9a. Over the course of 6 hours, a chemical conversion took place between two different redox-active compounds, which were previously observed in the concentration dependence results. A comparison of the first ( $t = 0.5 \text{ min}$ ) and last ( $t = 382 \text{ min}$ ) CVs with the CVs obtained without acid and with 100 mM  $\text{HNEt}_3\text{PF}_6$  shows that almost full conversion took place of the species with the less negative redox potential into the species with the more negative redox potential (Figure 4.9b). However, an additional shoulder is still present on both the reduction and oxidation domain indicates an equilibrium between the two species. Further analysis of the data (Appendix C.7) confirmed a species distribution ratio of 0.8 to 0.2. The combination of the  $\text{HNEt}_3^+$  concentration dependence and the establishment of an equilibrium over time, indicates that protonation of the complex plays a role. By monitoring the species distribution as a function of time, the reaction order of this chemical conversion was determined. A plot of the natural logarithm of the species concentration vs. time (Figure C.9d) revealed that during the first 3 hours of the reaction it is governed by a first-order rate law. The resulting reaction rate was determined to be  $8.27 \times 10^{-5} \text{ s}^{-1}$ , with a half-life of 140 minutes.

In addition to the electrochemical measurements, a solution with the same composition was monitored separately using UV-vis spectroscopy. Upon addition of  $\text{HNEt}_3\text{PF}_6$  (50 mM), the absorption band corresponding to the characteristic  $\text{Cu}^{\text{II}}$  d–d transition is blue-shifted by 25 nm (Figure C.10). Over the course of 6 hours, a UV-vis spectrum was recorded every 5 minutes. However, the only change in the UV-vis spectrum over this period was a slight increase in the broad band around 300 nm, as



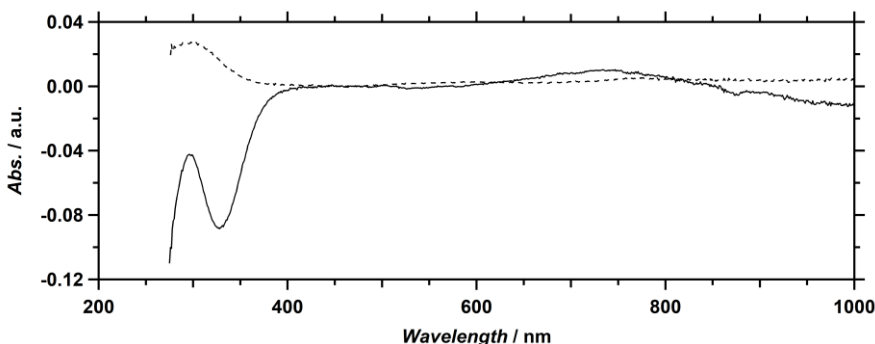


**Figure 4.10.** Difference spectrum after addition of  $\text{HNEt}_3\text{PF}_6$  (black trace) to the electrolyte solution containing 0.3 mM Cu-tmpa and 100 mM  $\text{NBu}_4\text{PF}_6$  in MeCN, and between the start at  $t = 0$  min, and the end at  $t = 360$  min (dashed trace).

shown in the difference spectrum of the UV-vis absorbance spectra at the start and end of the experiment (Figure 4.10).

#### 4.2.7. Catalyst concentration dependence

To get more insight into the catalytic mechanism for the ORR by Cu-tmpa in MeCN, the relationship between the catalytic current and the catalyst concentration was investigated in the presence of HOAc and  $\text{HNEt}_3^+$ . CVs were measured in the presence of 1 atm of  $\text{O}_2$  over a range of Cu-tmpa concentrations (10–300  $\mu\text{M}$ ). After a background correction was applied to filter out the catalytic activity caused by the GC electrode itself, a linear first-order relationship between the catalytic current and the catalyst concentration was observed, both for  $\text{HNEt}_3\text{PF}_6$  and HOAc (Figure 4.11). The different acid concentrations, 50 mM  $\text{HNEt}_3\text{PF}_6$  and 100 mM HOAc, result in the same peak catalytic currents, indicating that the acid concentration does not have a significant current-limiting effect on the catalysis under these conditions. Additionally, it shows that the ORR is not limited in  $\text{O}_2$  at a catalyst concentration of 0.3 mM, as good linearity of  $i_{\text{cat}}$  is maintained in this higher catalyst concentration range.

#### 4.2.8. Quantification of catalyst performance

To compare the electrocatalytic performance of Cu-tmpa for ORR in MeCN under different conditions, the observed catalytic rate constant  $k_{\text{obs}}$  (or turnover frequency; TOF) was determined from the catalytic current enhancement by applying equation 4.4.<sup>[28]</sup> The current enhancement was determined using the  $i_{\text{cat}}$  obtained over a range of catalyst concentrations (Figure 4.11), while  $i_p$  was calculated based on the diffusion coefficient of Cu-tmpa in the absence of any acid, using the Randles-Sevcik equation. Scan-rate dependence studies to obtain the diffusion coefficient in the presence of

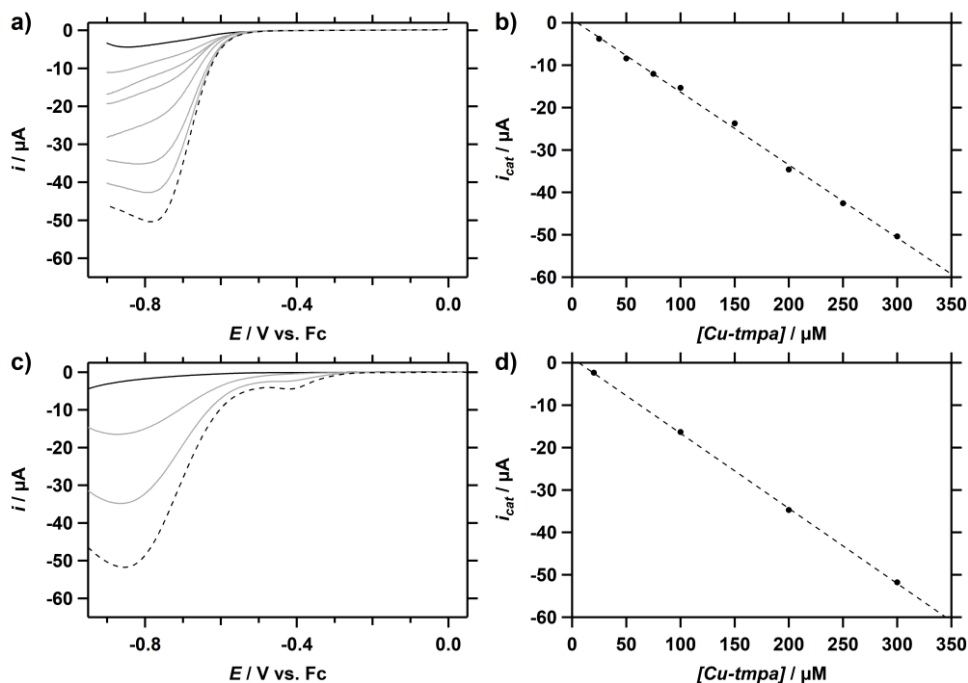


**Figure 4.11.** (a) Background-corrected LSVs of the catalytic ORR by Cu-tpma in the presence of HNEt<sub>3</sub>PF<sub>6</sub> (50 mM) under 1 atm O<sub>2</sub>, for catalyst concentrations ranging from 25 (black) to 300 (dashed)  $\mu\text{M}$ . (b) Peak catalytic current  $i_{\text{cat}}$  at  $-0.78$  V vs. Fc. (c) Background-corrected LSV of the catalytic ORR by Cu-tpma in the presence of HOAc (100 mM) under 1 atm O<sub>2</sub>, for catalyst concentrations ranging from 20 to 300  $\mu\text{M}$ . (d) Peak catalytic current  $i_{\text{cat}}$  at  $-0.85$  V vs. Fc. Conditions: NBu<sub>4</sub>PF<sub>6</sub> (100 mM) in MeCN, 100 mV s<sup>-1</sup>, 293 K.

different acids and acid-conjugate base mixtures revealed that often two different redox couples were present (Appendix C.1), whose distribution are also both concentration and time-dependent (see Section 4.2.6). This prevented accurate determination of diffusion coefficients under these conditions. As this was not an issue in the absence of acid, the diffusion coefficient of Cu-tpma in an MeCN solution without acid was used as an approximation to determine the  $i_p$  in the presence of acid. Applying Eq. 4.4 resulted in  $k_{\text{obs}}$  for the ORR by Cu-tpma of  $4.5 \pm 0.4 \text{ s}^{-1}$  and  $5.0 \pm 0.3 \text{ s}^{-1}$  for solutions containing HNEt<sub>3</sub>PF<sub>6</sub> (50 mM) or HOAc (100 mM), respectively.

$$\frac{i_{\text{cat}}}{i_p} = 2.24n \sqrt{\frac{RT}{Fv} k_{\text{obs}}} \quad (4.4)$$

As described in Section 4.2.7 and as evidenced by the low  $k_{\text{obs}}$ , catalysis is not limited by O<sub>2</sub> concentration in the presence of 0.3 mM Cu-tpma, which allows for the determination of the  $k_{\text{obs}}$  from any CV that was measured at this concentration and thus does not require a catalyst concentration dependence series. Thus,  $k_{\text{obs}}$  were

**Table 4.5.** Overview of  $k_{\text{obs}}$  obtained for the ORR and HPRR by Cu-tmpa under different catalytic conditions. Determined directly from CV measurements at 0.3 mM catalyst concentration.

Proton source	$k_{\text{obs,ORR}} \text{ (s}^{-1}\text{)}$	$k_{\text{obs,HPRR}} \text{ (s}^{-1}\text{)}$	
HNEt <sub>3</sub> PF <sub>6</sub>	4.6	35.9 <sup>a</sup>	11.3 <sup>b</sup>
HNEt <sub>3</sub> PF <sub>6</sub> /NEt <sub>3</sub>	2.7	37.8	2.5 <sup>c</sup>
HOAc	5.6	42.9	
HOAc/OAcNBu <sub>4</sub>	1.5	4.5	2.2 <sup>b</sup>

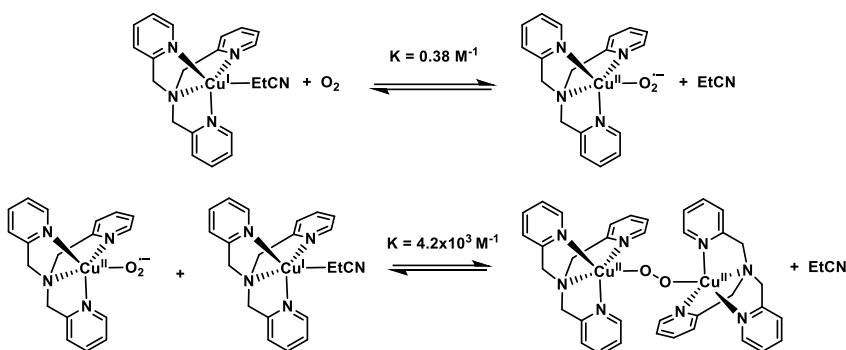
<sup>a</sup> The maximum catalytic current was used as  $i_{\text{cat}}$ , <sup>b</sup>  $i_{\text{cat}}$  values were determined at  $-0.80 \text{ V vs. Fc}$ , <sup>c</sup>  $i_{\text{cat}}$  values were determined at  $-0.75 \text{ V vs. Fc}$ . For the ORR a catalytic electron transfer number of  $n = 4$  was used.

determined for solutions containing either HNEt<sub>3</sub><sup>+</sup>, HNEt<sub>3</sub><sup>+</sup>/NEt<sub>3</sub>, HOAc, or HOAc/OAc<sup>−</sup>, using the same concentrations as were used for the determination of the  $E_{\text{BH}}^+$  (Section 4.2.5). This was done for both the ORR and HPRR catalysed by Cu-tmpa (0.3 mM). For this purpose,  $i_{\text{cat}}$  values were determined from background corrected LSVs (Figure C.3). The resulting  $k_{\text{obs}}$  are shown in Table 4.5. For the  $k_{\text{obs,ORR}}$ , the catalytic electron transfer number used was 4, as under all four conditions both O<sub>2</sub> and H<sub>2</sub>O<sub>2</sub> reduction take place at the potential where the  $k_{\text{obs}}$  was determined (Figure C.4, Appendix C.3). The  $k_{\text{obs,ORR}}$  for HNEt<sub>3</sub><sup>+</sup> and HOAc are in good agreement with the  $k_{\text{obs}}$  obtained at low catalyst concentration for these acids. For three of the four conditions, two different  $k_{\text{obs}}$  values are calculated for the HPRR, as multiple catalytic waves were observed in the CVs and LSVs. Under those conditions, two distinct catalytic waves were visible in the LSV, and the smallest  $k_{\text{obs}}$  value corresponds to the catalytic current of first, smaller reduction wave, while the larger value corresponds to the maximum catalytic current, which takes place at more negative potentials. Compared to the rate constants observed in aqueous solution, the rate constants obtained in MeCN are several orders of magnitude lower, particularly for the ORR. This is in line with the very low equilibrium constant of formation for  $[\text{Cu}^{\text{II}}(\text{O}_2^{\bullet-})(\text{tmpa})]^+$  that was observed in propionitrile (EtCN).<sup>[3]</sup>

## 4.3. Discussion

### 4.3.1. The redox behaviour of Cu-tmpa in the absence of acids

The reaction of Cu<sup>I</sup>-tmpa with O<sub>2</sub> in the non-protic solvents EtCN, THF, and acetone has been well-studied.<sup>[2-3, 11]</sup> It has been shown that the initially formed Cu<sup>I</sup>-tmpa complex reacts with O<sub>2</sub> to form an end-on Cu<sup>II</sup> superoxide complex  $[\text{Cu}^{\text{II}}(\text{O}_2^{\bullet-})(\text{tmpa})]^+$ . However, nitriles are strongly coordinating ligands for Cu<sup>I</sup>.<sup>[2, 29]</sup> In EtCN, the equilibrium constant of formation for  $[\text{Cu}^{\text{II}}(\text{O}_2^{\bullet-})(\text{tmpa})]^+$  at room temperature is only  $0.38 \text{ M}^{-1}$  due to competition of O<sub>2</sub> with EtCN as a ligand for the Cu<sup>I</sup>-tmpa complex (Scheme 4.2).<sup>[3]</sup> Additionally, the dimerization reaction of  $[\text{Cu}^{\text{II}}(\text{O}_2^{\bullet-})(\text{tmpa})]^+$  with  $[\text{Cu}^{\text{I}}(\text{tmpa})(\text{EtCN})]^+$  to form  $[\{\text{Cu}^{\text{II}}(\text{tmpa})\}_2(\mu\text{-O}_2)]^{2+}$  occurs more slowly than the formation of the initial



**Scheme 4.2.** Reaction scheme for the reaction of  $[\text{Cu}^{\text{I}}(\text{tmpa})(\text{EtCN})]^+$  with  $\text{O}_2$ , with equilibrium constant of formation as reported in the literature.<sup>[2-3]</sup>

monomeric superoxide species, with a formation rate constant of  $6.7 \times 10^6 \text{ M}^{-1} \text{ s}^{-1}$  against  $5.8 \times 10^7 \text{ M}^{-1} \text{ s}^{-1}$  for the latter, but has a much higher equilibrium constant of formation of  $4.2 \times 10^3 \text{ M}^{-1}$ , indicating better stability.

Our electrochemical measurements of Cu-tmpa in MeCN in the presence of dioxygen show a significant degree of irreversibility (Figures 4.1b and 4.1c). This poor electrochemical reversibility is characterized by an increased  $\Delta E_p$ , a lowered oxidative current, and an irreversible reduction at a potential below  $-0.8 \text{ V}$  vs.  $\text{Fc}^+/\text{Fc}$ . The lower oxidative current of the  $\text{Cu}^{\text{II/I}}$  redox couple is partially the result of the above mentioned equilibrium constant of  $[\text{Cu}^{\text{II}}(\text{O}_2^{\bullet-})(\text{tmpa})]^+$ , which is expected to be of a similar magnitude in MeCN. Due to the equilibrium between  $[\text{Cu}^{\text{I}}(\text{tmpa})(\text{L})]^+$  and  $[\text{Cu}^{\text{II}}(\text{O}_2^{\bullet-})(\text{tmpa})]^+$  part of the  $\text{Cu}^{\text{I}}$  is sequestered as the superoxido species upon reacting with  $\text{O}_2$ , thus lowering the oxidation current of the  $\text{Cu}^{\text{II/I}}$  redox couple. However, in the timeframe of the CV only a small or even negligible reduction in oxidative current would be expected due the very fast rates associated with this forward and reverse reactions (in Scheme 4.2), maintaining the equilibrium while the electrochemical oxidation of  $\text{Cu}^{\text{I}}$  takes place. Additionally, formation of the dimeric peroxido species may explain the increase in  $\Delta E_p$ , due to lower reversibility of the redox chemistry caused by sequential electrochemical and chemical reactions. This would also contribute to the reduced redox current over multiple scans (Figure 4.1c), as over time some of the dimer may accumulate near the electrode. A complicating factor is the presence of trace amounts of water, and thus protons, in MeCN. For the experiments shown in Figure 4.1,  $0.5 \text{ mM}$  of  $\text{H}_2\text{O}$  was detected using Karl-Fisher titration following drying of the solvent, which is close to a 1:2 ratio of catalyst to water. A proton-coupled electron transfer (PCET) step from the initially formed superoxido species would result in the formation of the hydroperoxide complex  $[\text{Cu}^{\text{II}}(\text{OOH})(\text{tmpa})]^+$ . This species could react further, resulting in the formation of  $\text{H}_2\text{O}$ ,

or even  $\text{H}_2\text{O}_2$  following a simple protonation. Alternatively, the dimer, which has been shown to be able to catalyse the ORR in acetone using Fc as a reductant, can be further reduced to a  $\text{Cu}^{\text{I}}\text{--OO--Cu}^{\text{II}}$  species. The irreversible reduction that is observed below  $-0.8$  V can be the result of either of these proposed steps. While the magnitude of the reductive current is similar to that of the one-electron reduction of  $\text{Cu}^{\text{II}}\text{-tmpa}$  to  $\text{Cu}^{\text{I}}\text{-tmpa}$ , it cannot be excluded that this is actually a small catalytic wave resulting from the presence of trace amounts of water.

#### 4.3.2. Redox behaviour of Cu-tmpa in the presence of different acids

For several of the studied electrochemical conditions, multiple redox couples were observed during CV measurements of Cu-tmpa. Reproducibility of the redox couple of Cu-tmpa in acetonitrile in the presence of  $\text{HNEt}_3^+$  (50 mM) appeared to be poor, as two redox couples with varying relative intensity were observed in several experiments. Initially, it was assumed that perhaps variable water content in the electrolyte solution was the cause of the varying ratios of the two visible redox couples. However, the ultimate cause appeared to be a time-dependent chemical conversion that takes place in the electrolyte solution. Indeed, most experiments that were performed under these conditions show a different distribution of the two distinct redox couples, which seems to be an effect of the difference in time between preparation of the solution and the actual electrochemical measurement. The redox couple at the less negative potential overlaps to a large degree with the redox couple of Cu-tmpa in  $\text{NBu}_4\text{PF}_6$ , which is assigned to  $[\text{Cu}(\text{tmpa})(\text{CH}_3\text{CN})]^{2+}$ . This is particularly clear at lower concentrations of  $\text{HNEt}_3^+$  concentrations (Figure 4.8a).

We observed both a time-dependent conversion and a concentration-dependent effect, where higher initial  $\text{HNEt}_3^+$  concentrations resulted in an increased redox current of the species with the more negative  $E_{1/2}$ , which indicates that protonation of the ligand plays a role. This is also in line with the observed stability of the ratio between the two redox couples over time in the buffered electrolyte solution containing  $\text{HNEt}_3^+/\text{NEt}_3$  in a 1:1 ratio, where no new equilibrium is established. UV-Vis absorption spectra of a solution containing Cu-tmpa upon addition of  $\text{HNEt}_3^+$  (or  $\text{HNEt}_3^+/\text{NEt}_3$ ) showed a small blueshift of the d-d transition band by 25 nm, which may indicate protonation of coordinated nitrogen atoms but this is not conclusive. However, no significant changes in the absorption were observed over time, contrary to the clear chemical conversion observed during the CV measurements. Several considerations can be made on the nature of the redox-active species associated with the redox couple at more negative potentials. The possibility of coordination of the  $\text{NEt}_3$  conjugate base can largely be discounted as nitriles such as MeCN are much better ligands for  $\text{Cu}^{\text{II}}$  and  $\text{Cu}^{\text{I}}$  species. Protonation of one or multiple nitrogen atoms in the ligand could result in

the dissociation of one of the N-donors. Dissociation of one of the pyridine arms of the ligand caused by the protonation of the pyridine seems unlikely, as  $\text{NEt}_3$  (conjugate acid  $\text{pK}_a = 18.8$ ) is also a stronger base than pyridine (conjugate acid  $\text{pK}_a = 12.5$ ) in MeCN.<sup>[30]</sup> This would have resulted in an increase of the redox potential of the species, as opposed to the observed decrease, as observed for copper complexes containing the bis(2-pyridylmethyl)amine ligand.<sup>[31-32]</sup> Additionally, it has been shown the tertiary aliphatic amine in the free tmpa ligand is less basic than the pyridine N-atom, contrary to the generally expected higher basicity of tertiary aliphatic amines.<sup>[33-35]</sup> While selective protonation of the tertiary amine of tmpa has been observed in a strained environment,<sup>[36-37]</sup> it is not known whether the same would occur when coordinated to a copper ion. For a wide range of copper complexes with multidentate ligands, it has been shown that the  $\text{Cu}^{\text{II}}$  redox potential is mainly influenced by the stability of the  $\text{Cu}^{\text{II}}$  species, while the corresponding  $\text{Cu}^{\text{I}}$  species show near uniform stability.<sup>[38-39]</sup> How protonation of the tmpa ligand would result in a more stable  $\text{Cu}^{\text{II}}$  complex, with better orbital overlap or increased electron density on the copper centre, is unclear and the exact nature of the species can not be predicted based on the available data.

The  $\text{Cu}^{\text{II}}$  redox couple of Cu-tmpa in the electrolyte solution containing HOAc is located at the same potential ( $-0.40$  V) as in the acid-free electrolyte solution. This would indicate that no chemical conversion takes place upon addition of low (20 mM) amounts of acid and  $[\text{Cu}(\text{tmpa})(\text{CH}_3\text{CN})]^{2+}$  is still the main species in solution. As the HOAc concentration is increased from 20 to 100 mM, the current of the redox couple decreases only slightly and a second smaller redox couple is observed at a more negative potential. However, HOAc is a weaker acid than  $\text{HNEt}_3^+$  (Table 4.1) and ligand protonation is therefore unlikely to play a role. The CVs of Cu-tmpa in the buffered acid-conjugate base HOAc/OAc<sup>-</sup> solution shows a single well-defined redox couple at a more negative potential ( $-0.73$  V), while UV-vis absorption spectra under the same conditions show the presence of a LMCT band and blueshifted d-d band, which indicates the coordination of anionic acetate to the copper centre (Appendix C.9). Acetate is a good ligand for copper and is not readily replaced by MeCN under standard conditions.<sup>[40-42]</sup> Indeed, it has been previously shown that the addition of trifluoroacetic acid to  $[\text{Cu}^{\text{II}}(\text{tmpa})]^{2+}$  in acetone resulted in the formation of  $[\text{Cu}^{\text{II}}(\text{tmpa})(\text{CF}_3\text{COO}^-)]^+$ , causing a  $-300$  mV shift in the redox potential due to the increased electron density on the Cu centre.<sup>[14]</sup> Thus, the redox couple at  $-0.73$  V is associated with the compound  $[\text{Cu}^{\text{II}}(\text{OAc})(\text{tmpa})]^+$ . In contrast, for unbuffered solutions containing HOAc, the concentration of available OAc<sup>-</sup> is not high enough to replace MeCN in the coordination sphere, which would explain why the intensity of the second redox event is low.

#### 4.3.3. Catalytic performance of Cu-tmpa for the ORR in MeCN

The electrocatalytic reduction of O<sub>2</sub> by Cu-tmpa in MeCN is significantly slower than in aqueous solution, despite oxygen having a six times higher solubility in MeCN than in water at 1 atm O<sub>2</sub> at room temperature.<sup>[17]</sup> The  $k_{\text{obs}}$  for ORR that were calculated based on the current enhancement in MeCN (1.5-5.6 s<sup>-1</sup>) are a factor 10<sup>5</sup> lower than the TOF in a neutral aqueous solution (1.5×10<sup>5</sup> s<sup>-1</sup>, Chapter 2). The overpotential (defined by  $E_{\text{cat}/2}$ ) for the ORR with Cu-tmpa are lower in the buffered MeCN solutions (below 0.8 V) than in neutral aqueous solution (0.92 V), as shown in Table 4.4. For both HOAc and HNEt<sub>3</sub><sup>+</sup> a linear relationship between the catalytic current and the Cu-tmpa concentration was observed, indicating a first-order catalytic reaction in catalyst, as was also observed in a neutral aqueous solution. Interestingly, a first-order dependence of the catalytic current on the acid concentration was found with HOAc in MeCN, while in the case of HNEt<sub>3</sub><sup>+</sup> the catalytic rates were independent of the acid concentration, as shown in Appendix C.4. These findings indicate that the rate-determining step of the catalytic reaction in the presence of HOAc does not only involve the catalyst, but also the acid (or H<sup>+</sup>) species. For HNEt<sub>3</sub><sup>+</sup>, the changing catalytic behaviour can be directly linked to the concentration-induced change of the redox active species. Once this interconversion is fully completed, a further increase in acid concentration does not lead to an appreciable increase in catalytic current (Figure 4.8). Thus, different rate laws govern the ORR by Cu-tmpa in the presence of HOAc and HNEt<sub>3</sub><sup>+</sup>.

With these observations, the catalytic mechanism for the ORR in MeCN in the presence of AcOH shows strong similarities to the mechanism observed in aqueous solution, as shown in Scheme 4.1, with some small modifications. As stated, the rate-determining step involves a single Cu centre, but also involves a protonation step, likely the H<sup>+</sup>/e<sup>-</sup> PCET step from [Cu<sup>II</sup>(O<sub>2</sub><sup>•-</sup>)(tmpa)]<sup>+</sup> to [Cu<sup>II</sup>(OOH)(tmpa)]<sup>+</sup>. Despite the expected unfavourable thermodynamic equilibrium for the binding of O<sub>2</sub> to [Cu<sup>I</sup>(MeCN)(tmpa)]<sup>+</sup>, the kinetic rate constant of formation ( $k_1$ ) is very high (5.8×10<sup>7</sup> M<sup>-1</sup> s<sup>-1</sup> in EtCN).<sup>[3]</sup> When a rapid equilibrium, like the reversible binding of O<sub>2</sub> to Cu<sup>I</sup>, is followed by a slow step, the overall observed rate constant is a function of both the equilibrium constant and the rate constant of the subsequent slower reaction step, in accordance with the pre-equilibrium approximation.<sup>[43]</sup> Thus, while the PCET step would be the rate-determining step, the binding of O<sub>2</sub> is still involved in the overall rate constant of the ORR catalysed by Cu-tmpa in MeCN.

#### 4.3.4. Catalytic performance of Cu-tmpa towards the HPORR in MeCN

Like the reduction of O<sub>2</sub>, the reduction of H<sub>2</sub>O<sub>2</sub> in MeCN ( $k_{\text{obs}} = 2.2\text{--}43\text{ s}^{-1}$ ) is slower than in neutral aqueous solution ( $k_{\text{obs}} = 4.8\times 10^3\text{ s}^{-1}$ , Chapter 3), but only by a factor 100 to 1000. Additionally, in MeCN, the HPORR is generally faster under these conditions than

the ORR, whereas in water the opposite is the case. This holds true both in the presence and absence of base. This behaviour seems to point at  $\text{Cu}^{\text{II}}\text{-OOH}$  being more readily formed from the reaction of  $\text{Cu}^{\text{I}}\text{-tmpa}$  with  $\text{H}_2\text{O}_2$  than with  $\text{O}_2$  in MeCN, perhaps mediated by the presence of 30 mM of  $\text{H}_2\text{O}$  in the solution. Indeed, in the presence of a base and  $\text{H}_2\text{O}_2$   $[\text{Cu}^{\text{II}}(\text{OOH})(\text{tmpa})]^+$  is spontaneously formed from  $[\text{Cu}^{\text{II}}(\text{tmpa})(\text{L})]^{2+}$  (Appendix C.9).

A comparison of the maximum HPRR  $k_{\text{obs}}$  under different conditions shows similar values in solutions containing  $\text{HNEt}_3^+$ ,  $\text{HNEt}_3^+/\text{NEt}_3$ , or HOAc (Table 4.5). However, the  $k_{\text{obs}}$  (of the first and second catalytic wave) is at least one order of magnitude lower in the presence of the acid-conjugate base pair  $\text{HOAc}/\text{OAc}^-$  than for the other conditions. This behaviour validates the previously discussed formation of  $[\text{Cu}^{\text{II}}(\text{tmpa})(\text{OAc})]^+$  when  $\text{HOAc}/\text{OAc}^-$  is present in solution. Formation of this species results in a lowered catalytic activity for the HPRR caused by the stronger coordination of acetate compared to MeCN, in essence blocking the active site of the catalyst for  $\text{H}_2\text{O}_2$  binding. While spontaneous formation of the  $\text{Cu}^{\text{II}}\text{-OOH}$  species was detected under non-catalytic conditions in MeCN, the UV-vis absorbance around 400 nm associated with this species was almost three times lower in the presence of  $\text{HOAc}/\text{OAc}^-$  versus  $\text{HNEt}_3^+/\text{NEt}_3$ . Furthermore, the absorption band at 400 nm was also only visible 22 hours after addition of  $\text{H}_2\text{O}_2$  to the solution containing  $\text{HOAc}/\text{OAc}^-$ , as opposed to the immediate appearance of this band in the presence of  $\text{HNEt}_3^+/\text{NEt}_3$ . This again shows that the formation of the  $\text{Cu}^{\text{II}}\text{-OOH}$  species is slower for  $[\text{Cu}^{\text{II}}(\text{OAc})(\text{tmpa})]^+$ . However, the effect of the strong homoconjugation of acetic acid cannot be excluded in this discussion, as the lowered proton availability could also explain part of the lowered catalytic activity of  $\text{Cu-tmpa}$  towards HPRR in presence of HOAc. The second catalytic wave in the presence of  $\text{HOAc}/\text{OAc}^-$ , might be the result of  $\text{H}_2\text{O}$  acting as the proton source, which would require a higher driving force, and thus a higher overpotential.

## 4.4. Conclusion

The influence was investigated of different acids and acid-conjugate base mixtures on the electrocatalytic  $\text{O}_2$  and  $\text{H}_2\text{O}_2$  reduction by  $\text{Cu-tmpa}$  in acetonitrile. It was shown that the use of proton donors with a lower  $\text{p}K_{\text{a}}$  resulted in destabilisation of the  $\text{Cu-tmpa}$  compound. This was apparent from the lack of reversible redox couples in the presence of HTFA and  $\text{HDMF}^+$ , something which was also observed for  $\text{Cu-tmpa}$  at lower pH (<4) in aqueous electrolyte solution. In all cases, higher catalytic  $k_{\text{obs}}$  were observed for the ORR in the unbuffered electrolyte solutions containing only the acid species. Coordination of acetate is the likely cause of the reduced catalytic activity in solution containing  $\text{HOAc}/\text{OAc}^-$ , which is harder to replace in the coordination sphere, thus inhibiting catalysis. This is even more obvious for the HPRR. The reduction of the



catalytic activity is smaller in the presence of triethylamine, and is likely the result of the established equilibrium between  $[\text{Cu}(\text{tmpa})(\text{CH}_3\text{CN})]^{2+}$  and the as of yet unidentified species with a more negative redox potential. In contrast to the catalytic behaviour of Cu-tmpa in neutral aqueous solutions, higher TOFs were observed for the HPRR than for the ORR in MeCN under each of the different conditions that were investigated. This points to a more positive formation constant for the  $\text{LCu}^{\text{II}}\text{-OOH}$  complex than for  $\text{LCu}^{\text{II}}\text{-OO}^{\bullet-}$  under these conditions. As was observed under aqueous conditions, the catalytic rate showed a first-order dependence in catalyst concentration, confirming a mononuclear catalytic mechanism for Cu-tmpa under electrochemical conditions. Interestingly, the  $k_{\text{obs}}$  for the ORR shows a first-order dependence on the acid concentration in the electrolyte solution containing HOAc. These results confirm that in the presence of HOAc the catalytic mechanism for ORR in MeCN is largely the same as in water, although the rate-determining step in MeCN is the PCET step from  $[\text{Cu}^{\text{II}}(\text{O}_2^{\bullet-})(\text{tmpa})]^+$  to form  $[\text{Cu}^{\text{II}}(\text{OOH})(\text{tmpa})]^+$ .

## 4.5. Experimental

### 4.5.1. General

Tetrabutylammonium hexafluoridophosphate ( $\geq 99.0\%$ , for electrochemical analysis) tetrabutylammonium hydroxide (1.1 M in MeOH), ammonium hexafluoridophosphate, and acetic acid (99.99% trace metal basis) were obtained from Sigma-Aldrich. Triethylamine ( $\geq 99.8\%$ , for LC-MS) was obtained from VWR and ferrocene ( $>98\%$ ) was obtained from Fluka. The copper complex  $[\text{Cu}(\text{tmpa})(\text{MeCN})](\text{OTf})_2$  was synthesized as described in Chapter 2. Acetonitrile (99.9%, HPLC grade, BioSolve) was further dried over activated molecular sieves for 4 days. Molecular sieves (3 Å, Sigma Aldrich) were first rinsed with acetonitrile to remove impurities and loose solid particles, and activated by drying at 140 °C in a vacuum oven at  $<10$  mbar for 2 days.

### 4.5.2. Electrochemical measurements

Autolab PGSTAT 12, 204, and 128N potentiostats in combination with Autolab NOVA 2 software were used for all measurements. Electrochemical measurements were performed in a custom-build 10 mL glass single-compartment cell with a three-electrode setup, or a single compartment cell based on single-use 20 mL glass vials, allowing for a four-electrode setup, in the same approach as reported by Roberts and Bullock.<sup>[21]</sup>

The 10 mL single-compartment cell used during the electrochemical measurements was regularly cleaned to remove impurities by overnight submersion in an aqueous 0.5 M  $\text{H}_2\text{SO}_4$  solution containing 1 mg/mL (6.3 mM)  $\text{KMnO}_4$ , followed by removal of excess

KMnO<sub>4</sub> and MnO<sub>2</sub> from the glassware with diluted H<sub>2</sub>SO<sub>4</sub> and H<sub>2</sub>O<sub>2</sub>. Finally, the glassware was rinsed five times and subsequently boiled two times in Milli-Q water. Prior to each experiment all glassware was boiled once in Milli-Q water and oven-dried overnight at 120 °C. A PEEK encapsulated glassy carbon ( $A = 0.0707 \text{ cm}^2$ , Metrohm) was used as the working electrode in a submerged setup. Before every experiment, the GC electrodes were manually polished for 5 mins each with 1.0, 0.3, and 0.05  $\mu\text{m}$  alumina suspensions on Buehler cloth polishing pads, followed by sonication in MeCN for 10 minutes. A gold wire was used as the counter electrode and was flame annealed and rinsed with Milli-Q water before each experiment. A double-junction reference electrode (Metrohm) was used, either used as a 0.3 M Ag/AgCl reference, or as a Ag/AgNO<sub>3</sub> reference. For the Ag/AgNO<sub>3</sub> solution, the inner junction was filled with 10 mM AgNO<sub>3</sub> in MeCN, while the outer junction was filled with 100 mM NBu<sub>4</sub>PF<sub>6</sub> in MeCN. The potential and stability of the Ag/AgNO<sub>3</sub> reference electrode was carefully monitored, and the solution was refreshed when necessary (Appendix C.6). All measurements were referenced to the Fc<sup>+</sup>/Fc redox couple.

All gasses used during electrochemical measurements, O<sub>2</sub> (5.0 grade), and argon (5.0 grade), were supplied by Linde. Oxygen-free electrolyte solutions were prepared by sparging the solution for 30 minutes with argon, after which a 1 atm argon atmosphere was maintained. Oxygen-saturated electrolyte solutions were obtained by sparging the cell for 20 minutes with O<sub>2</sub>, after which a 1 atm O<sub>2</sub> atmosphere was maintained. All gases were pre-saturated with MeCN through a pre-bubbler before being passed through the electrochemical cell.

#### 4.5.3. OCP measurements

A Pt wire was used for the determination of the open circuit potential (OCP). The Pt wire was flame-annealed and subsequently electropolished in a 0.1 M H<sub>2</sub>SO<sub>4</sub> aqueous solution for 25 to 50 cycles at 500 mV s<sup>-1</sup> between -0.05 and 1.9 V vs. RHE before every experiment. For every different electrolyte mixture, a new 20 mL glass vial was used thoroughly rinsed with MeCN and dried in the oven. The hydrogen and argon gas were pre-saturated with solvent by bubbling through acetonitrile, which was dried over activated molecular sieves (3Å). 5 mL of the desired MeCN electrolyte solution, containing both NBu<sub>4</sub>PF<sub>6</sub> (100 mM) and the desired acid-conjugated base mixture, was added to the glass vial, followed by bubbling with a MeCN saturated flow of H<sub>2</sub> for 2-5 minutes. The OCP was measured by the Pt wire electrode over a period of 60 seconds, while vigorously bubbling the solution with H<sub>2</sub>. This was repeated until a stable OCP value was found. Subsequently Fc was added to the solution, and under a H<sub>2</sub> flow over the solution, a CV was measured with a GC electrode to obtain the  $E_{1/2}$  of Fc<sup>+</sup>/Fc.

#### 4.5.4. Catalyst concentration dependence studies

For the determination of the catalytic current  $i_{\text{cat}}$  as a function of Cu-tmpa concentration, the GC electrode was polished with 0.05  $\mu\text{m}$  alumina suspension for 5 minutes, rinsed with MilliQ and subsequently sonicated in MeCN for 10 minutes for every different catalyst concentration. Upon addition of aliquots of Cu-tmpa (10 mM in MeCN), the electrolyte solution was mixed thoroughly in both cell compartments and the solution was saturated with oxygen by bubbling the solution for 10 minutes with  $\text{O}_2$  pre-saturated with MeCN. After the last measurement, Fc was added to the solution and the  $E_{1/2}$  of  $\text{Fc}^+/\text{Fc}$  was measured. Additionally, a blank CV was measured of the GC electrode in an oxygen-saturated electrolyte solution in the absence of Cu-tmpa. The catalytic currents from CV measurements obtained in the presence of Cu-tmpa were corrected using this blank measurement, giving the catalytic current without any contribution from the GC electrode.

#### 4.5.5. Acid concentration dependence studies

For the determination of the catalytic current  $i_{\text{cat}}$  as a function of acid concentration, the GC electrode was polished with 0.05  $\mu\text{m}$  alumina suspension for 5 minutes, rinsed with MilliQ and subsequently sonicated in MeCN for 10 minutes for each different catalyst concentration. Cu-tmpa (0.3 mM) and Fc were dissolved in the electrolyte solution (100 mM  $\text{NBu}_4\text{PF}_6$ ) and transferred to the electrochemical cell. Of this solution, 1 mL was used to dissolve the solid  $\text{HNEt}_3\text{PF}_6$ , kept under argon, which was transferred back into the electrochemical cell to reach the required acid concentration. The solution was thoroughly mixed and subsequently saturated with argon by bubbling for 10 minutes with 1 atm Ar pre-saturated with MeCN. A CV was measured to obtain the redox couple of Cu-tmpa, after which the solution was saturated with oxygen by bubbling for 10 minutes with  $\text{O}_2$  pre-saturated with MeCN. After a CV was measured to obtain the catalytic current, a CV was measured in a potential window between 0.1 to 0.8 V vs. Ag/AgCl to obtain the  $E_{1/2}$  of Fc. This process was repeated for all the different acid concentrations. The same methodology was followed to measure blank CVs of the GC electrode in the absence of Cu-tmpa.

#### 4.5.6. Synthesis

##### 4.5.6.1. Synthesis of triethylammonium hexafluoridophosphate ( $\text{HNEt}_3\text{PF}_6$ )

$\text{NH}_4\text{PF}_6$  (6.52 g, 40 mmol) was suspended in toluene (40 mL), followed by the addition of triethylamine (5.58 mL, 40 mmol). The mixture was stirred and refluxed for 2 hours, after which the solution was allowed to cool down. The precipitate was filtered by vacuum filtration and washed with toluene (4x 15 mL). After drying in air, the product

was obtained as a white crystalline solid. The NMR is in good agreement with those reported in the literature.<sup>[44]</sup> Yield: 99% (9.78 g, 39.6 mmol). <sup>1</sup>H NMR (400 MHz, DMSO-d<sub>6</sub>) δ 3.37 (br), 3.09 (q, *J* = 7.3 Hz, 6H), 1.17 (t, *J* = 7.3 Hz, 9H).

#### 4.5.6.2. *Synthesis of tetrabutylammonium acetate*

Tetrabutylammonium acetate was prepared in methanol (MeOH) as described in literature.<sup>[45-47]</sup> Acetic acid (630 μL, 11 mmol) was dissolved in MeOH (10 mL). NBu<sub>4</sub>OH in MeOH (7.9 mL, 11 mmol) was added. The reaction was stirred over night at room temperature. The solvents were evaporated at reduced pressure (65 °C) and the resulting product was liquid at high temperatures (65 °C). When cooled to room temperature the product crystallizes. The solid was washed twice with hexane (10 mL). Recrystallisation was done by dissolving the product in toluene (5 mL) and was crashed out by adding an excess amount of hexane. The hexane was removed by decantation and additional hexane was added twice leaving the product on the bottom of the round bottom flask. The product was dissolved in toluene (10 mL). The toluene was removed at reduced pressure. The product (quantitative yield) was further dried at low vacuum (<1 mbar) overnight. <sup>1</sup>H NMR (300 MHz, Chloroform-d) δ 3.38 – 3.29 (m, 9H), 1.94 (s, 3H), 1.72 – 1.57 (m, 9H), 1.42 (h, *J* = 7.3 Hz, 9H), 0.99 (t, *J* = 7.3 Hz, 12H).

#### 4.5.6.3. *Synthesis of dimethylformamidium trifluoromethanesulfonate ((HDMF)OTf)*

Dimethylformamidium trifluoromethanesulfonate ([HDMF]<sup>+</sup>OTf<sup>-</sup>) was synthesized following the reported procedure. Dimethylformamide (DMF) (0.87 mL, 11.3 mmol) was added to dichloromethane (DCM) (30 mL) using a glass pipette. The mixture was stirred and triflic acid (HOTf) (1.0 mL, 11.3 mmol) was added dropwise to the mixture using a glass pipette. The mixture was stirred for 10 minutes for the reactants to react in a one-step protonation. After 10 minutes a clear solution was obtained and the solvents were evaporated: first DCM was removed (40 °C, 700 mbar). After DCM was evaporated the temperature was increased and the pressure lowered (70 °C, 10mbar). After 30 minutes about 1-2 mL of clear solution was left in the round-bottom flask. The solution crystalized into a white crystalline solid after cooling to room temperature at normal pressure. The crystalline solid was dried overnight at low vacuum, yielding a white crystalline solid (2.5 g, quantitative yield). The crystals were stored under inert atmosphere. <sup>1</sup>H NMR (400 MHz, Chloroform-d) δ 8.89 (br s, 1H), 8.49 (s, 1H), 3.32 (s, 3H), 3.16 (s, 3H).

## 4.6. References

- [1] M. Langerman, D. G. H. Hetterscheid, *Angew. Chem. Int. Ed.* **2019**, *58*, 12974-12978.
- [2] H. C. Fry, D. V. Scaltrito, K. D. Karlin, G. J. Meyer, *J. Am. Chem. Soc.* **2003**, *125*, 11866-11871.
- [3] C. X. Zhang, S. Kaderli, M. Costas, E.-i. Kim, Y.-M. Neuhold, K. D. Karlin, A. D. Zuberbühler, *Inorg. Chem.*

**2003**, *42*, 1807-1824.

- [4] Y. Lee, et al., *Inorg. Chem.* **2009**, *48*, 11297-11309.
- [5] T. Fujii, A. Naito, S. Yamaguchi, A. Wada, Y. Funahashi, K. Jitsukawa, S. Nagatomo, T. Kitagawa, H. Masuda, *Chem. Commun.* **2003**, 2700-2701.
- [6] H. R. Lucas, G. J. Meyer, K. D. Karlin, *J. Am. Chem. Soc.* **2010**, *132*, 12927-12940.
- [7] M. J. Baldwin, P. K. Ross, J. E. Pate, Z. Tyeklar, K. D. Karlin, E. I. Solomon, *J. Am. Chem. Soc.* **1991**, *113*, 8671-8679.
- [8] L. M. Mirica, X. Ottenwaelder, T. D. P. Stack, *Chem. Rev.* **2004**, *104*, 1013-1046.
- [9] C. E. Elwell, N. L. Gagnon, B. D. Neisen, D. Dhar, A. D. Spaeth, G. M. Yee, W. B. Tolman, *Chem. Rev.* **2017**, *117*, 2059-2107.
- [10] S. Itoh, *Curr. Opin. Chem. Biol.* **2006**, *10*, 115-122.
- [11] S. Fukuzumi, H. Kotani, H. R. Lucas, K. Doi, T. Suenobu, R. L. Peterson, K. D. Karlin, *J. Am. Chem. Soc.* **2010**, *132*, 6874-6875.
- [12] L. Tahsini, H. Kotani, Y. M. Lee, J. Cho, W. Nam, K. D. Karlin, S. Fukuzumi, *Chem. Eur. J.* **2012**, *18*, 1084-1093.
- [13] S. Fukuzumi, L. Tahsini, Y.-M. Lee, K. Ohkubo, W. Nam, K. D. Karlin, *J. Am. Chem. Soc.* **2012**, *134*, 7025-7035.
- [14] S. Kakuda, R. L. Peterson, K. Ohkubo, K. D. Karlin, S. Fukuzumi, *J. Am. Chem. Soc.* **2013**, *135*, 6513-6522.
- [15] D. Das, Y.-M. Lee, K. Ohkubo, W. Nam, K. D. Karlin, S. Fukuzumi, *J. Am. Chem. Soc.* **2013**, *135*, 2825-2834.
- [16] N. Le Poul, et al., *J. Am. Chem. Soc.* **2009**, *131*, 17800-17807.
- [17] M. L. Pegis, C. F. Wise, D. J. Martin, J. M. Mayer, *Chem. Rev.* **2018**, *118*, 2340-2391.
- [18] M. König, J. Vaes, E. Klemm, D. Pant, *iScience* **2019**, *19*, 135-160.
- [19] S. Garg, M. Li, A. Z. Weber, L. Ge, L. Li, V. Rudolph, G. Wang, T. E. Rufford, *J. Mater. Chem. A* **2020**, *8*, 1511-1544.
- [20] L. Sun, V. Reddu, A. C. Fisher, X. Wang, *Energy Environ. Sci.* **2020**, *13*, 374-403.
- [21] J. A. S. Roberts, R. M. Bullock, *Inorg. Chem.* **2013**, *52*, 3823-3835.
- [22] M. L. Pegis, J. A. S. Roberts, D. J. Wasylenko, E. A. Mader, A. M. Appel, J. M. Mayer, *Inorg. Chem.* **2015**, *54*, 11883-11888.
- [23] I. M. Kolthoff, M. K. Chantooni, *J. Am. Chem. Soc.* **1963**, *85*, 426-430.
- [24] J. F. Coetzee, G. R. Padmanabhan, *J. Am. Chem. Soc.* **1965**, *87*, 5005-5010.
- [25] Z. Pawlak, G. Zundel, J. Fritsch, A. Wawrzynów, S. Kuna, M. Tusk, *Electrochim. Acta* **1984**, *29*, 391-395.
- [26] M. Asahi, S.-i. Yamazaki, S. Itoh, T. Ioroi, *Electrochim. Acta* **2016**, *211*, 193-198.
- [27] M. L. Pegis, B. A. McKeown, N. Kumar, K. Lang, D. J. Wasylenko, X. P. Zhang, S. Rauegi, J. M. Mayer, *ACS Cent. Sci.* **2016**, *2*, 850-856.
- [28] R. M. Bullock, A. M. Appel, M. L. Helm, *Chem. Commun.* **2014**, *50*, 3125-3143.
- [29] F. H. Jardine, in *Advances in Inorganic Chemistry and Radiochemistry*, Vol. 17 (Eds.: H. J. Emeléus, A. G. Sharpe), Academic Press, **1975**, pp. 115-163.
- [30] S. Tshepelevitsh, A. Kütt, M. Lökov, I. Kaljurand, J. Saame, A. Heering, P. G. Plieger, R. Vianello, I. Leito, *Eur. J. Org. Chem.* **2019**, *2019*, 6735-6748.
- [31] A. Kunishita, J. D. Scanlon, H. Ishimaru, K. Honda, T. Ogura, M. Suzuki, C. J. Cramer, S. Itoh, *Inorg. Chem.* **2008**, *47*, 8222-8232.
- [32] M. Asahi, S.-i. Yamazaki, S. Itoh, T. Ioroi, *Dalton Trans.* **2014**, *43*, 10705-10709.
- [33] G. Anderegg, K. Popov, P. S. Pregosin, *Helv. Chim. Acta* **1986**, *69*, 329-332.
- [34] A. Hazell, J. McGinley, H. Toftlund, *Dalton Trans.* **1999**, 1271-1276.
- [35] G. Anderegg, E. Hubmann, N. G. Podder, F. Wenk, *Helv. Chim. Acta* **1977**, *60*, 123-140.
- [36] L. Zhiquan, H. Xie, S. E. Border, J. Gallucci, R. Z. Pavlović, J. D. Badjić, *J. Am. Chem. Soc.* **2018**, *140*, 11091-11100.
- [37] G. Qiu, C. Colombari, N. Vanthuyne, M. Giorgi, A. Martinez, *Chem. Commun.* **2019**, *55*, 14158-14161.
- [38] E. A. Ambundo, M.-V. Deydier, A. J. Grall, N. Agüera-Vega, L. T. Dressel, T. H. Cooper, M. J. Heeg, L. A. Ochrymowycz, D. B. Rorabacher, *Inorg. Chem.* **1999**, *38*, 4233-4242.
- [39] D. B. Rorabacher, *Chem. Rev.* **2004**, *104*, 651-698.
- [40] M. Vaidyanathan, R. Viswanathan, M. Palaniandavar, T. Balasubramanian, P. Prabhakaran, P. Muthiah, *Inorg. Chem.* **1998**, *37*, 6418-6427.
- [41] H. Adams, N. A. Bailey, C. O. R. de Barbarin, D. E. Fenton, Q.-Y. He, *J. Chem. Soc., Dalton Trans.* **1995**, 2323-

- 2331.
- [42] S. Meghdadi, M. Amirnasr, A. Amiri, Z. Musavizadeh Mobarakeh, Z. Azarkamanzad, *C. R. Chim.* **2014**, *17*, 477-483.
- [43] M. Rae, M. N. Berberan-Santos, *Chem. Phys.* **2002**, *280*, 283-293.
- [44] B. M. Trost, R. C. Livingston, *J. Am. Chem. Soc.* **2008**, *130*, 11970-11978.
- [45] S. E. Denmark, M. T. Burk, A. J. Hoover, *J. Am. Chem. Soc.* **2010**, *132*, 1232-1233.
- [46] P. Hamankiewicz, J. M. Granda, J. Jurczak, *Tetrahedron Lett.* **2013**, *54*, 5608-5611.
- [47] H. Nagae, R. Aoki, S.-n. Akutagawa, J. Kleemann, R. Tagawa, T. Schindler, G. Choi, T. P. Spaniol, H. Tsurugi, J. Okuda, K. Mashima, *Angew. Chem. Int. Ed.* **2018**, *57*, 2492-2496.



# Chapter 5

---

## *On the scaling relation between the reduction potential of copper catalysts and the turnover frequency for the oxygen and hydrogen peroxide reduction reactions*

*Structural changes to the coordination geometry of copper complexes can result in significant changes in their electronic structures, which can have a remarkable impact on the catalytic rates, selectivity, and the overpotential of electrocatalytic reactions. We have investigated the effect of varying the length of the alkyl spacer of one of the pyridine rings in the tris(2-pyridylmethyl)amine (tpma) ligand on the redox potential of the corresponding pyridylalkylamine copper complexes, and the resulting changes in their catalytic activity for the oxygen reduction reaction in neutral aqueous solution. We confirmed the strong influence of the coordination geometry on the  $E_{1/2}$  of the complex, with a more constrained Cu<sup>I</sup> coordination geometry resulting in the largest positive shift of the redox couple. Likewise, the catalytic onset for the oxygen reduction was equally shifted to a higher potential, resulting in a reduction of the overpotential. All synthesized complexes were shown to catalyse the hydrogen peroxide reduction reaction. A clear linear relationship was established between the maximum rate constants of the reduction of O<sub>2</sub> and H<sub>2</sub>O<sub>2</sub>, as determined by foot-of-the-wave analysis, and the  $E_{1/2}$  of the catalyst, where the catalytic rates decrease as the onset potential increases. Thus, while trade-off between rates and efficiencies remain, significant decreases of the overpotential by 300 mV were achieved by modifying the primary coordination environment of pyridylalkylamine copper complexes.*

To be submitted as a full article; M. Langerman, H. van de Vijver, M. A. Siegler, and D. G. H. Hetterscheid, *manuscript in preparation*.



## 5.1. Introduction

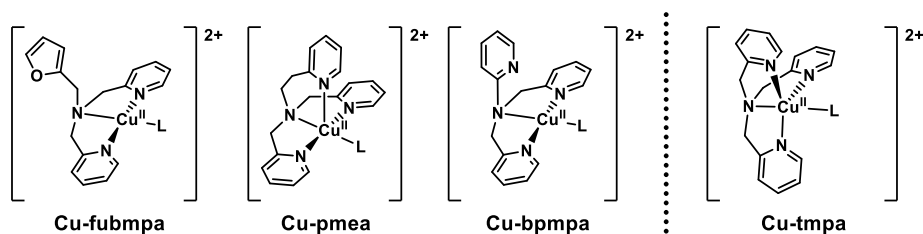
The electrochemical oxygen reduction reaction (ORR) can either result in the four-electron reaction product ( $\text{H}_2\text{O}$ ), or the two-electron reaction product ( $\text{H}_2\text{O}_2$ ), both involving different standard equilibrium potentials for the respective reactions involved, as shown in Scheme 5.1. Additionally, the four-electron pathway may proceed via  $\text{H}_2\text{O}_2$  as an intermediate as a result of two consecutive  $2\text{H}^+/2\text{e}^-$  reaction steps. Both the four-electron reduction of dioxygen ( $\text{O}_2$ ) to water and two-electron reduction to  $\text{H}_2\text{O}_2$  are important reactions, in relation to their application in fuel cell technology, and the use of  $\text{H}_2\text{O}_2$  as a powerful oxidant and potential energy carrier.<sup>[1-7]</sup>



**Scheme 5.1.** Standard electrode potentials of the different catalytic reactions involved in the ORR.

As described in Chapter 2, the tetradentate copper complex  $[\text{Cu}(\text{tmpa})(\text{L})]^{2+}$  ( $\text{Cu-tmpa}$ ) ( $\text{tmpa}$  = tris(2-pyridylmethyl)amine,  $\text{L}$  = solvent) has very high reaction rates for the electrochemical ORR.<sup>[8]</sup> It was shown that the stepwise 4-electron reduction took place, with  $\text{H}_2\text{O}_2$  observed as a detectable intermediate. Both the partial reduction of  $\text{O}_2$  to water (Chapter 2) and the reduction of  $\text{H}_2\text{O}_2$  (Chapter 3) catalysed by  $\text{Cu-tmpa}$  demonstrated high catalytic rate constants, with only a small difference in onset potential between the 2-electron ORR and the hydrogen peroxide reduction reaction (HPRR), resulting in only a small potential window where  $\text{H}_2\text{O}_2$  is the primary product during catalysis. Additionally, the fast catalytic rates for both reactions come at the cost of a significant overpotential. In order to reduce the overpotential and steer the selectivity towards either the full 4-electron or 2-electron reduction of dioxygen, a better fundamental understanding is necessary between the (electronic) structure of the copper catalyst and the catalytic activity for the ORR and HPRR.

The effect of ligand denticity and flexibility on the geometry and electronic structure of copper complexes has been a subject of intense study.<sup>[9-17]</sup> A significant library of different ligand modifications have been investigated for copper complexes based on the tetradentate pyridine ligand scaffold of  $\text{Cu-tmpa}$ .<sup>[18-20]</sup> Interestingly, a larger positive shift of the  $\text{Cu}^{\text{II/I}}$  redox potential (versus  $\text{Cu-tmpa}$ ) is observed for copper complexes with modifications in the length of the alkyl spacer between the central tertiary amine and the pyridine moieties than by adding electron withdrawing or donating functionalities on the pyridine moieties. For the latter, the largest shift of the  $\text{Cu}^{\text{II/I}}$  redox potential was observed for a complex where an -NHR ( $\text{R}$  = pivaloyl) group



**Scheme 5.2.** Overview of the structures of the three different copper(II) complexes investigated in this work, in addition to Cu-tpma.

was substituted on the ortho position of a single pyridine group.<sup>[20]</sup> The resulting +200 mV shift is significantly less than the shift for some of the complexes with modified alkyl spacer lengths.

We set out to investigate how changes to the tpm ligand scaffold would affect the catalytic activity of copper complexes for the ORR and HPRR. Desirable changes to the catalytic performance would be a more positive onset potential for the ORR or an increased selectivity for the production of  $\text{H}_2\text{O}_2$ , thereby eliminating or significantly reducing the ability of the catalyst to reduce  $\text{H}_2\text{O}_2$ . Alternatively, increased rates of HPRR versus the ORR could result in a clean 4-electron reduction of oxygen, where no significant amounts of  $\text{H}_2\text{O}_2$  are produced. Therefore, we investigated three different mononuclear copper complexes, shown in Scheme 5.2. In two of these,  $[\text{Cu}(\text{pmea})(\text{L})]^{2+}$  (Cu-pmea; pmea = bis[(2-pyridyl)methyl]-2-(2-pyridyl)ethylamine) and  $[\text{Cu}(\text{bpmpa})(\text{L})]^{2+}$  (Cu-bpmpa; bpmpa = bis[(2-pyridyl)methyl]-2-pyridylamine), the distance between the central tertiary amine and one of the pyridine arms was varied by changing methylene to an ethylene spacer (Cu-pmea) or removing it altogether, resulting in an aminopyridine moiety (Cu-bpmpa). A crystal structure of  $[\text{Cu}(\text{bpmpa})(\text{Cl})]\text{ClO}_4$  shows that the pyridine N of the aminopyridine does not coordinate to the copper centre but is rotated away from the copper centre.<sup>[12]</sup> The final novel complex,  $[\text{Cu}(\text{fubmpa})(\text{H}_2\text{O})(\text{OTf})_2]$  (Cu-fubmpa; fubmpa = *N*-(furan-2-ylmethyl)-*N*-[bis(2-pyridyl)methyl]amine) was designed as an analogue of the copper complex  $[\text{Cu}(\text{bmpa})(\text{L})]^{2+}$  (bmpa = bis(2-pyridylmethyl)amine),<sup>[21]</sup> by introduction of the non-coordinating furanyl moiety while maintaining the nature of the central tertiary amine. Here we show that these ligand-induced changes in the geometry and electronic structure of the copper complexes have a significant impact on the observed catalytic reactivity versus the ORR and HPRR.

## 5.2. Results and Discussion

### 5.2.1. Synthesis

The polypyridyl ligands bis[(2-pyridyl)methyl]-2-(2-pyridyl)ethylamine (pmea) and bis[(2-pyridyl)methyl]-2-pyridylamine (bpmpa) have been previously reported and were synthesized in a one-step reaction via reductive amination and nucleophilic substitution ( $S_N2$ ), respectively.<sup>[12]</sup> The novel ligand *N*-(furan-2-ylmethyl)-*N*-[bis(2-pyridyl)methyl]amine (fubmpa) was synthesized from the commercially available furan-2-ylmethanamine and 2-pyridinecarboxaldehyde via a reductive amination in a one-step reaction. Following purification by column chromatography, fubmpa was characterized by  $^1\text{H}$  NMR,  $^{13}\text{C}$  NMR and electrospray ionization mass spectrometry (ESI MS). The copper complexes  $[\text{Cu}(\text{pmea})(\text{CH}_3\text{CN})](\text{OTf})_2$  and  $[\text{Cu}(\text{bpmpa})(\text{CH}_3\text{CN})](\text{OTf})_2$  were synthesized by mixing the respective ligand with  $\text{Cu}(\text{OTf})_2$  in a 1:1 ratio in dry  $\text{CH}_3\text{CN}$  under inert atmosphere, and characterization was performed by ESI MS and elemental analysis (see section 5.4.2). The novel copper complex  $[\text{Cu}(\text{fubmpa})(\text{H}_2\text{O})(\text{OTf})_2]$  was synthesized by mixing fubmpa with  $\text{Cu}(\text{OTf})_2$  in a 1:1 ratio in  $\text{CH}_3\text{CN}$ . The resulting complex was purified by crystallizing the complex twice from  $\text{CH}_3\text{CN}$  by addition of diethyl ether. Characterization of Cu-fubmpa was done by elemental analysis, X-ray crystallography, and UV-vis spectroscopy. The single crystals for X-ray crystallography were obtained via liquid-liquid diffusion in an NMR tube, with Cu-fubmpa dissolved in chloroform and layered with diethyl ether. A projection of the structure is shown in Figure 5.1. In the crystal structure, the top axial OTf<sup>-</sup> ligand has a

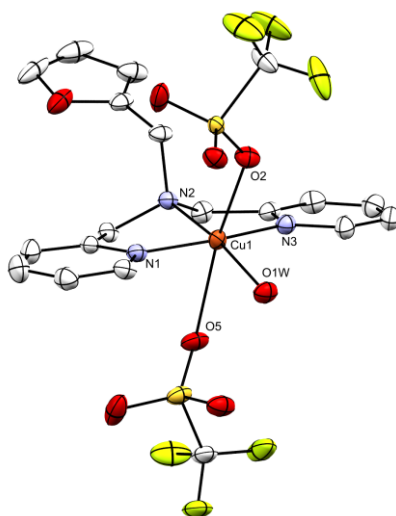


**Figure 5.1.** Crystal structure of Cu-fubmpa as determined by X-ray crystallography. All hydrogen atoms are omitted for clarity.

Cu–O bond distance of 2.375(1) Å. However, the Cu1–O5 distance between the copper centre and the second triflate is 2.665(2) Å. This is on the long side for an axial Cu–O bond, and points to a more square pyramidal coordination environment rather than an octahedral geometry.<sup>[22–25]</sup> Both elemental analysis and X-ray crystallography show that a water molecule is coordinated to the copper centre, likely originating from the Cu(OTf)<sub>2</sub> salt, which has a tendency to form hydrates when exposed to air. The coordinated water molecule forms a hydrogen bond (1.980 Å) with one of the oxygen atoms of the axial triflate ligand below the plane. Additionally, the crystal structure confirms that the furanyl group does not coordinate to the Cu centre. UV-vis spectra were measured in MilliQ water, and the extinction coefficient ( $\epsilon$ ) for the d-d transition at 660 nm is  $1.0 \times 10^2 \text{ L mol}^{-1} \text{ cm}^{-1}$ , and for the absorption peak at 251 nm an  $\epsilon$  of  $9.7 \times 10^3 \text{ L mol}^{-1} \text{ cm}^{-1}$  was found (Appendix D.1).

### 5.2.2. Electrochemistry of Cu-fubmpa, Cu-bmpa, and Cu-pmea

To study the effect of the different ligands on the redox chemistry of the complexes, cyclic voltammograms of the complexes in a pH 7 phosphate buffer (PB) solution under argon atmosphere were recorded using a Glassy Carbon (GC) working electrode ( $A = 0.0707 \text{ cm}^2$ ). The resulting redox couples recorded of Cu-fubmpa, Cu-bmpa, and Cu-pmea with a scan rate of  $100 \text{ mV s}^{-1}$  are combined in Figure 5.2, with Cu-tmpa as the reference complex. The  $E_{1/2}$  of the Cu<sup>II/I</sup> redox couples of these complexes span a wide potential range (Table 5.1), shifting positively from the  $E_{1/2}$  of 0.21 V for Cu-tmpa to 0.25 V for Cu-fubmpa, 0.37 V Cu-pmea, and 0.49 V for Cu-bmpa. All three complexes

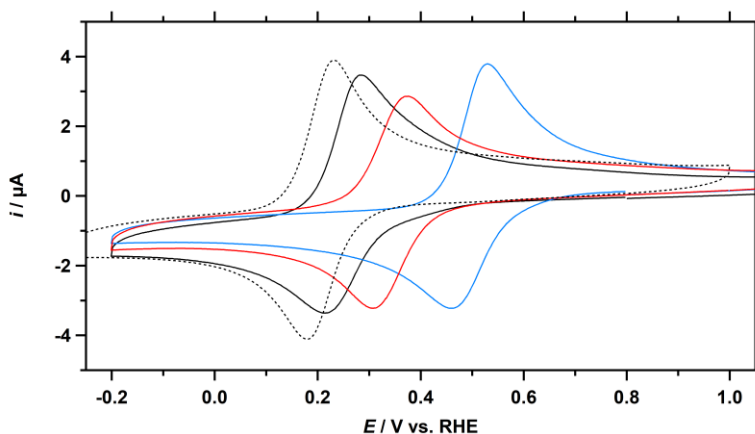


**Figure 5.2.** Cyclic voltammograms of Cu-fubmpa (black), Cu-pmea (red), and Cu-bmpa (blue), including Cu-tmpa (dotted) as a reference, in a pH 7 phosphate buffer under 1 atm Ar. For each copper complex a concentration of 0.3 mM was used. Conditions: pH 7 PB ([PO<sub>4</sub>] = 100 mM), 293 K,  $100 \text{ mV s}^{-1}$  scan rate,  $0.0707 \text{ cm}^2$  electrode surface area.

**Table 5.1.** Overview of the redox potentials ( $E_{1/2}$ ), the peak-to-peak separation ( $\Delta E_p$ ) between the peak oxidation and peak reduction potentials, and the diffusion coefficients of the different investigated copper complexes.

Complex	$E_{1/2}$ (V vs. RHE) <sup>a</sup>	$\Delta E_p$ (mV) <sup>a</sup>	$D$ (cm <sup>2</sup> s <sup>-1</sup> ) <sup>b</sup>
<i>Cu-tmpa</i> <sup>c</sup>	0.206	56	$4.9 \times 10^{-6}$
<i>Cu-fubmpa</i>	0.248(2)	73	$2.4 \times 10^{-6}$
<i>Cu-pmea</i>	0.341(2)	68	$2.9 \times 10^{-6}$
<i>Cu-bpmpa</i>	0.494(2)	71	$2.3 \times 10^{-6}$

<sup>a</sup> Determined from CV measured at 100 mV s<sup>-1</sup>. <sup>b</sup> Determined from  $i_{pc}$ . <sup>c</sup> Data from Chapter 2.

show lower peak redox currents ( $i_p$ ) than Cu-tmpa for both the cathodic ( $i_{pc}$ ) and anodic ( $i_{pa}$ ) peaks.

To determine the diffusion coefficient ( $D$ ) for these complexes, CVs were measured at different scan rates, varying from 10 to 500 mV s<sup>-1</sup>, for each complex and are shown in Figure D.2. In the same figure, the corresponding Randles-Sevcik plots show that good linearity ( $R^2 > 0.99$ ) is achieved for the  $i_{pc}$  and  $i_{pa}$  as a function of the square root of the scan rate. This indicates that the complexes behave as diffusive homogenous species near the electrode under inert conditions, and potential deposition of the complex on the electrode surface does not play a significant role. By applying the Randles-Sevcik equation (Eq. 5.1), the diffusion coefficients of the Cu<sup>II</sup> species were determined from the  $i_{pc}$  values, which resulted in diffusion coefficients of  $1.3 \times 10^{-6}$  cm<sup>2</sup> s<sup>-1</sup> for Cu-fubmpa,  $2.3 \times 10^{-6}$  cm<sup>2</sup> s<sup>-1</sup> for Cu-bpmpa, and  $2.9 \times 10^{-6}$  cm<sup>2</sup> s<sup>-1</sup> for Cu-pmea, which are lower than that of Cu-tmpa ( $4.9 \times 10^{-6}$  cm<sup>2</sup> s<sup>-1</sup>).<sup>[8]</sup>

$$i_p = 0.446nFSC_{cat}^0 \sqrt{\frac{Fv}{RT} D_{cat}} \quad (5.1)$$

The redox couples of all the complexes seem to be fully reversible, but analysis of the peak-to-peak separation ( $\Delta E_p$ ) shows a small deviation from the ideal 59 mV peak-to-peak separation for a fully reversible system, averaging a  $\Delta E_p$  increase of 10 mV at a 100 mV s<sup>-1</sup> scan rate. To investigate whether this is the case over a larger range of scan rates, Laviron plots of the oxidative ( $E_{pa}$ ) and reductive peak ( $E_{pc}$ ) potentials were constructed (Figure D.3). An increase of the  $\Delta E_p$  with increasing scan rate is observed for all three complexes, especially at scan rates above 100 mV s<sup>-1</sup>. This increase is largely caused by a shift of the  $E_{pa}$  of the respective complexes towards higher potentials, while the  $E_{pc}$  remain stable or show much smaller shifts. As a result, the  $E_{1/2}$ , which is defined as the midway potential between the  $E_{pc}$  and  $E_{pa}$ , is also affected. For Cu-fubmpa and Cu-bpmpa, this leads to an apparent positive shift of the  $E_{1/2}$  at scan rates above 100 mV s<sup>-1</sup> (Figure D.4). Cu-pmea sees both the  $E_{pa}$  and  $E_{pc}$  equally shift towards higher

and lower potentials, respectively, leading to a stable  $E_{1/2}$  as a function of scan rate. The increase in peak-to-peak separation resulting from a shifting  $E_{pa}$  may point to slower electron transfer rate for the oxidation of the  $\text{Cu}^{\text{I}}$  species,<sup>[26]</sup> although the effect is marginal with only an increase of 15–20 mV observed for the  $\Delta E_p$ .

### 5.2.3. Electrocatalytic performance towards the ORR and HPRR

We have previously shown that Cu-tpma produces  $\text{H}_2\text{O}_2$  as a detectable intermediate during the electrocatalytic reduction of  $\text{O}_2$ ,<sup>[8]</sup> but it can also further reduce  $\text{H}_2\text{O}_2$  to  $\text{H}_2\text{O}$  (Chapters 2 and 3). Therefore, both the oxygen reduction reaction (ORR) and the hydrogen peroxide reduction reaction (HPRR) were studied for Cu-fubmpa, Cu-bpmpa, and Cu-pmea. CVs were measured in a pH 7 phosphate buffer solution containing 0.3 mM of the complex under 1 atm  $\text{O}_2$  or with 1.1 mM  $\text{H}_2\text{O}_2$  under 1 atm Ar. The resulting catalytic waves for the reduction of  $\text{O}_2$  and  $\text{H}_2\text{O}_2$  are shown in Figure 5.3 separately for each catalyst. One observation that can immediately be made is that the ORR current is greater than the HPRR current for all the analysed complexes, which was also observed for Cu-tpma. For Cu-fubmpa, the onset of the ORR appears to be ca. 40 mV

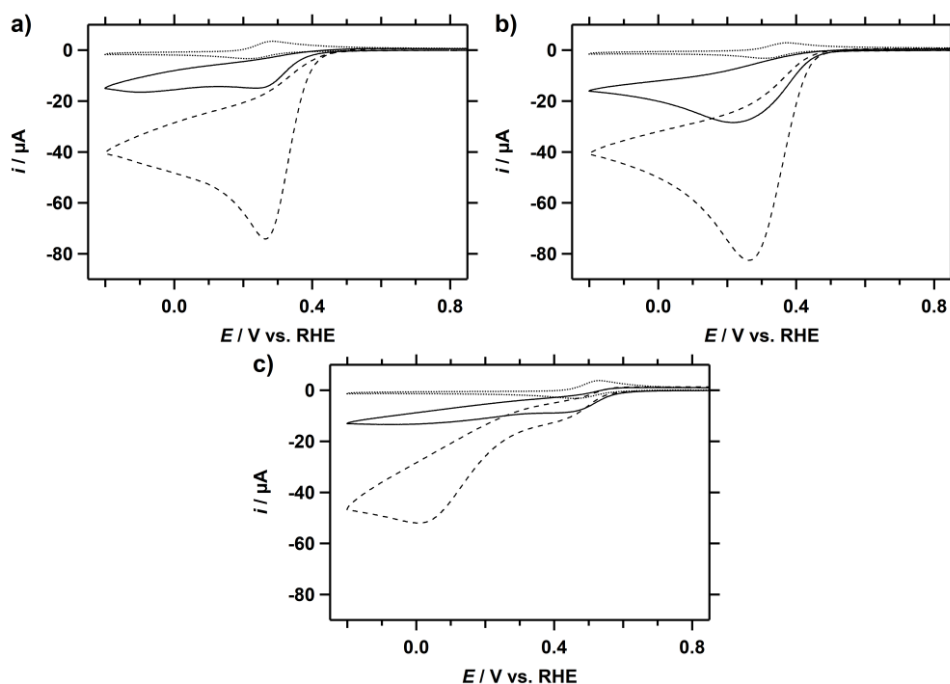


**Figure 5.3.** CVs of Cu-fubmpa (a), Cu-pmea (b), and Cu-bpmpa (c) in a PB pH 7 electrolyte solution under 1 atm Ar (dotted line), 1 atm  $\text{O}_2$  (dashed line), or with 1.1 mM  $\text{H}_2\text{O}_2$  under 1 atm Ar (solid line). For each catalyst, a concentration of 0.3 mM was used. Conditions: pH 7 PB ( $[\text{PO}_4] = 100$  mM), 293 K,  $100 \text{ mV s}^{-1}$  scan rate,  $0.0707 \text{ cm}^2$  electrode surface area.

lower compared to the onset of the HPRR (Figure D.5). On the other hand, both Cu-bmpa and Cu-pmea each show overlapping catalytic onsets for the ORR and HPRR. The HPRR onset for Cu-fubmpa is shifted to a lower potential, something that was also observed for Cu-tmpa (Chapter 3).

The catalytic linear sweep voltammograms (LSV) of complexes Cu-fubmpa, Cu-bmpa, and Cu-pmea of the ORR and HPRR have been combined in Figure 5.4 to allow for a straightforward comparison between the catalysts. The catalytic wave of the ORR in the presence of Cu-fubmpa overlaps neatly with the catalytic wave of Cu-tmpa, while the catalytic onset potential of Cu-pmea is slightly higher. However, both catalysts reach somewhat lower peak catalytic current  $i_{cat}$  than Cu-tmpa, indicating a lower catalytic rate, while taking into account that  $O_2$  diffusion limitations come into play at 1 atm  $O_2$  for Cu-tmpa. Cu-bmpa on the other hand shows a much earlier onset than the other catalysts, nearer to the 0.695 V vs. RHE equilibrium potential of the  $O_2/H_2O_2$  couple. However, a trade-off for this higher onset potential is the much lower catalytic activity exhibited by the catalyst. Additionally, a second, larger catalytic wave is observed at a much lower potential. The half-wave potential of the first catalytic wave of Cu-bmpa is the same as the equilibrium potential of the redox couple in the absence of  $O_2$ . This equivalence, where  $E_{1/2}$  is equal to  $E_{cat/2}$ , is expected for a system that is not limited in substrate. This behaviour is not observed for the  $E_{cat/2}$  of Cu-fubmpa (+90 mV) or Cu-pmea (+25 mV) at catalyst concentration of 0.3 mM. However, for Cu-bmpa no limiting current plateau is maintained and the catalytic current increases again at potentials below 0.3 V vs. RHE. In this potential window, the background current generated by the glassy carbon electrode needs to be accounted for, as GC readily reduces  $O_2$  to  $H_2O_2$  below 0.3 V. This could be the main contributing factor to the catalytic current observed in the lower potential region. Background correction on the

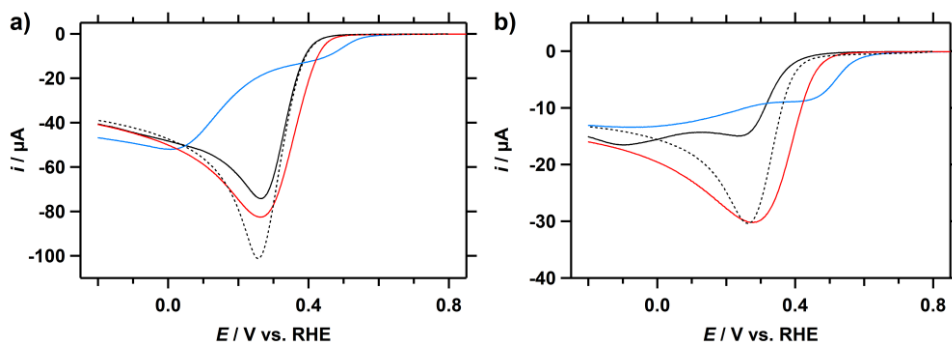


**Figure 5.4.** Linear sweep voltammograms (LSV) of Cu-fubmpa (black), Cu-pmea (red), and Cu-bmpa (blue), including Cu-tmpa (dotted) as a reference, under 1 atm  $O_2$  (a), or in the presence of 1.1 mM  $H_2O_2$  under 1 atm Ar (b). For each catalyst, a concentration of 0.3 mM was used. Conditions: pH 7 PB ( $[PO_4] = 100$  mM), 293 K,  $100$  mV  $s^{-1}$  scan rate,  $0.0707$  cm $^2$  electrode surface area.

**Table 5.2.** Catalytic parameters for the ORR by Cu-fubmpa, Cu-pmea, and Cu-bpmpa, in a pH 7 phosphate buffer under 1 atm O<sub>2</sub> (1.2 mM).

Complex	$E_{\text{onset, ORR}}$	$E_{\text{cat}/2}$	$E_{\text{cat, ORR}}$	$i_{\text{cat}} (\mu\text{A})$
<i>Cu-tmpa</i> <sup>c</sup>	0.50	0.31	0.23	−90
<i>Cu-fubmpa</i>	0.49	0.34	0.26	−62
<i>Cu-pmea</i>	0.50	0.37	0.26	−79
<i>Cu-bpmpa</i>	0.61	0.50 <sup>a</sup>	0.40 <sup>a</sup>	−24 <sup>a</sup>
		0.19 <sup>b</sup>	0.10 <sup>b</sup>	−12 <sup>b</sup>

<sup>a</sup> values for the first catalytic wave. <sup>b</sup> values for the second catalytic wave. <sup>c</sup> Data from Chapter 2. Potentials are reported vs. RHE. Conditions: pH 7 PB ([PO<sub>4</sub>] = 100 mM), 0.3 mM catalyst concentration, 293 K, 100 mV s<sup>−1</sup> scan rate, 0.0707 cm<sup>2</sup> electrode surface area.

catalytic waves was performed (Figure D.6), which shows that the second catalytic wave is much less prominent than in Figure 5.4, but is still present and reaches a peak catalytic current  $i_{\text{cat}}$  at 0.1 V vs. RHE. An overview of the catalytic parameters for the ORR by all three complexes is shown in Table 5.2.

The voltammetry data from the HPRR show a similar trend for the onset potential of the catalytic reaction, with the onset in presence of Cu-fubmpa < Cu-pmea < Cu-bpmpa (Figure 5.4bb). Of the three catalysts investigated here, the highest catalytic rates are observed for Cu-pmea, reaching an  $i_{\text{cat}}$  of −30  $\mu\text{A}$ , which is the same maximum current as observed for Cu-tmpa. However, the slope of the catalytic wave is somewhat less steep than that of Cu-tmpa, while the peak-width is larger. A lower slope, and thus a smaller increase in catalytic rate as a function of applied potential, hints at a lower HPRR rate constant for Cu-pmea. The catalytic current of Cu-fubmpa is significantly lower, with an  $i_{\text{cat}}$  of −15  $\mu\text{A}$ , and seemingly reaches a plateau, although the  $E_{\text{cat}/2}$  is still roughly 80 mV higher than the  $E_{1/2}$  of the catalyst. It is therefore unclear whether this points to a S-shaped catalytic curve where substrate diffusion is no longer the limiting factor, or whether another process is inhibiting catalytic activity as the applied potential

**Table 5.3.** Catalytic parameters for the HPRR by Cu-fubmpa, Cu-pmea, and Cu-bpmpa, in a pH 7 phosphate buffer in the presence of 1.1 mM H<sub>2</sub>O<sub>2</sub> under 1 atm Ar.

Complex	$E_{\text{onset, HPRR}}$	$E_{\text{cat}/2}$	$E_{\text{red, HPRR}}$	$i_{\text{cat}} (\mu\text{A})$
<i>Cu-tmpa</i> <sup>a</sup>	0.45	0.34	0.26	−30
<i>Cu-fubmpa</i>	0.45	0.33	0.23	−15
<i>Cu-pmea</i>	0.52	0.36	0.28	−30
<i>Cu-bpmpa</i>	0.61	0.52	0.40	−11

<sup>a</sup> Data from Chapter 3. Potentials are reported vs. RHE. Conditions: pH 7 PB ([PO<sub>4</sub>] = 100 mM), 0.3 mM catalyst concentration, 293 K, 100 mV s<sup>−1</sup> scan rate, 0.0707 cm<sup>2</sup> electrode surface area.



is reduced. A small second peak is observed at potentials below 0 V vs. RHE. Curiously, a second broad catalytic wave is once again visible for Cu-bpmpa during the HPPR, similar to what was observed for the ORR. The catalytic parameters for the HPPR are summarized in Table 5.3.

#### 5.2.4. Determination of catalytic rate constants for the ORR and HPPR using the foot-of-the-wave analysis

While comparing voltammograms of different complexes under catalytic conditions can already hint at the relative catalytic performance of these catalysts, it will not give the entire picture. This is especially true when the catalytic conditions are such that substrate limitations occur, as can easily be the case during the ORR which is limited to an O<sub>2</sub> concentration of roughly 1.2 mM at room temperature (293 K) under atmospheric pressure. In the case of Cu-tmpa this was shown to be a limiting factor for the catalytic reaction. Thus, limitations in substrate diffusion may result in similar peak catalytic currents for catalysts with significant variation in catalytic rate constants. Two different approaches can be taken to elucidate the catalytic rate constants for a given catalyst; by determining the current enhancement under non-limiting conditions, which in practice means lowering the catalyst concentration; alternatively, the foot-of-the-wave analysis (FOWA) method can be used. The FOWA extrapolates the ideal or maximum turnover frequency (TOF<sub>max</sub>) of the catalyst from the foot of the catalytic wave, close to the onset of the catalytic reaction (see Appendix A for a detailed description). While a very powerful tool, care must be taken in choosing the parameters with which to perform the calculations. The catalytic electron number  $n_{\text{cat}}$  is one such parameter, and the reduction of O<sub>2</sub> can either lead to H<sub>2</sub>O<sub>2</sub> ( $n_{\text{cat}} = 2$ ) or H<sub>2</sub>O ( $n_{\text{cat}} = 4$ ) as the product. In the previous section, Cu-bpmpa and Cu-pmea were shown to each have the same onset for the ORR and HPPR, therefore a  $n_{\text{cat}}$  of 4 is appropriate for these complexes. Conversely, Cu-fubmpa has a 40 mV lower onset potential for the HPPR than for the ORR. By comparing the CVs of the ORR and HPPR in the foot of the wave potential window, it was determined that the charge transferred during the HPPR is less than 10% of the total charge for ORR in the region where the potential windows overlap. This makes a  $n_{\text{cat}}$  of 2 more appropriate when determining the TOF<sub>max</sub> of Cu-fubmpa for the ORR, as the contribution of hydrogen peroxide reduction is minimal. For the FOWA, CVs were measured in triplicate in a PB (pH 7) electrolyte solution containing 0.3 mM complex and 1 atm O<sub>2</sub> (for the ORR), or 1.1 mM H<sub>2</sub>O<sub>2</sub> in the presence of 1 atm Ar (for the HPPR), using a freshly polished GC electrode for each measurement. These voltammograms were used to construct plots of the current enhancement  $i_c/i_p$  vs  $(1 + \exp[F/RT(E - E_{1/2})])^{-1}$ , where  $i_c$  is the catalytic current measured in the presence of catalyst and substrate (O<sub>2</sub> or H<sub>2</sub>O<sub>2</sub>) at the applied potential  $E$ . In the foot-of-the-wave

**Table 5.4.**  $\text{TOF}_{\text{max}}$  for the ORR and HPRR derived from the foot-of-the-wave analysis (FOWA).

Complex	$\text{TOF}_{\text{max}} (\text{s}^{-1})$	
	ORR	HPRR
<i>Cu-tmpa</i> <sup>c</sup>	$1.8 \times 10^6 \pm 0.6 \times 10^6$ <sup>a</sup>	$2.1 \times 10^5 \pm 0.1 \times 10^5$
<i>Cu-fubmpa</i>	$1.3 \times 10^5 \pm 0.3 \times 10^5$ <sup>a</sup>	$0.8 \times 10^3 \pm 0.1 \times 10^3$
<i>Cu-pmea</i>	$3.7 \times 10^2 \pm 0.6 \times 10^2$ <sup>b</sup>	$1.0 \times 10^3 \pm 0.3 \times 10^3$
<i>Cu-bpmpa</i>	$0.7 \pm 0.1$ <sup>b</sup>	$6.4 \pm 0.9$

<sup>a</sup>  $n_{\text{cat}} = 2$ . <sup>b</sup>  $n_{\text{cat}} = 4$ . <sup>c</sup> Data from Chapters 2 and 3. Conditions: 0.3 mM catalyst concentration, pH 7 PB ([ $\text{PO}_4$ ] = 100 mM), 293 K, 100  $\text{mV s}^{-1}$  scan rate, 0.0707  $\text{cm}^2$  electrode surface area.

potential window, a linear fit was obtained between the catalytic onset and the potential where  $i_c/i_p$  is at least equal to 1.6. The onset is defined as  $i_c/i_{\text{redox}} \geq 2$ , where  $i_{\text{redox}}$  is the current measured at the applied potential  $E$  in the presence of the catalyst, but without any substrate present in solution. The  $\text{TOF}_{\text{max}}$  was determined from the slope of the linear fit, by applying Eq. 5.2.

$$\frac{i_c}{i_p} = \frac{2.24n_{\text{cat}}\sqrt{\frac{RT}{Fv}}\text{TOF}_{\text{max}}}{1 + \exp\left[\frac{F}{RT}(E - E_{1/2})\right]} \quad (5.2)$$

The resulting  $\text{TOF}_{\text{max}}$  for the ORR and HPRR are reported in Table 5.4. For the ORR, Cu-fubmpa has the highest  $\text{TOF}_{\text{max}}$ , while Cu-bpmpa has the lowest ( $0.7 \text{ s}^{-1}$ ). For the HPRR, Cu-pmea shows the highest  $\text{TOF}_{\text{max}}$ , but is closely followed by Cu-fubmpa. All catalyst discussed here have a lower  $\text{TOF}_{\text{max}}$  than Cu-tmpa for both catalytic reactions. Comparison of the ORR and HPRR  $\text{TOF}_{\text{max}}$  reveals an interesting trend. The relative magnitude of the  $\text{TOF}_{\text{max}}$  of both catalytic reactions changes with increasing  $E_{1/2}$  of the complexes. For Cu-fubmpa, the ORR is much faster than the HPRR, while for Cu-bpmpa, which has the highest  $E_{1/2}$ , the ORR is slower than the HPRR. For Cu-pmea, both reactions show similar  $\text{TOF}_{\text{max}}$ . Thus, the higher the  $E_{1/2}$ , and thus the catalytic onset potential, the more the reduction of  $\text{H}_2\text{O}_2$  seems to be favoured over the reduction of  $\text{O}_2$ . However, the FOWA does not consider the second, higher catalytic wave observed for Cu-bpmpa in the presence of  $\text{O}_2$ , as the  $\text{TOF}_{\text{max}}$  is derived from the initial slope around 0.6 V vs. RHE. This second catalytic wave, which is centred at 0.1 V vs. RHE, cannot be accurately probed by the FOWA but shows that higher catalytic rates can be achieved by Cu-bpmpa (or a different catalytic species, see discussion below) at the cost of a significantly increased overpotential.

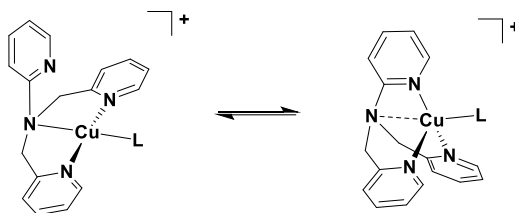
### 5.2.5. Comparison between FOWA and catalytic current enhancement at low catalyst concentrations

Another method to determine the catalytic performance is by direct determination using the catalytic current enhancement derived from the  $i_{pc}$  of the catalyst and the  $i_{cat}$ .<sup>[27]</sup> Ideally, this should be done under more reliable kinetic conditions, such that substrate diffusion is not the main limiting factor during the catalytic reaction. In the case of a highly active ORR catalyst, this requires measurement of the current enhancement at low catalyst concentration. However, the determination of the  $i_{pc}$  at low catalyst concentration is complicated by the relatively much larger double layer current of the electrode. Therefore, the  $i_{pc}$  is derived from the Randles-Sevcik equation (Eq. 5.1), using the calculated diffusion coefficient of the catalyst and the catalyst concentration. The  $i_{cat}$  values were obtained from background-corrected LSVs measured at several catalyst concentrations in the range of 1 to 30  $\mu$ M, depending on the catalyst, under 1 atm O<sub>2</sub> (see Appendix D.7). The  $k_{obs}$  were derived from the current enhancement ( $i_{cat}/i_p$ ) using Eq. 5.3, in the concentration range where a linear dependency of the  $i_{cat}$  on the catalyst concentration was observed. Eq 5.3 and Eq 5.2 are equal for the case when the applied potential  $E$  is lower than the  $E_{1/2}$ , as the  $(1 + \exp[F/RT(E - E_{1/2})])^{-1}$  term goes to unity, and a maximum catalytic current is reached, where  $i_c = i_{cat}$ .

$$\frac{i_{cat}}{i_{pc}} = 2.24n \sqrt{\frac{RT}{Fv}} k_{obs} \quad (5.3)$$

This resulted in ORR  $k_{obs}$  of  $2.0 \times 10^3 \pm 0.6 \times 10^3 \text{ s}^{-1}$  for Cu-fubmpa,  $2.0 \times 10^4 \pm 0.2 \times 10^4 \text{ s}^{-1}$  for Cu-pmea, and  $0.7 \times 10^3 \pm 0.1 \times 10^3 \text{ s}^{-1}$  for Cu-bmpa (Figure 5.5a), all of which are lower than the  $k_{obs}$  of Cu-tmpa ( $2.0 \times 10^5$ ) which was determined using the same method.<sup>[8]</sup> Comparing the  $k_{obs}$  to the previously determined TOF<sub>max</sub>, a large difference of three orders of magnitude is observed for the rate constants of Cu-bmpa. As mentioned in the last section, the TOF<sub>max</sub> of this complex describes the catalytic rate constant associated with the first catalytic wave, while the  $k_{obs}$  was determined from the peak catalytic current around 0.13 V at low catalyst concentration (Figure D.7e), which corresponds to the second catalytic wave observed. A catalytic current associated with the first catalytic wave cannot be observed at these low catalyst concentrations (Figure D.7e).

If Eq 5.3 is applied to the smaller first catalytic wave in the presence of 0.3 mM Cu-bmpa and 1 atm O<sub>2</sub> (Figure D.4), a  $k_{obs}$  of  $0.6 \text{ s}^{-1}$  is obtained. Here, the catalytic peak current of the first catalytic wave ( $E_{cat} = 0.4 \text{ V vs. RHE}$ ) was used as  $i_{cat}$ , while  $i_{pc}$  was obtained from the redox couple of the complex under inert atmosphere. This  $k_{obs}$



**Scheme 5.3.** Proposed conversion to a more tetrahedral coordination geometry of the Cu<sup>I</sup>-bpmpa complex.

value ( $0.6 \text{ s}^{-1}$ ) corresponds closely to the FOWA-derived  $\text{TOF}_{\text{max}}$  of the ORR ( $0.7 \text{ s}^{-1}$ ) under the same catalytic conditions ( $0.3 \text{ mM Cu-bpmpa}$ ,  $1 \text{ atm O}_2$ ).

The cause of the two distinct catalytic waves during the ORR at  $0.4$  and  $0.1 \text{ V vs. RHE}$  is unclear. It is not the result of different onsets of the (partial) ORR and the HPORR, which could result in  $\text{H}_2\text{O}_2$  only being reduced at a lower potential, as these catalytic reactions have the same onsets (see Table 5.2 and 5.3). Moreover, the HPORR is an order of magnitude faster than the ORR at the first catalytic wave. One possibility for the increased ORR activity at a lower potential is a change in the coordination geometry of the Cu<sup>I</sup> complex. Crystal structures of  $[\text{Cu}^{\text{II}}(\text{bpmpa})(\text{Cl})(\text{ClO}_4)]$  and  $[\text{Cu}^{\text{II}}(\text{bpmpa})\text{Cl}_2]$  complexes show a (distorted) square-pyramidal coordination environment, with bpmpa coordinating through the two pyridyl nitrogen atoms and the tertiary amine nitrogen as a tridentate ligand.<sup>[12]</sup> This is a similar coordination geometry as observed for Cu<sup>II</sup>-bmpa (bmpa = bis(2-pyridylmethyl)amine).<sup>[28]</sup> In contrast, Cu<sup>I</sup> complexes favour a tetrahedral geometry, which is difficult to attain due to the tridentate nature of the bpmpa ligand.<sup>[29]</sup> For Cu<sup>I</sup>-tmpa it has been shown that the Cu–N<sub>amine</sub> bond can be elongated, facilitating a more tetrahedral-like geometry.<sup>[30]</sup> While no crystal structures for Cu<sup>I</sup> complexes of Cu-bpmpa have been reported thus far, elongation of the Cu–N<sub>amine</sub> bond followed by coordination of the previously uncoordinated pyridine to the Cu centre may result in a more tetrahedral coordination environment (Scheme 5.3). As the pyridine donor in the aminopyridine moiety has a more electron-donating character than the tertiary amine, this would result in more electron density on the Cu<sup>I</sup> centre, which would coincide with a lower equilibrium potential. This proposed reorganization of the ligand in the coordination environment may be assisted by the coordination of dioxygen and formation of the Cu<sup>II</sup>–OO<sup>•−</sup> complex, which would facilitate the elongation of the Cu–N<sub>amine</sub> bond.

The  $k_{\text{obs}}$  of Cu-pmea was found to be slightly less than two orders of magnitude higher than the  $\text{TOF}_{\text{max}}$ . In general, for the same catalytic reaction and catalytic species, the  $k_{\text{obs}}$  obtained from the peak catalytic current is lower than the ideal  $\text{TOF}_{\text{max}}$ . While substrate depletion has been reduced by increasing the ratio between  $\text{O}_2$  and the

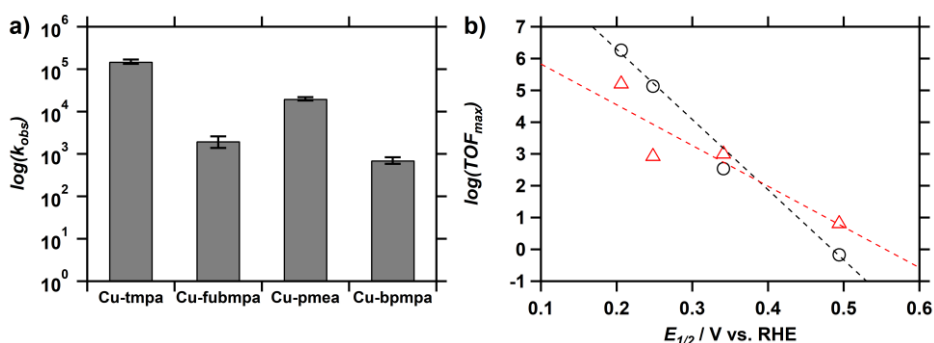


**Figure 5.5.** a) Plot of the ORR  $k_{\text{obs}}$  of Cu-fubmpa, Cu-pmea, and Cu-bpmpa derived from the current enhancement ( $i_c/i_p$ ) at low catalyst concentration. b) Plot of the logarithm of the  $\text{TOF}_{\text{max}}$  of the ORR (circles; 1 atm  $\text{O}_2$ ) and HPRR (triangles; 1.1 mM  $\text{H}_2\text{O}_2$ ) versus the  $E_{1/2}$  of the respective catalysts, including Cu-tmpa ( $E_{1/2} = 0.21$  V).

catalyst under the conditions where the  $k_{\text{obs}}$  for Cu-pmea was determined, other processes may still negatively affect the catalytic reaction and thus decrease the measured  $k_{\text{obs}}$ . This holds true for the other two catalysts described here, including Cu-tmpa.<sup>[8]</sup> The contradictory results for Cu-pmea can also not be explained by a potential erroneous choice of  $n_{\text{cat}}$  in the previous section, as even if a  $n_{\text{cat}}$  of 2 is used for the FOWA, it would still result in a lower  $\text{TOF}_{\text{max}}$  than the  $k_{\text{obs}}$ . Additionally, at low catalyst concentration the half-wave potential  $E_{\text{cat}/2}$  during ORR is equal to the  $E_{1/2}$  of the catalyst, confirming that the species present under non-catalytic conditions is also responsible for the peak current under catalytic conditions and thus for the measured  $k_{\text{obs}}$ . While no overlapping catalytic peaks are observed during differential pulse voltammetry measurements under catalytic conditions (Figure D.8), it is possible that an equilibrium between two different Cu-pmea complexes is present. One candidate would be the copper complex wherein one of the pyridine arms is not coordinated, which would have a redox potential closer to that of Cu-fubmpa. This species may be in an unfavourable equilibrium with the fully (tetradentate) coordinated copper complex, resulting in different catalytic rate constants being observed in the two different potential windows.

Variation in the length of the  $(-\text{CH}_2)_n$  spacer (where  $n = 0-2$ ) between the central tertiary amine and one of the pyridine moieties results in a significant shift in the equilibrium potential of the  $\text{Cu}^{\text{II}}/\text{Cu}^{\text{I}}$  redox couple. The shifts of Cu-pmea and Cu-bpmpa towards a higher potential are much larger than observed for Cu-fubmpa, in which one of the pyridine arms is replaced for a furanyl group, thereby keeping the central tertiary amine intact while preventing coordination of a third ligand arm to the Cu centre. In this way the effect of a lower denticity on the catalytic activity could be investigated without removing the pyridine arm entirely, which would introduce a secondary amine

that could be easily oxidized during the catalytic cycle. Indeed, the  $E_{1/2}$  of Cu-fubmpa and Cu-bmpa (bmpa = bis(2-pyridylmethyl)amine) are nearly identical in a pH 7 phosphate buffer,<sup>[21]</sup> indicating that coordination of the furanyl group does not occur while in solution.

A linear relationship between the maximum TOF [ $\log(\text{TOF}_{\text{max}})$ ] and the  $E_{1/2}$  of the catalytic species is observed, as visualized in Figure 5.5b. As the catalyst  $E_{1/2}$  increases, and thus the overpotential decreases, the rate of the reaction decreases. This behaviour seems to hold for both the ORR and the HPRR, although a lower slope is apparent for the decline in HPRR  $\text{TOF}_{\text{max}}$ . The slopes associated with these linear relationships are 44 mV per decade for the ORR, and 65 mV per decade for the HPRR. Similar behaviour has been observed for proton reduction by molecular nickel catalysts, where a linear relationship was observed between the  $\log(\text{TOF})$  and the driving force for  $\text{H}_2$  elimination,  $\Delta G^\circ_{\text{H}_2}$ , which is directly dependent on the  $E_{1/2}$  of the  $\text{Ni}^{\text{II/I}}$  redox couple and the  $\text{pK}_a$  of the pendant amine in the second coordination sphere.<sup>[31]</sup> This scaling of the  $\text{TOF}_{\text{max}}$  with the overpotential is a well-known phenomenon for molecular electrocatalysts, and has been shown for a range of nickel, cobalt and iron complexes capable of catalysing the ORR or hydrogen evolution reaction (HER).<sup>[31-35]</sup> Thus far, this scaling relationship has only been circumvented by designing a catalyst of which the  $E_{1/2}$  is sensitive to  $\text{pK}_a$  changes and the nature of the acid–conjugate base mixture.<sup>[36]</sup> We were able to reduce the overpotential of the ORR by almost 300 mV by changing the spacer length of one the pyridine arms. This resulted in an overpotential of less than 200 mV for the 2-electron ORR ( $E^0 = 0.695$  V vs. RHE) catalysed by Cu-bmpa. However, the copper catalysts are still subject to the scaling relations, limiting the catalytic rates at the lower overpotentials. Interestingly, Figure 5.5b also shows that at a certain potential the relative activities for the ORR and HPRR invert, and the HPRR becomes the faster catalytic reaction of the two reactions as the  $E_{1/2}$  of the catalyst is increased. This indicates that the reduction of  $\text{H}_2\text{O}_2$  is less affected by the thermodynamic and kinetic limitations that govern the scaling relations, as the rate at which the HPRR  $\text{TOF}_{\text{max}}$  decreases with increasing  $E_{1/2}$  (or with the reduction of the overpotential) is less than observed for the ORR.

### 5.3. Conclusion

The influence of structural changes of the tetradentate tmpa-based ligand scaffold on the electrochemical reduction of  $\text{O}_2$  and  $\text{H}_2\text{O}_2$  has been investigated. The changes of the coordination geometry around the Cu centre, induced by varying the length of the  $(-\text{CH}_2)_n$  spacer of one of the pyridine arms, resulted in significant positive shifts of the thermodynamic  $\text{Cu}^{\text{II/I}}$  redox potentials of up to 300 mV for Cu-bmpa ( $n = 0$ ). The magnitude of the potential shift seems to be related to the strain that is placed on

the preferred coordination environment of the Cu<sup>II</sup> or Cu<sup>I</sup> centres. The increase in redox potentials relative to Cu-tmpa resulted in a corresponding increase of the catalytic onset potentials, which for the ORR was confirmed under conditions where substrate limitations were minimized, for which a clear increase of the catalytic half-wave potential was observed. Thus, the overpotential for the ORR and HPORR directly relate to the redox potential of the copper catalyst. Additionally, a clear linear scaling relationship was observed between the log(TOF<sub>max</sub>) for the ORR and the  $E_{1/2}$  of the catalyst. The maximum TOF decreases as the onset potential increases, highlighting the well-established trade-off between kinetics and thermodynamics which has been observed for many electrochemical reactions, both for heterogeneous catalysts and homogeneous molecular catalysts. However, to the best of our knowledge this is the first time that this has been demonstrated for the 2-electron reduction of O<sub>2</sub> to H<sub>2</sub>O<sub>2</sub> by a molecular copper catalyst. The same relationship was observed for the reduction of H<sub>2</sub>O<sub>2</sub>, although a smaller decrease of TOF<sub>max</sub> was observed with increasing redox potential. This also resulted in higher rate constants for the HPORR than the ORR in the case of Cu-bpmpa, which is contrary to the catalytic behaviour observed for the other copper complexes. This eliminates H<sub>2</sub>O<sub>2</sub> as significant a by-product of the ORR by Cu-bpmpa, over the entire catalytic potential window.

Thus, we were able to significantly reduce the overpotential related to the ORR by modifying the primary coordination sphere of the copper complexes, and have shown that this results in a linear relationship, and a trade-off, between the catalytic rate and the overpotential for these copper-based electrocatalysts.

## 5.4. Experimental

### 5.4.1. General

All precursors used in the ligand synthesis were obtained from Sigma-Aldrich/Merck. Cu(OTf)<sub>2</sub> was obtained from Alfa Aesar. All other chemicals and solvents were purchased from commercial suppliers. Whatman® RC60 membrane filters were used for the filtration and isolation of the synthesized copper complexes. NMR spectra were recorded on a Bruker 400 MHz or Bruker DPX 300 spectrometer. ESI MS mass spectra were obtained on a Thermo Fisher Scientific MSQ Plus. UV-vis spectra were recorded on a Varian Cary® 40 UV-vis spectrophotometer, or a HORIBA Aqualog spectrophotometer. Elemental analysis was performed by Mikroanalytisches Laboratorium Kolbe. Aqueous electrolyte solutions were prepared using NaH<sub>2</sub>PO<sub>4</sub> (Suprapur®, Merck) and Na<sub>2</sub>HPO<sub>4</sub> (Suprapur®, Merck). Milli-Q Ultrapure grade water was used in all electrochemical experiments and for the preparation of all aqueous electrolyte solutions. H<sub>2</sub>O<sub>2</sub> was obtained from Sigma-Aldrich (≥30%, for ultratrace analysis), and the exact concentration was determined via permanganate titration. pH

measurements were performed on a Hanna Instruments HI 4222 pH meter which was calibrated by five-point calibration using IUPAC standard buffers. Alumina suspensions (1.0, 0.3, and 0.05  $\mu\text{m}$ ) for electrode polishing were obtained from Buehler. All gasses used during electrochemical measurements,  $\text{H}_2$ ,  $\text{O}_2$ , and argon (each 5.0 grade), were supplied by Linde.

## 5.4.2. Synthesis

### 5.4.2.1. *N*-(Furan-2-ylmethyl)-*N*-[bis(2-pyridyl)methyl]amine (*fubmpa*)

2-pyridine carboxaldehyde (0.38 mL, 4 mmol) and furan-2-ylmethanamine (0.18 mL, 2 mmol) were added to dry 1,2-dichloroethane (10 mL) and stirred for 1 hour. Sodium triacetoxymethylborohydride (1.272 g, 6 mmol) was added and the mixture was stirred for 24 hours at room temperature under  $\text{N}_2$  atmosphere.  $\text{NaHCO}_3$  (sat.aq.; 10 mL) was added to the mixture and stirred for one hour to quench the reaction. The organic layer was then separated, concentrated and the residue was purified over alumina column eluting with EtOAc/PetEt/MeOH = 50:50:0.5. After removal of the solvent by rotary evaporation at reduced pressure, the product was obtained as a pale, yellow oil (0.388 g, 1.39 mmol, 69% yield). ESI MS  $m/z$  (found (calc)): 280.0 (280.1,  $[\text{M} + \text{H}]^+$ ).  $^1\text{H}$  NMR (400 MHz,  $\text{CDCl}_3$ )  $\delta$  8.52 (ddd,  $J$  = 4.9, 1.8, 1.0 Hz, 2H, py-*H*6), 7.65 (ddd,  $J$  = 7.8, 7.4, 1.8 Hz, 2H, py-*H*4), 7.58 (ddd,  $J$  = 7.8, 1.2, 1.0 Hz, 2H, py-*H*3), 7.38 (d,  $J$  = 1.8 Hz, 1H, fu-*H*5), 7.13 (ddd,  $J$  = 7.4, 4.9, 1.2 Hz, 2H, py-*H*5), 6.30 (dd,  $J$  = 3.2, 1.8 Hz, 1H, fu-*H*4), 6.23 (d,  $J$  = 3.2 Hz, 1H, fu-*H*3), 3.85 (s, 4H, py- $\text{CH}_2$ ), 3.74 (s, 2H, fu- $\text{CH}_2$ ).  $^{13}\text{C}$  NMR (101 MHz,  $\text{CDCl}_3$ )  $\delta$  159.5 (py-*C*2), 152.1 (fu-*C*2), 149.0 (py-*C*6), 142.1 (fu-*C*5), 136.5 (py-*C*4), 122.9 (py-*C*3), 122.0 (py-*C*5), 110.1 (fu-*C*4), 109.0 (fu-*C*3), 59.7 (py- $\text{CH}_2$ ), 50.4 (fu- $\text{CH}_2$ ).

### 5.4.2.2. *N*-[bis(2-pyridyl)methyl]-2-pyridylamine (*bpmpa*)

A modified literature procedure was used for the synthesis of *bpmpa*. Sodium hydride (60% in mineral oil; 720 mg, 18 mmol) was added to anhydrous DMF (15 mL) under  $\text{N}_2$ . 2-aminopyridine (286 mg, 3 mmol) was dissolved in anhydrous DMF (15 mL) under  $\text{N}_2$  and subsequently added to the sodium hydride solution and stirred for 30 minutes. 2-chloromethylpyridine•HCl (984 mg, 6 mmol) in anhydrous DMF (20 mL) was added dropwise to the solution over a period of 30 minutes under  $\text{N}_2$ . The solution was heated to 50  $^\circ\text{C}$  and stirred for 24 hours. The resulting black solution was carefully quenched with water (50 mL) which resulted in a yellow solution. A saturated  $\text{NaHCO}_3$  solution (50 mL) was added, followed by extraction with DCM (4  $\times$  120 mL). The combined organic fractions were subsequently washed with more saturated  $\text{NaHCO}_3$  solution (3  $\times$  50 mL). The solvent was evaporated by rotary evaporation under reduced pressure and the resulting dried crude product was further purified by silica column chromatography. The crude was dissolved in a few millilitres of DCM, loaded on silica,



and the product was obtained with a 98:2 DCM/MeOH mixture as eluent. The product fractions were combined, and the solvent removed by rotary evaporation under reduced pressure. The product was obtained as a slightly yellow oil (441 mg, 1.6 mmol, 53% yield).  $^1\text{H}$  NMR (400 MHz,  $\text{CDCl}_3$ )  $\delta$  8.53 (dd,  $J$  = 5.0, 1.9, 2H), 8.17 (ddd,  $J$  = 5.0, 2.0, 1.0 Hz, 1H), 7.58 (td,  $J$  = 7.7, 1.9 Hz, 2H), 7.37 (ddd,  $J$  = 8.6, 7.2, 1.9 Hz, 1H), 7.22 (d,  $J$  = 7.7 Hz, 2H), 7.13 (dd,  $J$  = 7.7, 5.0, 2H), 6.59 (7.2, 5.0, 1H), 6.47 (dd,  $J$  = 8.6, 1.0 Hz, 1H), 4.96 (s, 4H).

#### 5.4.2.3. *bis[(2-pyridyl)methyl]-2-(2-pyridyl)ethylamine (pmea)*

Pyridine-2-carboxyaldehyde (2.25 g, 21 mmol, 2 equiv.) was added to a stirred mixture of 2-(2-pyridyl)ethylamine (1.28 g, 10.5 mmol, 1 equiv.) and sodium triacetoxymethylborohydride (6.21 g, 21 mmol, 1 equiv.) in dry EDC (100 mL). Molecular sieves were added to remove  $\text{H}_2\text{O}$  during the reaction. This mixture was stirred under argon for seven days. Subsequently,  $\text{NaHCO}_3$  (sat.aq.; 100 mL) was added and the mixture was stirred for 30 minutes. The mixture was filtered to remove molecular sieves. The crude mixture was then washed with  $\text{NaHCO}_3$  (sat.aq) (2x 50 mL) and the organic phase was dried with  $\text{MgSO}_4$  and filtered again. The EDC was evaporated at 40 °C by rotary evaporation. The crude was dissolved in DCM and extracted with an aqueous solution of pH 4 (acidified with HCl; 3 x 30 mL). The pH of the combined aqueous solution was increased to pH 9 by addition of saturated  $\text{NaHCO}_3$  and extracted with DCM (6 x 50 mL). The combined organic layers were dried with  $\text{Na}_2\text{SO}_4$  followed by filtration. The solvent was removed by rotary evaporation at reduced pressure. TLC (Aluminium oxide; 100:10 EtOAc/MeOH) revealed the presence of some impurities close to the baseline. The crude was dissolved in a few millilitres of DCM, loaded on Aluminium oxide, and the product ( $R_f$  = 0.7) was obtained using a 100:10 EtOAc/MeOH mixture as eluent. The product fractions were combined, and the solvent removed by rotary evaporation under reduced pressure. The resulting brown oil was exhaustively extracted with warm pentane. Evaporation of the pentane resulted in a colourless oil (1.92 g, 6.3 mmol, 60% yield). ESI MS  $m/z$  (found (calc)): 305.2 (305.2,  $[\text{M} + \text{H}]^+$ ), 327.1 (327.2,  $[\text{M} + \text{Na}]^+$ ).  $^1\text{H}$  NMR (300 MHz,  $\text{CDCl}_3$ )  $\delta$  8.53 – 8.42 (m, 3H), 7.54 (qd,  $J$  = 7.5, 1.8 Hz, 3H), 7.33 (dt,  $J$  = 7.8, 1.1 Hz, 2H), 7.09 (m, 4H), 3.87 (s, 4H,  $\text{CH}_2$ ), 3.08 – 2.89 (m, 4H,  $\text{CH}_2\text{-CH}_2$ ).

#### 5.4.2.4. *Synthesis of $[\text{Cu}(\text{fubmpa})(\text{H}_2\text{O})(\text{OTf})_2]$*

Fubmpa (0.2 g, 0.716 mmol) and  $\text{Cu}(\text{OTf})_2$  (0.259 g, 0.716 mmol) were dissolved in  $\text{CH}_3\text{CN}$  (10 mL) and together stirred for 1 hour. Following this, the solvent was removed by rotary evaporation at reduced pressure and the complex was dissolved in a minimal amount of  $\text{CH}_3\text{CN}$  until fully dissolved. Diethyl ether was slowly added until the solution became clouded, upon which a few drops of  $\text{CH}_3\text{CN}$  were added to make sure the complex was fully dissolved, and the solution remain homogenous. The solution was

put in the freezer at  $-18\text{ }^{\circ}\text{C}$  for the crystals to form. This crystallization was done twice to make sure the complex was pure. After filtration of mixture, the complex;  $[\mathbf{1}](\text{OTf})_2$  was obtained as a navy blue solid (0.315 g, 0.479 mmol, 67%). ESI MS  $m/z$  (found (calc)): 211.9 (212.0  $[\text{M} - \text{OH}_2 - 2\text{OTf} + 2\text{MeCN}]^{2+}$ ), 387.0 (387.1  $[\text{M} - \text{OH}_2 - 2\text{OTf} + \text{HCOO}^-]^+$ ). Elemental analysis calcd (%) for  $\text{C}_{19}\text{H}_{19}\text{CuF}_6\text{N}_3\text{O}_8\text{S}_2$ : C 34.63, H 2.91, N 6.38; found: C 34.27, H 3.04, N 6.66. UV-Vis:  $\lambda_{\text{max}}$  ( $\epsilon$  in  $\text{L mol}^{-1} \text{cm}^{-1}$ ) in milliQ water = 251 nm (9740); 660 nm (99).

#### 5.4.2.5. *Synthesis of $[\text{Cu}(\text{bpmpa})(\text{CH}_3\text{CN})](\text{OTf})_2$*

$\text{Cu}(\text{OTf})_2$  (1.5 mmol, 542 mg) was dissolved in dry  $\text{CH}_3\text{CN}$  (5 mL) under  $\text{N}_2$  atmosphere. and bpmpa (1.5 mmol, 419 mg) in dry  $\text{CH}_3\text{CN}$  (30 mL) was subsequently added to the solution. A dark green solution formed immediately, and the solution was stirred for 1 hour. The solvent was removed by rotary evaporation under reduced pressure and the dark green solid was dissolved in a minimal amount of  $\text{CH}_3\text{CN}$  until fully dissolved. Diethyl ether was added until the solution became clouded, after which a few drops of  $\text{CH}_3\text{CN}$  were added to make sure the complex was fully dissolved. The solution was put in the freezer at  $-18\text{ }^{\circ}\text{C}$  for 3 days, allowing for crystallization of the complex. The dark turquoise crystals were filtered off and washed with  $\text{Et}_2\text{O}$ . Yield: 72% (1.08 mmol, 730 mg). ESI MS  $m/z$  (found (calc)): 210.6 (210.5  $[\text{M} - 2\text{OTf} + 2\text{MeCN}]^{2+}$ ), 384.0 (384.1  $[\text{M} - 2\text{OTf} + \text{HCOO}^-]^+$ ). Elemental analysis calcd (%) for  $\text{C}_{21}\text{H}_{19}\text{CuF}_6\text{N}_5\text{O}_6\text{S}_2 + 0.6 \text{H}_2\text{O}$ : C 36.56, H 2.95, N 10.15; found: C 36.50, H 2.83, N 10.08.

#### 5.4.2.6. *Synthesis of $[\text{Cu}(\text{pmea})(\text{CH}_3\text{CN})](\text{OTf})_2$*

$\text{Cu}(\text{OTf})_2$  (3 mmol, 913 mg) was dissolved in dry  $\text{CH}_3\text{CN}$  (5 mL) under  $\text{N}_2$  atmosphere. and bpmpa (3 mmol, 1085 mg) in dry  $\text{CH}_3\text{CN}$  (30 mL) was subsequently added to the solution. A dark turquoise solution formed immediately, and the solution was stirred for 1 hour. The solvent was removed by rotary evaporation under reduced pressure. The crude complex was dissolved in minimal amounts of  $\text{CHCl}_3$  until fully dissolved. Methyl tert-butyl ether (MTBE) was added until the solution became clouded, after which a few drops of  $\text{CHCl}_3$  were added to make sure the complex was fully dissolved. The solution was put in the freezer at  $-18\text{ }^{\circ}\text{C}$  for 7 days, allowing for crystallization of the complex. The solution separated into a dark blue crystalline solid and a small amount of a green oil-like substance. The supernatant, including the green oil, were decanted from the round-bottom flask, and the remaining blue crystalline solid was washed with a 30:70  $\text{CHCl}_3/\text{MTBE}$  (50 mL) and filtered off. The solid was crushed into smaller pieces and dried under vacuum. Yield: 82% (2.46 mmol, 1.74 g). ESI MS  $m/z$  (found (calc)): 204.2 (204.0  $[\text{M} - 2\text{OTf}]^{2+}$ ), 412.1 (412.1  $[\text{M} - \text{MeCN} - 2\text{OTf} + \text{HCOO}^-]^+$ ), 516.0 (516.1  $[\text{M} - \text{MeCN} - \text{OTf}]^+$ ). Elemental analysis calcd (%) for  $\text{C}_{23}\text{H}_{23}\text{CuF}_6\text{N}_5\text{O}_6\text{S}_2 + 0.3 \text{CHCl}_3$ : C 37.67, H 3.16, N 9.43; found: C 37.78, H 3.22, N 9.41.

### 5.4.3. Electrochemical measurements

All electrochemical experiments were performed using a custom-built 10 mL single-compartment glass cell with a three-electrode setup. The measurements were performed using Autolab PGSTAT 12, 204, and 128N potentiostats, operated by the Autolab NOVA 2 software. The working electrode is a PEEK encapsulated GC disk ( $A = 0.071 \text{ cm}^2$ , Metrohm) submerged in the solution. Unless otherwise stated, the GC electrode was manually polished before each catalytic measurement for 5 mins with 1.0, 0.3, and 0.05  $\mu\text{m}$  alumina suspensions on Buehler cloth polishing pads, or with a Struers LaboPol-30 polishing machine using 1.0  $\mu\text{m}$  diamond and 0.04  $\mu\text{m}$  silica suspension on polishing cloths (Dur-type) for 1 min each. This was followed by sonication of the electrode in Milli-Q purified water for 10–15 minutes. A gold wire was used as a counter electrode and was flame annealed and rinsed with Milli-Q purified water. The reference electrode was a reversible hydrogen electrode (RHE) made from a Pt mesh submerged in same electrolyte solution as the main cell compartment, connected via a Luggin capillary, and the reference compartment was continuously saturated with  $\text{H}_2$  gas. Oxygen-free electrolyte solutions were prepared by saturating the cell for 20 to 30 minutes with Ar, after which an atmosphere of 1 atm Ar was maintained over the solution. Oxygen-saturated electrolyte solutions were obtained by saturating the cell for 20 minutes with  $\text{O}_2$ , after which a 1 atm  $\text{O}_2$  atmosphere was maintained over the solution.

Prior to each experiment, the glassware was fully submerged and boiled in MilliQ purified water. Additionally, all glassware was regularly cleaned by submersion in an aqueous oxidizing solution containing 0.5 M  $\text{H}_2\text{SO}_4$  and 1 mg/mL (6.3 mM)  $\text{KMnO}_4$  overnight. This is followed by removal of excess  $\text{KMnO}_4$  and  $\text{MnO}_2$  from the glassware with diluted  $\text{H}_2\text{SO}_4$  and  $\text{H}_2\text{O}_2$ , followed by rinsing the glassware three times with water and boiling twice submerged in Milli-Q purified water.

## 5.5. References

- [1] H. A. Gasteiger, S. S. Kocha, B. Sompalli, F. T. Wagner, *Appl. Catal. B* **2005**, *56*, 9-35.
- [2] O. Gröger, H. A. Gasteiger, J.-P. Suchsland, *J. Electrochem. Soc.* **2015**, *162*, A2605-A2622.
- [3] Z. P. Cano, D. Banham, S. Ye, A. Hintennach, J. Lu, M. Fowler, Z. Chen, *Nat. Energy* **2018**, *3*, 279-289.
- [4] S. Fukuzumi, Y. Yamada, K. D. Karlin, *Electrochim. Acta* **2012**, *82*, 493-511.
- [5] L. An, T. S. Zhao, X. L. Zhou, L. Wei, X. H. Yan, *RSC Adv.* **2014**, *4*, 65031-65034.
- [6] S. H. Zeronian, M. K. Inglesby, *Cellulose* **1995**, *2*, 265-272.
- [7] G. Grigoropoulou, J. H. Clark, J. A. Elings, *Green Chem.* **2003**, *5*, 1-7.
- [8] M. Langerman, D. G. H. Hetterscheid, *Angew. Chem. Int. Ed.* **2019**, *58*, 12974-12978.
- [9] K. D. Karlin, J. C. Hayes, S. Juen, J. P. Hutchinson, J. Zubieta, *Inorg. Chem.* **1982**, *21*, 4106-4108.
- [10] E. A. Ambundo, M.-V. Deydier, A. J. Grall, N. Agüera-Vega, L. T. Dressel, T. H. Cooper, M. J. Heeg, L. A. Ochrymowycz, D. B. Rorabacher, *Inorg. Chem.* **1999**, *38*, 4233-4242.
- [11] M. Schatz, et al., *Inorg. Chem.* **2001**, *40*, 2312-2322.
- [12] Simon P. Foxon, O. Walter, S. Schindler, *Eur. J. Inorg. Chem.* **2002**, *2002*, 111-121.

- [13] T. Fujii, A. Naito, S. Yamaguchi, A. Wada, Y. Funahashi, K. Jitsukawa, S. Nagatomo, T. Kitagawa, H. Masuda, *Chem. Commun.* **2003**, 2700-2701.
- [14] D. Das, Y.-M. Lee, K. Ohkubo, W. Nam, K. D. Karlin, S. Fukuzumi, *J. Am. Chem. Soc.* **2013**, *135*, 2825-2834.
- [15] G. S. Patterson, R. H. Holm, *Bioinorganic Chemistry* **1975**, *4*, 257-275.
- [16] A. W. Addison, *Inorg. Chim. Acta* **1989**, *162*, 217-220.
- [17] H. Nagao, N. Komeda, M. Mukaida, M. Suzuki, K. Tanaka, *Inorg. Chem.* **1996**, *35*, 6809-6815.
- [18] H. R. Lucas, G. J. Meyer, K. D. Karlin, *J. Am. Chem. Soc.* **2010**, *132*, 12927-12940.
- [19] Y. Lee, et al., *Inorg. Chem.* **2009**, *48*, 11297-11309.
- [20] S. Kakuda, R. L. Peterson, K. Ohkubo, K. D. Karlin, S. Fukuzumi, *J. Am. Chem. Soc.* **2013**, *135*, 6513-6522.
- [21] N. W. G. Smits, B. van Dijk, I. de Bruin, S. L. T. Groeneveld, M. A. Siegler, D. G. H. Hetterscheid, *Inorg. Chem.* **2020**, *59*, 16398-16409.
- [22] B. J. Hathaway, P. G. Hodgson, *J. Inorg. Nucl. Chem.* **1973**, *35*, 4071-4081.
- [23] K. J. de Almeida, N. A. Murugan, Z. Rinkevicius, H. W. Hugosson, O. Vahtras, H. Ågren, A. Cesar, *Phys. Chem. Chem. Phys.* **2009**, *11*, 508-519.
- [24] R. F. See, R. A. Kruse, W. M. Strub, *Inorg. Chem.* **1998**, *37*, 5369-5375.
- [25] A. Nimmermark, L. Öhrström, J. Reedijk, **2013**, *228*, 311-317.
- [26] R. S. Nicholson, I. Shain, *Anal. Chem.* **1964**, *36*, 706-723.
- [27] R. M. Bullock, A. M. Appel, M. L. Helm, *Chem. Commun.* **2014**, *50*, 3125-3143.
- [28] N. Niklas, F. W. Heinemann, F. Hampel, T. Clark, R. Alsasser, *Inorg. Chem.* **2004**, *43*, 4663-4673.
- [29] M. Palaniandavar, R. J. Butcher, A. W. Addison, *Inorg. Chem.* **1996**, *35*, 467-471.
- [30] B. S. Lim, R. H. Holm, *Inorg. Chem.* **1998**, *37*, 4898-4908.
- [31] W. J. Shaw, M. L. Helm, D. L. DuBois, *BBA - Bioenergetics* **2013**, *1827*, 1123-1139.
- [32] M. L. Pegis, B. A. McKeown, N. Kumar, K. Lang, D. J. Wasylenko, X. P. Zhang, S. Rauegi, J. M. Mayer, *ACS Cent. Sci.* **2016**, *2*, 850-856.
- [33] Y.-H. Wang, M. L. Pegis, J. M. Mayer, S. S. Stahl, *J. Am. Chem. Soc.* **2017**, *139*, 16458-16461.
- [34] M. L. Pegis, C. F. Wise, B. Koronkiewicz, J. M. Mayer, *J. Am. Chem. Soc.* **2017**, *139*, 11000-11003.
- [35] C. M. Klug, A. J. P. Cardenas, R. M. Bullock, M. O'Hagan, E. S. Wiedner, *ACS Catal.* **2018**, *8*, 3286-3296.
- [36] D. J. Martin, B. Q. Mercado, J. M. Mayer, *Sci. Adv.* **2020**, *6*, eaaz3318.



# Chapter 6

---

Summary and outlook

## 6.1. Summary

The transition from fossil fuels to renewable energy is one of the most pressing challenges of this century. Many factors play a role in our ability to reduce our carbon footprint, while simultaneously being able to keep up with a growing demand for energy. Methods that allow us to be able to efficiently store electrical energy over longer periods of time are essential. This is especially important due to the intermittent nature of two of the most important renewable energy sources, solar and wind energy. While battery technology has progressed such that it is now the most viable option for powering (short-range) transportation with consumer vehicles, batteries are not easily scalable for large scale energy storage to power the industry. Alternatively, dihydrogen ( $H_2$ ) generated by water electrolysis can play an important role as a chemical energy carrier, which can be used to store and transport energy. Fuel cells can be used to convert  $H_2$  and  $O_2$  to  $H_2O$ , thereby generating an electrical current between the anode and cathode of the fuel cell. However, the half reaction at the cathode, the reduction of  $O_2$  to  $H_2O$ , is subject to significant energy losses. This multi-step catalytic reaction involves four protons and four electrons is subject to significant overpotential. Even the best platinum-based catalyst is not able to perform this reaction close to the equilibrium potential of 1.23 V. Developing alternative catalysts that are based on non-precious metals and are able to more efficiently catalyse the electrochemical reduction of dioxygen would increase both the cost and energy efficiency of fuel cells.

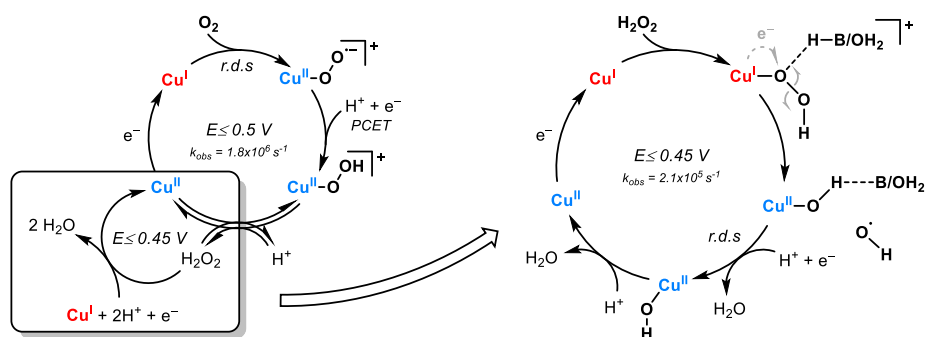
In nature, copper plays an important role in the active sites of many redox-active enzymes that are involved in the activation and reduction of dioxygen. Inspired by these natural systems, many molecular copper complexes have been studied for their dioxygen binding and activation reactivity throughout the past decades. Moreover, it has been shown that the multicopper oxidase enzyme Laccase is able to efficiently catalyse the reduction of dioxygen to water. Electrochemical studies on Laccase have shown that the reduction of  $O_2$  to  $H_2O$  takes places close to the  $O_2/H_2O$  equilibrium potential, with a lower overpotential than the platinum-based heterogenous catalysts currently responsible for the oxygen reduction reaction (ORR) in hydrogen fuel cells. This has led to a significant interest in the use of biomimetic molecular copper complexes as catalysts for the electrochemical ORR. The tris(2-pyridylmethyl)amine (tmpa) copper complex (Cu-tmpa) and similar derived complexes have been previously studied for the ORR using sacrificial reductants. Initial results suggested that perhaps a dinuclear species is formed during the catalytic reaction. However, the mechanism for the ORR by Cu-tmpa under electrochemical conditions had not been fully clarified yet, nor have the reaction kinetics for the electrochemical ORR been investigated. With the research presented in this thesis, we performed a detailed mechanistic and kinetic analysis of the electrochemical oxygen and hydrogen peroxide reduction reactions by

Cu-tmpa, under aqueous conditions and in an organic electrolyte. Additionally, three additional mononuclear copper complexes were investigated for their catalytic performance with respect to the reduction of  $O_2$  and  $H_2O_2$ .

In Chapter 2, the electrochemical analysis of Cu-tmpa as a homogenous electrocatalyst for the ORR is described. Because of the limited stability of Cu-tmpa under acidic conditions and our interest in the catalytic performance under neutral conditions, we performed the electrochemical measurements in an aqueous pH 7 phosphate buffered solution. Due to the fast ligand exchange kinetics associated with copper ions, we first determined the stability of Cu-tmpa under electrochemical conditions via in situ electrochemical quartz crystal microbalance (EQCM) experiments. These revealed that no measurable deposition takes place during the electrocatalytic ORR reaction, thus establishing the homogeneous nature of the catalytic species. Catalyst concentration studies showed a first-order dependence of the catalytic current on the copper concentration, demonstrating that the catalytic mechanism involves a single copper site, as opposed to the previously suggested copper dimer species. Another important aspect for the ORR is the nature of the reaction product and the amount of electrons involved in the catalytic reaction. Using the rotating ring-disk electrode (RRDE) and the resulting Koutecky-Levich analysis, an electron transfer number close to 4 was determined. This showed that  $H_2O$  is the primary product in the limiting-current regime. However, in the potential window before the limiting current is reached, a small oxidative current was observed at the ring. By modulating the potential of the Pt ring and varying the catalyst concentration, it was determined that this current response on the Pt ring was caused by the oxidation of  $H_2O_2$ . Chronoamperometric measurements confirmed that  $H_2O_2$  is the preferentially formed product at potentials close to the catalytic onset. Indeed, analysis of the Tafel Slopes for the full catalytic potential window showed two distinct catalytic regimes. Using the foot-of-the-wave analysis (FOWA), we were able to determine the catalytic first-order rate constant associated with the partial reduction of  $O_2$  to  $H_2O_2$ . This catalytic rate constant was shown to be an order of magnitude larger than the rate constant associated with the full four-electron reduction to  $H_2O$ . These results showed that competition between two distinct catalytic cycles takes place during the ORR (see scheme 6.1), in which  $H_2O_2$  is readily replaced in the copper coordination sphere.

Hydrogen peroxide was shown to play a pivotal role in the electrochemical reduction of dioxygen by Cu-tmpa. This shows similarities with the Fenton chemistry observed in several copper-containing enzymes. These enzymes activate and reduce  $O_2$ , and under certain conditions produce  $H_2O_2$ , or are able to use  $H_2O_2$  as a substrate for the oxidation reactions carried out by these enzymes. Understanding how hydrogen peroxide is activated by these copper enzymes and copper complexes is essential for





**Scheme 6.1.** The mechanistic cycles proposed in this thesis (Chapter 2 and 3) for the ORR and HPRR by Cu-tmpa. Here,  $k_{\text{obs}}$  refer to the rate constants obtained by FOWA.

the design of new selective catalysts for the reduction of O<sub>2</sub> or the electrochemical production of H<sub>2</sub>O<sub>2</sub>. Therefore, we set out to investigate the electrochemical hydrogen peroxide reduction reaction (HPRR) by Cu-tmpa in neutral aqueous solution, as is described in Chapter 3. The electrochemical HPRR was shown to have a first-order dependence in catalyst concentration, as was also shown to be the case for the ORR as described in Chapter 2. Kinetic studies revealed that the reduction of hydrogen peroxide is significantly slower by at least one order of magnitude than the reduction of dioxygen. By performing the same electrochemical analysis of the catalytic performance of Cu-tmpa in a phosphate buffered D<sub>2</sub>O electrolyte solution, we were able to determine the kinetic isotope effect (KIE) associated with the HPRR. Application of the FOWA and the determination of the rate constant through the direct current enhancement ( $i_{\text{cat}}/i_{\text{p}}$ ) at low catalyst concentrations both resulted in lower catalytic rate constants than in non-deuterated electrolyte solution. This translated to a solvent KIE of 1.4 to 1.7 for the HPRR by the copper catalyst. This indicates that an hydrogen or proton transfer is involved in the rate-determining step of the catalytic reaction. Following these results we proposed a mechanism similar to those suggested for the active sites of copper-containing monooxygenases, involving the formation of a Cu<sup>II</sup>-OH species and a free hydroxyl radical as intermediate species. The overall electrocatalytic mechanisms for the reduction of O<sub>2</sub> and H<sub>2</sub>O<sub>2</sub> by Cu-tmpa based on Chapter 2 and 3 is shown in Scheme 6.1.

While we have shown that the reduction of dioxygen by Cu-tmpa under neutral aqueous conditions follows a mononuclear reaction pathway, questions remained regarding the catalytic mechanism in organic solvents. The catalytic mechanism can be significantly affected by the reaction conditions. Different interactions between the solvents and the catalytic species or reaction intermediates, and differences in the nature of the proton source can all play a role. In Chapter 4 we describe the

investigation of the ORR and HPRR by Cu-tmpa in acetonitrile, evaluating the catalytic reactions in several acidic and buffered electrolyte solutions. Of the four different acids that were used, trifluoroacetic acid (HTFA) and dimethylformamidium trifluoromethanesulfonate (HDMF<sup>+</sup>) resulted in instability and decomposition of the Cu-tmpa complex. No reversible redox couples could be obtained in the presence of either of these two strong acids. For the milder acetic acid (HOAc) and triethylammonium (HNEt<sub>3</sub><sup>+</sup>) acids, reversible redox couples were observed for Cu-tmpa. Nitriles, such as EtCN and MeCN, act as strong ligands for the reduced Cu<sup>I</sup>-tmpa species, competing with the reversible binding of O<sub>2</sub>. In the case of EtCN, it has previously been shown that the equilibrium constant of formation for [Cu<sup>II</sup>(O<sub>2</sub><sup>•-</sup>)(tmpa)]<sup>+</sup> is only 0.38 M<sup>-1</sup> at room temperature due to competition with the coordination of the solvent to the copper centre. It is expected that this will have a significant suppressing effect on the catalytic ORR rate. Indeed, after studying the reaction kinetics of the electrocatalytic ORR in MeCN using the catalytic current enhancement, we observed a 10<sup>5</sup> times reduction of the observed rate constant  $k_{\text{obs}}$  compared to the ORR in an aqueous environment. Finally, we were able to show that while the kinetics of the catalytic reactions were significantly slower in MeCN, the overpotential associated with the ORR is more than 100 mV lower in the buffered MeCN solution than in neutral aqueous solution. Interestingly, catalytic rate constants were higher for the HPRR than for the ORR, a clear inversion from the behaviour observed under aqueous conditions. This study has shown that the catalytic mechanism for the reduction of O<sub>2</sub> in acetonitrile is largely similar to what we have observed in water, despite the significantly inhibited reaction kinetics due to the involvement of the competitive coordination of acetonitrile.

In Chapter 5, the synthesis and electrochemical analysis of three different pyridylalkylamine copper complexes is described. Here, we varied the distance between the central amine and one of the pyridine arms, thereby varying the amount of strain on the coordination sphere of the copper complex. Additionally, one ligand was synthesized as an analogue to bmpa (bmpa = bis(2-pyridylmethyl)amine), by introducing a non-coordinating furanyl group while maintaining the central tertiary amine, instead of the secondary amine present in bmpa. The largest increase of the redox potential was observed for Cu-bmpma (bmpma = bis[(2-pyridyl)methyl]-2-pyridylamine), with a +300 mV higher redox potential than Cu-tmpa. A general trend is observed where an increase in strain on the coordination environment of the Cu centre results in a higher redox potential of the complex. A clear linear scaling relationship between the redox potential and the catalytic rate constants of the reduction of O<sub>2</sub> and H<sub>2</sub>O<sub>2</sub> was established. The lower the redox potential of the given copper complex, the higher the catalytic rate constants. In the case of Cu-bmpma, this also results in a faster HPRR than ORR, contrary to the other complexes that were investigated. This shows

the HPORR and ORR catalytic cycles are not entirely linked, which provides additional confirmation that for mononuclear copper catalyst two separate catalytic cycles take place during the ORR.

## 6.2. Outlook

We have identified Cu-tmpa as an excellent electrocatalyst for the ORR, exhibiting exceedingly fast kinetics that resulted in a catalyst able to operate at maximum capacity even at catalyst concentrations in the low micromolar range. However, a significant overpotential ( $>0.9$  V) is associated with the ORR by Cu-tmpa. Attempts to reduce the overpotential by modifying the ligand strain placed on the coordination sphere were successful, but did result in significant decrease of the catalytic rate constants. We have also shown that the catalytic mechanism for the ORR proceeds via a mononuclear catalytic species. This result was obtained both under neutral aqueous conditions and in acetonitrile in the presence of weak acids. Thus, the suggested dimeric  $[\{Cu^{II}(tmpa)\}_2(O_2)]^{2+}$  species, which has been shown to form under non-catalytic conditions, and from which the ORR was able to take place, does not form under fully electrocatalytic conditions in the presence of protons. This highlights the necessity to study the catalytic mechanism under electrochemical conditions, when previously published results have been obtained using chemical reductants in stopped-flow experiments.

Furthermore, the apparent stepwise reduction of  $O_2$  to  $H_2O$  via  $H_2O_2$  by mononuclear copper catalysts based on the Cu-tmpa structural template shows that the 1.23 V vs RHE standard reduction potential of dioxygen is not the limiting factor in bringing down the overpotential of these catalysts, but the standard reduction potential of 0.695 V vs RHE associated with the partial reduction of  $O_2$  to  $H_2O_2$ . This has significant implications for the design of catalysts with even lower overpotentials for the 4-electron reduction of  $O_2$ . It points to the need of multinuclear copper catalysts that can avoid the formation of a hydroperoxo intermediate during the catalytic cycle and are instead able to cleave the O–O bond first. In principle, this would call for a catalyst in which two copper centres are spaced at the optimal distance from each other for the bridging of  $O_2^{2-}$ , and are connected via a mostly rigid ligand backbone. This can prevent the formation of hydroperoxo species, and thus the formation of  $H_2O_2$ . Additionally, the redox potential of the species will also have to be shifted closer to the equilibrium potential of the  $O_2/H_2O$  couple to give better overall catalytic performance than mononuclear copper complexes that are able reduce  $O_2$  and  $H_2O_2$  and operate close to the equilibrium potential of the  $O_2/H_2O_2$  couple.

# Appendix A

## Supplementary Information for Chapter 2

### A.1 Scan rate dependence

The peak redox current was found to be linearly dependent on the square root of the scan rate (Figure A.1) and the peak-to-peak separation  $\Delta E_p$  remained constant at  $56 \text{ mV} \pm 5 \text{ mV}$  at different scan rates. This is in agreement with a homogeneous system undergoing a reversible one-electron reduction and oxidation step. The diffusion coefficient of Cu-tmpa is  $4.9 \times 10^{-6} \text{ cm}^2 \text{ s}^{-1}$ , as derived by the Randles-Sevcik equation.

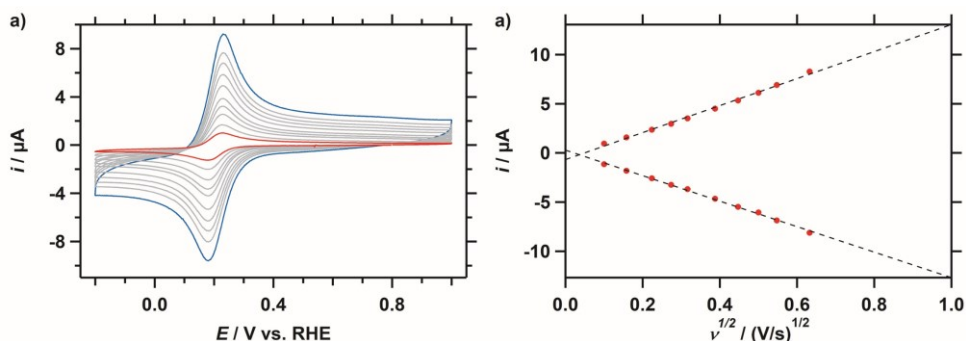


**Figure A.1.** a) CVs of 0.3 mM Cu-tmpa at a range of scan rates between 400 and  $10 \text{ mV s}^{-1}$  in the presence of 1 atm Ar. b) Plot of the peak oxidative and reductive currents of the redox couple as a function of  $v^{1/2}$ .

### A.2 EQCM measurements

As copper ions have very fast ligand exchange kinetics it is important to establish the homogeneity of the catalyst during the catalytic reaction.<sup>[1-2]</sup> Therefore, electrochemical quartz crystal microbalance experiments (EQCM) measurements were performed to investigate the stability of Cu-tmpa both under catalytic and non-catalytic conditions. During EQCM measurements, the frequency changes of an oscillating gold-coated quartz crystal are measured during the electrochemical experiment. These frequency changes can be directly correlated to the mass change of the electrode. A decrease in frequency corresponds to an increase in the mass of the electrode, while an increase in frequency corresponds to a decrease in mass. The EQCM experiments

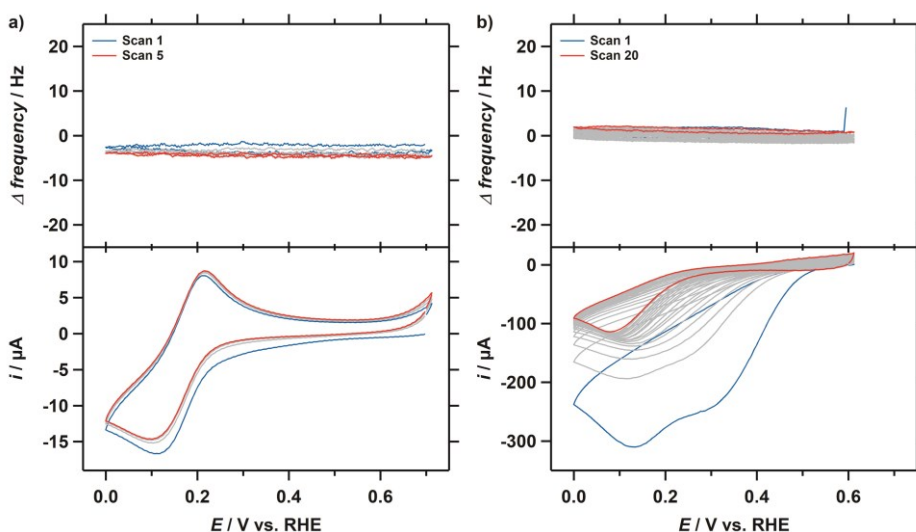


**Figure A.2.** EQCM experiments in a pH 7 PB (0.1 M), containing 0.3 mM Cu-tmpa. CVs (bottom panel) and the corresponding frequency response (top panel) are shown for both **(a)** argon-saturated and **(b)** oxygen-saturated solutions. CVs were obtained at a scan rate of 100 mV s<sup>-1</sup>.

were conducted using an Autolab PGSTAT 128N potentiostat and a 5 mL Autolab EQCM cell. An Autolab gold coated quartz crystal EQCM electrode ( $A = 0.35 \text{ cm}^2$ , gold layer thickness = 100 nm) was used as the working electrode and a coiled gold wire was used as the counter electrode. An RHE Luggin setup was used as the reference electrode. Cyclic voltammetry (CV) measurements were performed in a pH 7 phosphate buffer (0.1 M), containing 0.3 mM Cu-tmpa. EQCM measurements in an argon-saturated solution show a well-defined redox couple at 0.20 V, while little change in the frequency of the electrode is observed (Figure A.2a). The EQCM data for Cu-tmpa in a 1 atm O<sub>2</sub>-saturated solution is shown in Figure A.2b. Over subsequent scans the catalytic current decreases significantly, while at the same time no change in frequency of the electrode is observed during the ORR. The frequency changes observed in the presence of Cu-tmpa are in the same window as the EQCM data obtained for a bare gold electrode in a solution without any Cu-tmpa present (Figure A.3). The decreasing catalytic current corresponds to the depletion of dioxygen in the solution, and this behaviour can also be observed in the EQCM data for the bare gold electrode. These results clearly show that Cu-tmpa forms no surface deposits during the ORR. Comparison to Cu(OTf)<sub>2</sub> as a positive control for surface deposition shows clear frequency changes, corresponding to deposition in the presence of Ar followed by surface stripping in the presence of O<sub>2</sub>, respectively (Figure A.4).

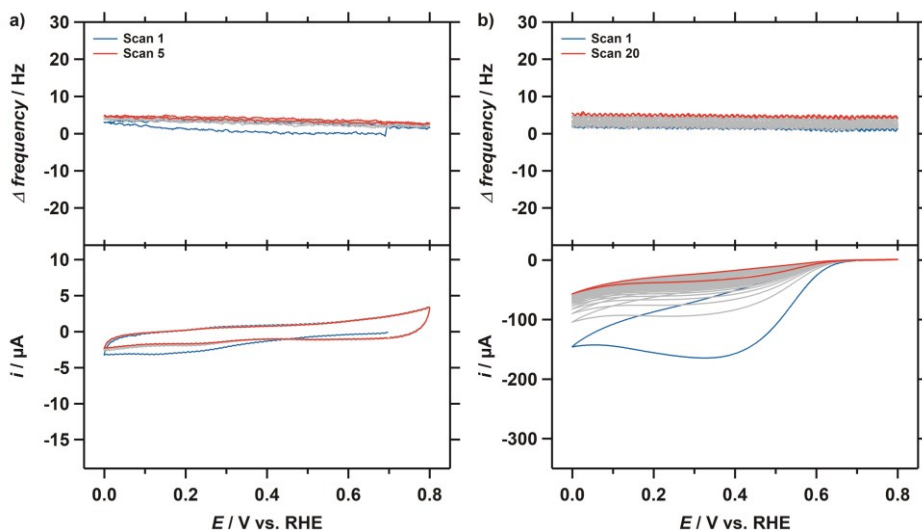


**Figure A.3.** EQCM experiments in a pH 7 PB (0.1 M). CVs (bottom panel) and the corresponding frequency response (top panel) for the bare gold-coated electrode are shown for both **(a)** argon-saturated and **(b)** oxygen-saturated solutions. CVs were measured at a scan rate of  $100 \text{ mV s}^{-1}$ .

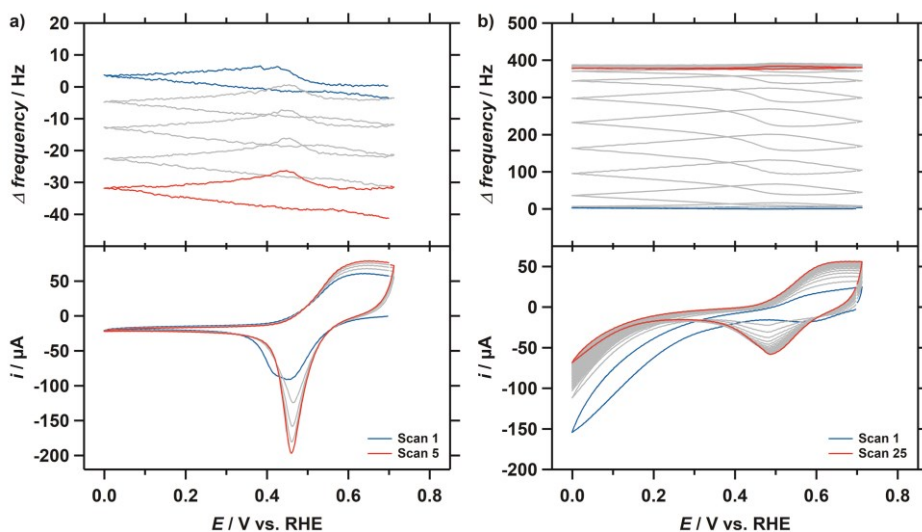


**Figure A.4.** EQCM experiments in a pH 7 PB (0.1 M), containing  $0.3 \text{ mM Cu(OTf)}_2$ . CVs (bottom panel) and the corresponding frequency response (top panel) are shown for both **(a)** argon-saturated and **(b)** oxygen-saturated solutions. CVs were measured at a scan rate of  $100 \text{ mV s}^{-1}$ .

### A.3 Concentration dependence studies

For the determination of the catalytic current  $i_{\text{cat}}$  at low Cu-tpma concentrations, the GC electrode was polished with 0.05  $\mu\text{m}$  alumina suspension for 5 minutes and subsequently sonicated in MilliQ for 15 minutes before every measurement. Additionally, a blank CV was measured of the GC electrode in an oxygen-saturated pH 7 PB electrolyte solution after every electrode polish. The currents obtained from CV measurements in presence of Cu-tpma were corrected using their corresponding blank measurement, giving the catalytic current without any contribution from the GC electrode.

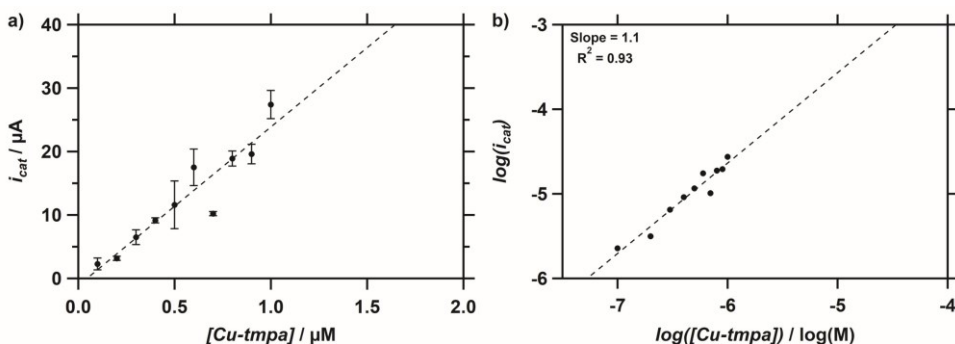


**Figure A.5.** a) Background corrected catalytic current  $i_{\text{cat}}$  as a function of Cu-tpma concentration. b) Log-log plot of the same data.

### A.4 RRDE experiments

RRDE experiments were conducted using an Autolab PGSTAT 12 potentiostat and a Pine Instruments MSR rotator. All measurements were done in a custom-build glass two-compartment cell with a three-electrode setup. A gold wire was used as a counter electrode, separated from the main compartment by a glass frit. GC disks ( $A = 0.196 \text{ cm}^2$ ) and Pt disks ( $A = 0.196 \text{ cm}^2$ ) were used in conjunction with a Pt ring in a Pine Instruments E6R1 ChangeDisk setup. Prior to use, the electrodes were separately manually polished for 5 minutes with 1.0, 0.3, and 0.05  $\mu\text{m}$  alumina suspensions on Buehler cloth polishing pads, for 5 minutes respectively, followed by sonication in Milli-Q water for 15 minutes. Additionally, the Pt disk was electropolished by CV between -0.5 V and 2 V vs. RHE at 1 V/s for 200 cycles in an aqueous 0.1 M  $\text{H}_2\text{SO}_4$  solution. The collection efficiency ( $N = 0.23$ ) of the Pt ring electrode was determined from the one-electron transfer  $\text{Cu}^{\text{II/I}}$  redox reaction of Cu-tpma, which is slightly lower than the collection efficiency supplied by the manufacturer ( $N = 0.25$ , Pine Instruments). This is in good agreement with the collection efficiency (22%) previously obtained for the  $[\text{Fe}(\text{CN})_6]^{4-}/\text{Fe}(\text{CN})_6]^{3-}$  redox couple using the same setup.<sup>[3]</sup> The current measured in

the absence of Cu-tmpa were subtracted from  $I_{ring}$  and  $I_{disk}$  obtained in the presence of Cu-tmpa and the resulting background corrected LSVs are shown in Figure A.5.

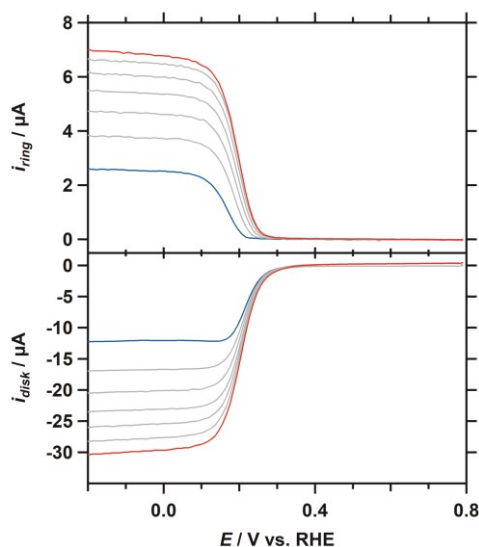


**Figure A.6.** RRDE LSV data used to determine the collection efficiency of the Pt ring electrode, 400 to 2800 RPM, 400 RPM increments. Conditions: pH 7 phosphate buffer ( $[PO_4] = 100$  mM),  $[Cu-tmpa] = 0.3$  mM, 293 K,  $50 \text{ mV s}^{-1}$  scan rate.

## A.5 Koutecky-Levich analysis

The limiting currents at different rotation rates for the ORR by Cu-tmpa shown in Figure 2.4 (main text) show good linearity in accordance with the behaviour described by the Koutecky-Levich equation:

$$\frac{1}{I} = \frac{1}{I_K} + \frac{1}{I_L} \quad (\text{A.1})$$

Where  $I_K$  is the kinetic current and  $I_L$  is the mass-transport limited current.  $I_L$  can be described through the Levich equation:

$$I_L = 0.62nFAD^{2/3}\nu^{-1/6}C\omega^{1/2} = B\omega^{1/2} \quad (\text{A.2})$$

Where  $n$  is the electron transfer number,  $F$  is the faradaic constant (C/mol),  $A$  is the surface area of the disk electrode ( $\text{cm}^2$ ),  $D$  is the diffusion coefficient of  $O_2$  ( $\text{cm}^2/\text{s}$ ),  $\nu$  is the kinematic viscosity ( $\text{cm}^2/\text{s}$ ),  $C$  is the concentration of  $O_2$  ( $\text{mol}/\text{cm}^3$ ), and  $\omega$  the rotation rate ( $\text{rad}/\text{s}$ ). These constants can be simplified with the Levich constant  $B$ . The linear relationship observed in the Koutecky-Levich plot provides a  $B$  value for the 4-electron ORR, according to Eq. A.3.

$$\text{slope} = \frac{1}{B} \quad (\text{A.3})$$



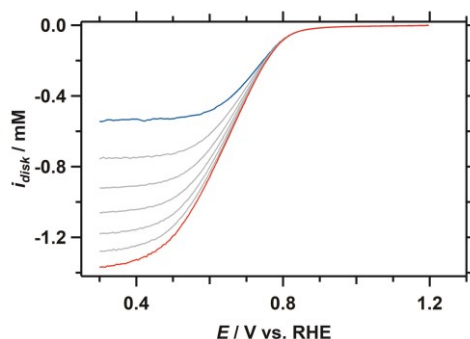


**Figure A.7.** RDE LSVs of polycrystalline Pt disk under 1 atm O<sub>2</sub> at different rotation rates from 400 RPM (blue line) to 2800 RPM (red line), 400 RPM increments. Conditions: pH 7 phosphate buffer ([PO<sub>4</sub>] = 100 mM), 293 K, 50 mV s<sup>-1</sup> scan rate.

A Pt disk was used to obtain a reference  $B$  value for the 4-electron ORR under our experimental conditions. This was done by measuring the ORR activity of a Pt disk at different rotation rates under the exact same conditions as the Cu-tmpa system, as shown in Figure A.7. Some discussion has arisen around the viability of the KL analysis for the ORR reaction.<sup>[4]</sup> Indeed, we also note that the  $n$  determined by the KL method ( $n_{KL}$ ) is not entirely independent of the angular velocity  $\omega$ . However, determination of  $n$  by the RRDE method ( $n_{RRDE}$ ) show similar values of  $n$  in the mass-transport limited regime.

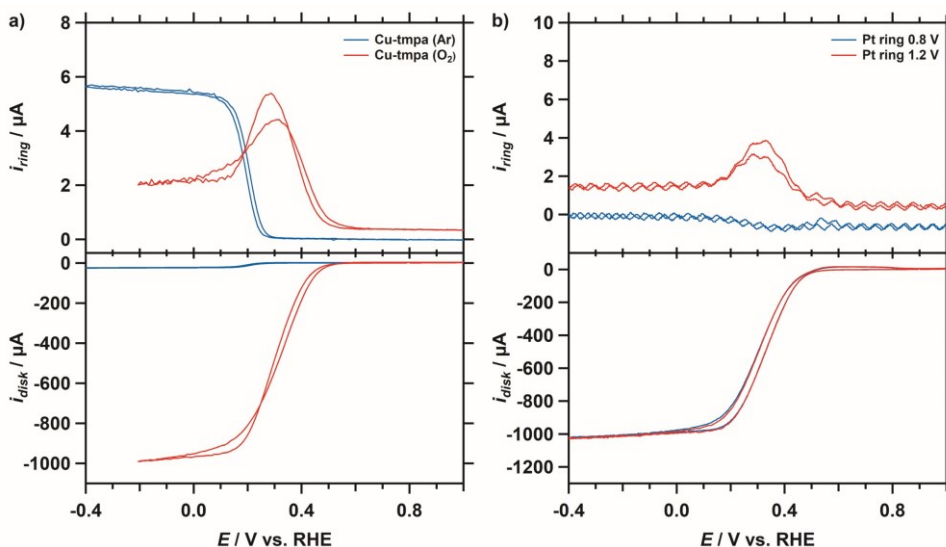


**Figure A.8. a)** RRDE CV comparison of Cu-tmpa under 1 atm Ar (blue line) or 1 atm O<sub>2</sub> (red line) at 1600 RPM. **b)** RRDE CV comparison of Cu-tmpa with the Pt ring potential set at 1.2 V (red line) or 0.8 V (blue line) vs. RHE under 1 atm O<sub>2</sub> at 1600 RPM. Conditions: pH 7 phosphate buffer ([PO<sub>4</sub>] = 100 mM), [Cu-tmpa] = 0.3 mM, 293 K, 50 mV s<sup>-1</sup> scan rate.

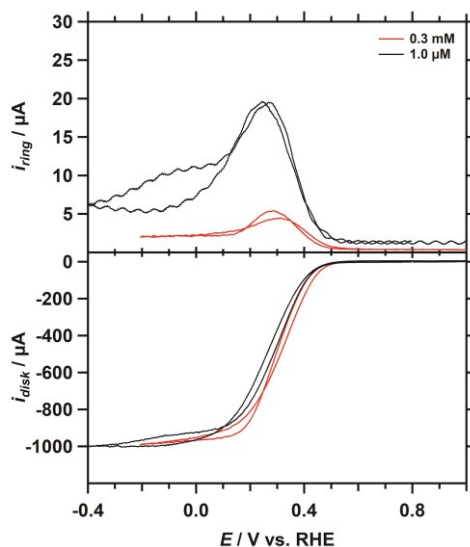


**Figure A.9.** RRDE CV comparison of the ORR at different Cu-tmpa concentrations. Conditions: pH 7 phosphate buffer ( $[\text{PO}_4] = 100 \text{ mM}$ ), 293 K, Pt ring at 1.2 V vs. RHE,  $50 \text{ mV s}^{-1}$  scan rate.

## A.6 Collection efficiency of $\text{H}_2\text{O}_2$ at the Pt ring

For the quantification of  $\text{H}_2\text{O}_2$  at the Pt ring the collection efficiency towards  $\text{H}_2\text{O}_2$  was determined. As the catalytic conversion of  $\text{H}_2\text{O}_2$  to  $\text{O}_2$  by Pt involves a reversible surface binding step, the collection efficiency can be expected to be lower to that of a one-electron oxidation of  $\text{Cu}^{\text{I}}\text{-tmpa}$  or  $[\text{Fe}(\text{CN})_6]^{4-}$ . Additionally, there is a significant phosphate buffer dependence present in the electrochemical oxidation of  $\text{H}_2\text{O}_2$  by Pt.<sup>[5]</sup> While a significant effect is shown at high  $[\text{H}_2\text{O}_2]$  and low  $[\text{PO}_4]$ , linear behaviour is observed with  $[\text{PO}_4] = 100 \text{ mM}$  in the low  $\text{H}_2\text{O}_2$  concentration range.

The collection efficiency for hydrogen peroxide ( $N_{\text{H}_2\text{O}_2}$ ) was determined by using a GC disk to generate  $\text{H}_2\text{O}_2$  through the 2-electron reduction of  $\text{O}_2$ . As the Pt disk should be held at a potential where oxidation of  $\text{H}_2\text{O}_2$  is mass-transport limited, CVs were measured on the Pt ring while rotating the RRDE setup at 1600 RPM in  $1.5 \text{ mM } \text{H}_2\text{O}_2$  (pH 7 phosphate buffer,  $[\text{PO}_4] = 100 \text{ mM}$ ). It was found that 1.2 V vs. RHE is within the  $\text{H}_2\text{O}_2$  mass-transport limited regime under our experimental conditions (Figure A.10a).

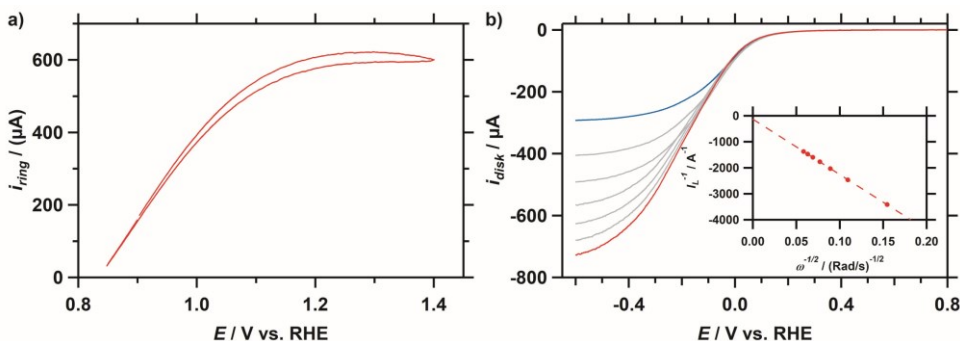


**Figure A.10.** a) CV measured at the Pt ring electrode in the presence of 1.5 mM  $\text{H}_2\text{O}_2$ . b) RDE LSVs of bare GC under 1 atm  $\text{O}_2$  at different rotation rates from 400 RPM (blue line) to 2800 RPM (red line), 400 RPM increments. The inset shows the KL plot of the inverse limiting current ( $i_L^{-1}$ ) at -0.6 V (vs. RHE.) as a function of the inverse square root of the rotation rate. Conditions: pH 7 PB ( $[\text{PO}_4] = 100 \text{ mM}$ ), 293 K, Pt ring at 1.2 V vs. RHE,  $50 \text{ mV s}^{-1}$  scan rate.

Secondly, the electron-transfer number of the ORR by GC under our conditions was established by performing a Koutecky-Levich analysis as previously described, resulting in  $n_{\text{KL}} = 2.04$  (Figure A.10b). For a reliable  $N_{\text{H}_2\text{O}_2}$ , chronoamperometric (CA) measurements were performed by applying several different potentials to the GC disk at 1600 RPM, while the Pt ring was held at 1.2 V vs. RHE. The disk potential was first held at 0.8 V for 60 seconds, followed by a potential step to either 0.1, 0.0, or -0.1 V, which was held for 180 seconds. A background correction was applied to the resulting ring current by subtracting the current measured on the ring while the disk was held at 0.8 V.  $N_{\text{H}_2\text{O}_2}$  was calculated by taking  $i_{\text{ring}}$  over  $i_{\text{disk}}$ , and was shown to be stable as function of time and applied potential (Figure A.11). The final  $N_{\text{H}_2\text{O}_2} = 0.125$  was obtained by averaging the values between  $t = 30 \text{ s}$  and  $t = 60 \text{ s}$ , and was used in further calculations.

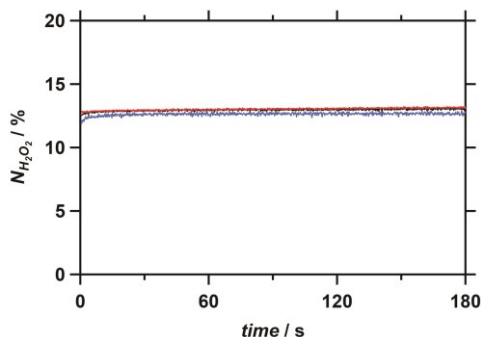


**Figure A.11.** Hydrogen peroxide collection efficiency ( $N_{\text{H}_2\text{O}_2}$ ) determined from RRDE CA measurements of the ORR (1 atm  $\text{O}_2$ ) by a GC disk performed at different  $E_{\text{disk}}$ : 0.1 (blue), 0.0 (black), and -0.1 V (red). Conditions: pH 7 PB ( $[\text{PO}_4] = 100 \text{ mM}$ ), 293 K, Pt ring at 1.2 V vs. RHE.

## A.7 Quantification of $\text{H}_2\text{O}_2$ during the ORR by Cu-tpmpa

The percentage  $\text{H}_2\text{O}_2$  ( $\%\text{H}_2\text{O}_2$ ) produced as a function of applied potential was determined using similar RRDE CA measurements as described in the previous section. The CA measurements were performed by applying several different potentials to the GC disk at 1600 RPM in the presence of 0.3 mM Cu-tpmpa, while the Pt ring was held at 1.2 V vs. RHE. First,  $E_{\text{disk}}$  was held at 0.8 V for 60 s, followed by a potential step to the desired potential, which was held for 300 s. The resulting current-response graphs are shown in Figure A.12a. A background correction was applied to the resulting  $i_{\text{ring}}$  by subtracting the current measured on the ring while the disk was held at 0.8 V. Additionally, a small background correction was applied to  $i_{\text{disk}}$  by subtracting the current measured at  $E_{\text{disk}} = 0.6$  V (Figure A.12a, broken line). The resulting  $\%\text{H}_2\text{O}_2$  were shown to be stable over time (Figure A.12b). The final values of  $\%\text{H}_2\text{O}_2$  were obtained by averaging over a 30 s time interval and the resulting  $\%\text{H}_2\text{O}_2$  as a function of applied potential are shown in the main text (Figure 2.5). The electron transfer number  $n_{\text{RRDE}}$  that was obtained using the same data set is shown in Figure A.12c, by using Eq. A.4. A

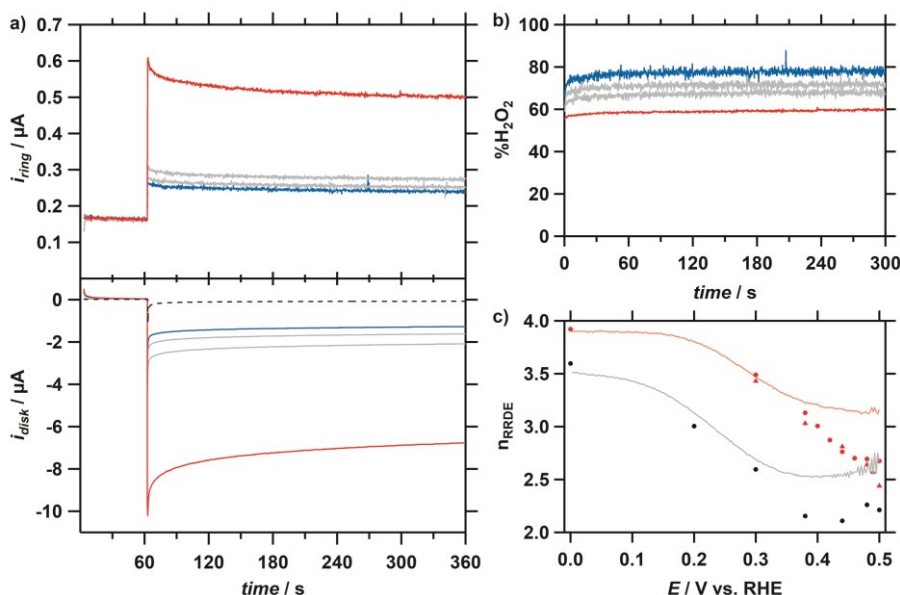


**Figure A.12.** **a)** RRDE CA measurements.  $E_{\text{disk}}$  at  $t = 0\text{--}60$  s was held at 0.8 V vs RHE, followed by a potential step. Blue to red traces: 0.50, 0.49, 0.48, 0.44 V vs. RHE. **b)**  $\%\text{H}_2\text{O}_2$  obtained from RRDE CA measurements with 0.3 mM Cu-tpmpa. **c)**  $n_{\text{RRDE}}$  obtained from RRDE CA (dots and triangles) and LSV (lines, 50 mV s<sup>-1</sup>) measurements as a function of applied potential at a rotation rate of 1600 RPM with 0.3 mM (red), and 1.0  $\mu\text{M}$  (black) Cu-tpmpa. Conditions: pH 7 PB ([ $\text{PO}_4$ ] = 100 mM), 293 K, Pt ring at 1.2 V vs. RHE.

duplicate experiment was performed and both datasets are plotted. For comparison %H<sub>2</sub>O<sub>2</sub> and  $n_{RRDE}$  obtained from LSV (50 mV s<sup>-1</sup>) are plotted in their relevant figures (Figure 2.5 and Figure A.12c). Significant underestimation of %H<sub>2</sub>O<sub>2</sub> is shown during LSV measurements at potentials closer to the onset of the ORR, compared to CA measurements. The same measurements were also performed at a Cu-tmpa concentration of 0.1 μM (Figure A.13).

$$n_{RRDE} = \frac{4 \times i_{disk}}{i_{disk} + (i_{ring}/N_{H2O2})} \quad (A.4)$$

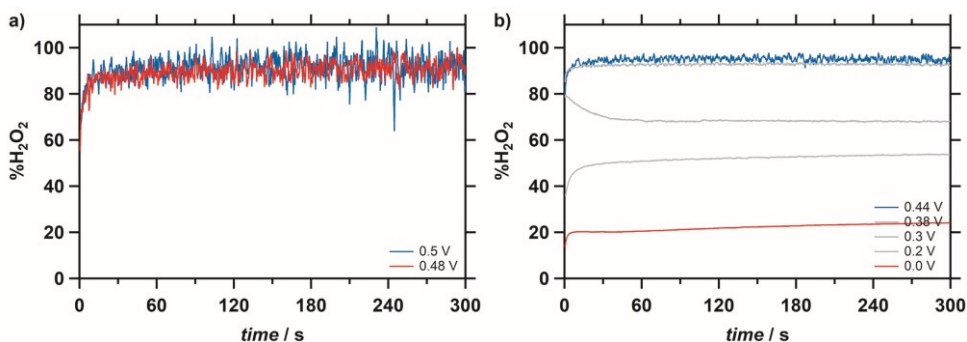


**Figure A.13.** %H<sub>2</sub>O<sub>2</sub> obtained from RRDE CA measurements at a rotation rate of 1600 RPM. Conditions: pH 7 PB ([PO<sub>4</sub>] = 100 mM), [Cu-tmpa] = 1.0 μM, 293 K, Pt ring at 1.2 V vs. RHE.

## A.8 Comparison of O<sub>2</sub> and H<sub>2</sub>O<sub>2</sub> reduction by Cu-tmpa

The onset potential of H<sub>2</sub>O<sub>2</sub> reduction (0.45 V) is ca. 50 mV lower than that of O<sub>2</sub> reduction, where onset is defined as the potential where the current in the presence of substrate is 3 times larger than the current in the absence of substrate ( $i_c/i > 3$ ).

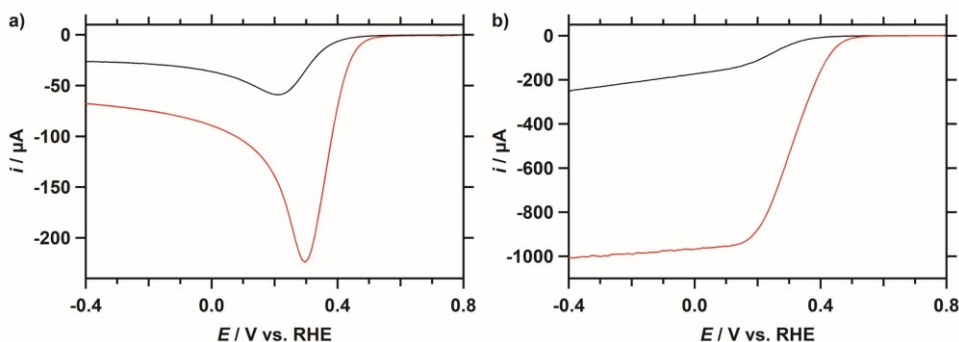


**Figure A.14.** LSVs of the reduction of 1 atm O<sub>2</sub> (red line) and 1.1 mM H<sub>2</sub>O<sub>2</sub> (black line) by Cu-tmpa. **a)** No rotation, **b)** 1600 RPM. Conditions: pH 7 PB ([PO<sub>4</sub>] = 100 mM), [Cu-tmpa] = 0.3 mM, 293 K, 50 mV s<sup>-1</sup> scan rate.

## A.9 Electrochemical kinetics measurements and calculations

The  $k_{\text{obs}}$  (or TOF) can be directly determined from the catalytic current enhancement via Eq. 2.2. However, this method has significant limitations for the ORR due to the previously mentioned  $\text{O}_2$  mass-transport limitation, which makes achieving kinetic conditions difficult. As the catalytic current by Cu-tpmpa is concentration-independent over a large concentration range, a useful, catalyst concentration-independent TOF can only be determined at low catalyst concentrations, where the catalytic current is not mass transport limited in  $\text{O}_2$ . Therefore,  $i_{\text{cat}}$  were obtained from CVs with catalyst concentrations in the range of 0.1–1.0  $\mu\text{M}$ . As no redox current can be observed at these low concentrations, the corresponding  $i_p$  values were calculated through the Randles-Sevcik equation, using the previously calculated diffusion coefficient of Cu-tpmpa. Thus, the current enhancement and TOF values were obtained by using the peak reductive current  $i_p$  calculated from the diffusion coefficient of Cu-tpmpa ( $D = 4.9 \times 10^{-6} \text{ cm}^2/\text{s}$ ). The measurements to obtain the catalytic current  $i_{\text{cat}}$  are described in section A.3. A plot of  $\log(\text{TOF})$  against the Cu-tpmpa concentration is shown in Figure A.16, revealing that the TOF is independent of catalyst concentration. The TOF values were averaged over the concentration range and reported with the standard error.

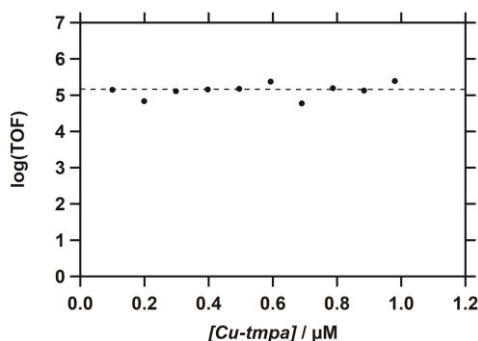
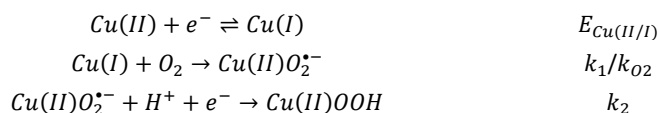


**Figure A.15.**  $\log(\text{TOF})$  as a function of catalyst concentration. Conditions: pH 7 PB ( $[\text{PO}_4] = 100 \text{ mM}$ ), 293 K,  $100 \text{ mV s}^{-1}$  scan rate.

To investigate the kinetics of the electrocatalytic ORR by Cu-tpmpa, we need to know which current-potential relationship applies to the catalytic system. The initial elemental steps involved in the reaction can be described as shown below, followed by consecutive (coupled) protonation and electron transfer steps.



FOWA only provides information about the first chemical step following the reduction of the catalyst<sup>[6]</sup>, and previous studies<sup>[7]</sup> on the ORR of Cu-tmpa in aqueous solution have shown no dependence of the peak catalytic current on the pH of the solution (and thus the proton concentration). When the rate is independent of proton concentration, the reaction is only limited by O<sub>2</sub> binding and  $k_{\text{obs}} = k_{\text{O}_2}[\text{O}_2]$ . Thus, the reaction can be simplified to an EC' type mechanism. So while the ORR is a much more complicated multielectron, multistep reaction, for the purpose of the FOWA the current-potential approximation as derived by Savéant *et al*<sup>[8-9]</sup> for an EC' type catalytic mechanism can be used for the electrochemical kinetics calculation (Eq. A.5). All electron transfer steps are considered to occur at the electrode, and no homogeneous electron transfer takes place between species.

$$i_c = \frac{nFSC_{\text{cat}}^0 \sqrt{D_{\text{cat}} k_{\text{obs}}}}{1 + \exp\left[\frac{F}{RT}(E - E_{1/2})\right]} \quad (\text{A. 5})$$

Where  $F$  is the faradaic constant,  $S$  the surface area of the catalyst,  $C_{\text{cat}}^0$  the bulk catalyst concentration,  $D_{\text{cat}}$  the diffusion coefficient of the catalyst,  $E_{1/2}$  the equilibrium potential of the catalyst redox couple, and  $k_{\text{obs}}$  the observed rate constant, with  $k_{\text{obs}} = \text{TOF}_{\text{max}}$ . Eq. A.5 can be normalized with the peak current of the one-electron reduction of the catalyst ( $i_p$ ) using the Randles-Sevcik equation (Eq. A.6), resulting in Eq. A.7.

$$i_p = 0.446nFSC_{\text{cat}}^0 \sqrt{\frac{Fv}{RT} D_{\text{cat}}} \quad (\text{A. 6})$$

$$\frac{i_c}{i_p} = \frac{2.24n \sqrt{\frac{RT}{Fv} k_{\text{obs}}}}{1 + \exp\left[\frac{F}{RT}(E - E_{1/2})\right]} \quad (\text{A. 7})$$

Where  $n$  is the number of electrons used in the catalytic cycle, which in this specific case is 2, considering only the partial reduction of O<sub>2</sub> to H<sub>2</sub>O<sub>2</sub> in the FOWA region. As a plateau current is not reached, the analysis can only be applied at the foot of the catalytic wave, where no side-phenomena take place. We also note that the half-wave potential of the catalytic wave  $E_{\text{cat}/2} > E_{1/2}$  due to substrate depletion near the electrode. As  $\exp[F/RT(E - E_{1/2})] \gg 1$  in this potential window, Eq. A.7 can be simplified to Eq. A.8. Using Eq. A.8,  $k_{\text{obs}}$  can be derived from the slope of  $i_c/i_p$  vs.  $\exp[-F/RT(E - E_{1/2})]$ .

$$\frac{i_c}{i_p} = 2.24n \sqrt{\frac{RT}{Fv} k_{\text{obs}}} \exp\left[-\frac{F}{RT}(E - E_{1/2})\right] \quad (\text{A. 8})$$

Mechanistic insight can be obtained from FOW analysis. In case of a first order relationship in catalyst, the catalytic current should be linear with  $1 + \exp[F/RT(E - E_{1/2})]$ , while for a homolytic second order reaction the catalytic current should be linear with  $(1 + \exp[F/RT(E - E_{1/2})])^{3/2}$ .<sup>[8]</sup> When the current-potential relationship for a binuclear homolytic reaction were applied, very poor linearity was observed. Thus, plots of  $i_c/i_p$  vs.  $\exp[F/RT(E - E_{1/2})]$  were fitted linearly between the onset of the ORR, here defined as  $i_c/i_{\text{redox}} \geq 2$ , and 0.38 V vs. RHE. Here,  $i_{\text{redox}}$  is the current of the catalyst measured at the applied potential, in the absence of O<sub>2</sub> (Figure A.17). Measurements were repeated five times and FOWA was performed on the individual measurements. Averaging of the results obtained for the individual experiments led to the TOFs as reported with the standard error.

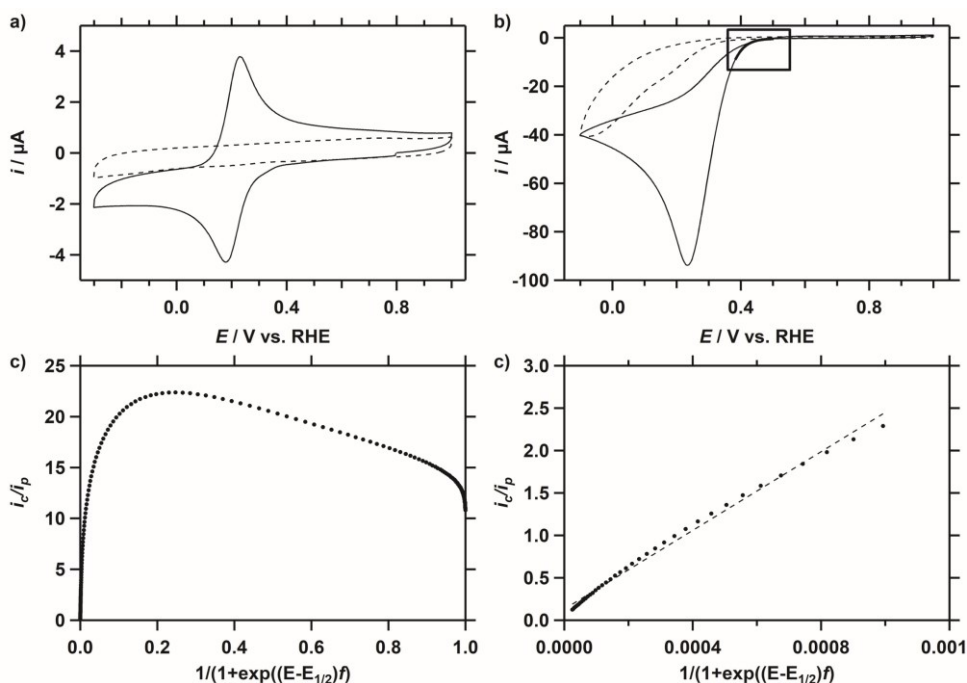


**Figure A.16.** **a)** CV of bare GC electrode (dotted line) and Cu-tmtpa under 1 atm Ar. **b)** CV of bare GC electrode (dotted line) and Cu-tmtpa under 1 atm (O<sub>2</sub>). **c)** FOW analysis of Cu-tmtpa, where  $f = F/RT$ . **d)** Fit of the linear region of the FOW analysis,  $R^2 = 0.99$ . Conditions: pH 7 phosphate buffer ([PO<sub>4</sub>] = 100 mM), [Cu-tmtpa] = 0.3 mM, 293 K, 100 mV s<sup>-1</sup> scan rate.

## A.10 References

- [1] H. Taube, *Chem. Rev.* **1952**, 50, 69-126.
- [2] D. T. Richens, *Chem. Rev.* **2005**, 105, 1961-2002.
- [3] B. van Dijk, J. P. Hofmann, D. G. H. Hetterscheid, *Phys. Chem. Chem. Phys.* **2018**, 20, 19625-19634.
- [4] R. Zhou, Y. Zheng, M. Jaroniec, S.-Z. Qiao, *ACS Catal.* **2016**, 6, 4720-4728.
- [5] S. B. Hall, E. A. Khudaish, A. L. Hart, *Electrochim. Acta* **1999**, 44, 4573-4582.



- [6] E. S. Rountree, B. D. McCarthy, T. T. Eisenhart, J. L. Dempsey, *Inorg. Chem.* **2014**, 53, 9983-10002.
- [7] M. Asahi, S.-i. Yamazaki, S. Itoh, T. Ioroi, *Electrochim. Acta* **2016**, 211, 193-198.
- [8] C. Costentin, J.-M. Savéant, *ChemElectroChem* **2014**, 1, 1226-1236.
- [9] C. Costentin, S. Drouet, M. Robert, J.-M. Savéant, *J. Am. Chem. Soc.* **2012**, 134, 11235-11242.

# Appendix B

## Supplementary Information for Chapter 2

### B.1 Catalyst concentration dependence studies

To determine the peak catalytic current  $i_{\text{cat}}$  at low Cu-tmpa concentrations, the GC working electrode was polished before every catalytic measurement using a Struers LaboPol-30 polishing machine, using 1.0  $\mu\text{m}$  diamond and 0.04  $\mu\text{m}$  silica suspension on polishing cloths (Dur-type) for 1 min each. This was followed by sonication for 10 to 15 minutes in Milli-Q purified water. A similar process was followed for the experiments in  $\text{D}_2\text{O}$ , as described in the Experimental section of Chapter 3. A blank CV was measured in a separate electrochemical cell by the GC electrode in an Ar saturated (1 atm) solution after every electrode polish to determine the quality of the polish and the size of the double layer. Fresh solutions containing Cu-tmpa and 1.1 mM  $\text{H}_2\text{O}_2$  were used for every incremental increase of catalyst concentration. The currents obtained from CV measurements in presence of Cu-tmpa were corrected using their corresponding blank measurement, giving the catalytic current without any contribution from the double layer of the GC electrode to the catalytic current of the HPOR by Cu-tmpa.

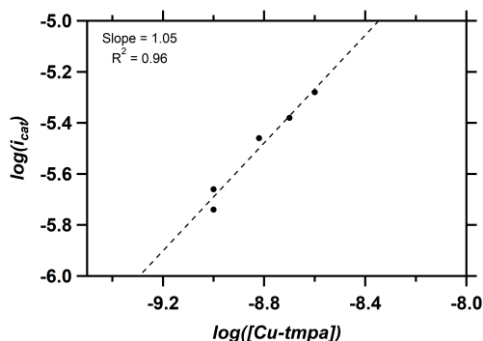


**Figure B.1.** Log-log plot of the  $i_{\text{cat}}$  (in A) vs. the Cu-tmpa concentration (in M) to determine the linearity of the dependence of the HPOR on Cu-tmpa, in the presence of 1.1 mM  $\text{H}_2\text{O}_2$ . The slope of the fit is 1.05 ( $R^2 = 0.96$ ).

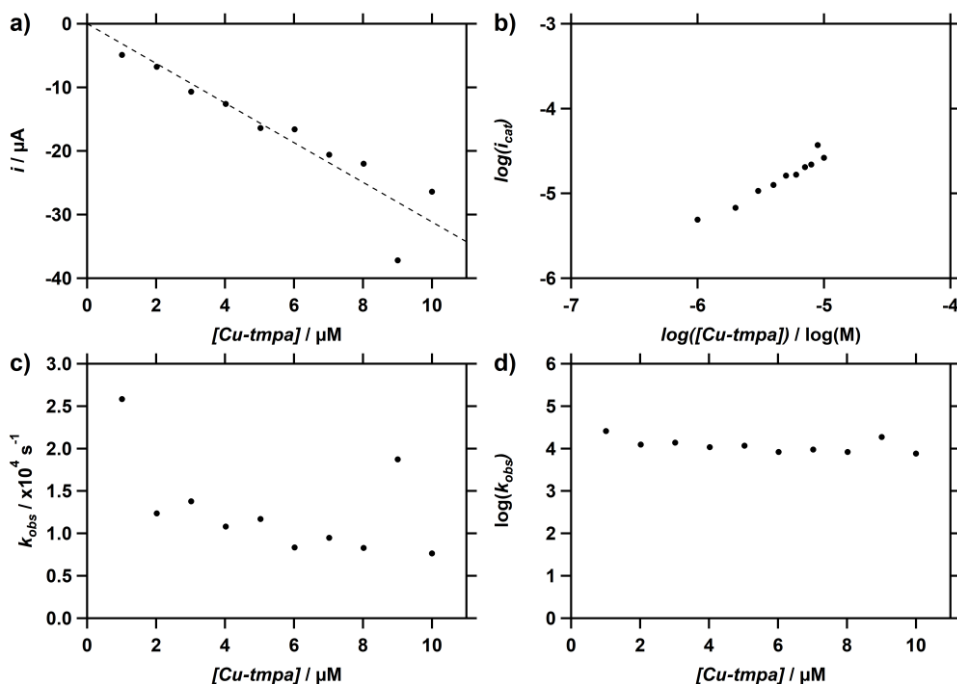


**Figure B.2.** **a)** Background corrected catalytic current  $i_{\text{cat}}$  as a function of Cu-tpma concentration with 10 mM  $\text{H}_2\text{O}_2$ . **b)** Log-log plot of the same data. **c)**  $k_{\text{obs}}$  of the reduction of  $\text{H}_2\text{O}_2$  as a function of Cu-tpma concentration with 10 mM  $\text{H}_2\text{O}_2$ . **d)**  $\log(k_{\text{obs}})$  as a function of catalyst concentration. Conditions: pH 7 PB ( $[\text{PO}_4] = 100 \text{ mM}$ ), 293 K,  $100 \text{ mV s}^{-1}$  scan rate.

## B.2 Catalytic oxidation at high $\text{H}_2\text{O}_2$ concentrations

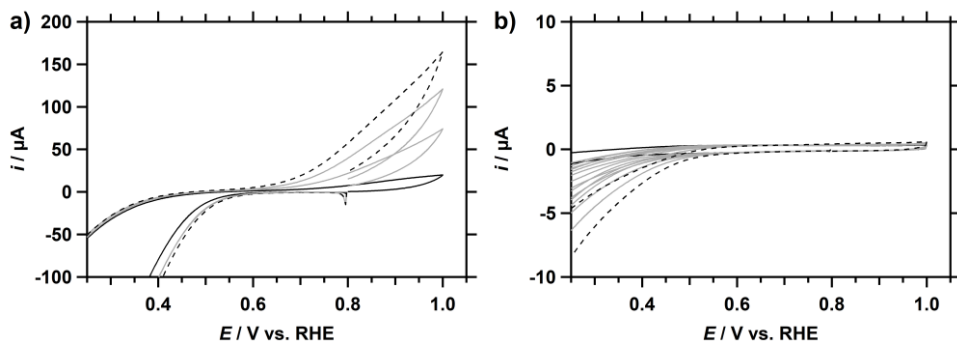


**Figure B.3.** **a)** Zoom of the observed oxidation during cyclic voltammetry measurements of the reduction of  $\text{H}_2\text{O}_2$  in the presence of 0.3 mM Cu-tpma for a range of  $\text{H}_2\text{O}_2$  concentrations; 40 (solid black)/60/80/100 (dashed) mM. **b)** CVs of a GC electrode in electrolyte solutions containing 1.5 (solid black) to 500 (dashed) mM  $\text{H}_2\text{O}_2$ . Conditions: pH 7 PB ( $[\text{PO}_4] = 100 \text{ mM}$ ), 293 K,  $100 \text{ mV s}^{-1}$  scan rate.

### B.3 FOWA of the HPRR in deuterated and non-deuterated solutions

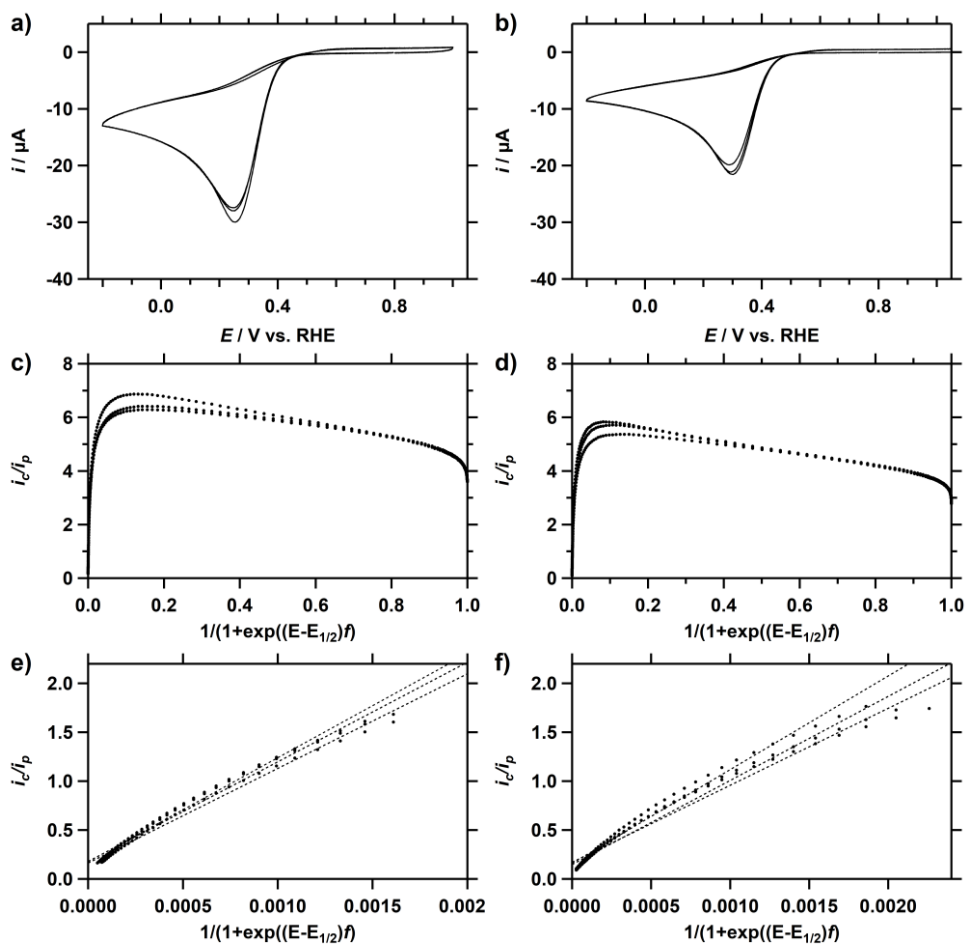


**Figure B.4.** Triplicate CVs of the reduction of 1.1 mM  $\text{H}_2\text{O}_2$  in the presence of 0.3 mM Cu-tmpa in non-deuterated (a) and deuterated (b) PB electrolyte solutions under 1 atm Ar. FOWA of the HPRR for non-deuterated (c) and deuterated (d) conditions, where  $f = F/RT$ . Corresponding fits of the linear regions of the FOWA for non-deuterated (e) and deuterated (f) conditions,  $R^2 \geq 0.98$ . Conditions: pH 7 PB ( $[\text{PO}_4] = 100$  mM), 293 K,  $100 \text{ mV s}^{-1}$  scan rate.

## B.4 Stability of Cu-tmpa in H<sub>2</sub>O<sub>2</sub>

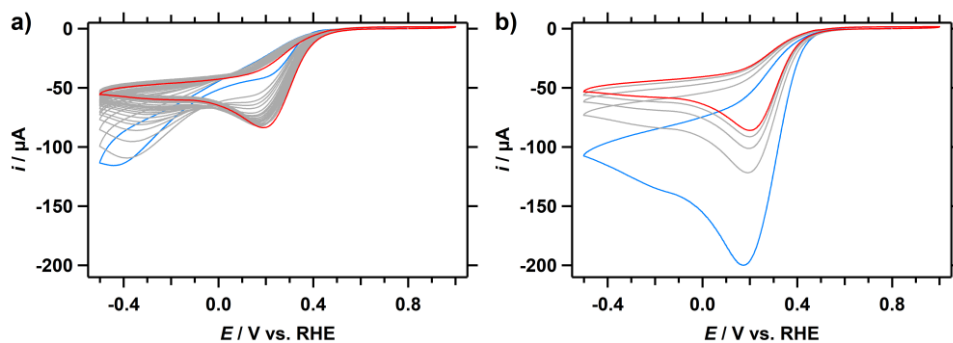


**Figure B.5.** **a)** CVs showing 25 consecutive scans of the catalytic reduction of H<sub>2</sub>O<sub>2</sub> (10 mM) by Cu-tmpa (8.0  $\mu\text{M}$ ) under 1 atm Ar. A clear increase in catalytic current is observed with each scan, from the first scan (blue) to the last scan (red). **b)** CVs of the same solution after mixing and saturating the solution for 1 min with 1 atm Ar, while keeping the electrode submerged in the solution. A large initial catalytic current is observed as the H<sub>2</sub>O<sub>2</sub> near the electrode has been replenished by mixing, indicating a deposition has formed on the electrode during the experiment shown in **(a)**. Conditions: pH 7 PB ([PO<sub>4</sub>] = 100 mM), 293 K, 100 mV s<sup>-1</sup> scan rate.

# Appendix C

## Supplementary Information for Chapter 4

### C.1 Scan rate dependence

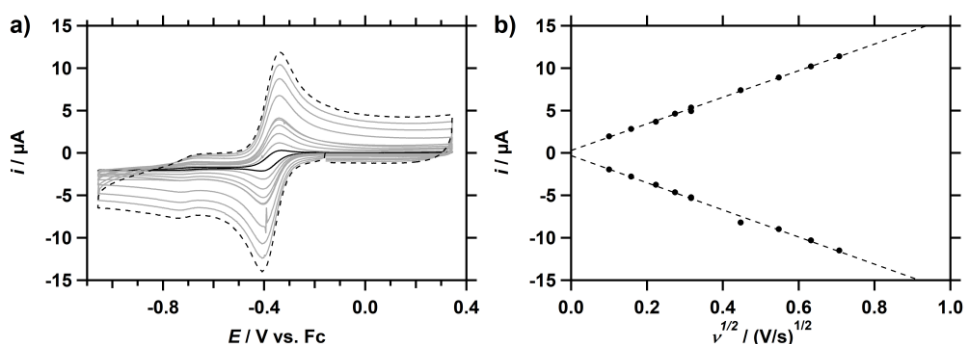


**Figure C.1.** a) CVs of Cu-tmpa (0.3 mM) in an electrolyte solution under argon at a range of different scan rates (10-500 mV s<sup>-1</sup>). b) The resulting Randles-Sevcik plot of  $i_{pc}$  and  $i_{pa}$ . Conditions: NBu<sub>4</sub>PF<sub>6</sub> (100 mM) in MeCN, 293 K.

The reported diffusion coefficients in Table C1 were determined using the Randles-Sevcik equation and are based on the peak reductive (cathodic) current  $i_{pc}$  as this corresponds the diffusion coefficient of Cu<sup>II</sup>-tmpa, the species that has to diffuse to the electrode. This distinction is especially important when the cathodic and anodic peak current show very different slopes as a function of scan rate. Due to the overlapping redox events, no diffusion coefficients were determined for Cu-tmpa in solutions containing HNEt<sub>3</sub><sup>+</sup> or HNEt<sub>3</sub><sup>+</sup>/NEt<sub>3</sub> mixtures (Figure C.2e/f).

**Table C.1.** Overview of diffusion coefficients of Cu-tmpa with different additives in the electrolyte

Conditions	$D_{red}$ (cm <sup>2</sup> s <sup>-1</sup> )
No Acid	$7.8 \times 10^{-6}$
HOAc	$4.4 \times 10^{-6}$
HOAc/OAc <sup>-</sup>	$11.5 \times 10^{-6}$

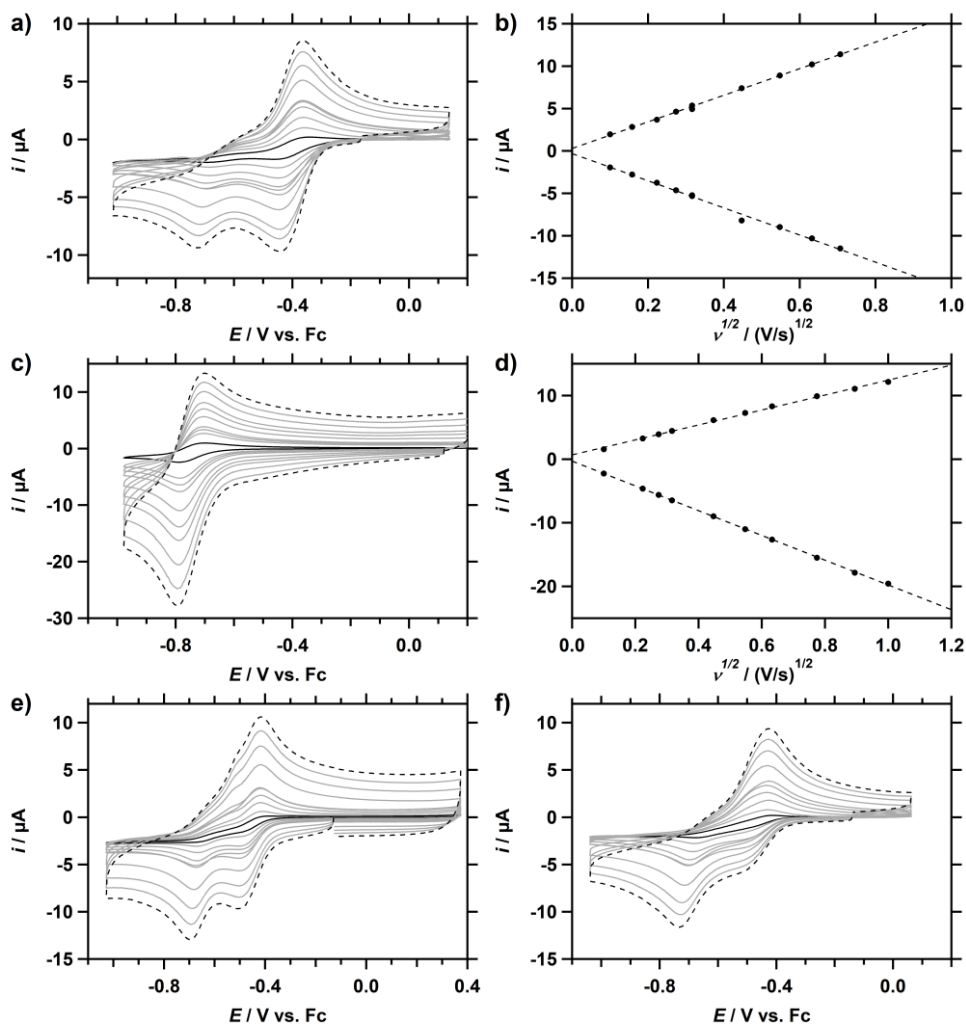


**Figure C.2.** CVs of Cu-tmpa (0.3 mM) in an electrolyte solution under argon containing different acid or acid-conjugate base mixtures. **a)** HOAc (100 mM) and **(b)** the corresponding Randles-Sevcik plot. **c)** HOAc/OAcNBu<sub>4</sub> (20 mM each) and **(d)** the corresponding Randles-Sevcik plot. **e)** HNET<sub>3</sub>PF<sub>6</sub> (60 mM). **f)** HNET<sub>3</sub>PF<sub>6</sub>/NET<sub>3</sub> (50 mM each). Conditions: NBu<sub>4</sub>PF<sub>6</sub> (100 mM) in MeCN, 293 K.

## C.2 DPV measurements

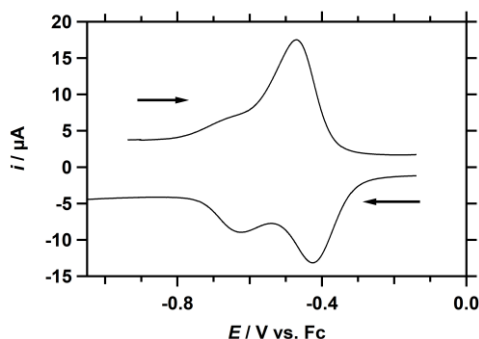


**Figure C.3.** Differential pulse voltammetry (DPV) measurements of Cu-tmpa (0.3 mM) in an electrolyte solution containing buffered HNet<sub>3</sub>PF<sub>6</sub>/Net<sub>3</sub> acid-conjugate base mixture (50 mM each) in the presence of 1 atm Ar. Conditions: NBu<sub>4</sub>PF<sub>6</sub> (100 mM) in MeCN, 293 K.

## C.3 Comparison of the ORR and HPRR in different conditions

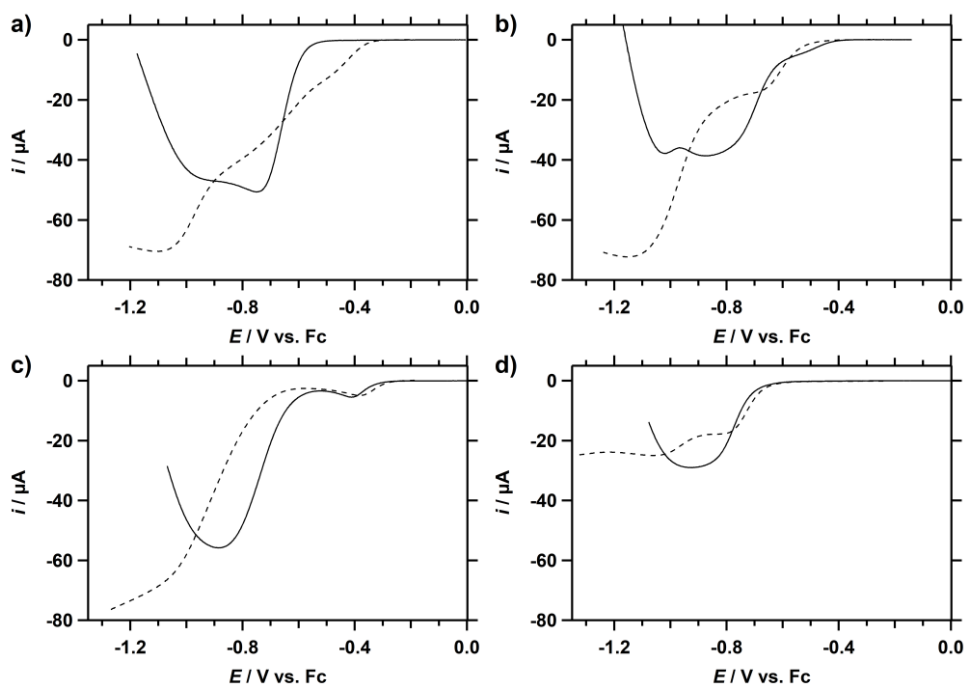


**Figure C.4.** Background-corrected LSVs of the ORR (solid line) and HPRR (dotted line), by Cu-tmpa in the presence of (a) 50 mM HNet<sub>3</sub>PF<sub>6</sub>, (b) 50 mM HNet<sub>3</sub>PF<sub>6</sub>/Net<sub>3</sub>, (c) 20 mM HOAc, and (d) 20 mM HOAc/OAc<sup>-</sup>. Conditions: NBu<sub>4</sub>PF<sub>6</sub> (100 mM) in MeCN, 100 mV s<sup>-1</sup>, 293 K.



## C.4 Acetic acid concentration dependence studies

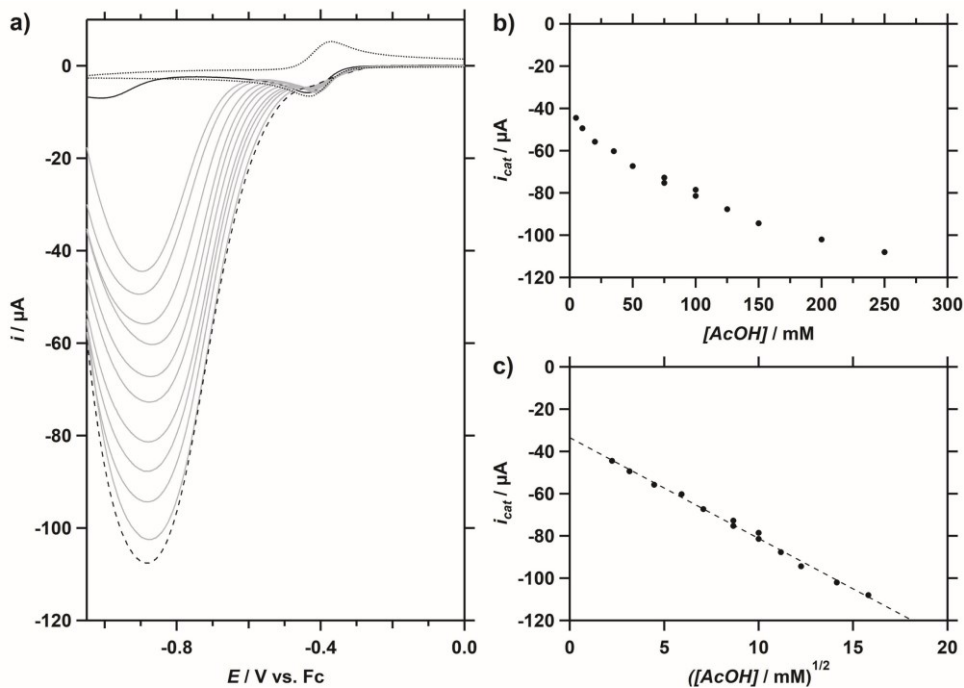


**Figure C.5.** **a)** Background-corrected LSV of the ORR by Cu-tpma (0.3 mM) in the presence of 0 (solid line) to 250 mM (dashed line) of HOAc, under 1 atm  $\text{O}_2$ . Redox couple under 1 atm Ar and 0 mM HOAc included as reference. **b)** The peak catalytic current  $i_{\text{cat}}$  plotted against  $[\text{HOAc}]$ . **c)** The peak catalytic current  $i_{\text{cat}}$  plotted against the square root of  $[\text{HOAc}]$ . Conditions:  $\text{NBu}_4\text{PF}_6$  (100 mM) in MeCN, 1 atm  $\text{O}_2$ , 100  $\text{mV s}^{-1}$ , 293 K.

The ORR catalysed by Cu-tpma in a  $\text{NBu}_4\text{PF}_6$  (100 mM in MeCN) electrolyte solution containing HOAc was further studied by extending the concentration range of HOAc. Cyclic voltammograms in solutions containing 0.3 mM Cu-tpma and 0 to 250 mM HOAc were measured with a glassy carbon electrode, freshly polished after each catalytic measurement. CVs were also measured in solutions using the same concentrations of acid without catalyst present to obtain the background current of the GC electrode towards the ORR. Background correction of the catalytic measurements resulted in the LSV shown in Figure C.5a. In Figure C.5b, the peak catalytic current  $i_{\text{cat}}$  is shown versus the HOAc concentration, where it is shown that it does not increase linearly with increasing acid concentration. Additionally, when a plot of the catalytic current against the square root of the concentration is constructed, a perfectly linear relationship ( $R^2 > 0.99$ ) is visible. Following Eq. 3.3,  $i_{\text{cat}}$  is a function of the square root of the observed rate constant  $k_{\text{obs}}$ , and as a linear relationship between  $i_{\text{cat}}$  and the square

root of the acid concentration is present,  $k_{\text{obs}}$  can be defined as shown in Eq. C.1, while Eq 3.3 can be rewritten as Eq. C.2.

$$k_{\text{obs}} = k[\text{AcOH}] \quad (\text{C. 1})$$

$$\frac{i_{\text{cat}}}{i_p} = 2.24n \sqrt{\frac{RT}{Fv}} k[\text{AcOH}] \quad (\text{C. 2})$$

However, as was discussed in section 4.2.6 of Chapter 4, the redox current decreases as a function of increasing HOAc concentration. This effect can not only be seen under non-catalytic conditions (Figure 4.7a, Chapter 4), but also in the presence of 1 atm  $\text{O}_2$ , as shown in a zoom of the catalytic LSV (Figure C.6a). When calculating the  $k_{\text{obs}}$  as described in section 4.2.8, Chapter 4, using the corresponding  $i_p$  at  $-0.41$  V for each different acid concentrations, a linear relationship between the TOF and acid concentration is observed. This type of linear dependency of the TOF on the acid concentration is indicative of a first-order in  $[\text{HOAc}]$ , when the catalytic rate shows a first order dependency on the catalyst concentration. As a first order relationship of the catalysis on the catalyst concentration was indeed observed (section 4.2.7), this confirms the above hypothesis and would result in  $r \approx k[\text{HOAc}][\text{Cu}]$  as the rate equation for the ORR.

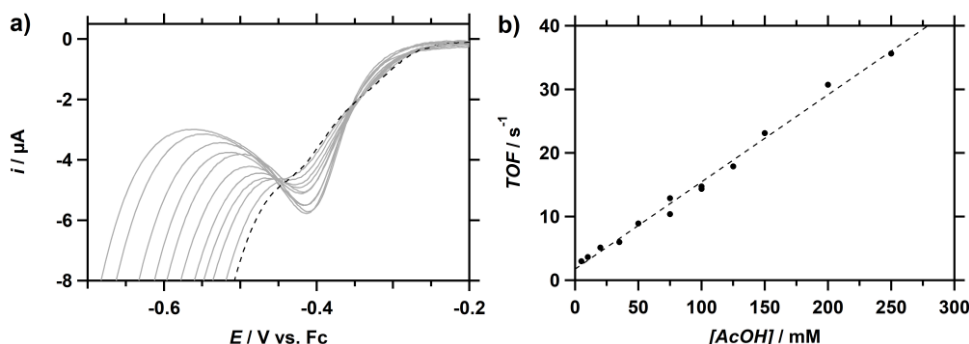


**Figure C.6.** a) Zoom of the background-corrected LSV of the ORR by Cu-tmpa in the presence of 1 atm  $\text{O}_2$  for different concentrations of HOAc, ranging from 5 mM (blue trace) to 100 mM (red trace). b) The resulting TOF ( $k_{\text{obs}}$ ) as a function of acid concentration. Conditions:  $\text{NBu}_4\text{PF}_6$  (100 mM) in MeCN, 100  $\text{mV s}^{-1}$ , 293 K.

## C.5 Shift of the Fc redox couple as a function of [HNEt<sub>3</sub>PF<sub>6</sub>]

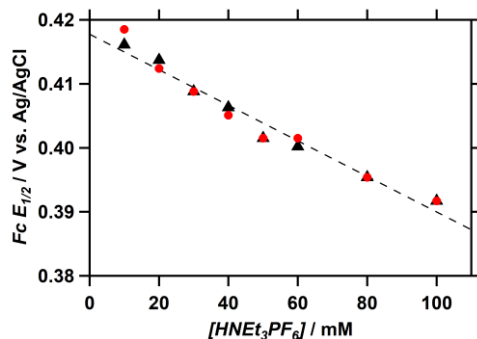


**Figure C.7.** Shift of the  $E_{1/2}$  of Fc as a function of HNEt<sub>3</sub><sup>+</sup> concentration, in the presence (red) and absence (black) of 0.3 mM Cu-tmpa. Conditions: NBu<sub>4</sub>PF<sub>6</sub> (100 mM) in MeCN, 100 mV s<sup>-1</sup>, 293 K.

## C.6 Stability of the Ag/AgNO<sub>3</sub> reference electrode over time

As AgNO<sub>3</sub> is photosensitive, the stability of the Ag/AgNO<sub>3</sub> electrode was monitored. When an Ag/AgNO<sub>3</sub> reference electrode was used during measurements and the Fc (0.6 mM) redox couple was measured as the reference, a shift of the  $E_{1/2}$  of the Fc redox couple was observed over the course of multiple experiments (Figure C.8). At the same time, a reduction in the solvent level in the outer junction and to a lesser degree the inner junction was observed. Both evaporation and leaking of the MeCN electrolyte through the diaphragm may have played a role. Repeated cleaning and refilling resulted in the same behaviour, highlighting the importance of measuring the Fc redox couple with every experiment. This issue was not observed with the reference electrode was used with Ag/AgCl, as the higher surface tension of H<sub>2</sub>O decreases evaporation and diffusion through the diaphragm of the electrode.

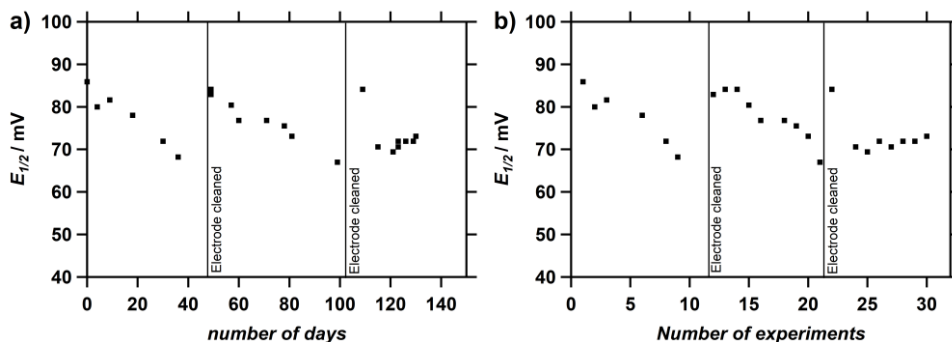


**Figure C.8.** The  $E_{1/2}$  of the redox couple of Fc<sup>+</sup>/Fc, measured with an Ag/AgNO<sub>3</sub> reference electrode. **a)** plotted against the time between experiments. **b)** plotted against the number of conducted experiments. Conditions: NBu<sub>4</sub>PF<sub>6</sub> (100 mM) in MeCN, 293 K.

## C.7 Determination of species distribution

In the case of a solution containing two different redox-active species, the current measured at a given potential is a linear combination of the redox current associated with the individual species at this given potential. Thus, the current at any given reduction or oxidation potential can be described by Eq. C.3 and Eq. C.4, where the fraction of species 1 is given by  $x_1 = [1]/[Cu]_{tot}$  and the fraction of species 2 is given by  $x_2 = [2]/[Cu]_{tot}$ . The potentials E1 and E2 were chosen at positions where the difference between the measured redox currents is greatest, as visualized in Figure C8a. If species 1 is not present in the solution, the reductive current at potential E1 ( $i_{red}^{E1}$ ) should be close to zero, while if species 2 is not present in the solution, the oxidative current at potential E2 ( $i_{ox}^{E2}$ ) should approach zero.

$$i_{red}^{E1} = x_1 \times i_{red,[1]}^{E1} + x_2 \times i_{red,[2]}^{E1} \quad (C.3)$$

$$i_{ox}^{E2} = x_1 \times i_{ox,[1]}^{E2} + x_2 \times i_{ox,[2]}^{E2} \quad (C.4)$$

Eq. C.3 can be rewritten as an expression of  $x_1$

$$x_1 = \frac{i_{red}^{E1} - x_2 \times i_{red,[2]}^{E1}}{i_{red,[1]}^{E1}} \quad (C.5)$$

Eq. C.5 can be inserted into equation C.4 and solved for  $x_2$ , while the same treatment can be done for  $x_1$ .

$$x_2 = \frac{i_{ox}^{E2} \times i_{red,[1]}^{E1} - i_{red}^{E1} \times i_{ox,[1]}^{E2}}{i_{red,[1]}^{E1} \times i_{ox,[2]}^{E2} - i_{ox,[1]}^{E2} \times i_{red,[2]}^{E1}} \quad (C.6)$$

$$x_1 = \frac{i_{ox}^{E2} \times i_{red,[2]}^{E1} - i_{red}^{E1} \times i_{ox,[2]}^{E2}}{i_{ox,[1]}^{E2} \times i_{red,[2]}^{E1} - i_{red,[1]}^{E1} \times i_{ox,[2]}^{E2}} \quad (C.7)$$

The total copper concentration in the solution  $[Cu]_{sol}$  at a given time can be calculated using  $x_1$  and  $x_2$  derived in the previous section.

$$[Cu]_{sol}(t) = x_1(t) \times [Cu]_{start} + x_2(t) \times [Cu]_{start} \quad (C.8)$$

Application of Eq. 8 resulted in Figure C.9b, where an increasing copper concentration is observed, which coincides with the observed solvent evaporation over the course of the experiment. Despite saturating the Ar flow with MeCN before passing it through the electrochemical cell, 1.2 mL out of 5 mL (24%) of the MeCN evaporated over the course of the 6-hour experiment, as confirmed after experiment completion. Normalizing the  $[Cu]_{sol}$  at every point in time to account for this evaporation of solvent is required to obtain the actual species distribution (Figure C9c). Alternatively, a linear rate of evaporation as a function of time between start and endpoint of the experiment

can be assumed, considering the constant flow rate of Ar and the constant surface area of the solution exposed to the Ar flow. Little deviation of the results from either method was observed.

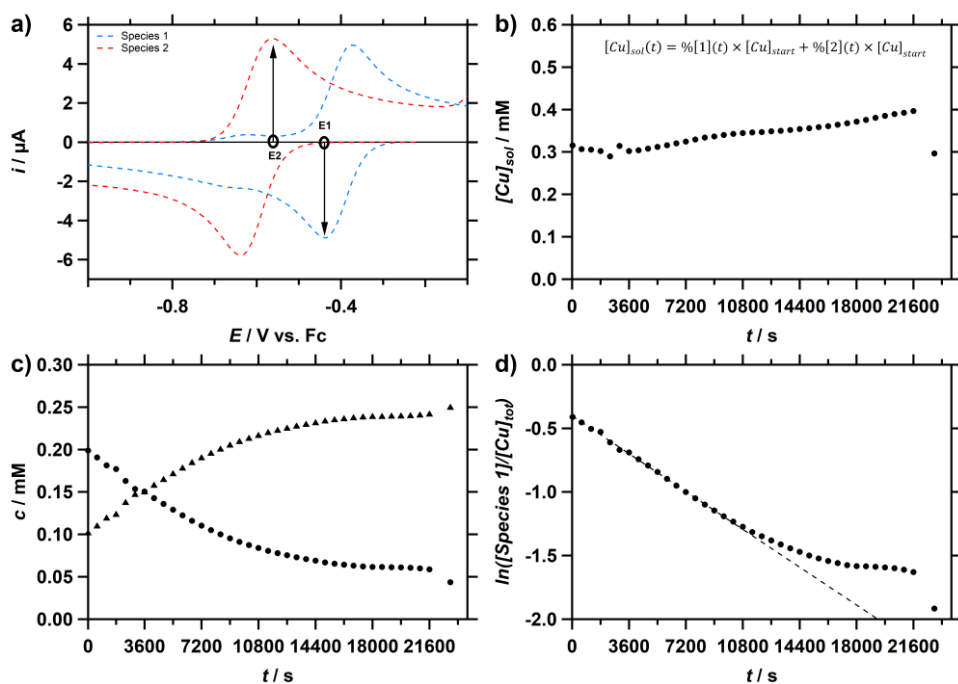


**Figure C.9.** a) CV of Cu-tmpa (0.3 mM) in the presence of 1 atm Ar and 100 mM HNEt<sub>3</sub>PF<sub>6</sub> (red trace) or no acid (blue trace) showing the positions of E1 and E2 for the determination of species distribution during the time-dependent conversion. b) Cu-tmpa concentration change as a function of time, showing the evaporation of MeCN during the experiment. c) Change in concentration of both species present in solution as a function of time. d) Plot of the natural logarithm of the initial species present in solution versus time. The reaction rate constant was determined from the slope of the linear fit. Conditions: NBu<sub>4</sub>PF<sub>6</sub> (100 mM) in MeCN, 100 mV s<sup>-1</sup>, 293 K.

## C.8 UV-vis time series measurements

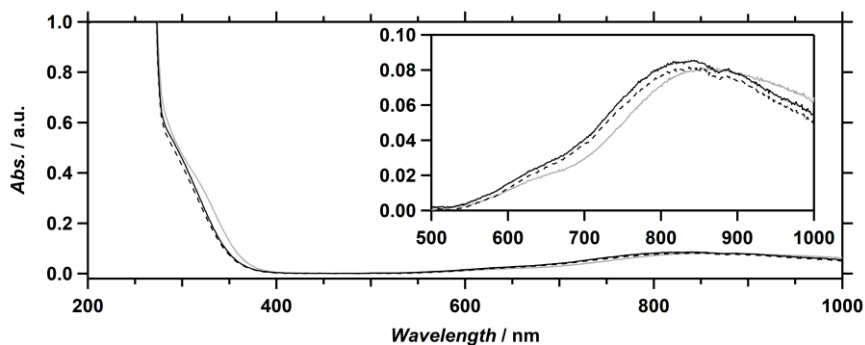


**Figure C.10.** UV-vis absorption spectra of an electrolyte solution containing 0.30 mM Cu-tmpa, 0.10 M NBu<sub>4</sub>PF<sub>6</sub> in MeCN, without acid (grey trace) or with 50 mM HNEt<sub>3</sub>PF<sub>6</sub> (dashed trace). The solid black trace was measured 360 min after addition of the acid. Insert: zoom of the d-d transition band.

## C.9 Absorption spectra and stability of Cu-tmpa in electrolyte solutions

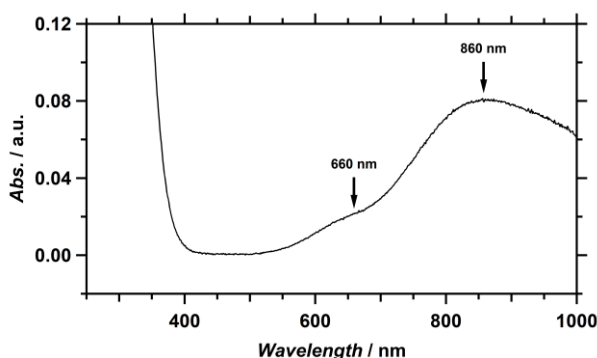


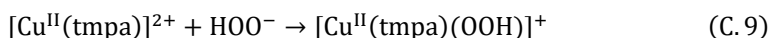
**Figure C.11.** UV-vis absorption spectrum of an electrolyte solution containing 0.30 mM [Cu<sup>II</sup>(tmpa)(CH<sub>3</sub>CN)]<sup>2+</sup> and 0.10 M NBu<sub>4</sub>PF<sub>6</sub> in MeCN at 293 K.

The UV-vis absorption spectrum of [Cu<sup>II</sup>(tmpa)(CH<sub>3</sub>CN)]<sup>2+</sup> in MeCN, in the presence of 100 mM NBu<sub>4</sub>PF<sub>6</sub> (Figure C.11) shows the characteristic absorption bands at 860 ( $\epsilon = 260 \text{ M}^{-1} \text{ cm}^{-1}$ ) and 660 nm in the d-d transition region, in good agreement with previously reported UV-vis spectra (in MeCN at RT).<sup>[1-2]</sup> This confirms that Cu-tmpa is present as a monomeric species in the resting state under these conditions.

To further study the stability of [Cu<sup>II</sup>(tmpa)(CH<sub>3</sub>CN)]<sup>2+</sup> and the possibility of adduct formation in the electrolyte solution used in this work, UV-vis absorption spectra were measured (Figure C.12). For each solution containing 0.30 mM Cu-tmpa, a CV was measured 30 seconds and 22 hours after addition of either the acid, acid-conjugate base mixture, or after addition of 8.1 mM H<sub>2</sub>O<sub>2</sub>. No change in the UV-vis spectra is

observed in the presence of HOAc or HNEt<sub>3</sub><sup>+</sup>, neither upon addition of H<sub>2</sub>O<sub>2</sub> to solutions containing these acids. In the presence of the acid-conjugate HNEt<sub>3</sub><sup>+</sup>/NEt<sub>3</sub> mixture, a slight blue-shift of the main d–d absorption by 25 nm is observed. In the presence of HOAc/OAc<sup>−</sup> a clear change is observed in the UV-vis absorbance, especially in the lower wavelengths. A new sharp absorption band at 299 nm appears, while at the same time the bands in the d–d region shift from 860 to 920 nm and from 660 to 720 nm. Additionally, an increase in absorbance is observed for the higher energy d–d band. Combined with the large change in redox potential (see main text),<sup>[3]</sup> this points to the formation of [Cu<sup>II</sup>(tmpa)(OAc)]<sup>+</sup>, with the 299 nm being the result of the AcO<sup>−</sup> → Cu ligand-to-metal charge transfer (LMCT) transition.

When H<sub>2</sub>O<sub>2</sub> is added to a solution containing HOAc/OAc<sup>−</sup>, an absorption band appears at 405 nm after 22 hours, while the d–d energy transitions are simultaneously decreased, indicating a loss of complex. Cu<sup>II</sup> complexes, including [Cu<sup>II</sup>(tmpa)]<sup>2+</sup>, are known to react with H<sub>2</sub>O<sub>2</sub> in the presence of a base, resulting in the formation of a [Cu<sup>II</sup>-OOH]<sup>+</sup> species (Equation C.9).<sup>[4-8]</sup> However, for Cu-tmpa and many other Cu pyridylalkylamine complexes, it has also been shown that these hydroperoxo species are often not stable over longer time periods.<sup>[6, 9]</sup> The appearance of the 405 nm band points to the formation of the hydroperoxo species, as the LMCT band of [Cu<sup>II</sup>(tmpa)(OOH)]<sup>+</sup> has been reported at 379 nm or 410 nm (in acetone),<sup>[3]</sup> and at 379 nm (in MeCN).<sup>[4]</sup>



When H<sub>2</sub>O<sub>2</sub> is added to a solution containing HNEt<sub>3</sub><sup>+</sup>/NEt<sub>3</sub>, the lowest energy d–d transition is blue-shifted by 55 nm to 805 nm. Additionally, a small band appears at 400 nm and a larger absorption peak appears at 305 nm. The resulting solution has a green colour, instead of the blue colour associated with [Cu<sup>II</sup>(tmpa)(CH<sub>3</sub>CN)]<sup>2+</sup>. After 22 hours, the band around 400 nm has increased significantly, although hard to separate from the much larger peak at 300/305 nm. This again coincides with the decrease of absorption in the d–d band region, resulting in significant bleaching of the solution. The shoulder around 400 nm should be indicative of formation of [Cu<sup>II</sup>(tmpa)(OOH)]<sup>+</sup>. It is unlikely that the large peak at 300 nm is the hydroperoxo species, as this would be at least 80 nm blue-shifted compared to the lowest reported values. Neither does it correspond to the most likely decomposition product of the ligand, pyridine-2-carbaldehyde, which does not absorb above ~250 nm.<sup>[10]</sup>

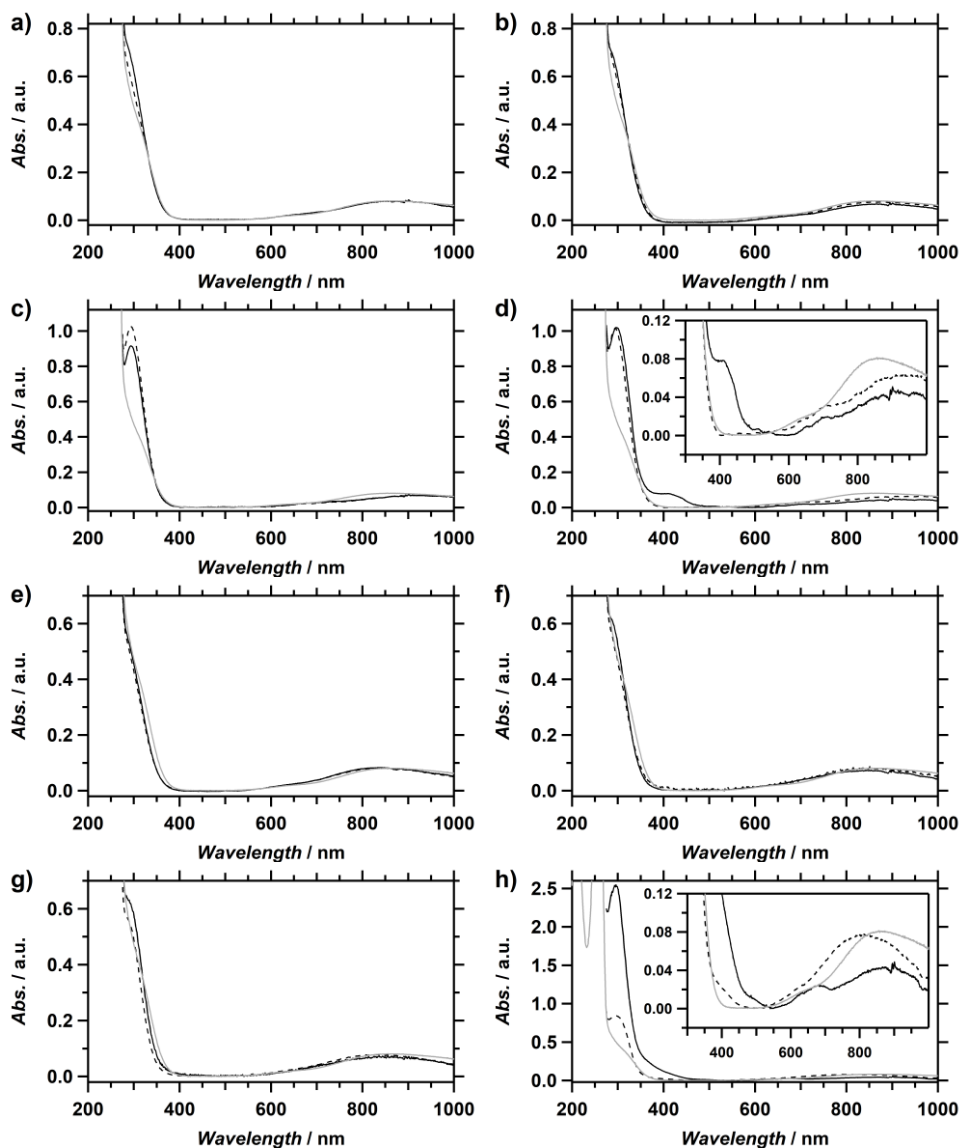


**Figure C.12.** UV-vis spectra of an electrolyte solution containing 0.30 mM Cu-tmpa and 0.10 M NBu<sub>4</sub>PF<sub>6</sub> in MeCN under ambient atmosphere at room temperature (293 K), with several different acid or acid-conjugate base compositions. **a)** 100 mM HOAc, **b)** + 8.1 mM H<sub>2</sub>O<sub>2</sub>. **c)** 20 mM HOAc/OAcNBu<sub>4</sub>, **d)** + 8.1 mM H<sub>2</sub>O<sub>2</sub>. **e)** 50 mM HNEt<sub>3</sub>PF<sub>6</sub>, **f)** + 8.1 mM H<sub>2</sub>O<sub>2</sub>. **g)** 50 mM HNEt<sub>3</sub>PF<sub>6</sub>/NET<sub>3</sub>, **h)** + 8.1 mM H<sub>2</sub>O<sub>2</sub>. Time after addition of Cu-tmpa to the electrolyte solution: 30 seconds (dashed line) or 22 hours (solid black line). Gray trace is the UV-vis absorbance in the absence of any acid or acid-conjugate base mixture, containing only the complex and supporting electrolyte. All UV-vis spectra were corrected for blank measurements of identical solutions in the absence of Cu-tmpa.



## C.10 References

- [1] M. Yamada, K. D. Karlin, S. Fukuzumi, *Chemical Science* **2016**, 7, 2856-2863.
- [2] J. Wang, M. P. Schopfer, S. C. Pui, A. A. N. Sarjeant, K. D. Karlin, *Inorg. Chem.* **2010**, 49, 1404-1419.
- [3] S. Kakuda, R. L. Peterson, K. Ohkubo, K. D. Karlin, S. Fukuzumi, *J. Am. Chem. Soc.* **2013**, 135, 6513-6522.
- [4] A. Wada, M. Harata, K. Hasegawa, K. Jitsukawa, H. Masuda, M. Mukai, T. Kitagawa, H. Einaga, *Angew. Chem. Int. Ed.* **1998**, 37, 798-799.
- [5] T. Fujii, A. Naito, S. Yamaguchi, A. Wada, Y. Funahashi, K. Jitsukawa, S. Nagatomo, T. Kitagawa, H. Masuda, *Chem. Commun.* **2003**, 2700-2701.
- [6] S. Yamaguchi, H. Masuda, *Science and Technology of Advanced Materials* **2005**, 6, 34-47.
- [7] S. Kim, J. W. Ginsbach, J. Y. Lee, R. L. Peterson, J. J. Liu, M. A. Siegler, A. A. Sarjeant, E. I. Solomon, K. D. Karlin, *J. Am. Chem. Soc.* **2015**, 137, 2867-2874.
- [8] A. Kunishita, J. D. Scanlon, H. Ishimaru, K. Honda, T. Ogura, M. Suzuki, C. J. Cramer, S. Itoh, *Inorg. Chem.* **2008**, 47, 8222-8232.
- [9] Y. Syuhei, W. Akira, N. Shigenori, K. Teizo, J. Koichiro, M. Hideki, *Chem. Lett.* **2004**, 33, 1556-1557.
- [10] E. P. Crowell, W. A. Powell, C. J. Varsel, *Anal. Chem.* **1963**, 35, 184-189.

# Appendix D

## Supplementary Information for Chapter 5

### D.1 UV-vis spectra of Cu-fubmpa

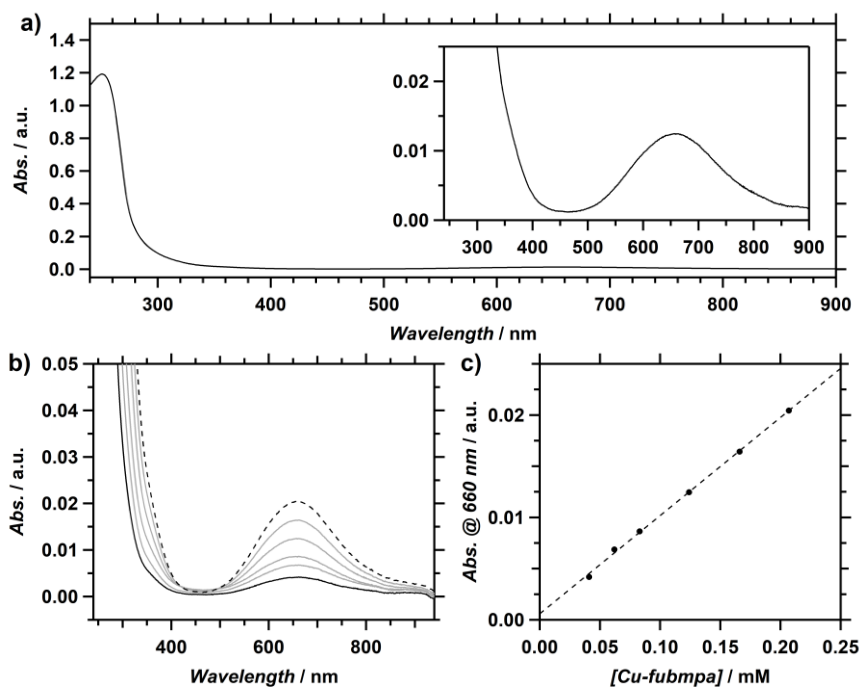


**Figure D.1.** **a)** UV-vis spectrum of 0.12 mM Cu-fubmpa in water (MilliQ). The inset shows the Cu<sup>II</sup> d-d transition. **b)** UV-vis spectra of 0.04 (solid black) to 0.2 (dashed) mM Cu-fubmpa in water (MilliQ). **c)** The linear relationship between catalyst concentration and the peak absorbance at 660 nm. Conditions: 293 K, 10 mm path length.

## D.2 Crystallography data of Cu-fubmpa

Crystal data	
Chemical formula	C <sub>19</sub> H <sub>19</sub> CuF <sub>6</sub> N <sub>3</sub> O <sub>8</sub> S <sub>2</sub> ·H <sub>2</sub> O
$M_r$	677.05
Crystal system, space group	Monoclinic, $P2_1/c$
Temperature (K)	110
$a, b, c$ (Å)	16.0028 (5), 9.8723 (3), 16.8915 (5)
$\beta$ (°)	100.870 (3)
$V$ (Å <sup>3</sup> )	2620.71 (14)
$Z$	4
Radiation type	Mo $K\alpha$
$\mu$ (mm <sup>-1</sup> )	1.09
Crystal size (mm)	0.42 × 0.13 × 0.04

Data collection	
Diffractometer	SuperNova, Dual, Cu at zero, Atlas
Absorption correction	Gaussian <i>CrysAlis PRO</i> 1.171.39.29c (Rigaku Oxford Diffraction, 2017) Numerical absorption correction based on gaussian integration over a multifaceted crystal model. Empirical absorption correction using spherical harmonics, implemented in SCALE3 ABSPACK scaling algorithm.
$T_{\min}, T_{\max}$	0.463, 1.000
No. of measured, independent and observed [ $I > 2\sigma(I)$ ] reflections	18658, 6012, 4878
$R_{\text{int}}$	0.032
$(\sin \theta/\lambda)_{\max}$ (Å <sup>-1</sup> )	0.650

Refinement	
$R[F^2 > 2\sigma(F^2)], wR(F^2), S$	0.035, 0.082, 1.04
No. of reflections	6012
No. of parameters	483
No. of restraints	501
H-atom treatment	H atoms treated by a mixture of independent and constrained refinement
$\Delta\rho_{\max}, \Delta\rho_{\min}$ (e Å <sup>-3</sup> )	0.42, -0.37

## D.3 Selected bond distances and angles for Cu-fubmpa

**Table D.1.** Selected bond distances and bond angles of the crystal structure of Cu-fubmpa

Bond	Distance (Å)	Bond sequence	Angle (Å)	Bond sequence	Angle (Å)
Cu1–N1	1.975(2)	N1–Cu1–N2	83.65(7)	N2–Cu1–O1W	168.08(7)
Cu1–N2	2.037(2)	N1–Cu1–N3	166.31(8)	N3–Cu1–O2	90.89(7)
Cu1–N3	1.962(2)	N1–Cu1–O1W	98.01(8)	N3–Cu1–O1W	93.61(8)
Cu1–O1W	1.973(2)	N1–Cu1–O2	96.87(7)	O2–Cu1–O1W	87.14(7)
Cu1–O2	2.375(1)	N2–Cu1–N3	83.50(7)		
Cu1–O5	2.665(2)	N2–Cu1–O2	104.43(6)		

## D.4 Diffusion Coefficients

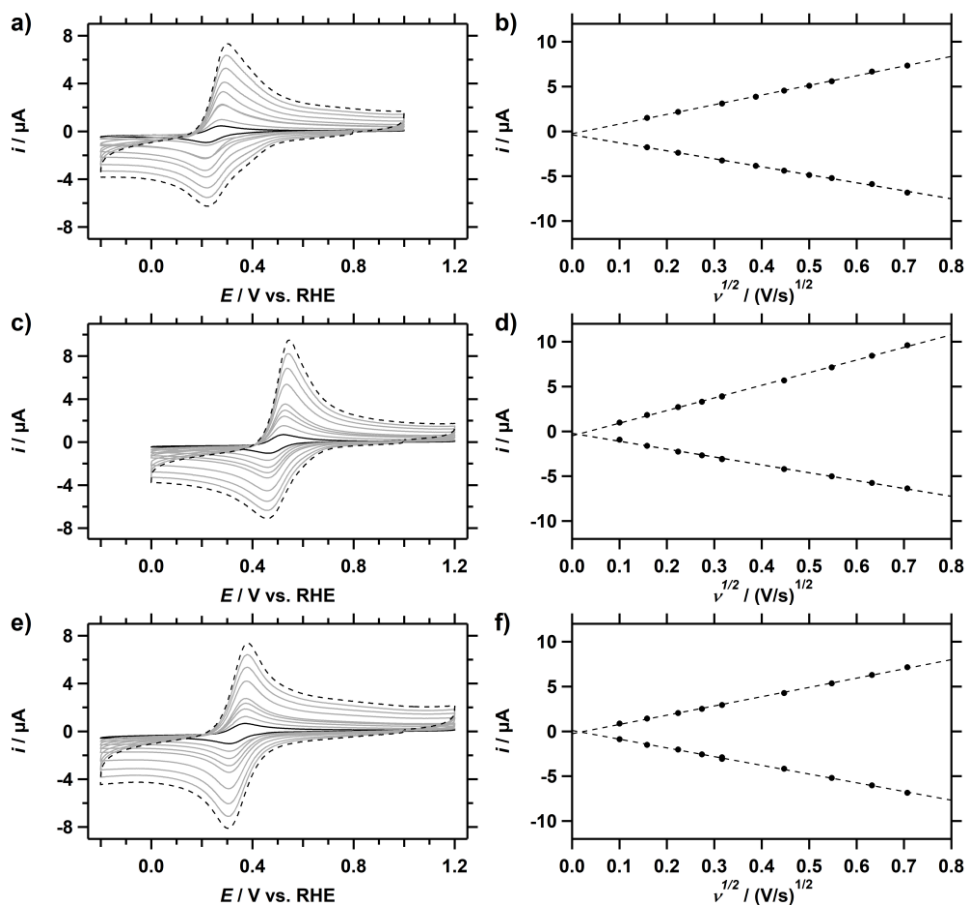


**Figure D.2.** CVs of Cu-fubmpa (a), Cu-bpmpa (b), and Cu-pmea (c) over a range of scan rates from 10 mV s<sup>-1</sup> (solid black) to 500 mV s<sup>-1</sup> (dashed). A concentration of 0.3 mM was used for each catalyst. Conditions: pH 7 PB ([PO<sub>4</sub>] = 100 mM), 293 K, 0.0707 cm<sup>2</sup> electrode surface area.

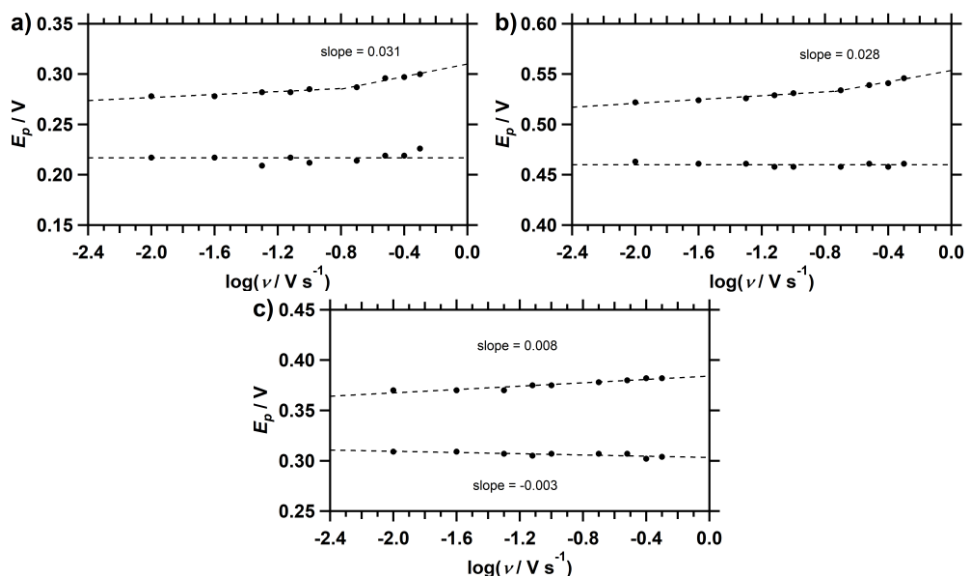


**Figure D.3.** Laviron plots showing the peak potentials as a function of the logarithm of the scan rate for Cu-fubmpa (a), Cu-bpmpa (b), and Cu-pmea (c). A concentration of 0.3 mM was used for each catalyst

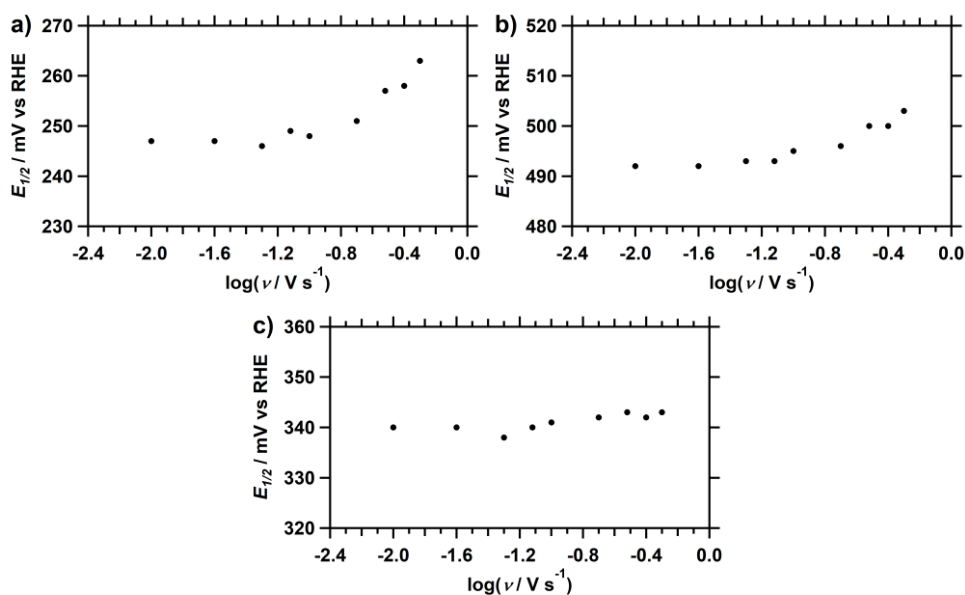


**Figure D.4.** Plot of redox half-wave potential as a function of scan rate for Cu-fubmpa (a), Cu-bpmpa (b), and Cu-pmea (c).

## D.5 Comparison of onset ORR and HPRR.

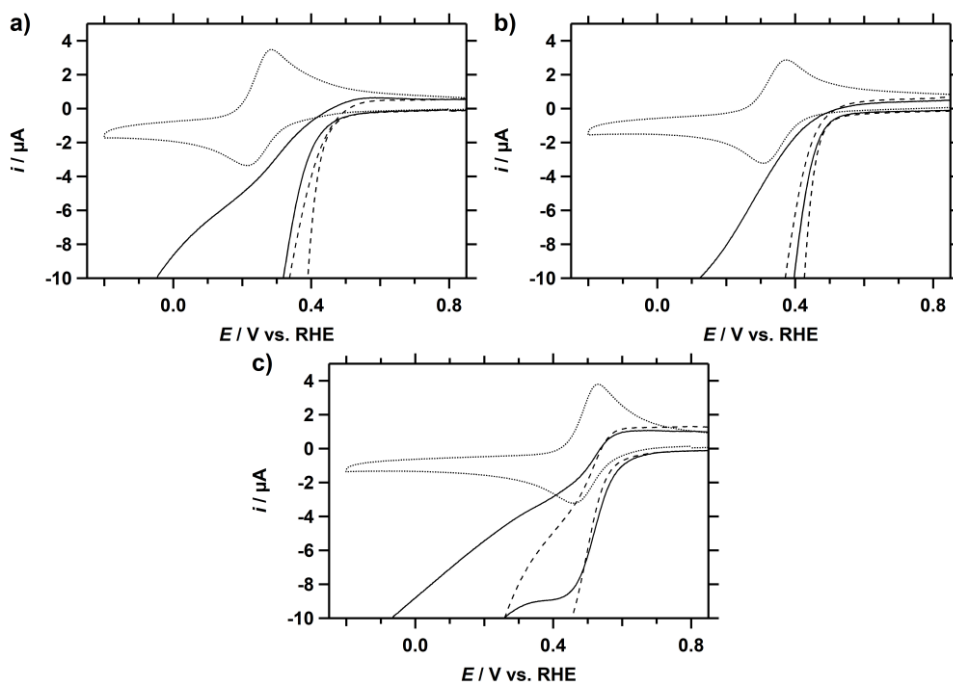


**Figure D.5.** CVs of Cu-fubmpa (a), Cu-pmea (b), and Cu-bpmpa (c) in a PB pH 7 electrolyte solution under 1 atm Ar (dotted line), 1 atm O<sub>2</sub> (dashed line), or with 1.1 mM H<sub>2</sub>O<sub>2</sub> under 1 atm Ar (solid line). For each catalyst, a concentration of 0.3 mM was used. Conditions: pH 7 PB ([PO<sub>4</sub>] = 100 mM), 293 K, 100 mV s<sup>-1</sup> scan rate, 0.0707 cm<sup>2</sup> electrode surface area.

## D.6 Background corrected LSV of the ORR

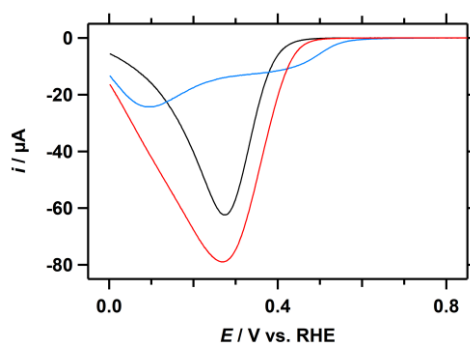


**Figure D.6.** LSV of Cu-fubmpa (black), Cu-pmea (red), and Cu-bpmpa (blue), under 1 atm O<sub>2</sub>. A catalyst concentration of 0.3 mM was used for each complex. Conditions: pH 7 PB ([PO<sub>4</sub>] = 100 mM), 293 K, 100 mV s<sup>-1</sup> scan rate, 0.0707 cm<sup>2</sup> electrode surface area.

## D.7 Catalytic ORR activity at low catalyst concentrations

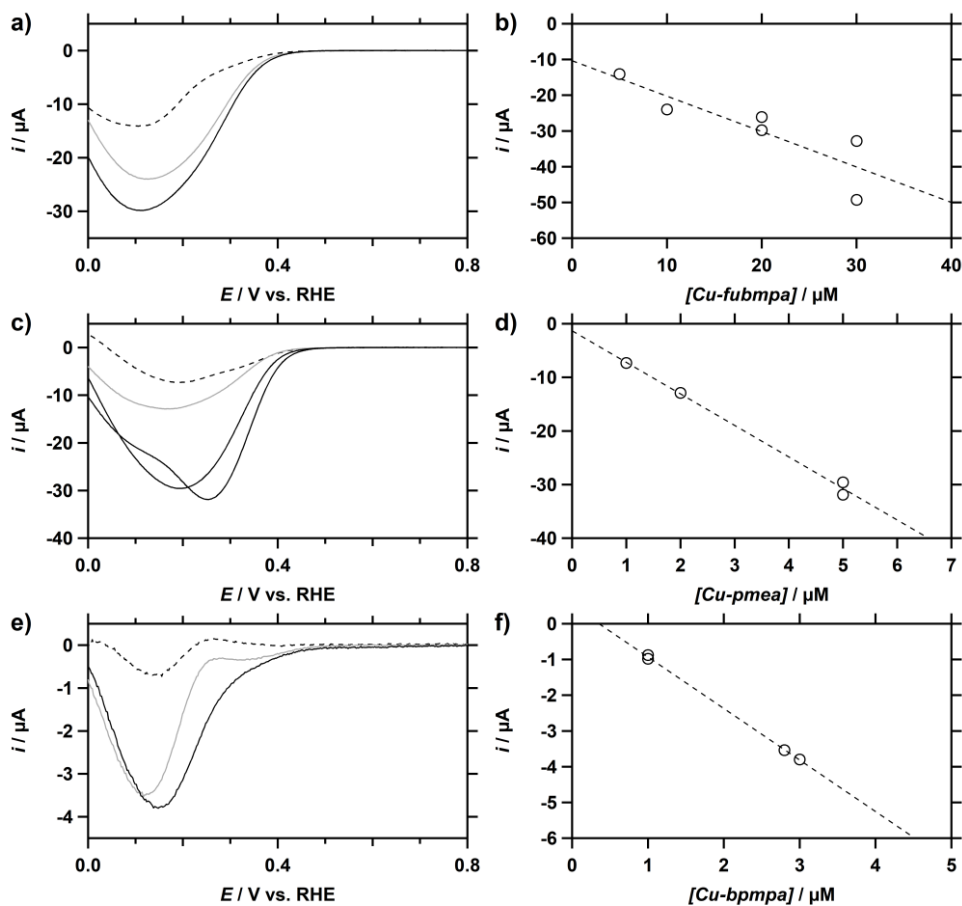


**Figure D.7.** Background-corrected LSV of-fubmpa (**a**), Cu-pmea (**c**), and Cu-bpmpa (**e**) at different catalyst concentrations in the presence of 1 atm  $\text{O}_2$ . On the right, the corresponding peak catalytic current obtained from the LSV of Cu-fubmpa (**b**), Cu-pmea (**d**), and Cu-bpmpa (**f**) as a function of catalyst concentration. Conditions: pH 7 PB ( $[\text{PO}_4] = 100 \text{ mM}$ ), 293 K,  $100 \text{ mV s}^{-1}$  scan rate,  $0.0707 \text{ cm}^2$  electrode surface area.

## D.8 DPV of Cu-pmea in the presence of dioxygen

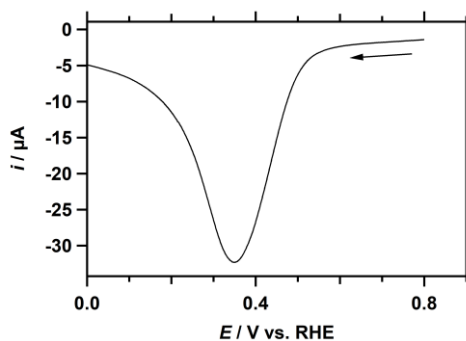


**Figure D.8.** DPV of Cu-pmea (0.3 mM) in the presence of 1 atm. O<sub>2</sub>. Conditions: pH 7 PB ([PO<sub>4</sub>] = 100 mM), 293 K, 100 mV s<sup>-1</sup> scan rate, 0.0707 cm<sup>2</sup> electrode surface area.

## D.9 NMR spectra

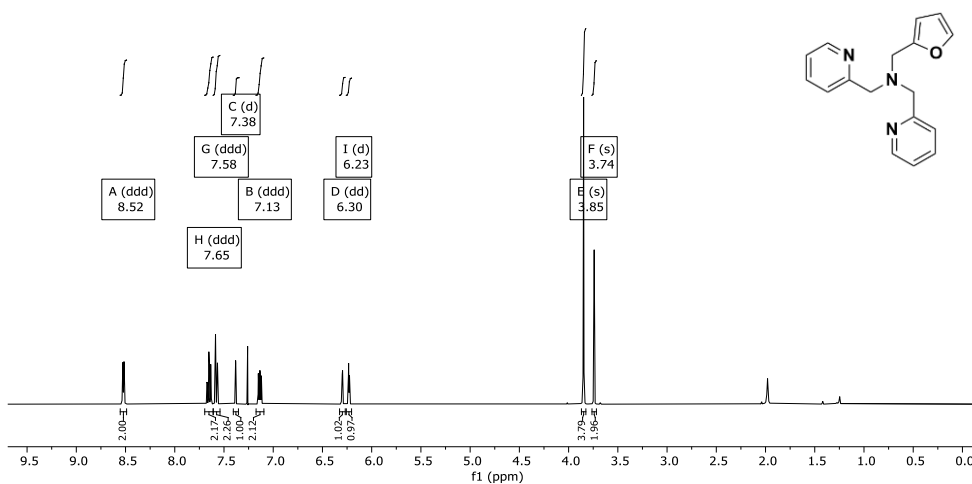


**Figure D.9.** <sup>1</sup>H NMR spectrum of *N*-(Furan-2-ylmethyl)-*N*-[bis(2-pyridyl)methyl]amine (fubmpa) in CDCl<sub>3</sub>.



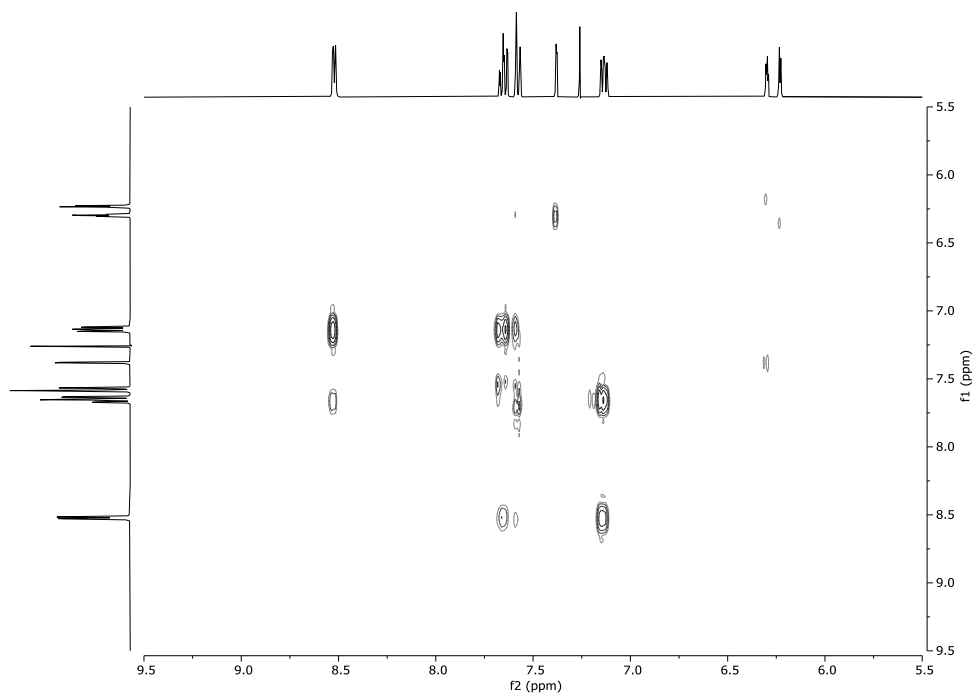


**Figure D.10.**  $^1\text{H}$ - $^1\text{H}$  COSY NMR spectrum of *N*-(Furan-2-ylmethyl)-*N*-[bis(2-pyridyl)methyl]amine (fubmpa) in  $\text{CDCl}_3$ .

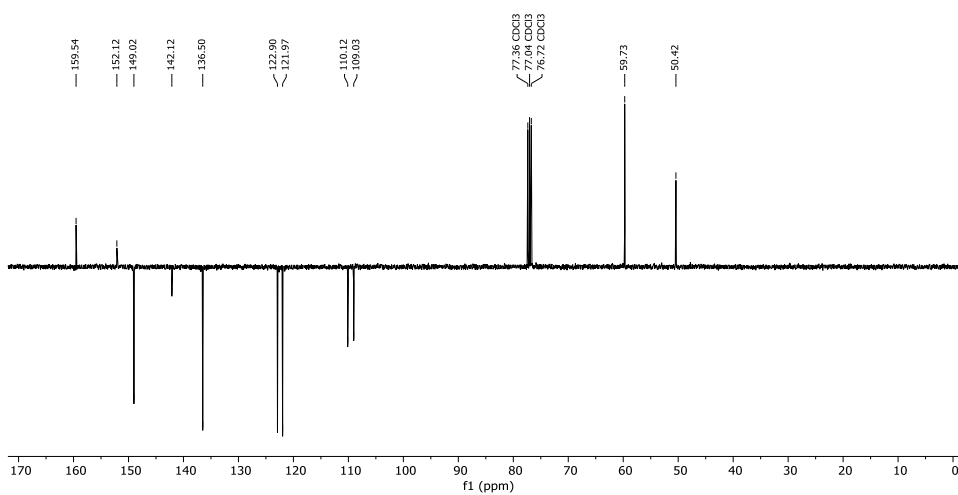


**Figure D.11.**  $^{13}\text{C}$  NMR spectrum of *N*-(Furan-2-ylmethyl)-*N*-[bis(2-pyridyl)methyl]amine (fubmpa) in  $\text{CDCl}_3$ .

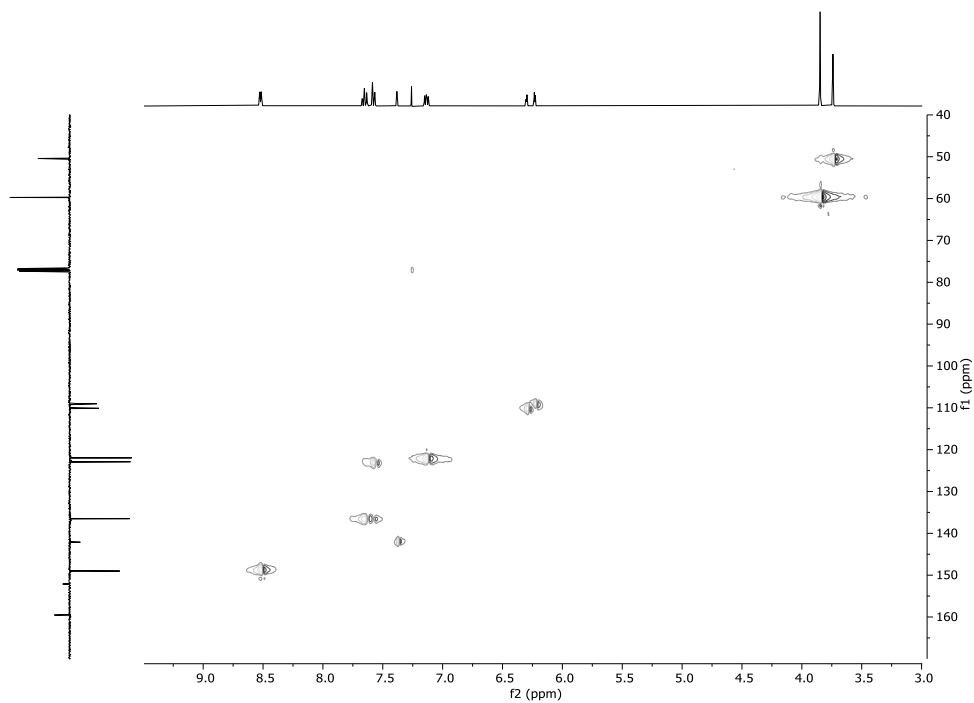


**Figure D.12.** 2D HSQC spectrum of *N*-(Furan-2-ylmethyl)-*N*-[bis(2-pyridyl)methyl]amine (fubmpa) in  $\text{CDCl}_3$ .

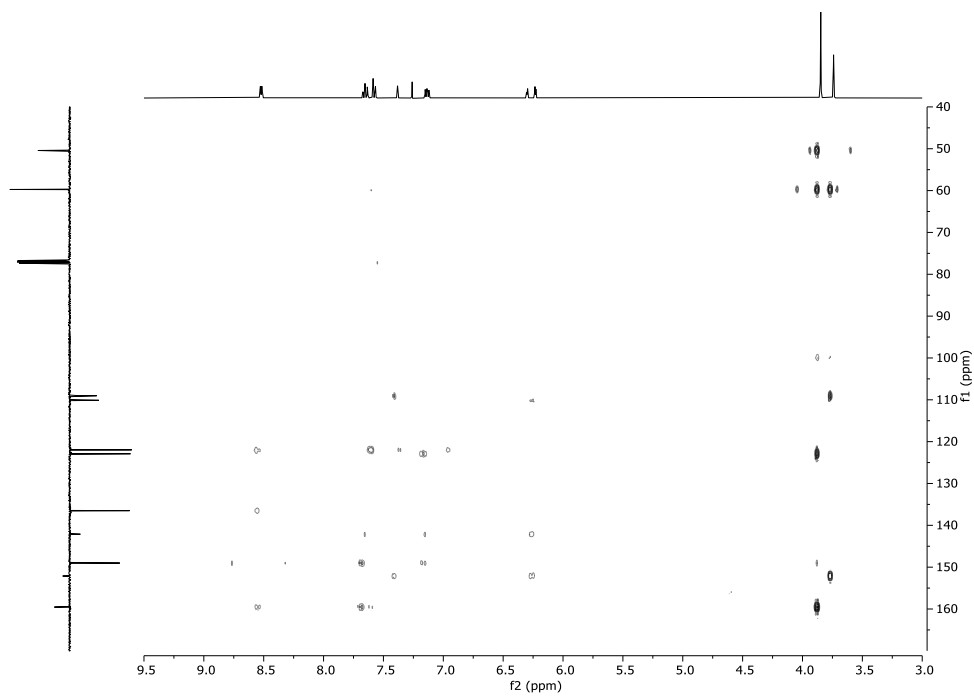


**Figure D.11.** 2D HMBC spectrum of *N*-(Furan-2-ylmethyl)-*N*-[bis(2-pyridyl)methyl]amine (fubmpa) in CDCl<sub>3</sub>.

# **Samenvatting en Toekomstperspectieven**

---

De elektrochemische reductie van zuurstof en  
waterstofperoxide door moleculaire  
koperkatalysatoren

## Samenvatting

De overgang van fossiele brandstoffen naar duurzame energiebronnen is een van de meest dringende uitdagingen van deze eeuw. Er spelen verschillende factoren een belangrijke rol bij het verminderen van onze CO<sub>2</sub>-voetafdruk en tegelijkertijd in de groeiende vraag naar energie te voorzien. Hierbij zijn efficiënte methoden om elektriciteit gedurende langere periodes op te slaan essentieel, vooral vanwege het feit dat de belangrijkste duurzame energiebronnen, zonne- en windenergie, niet continu stroom kunnen leveren. Hoewel de batterijtechnologie een grote vooruitgang heeft geboekt en batterijen inmiddels de meest aantrekkelijke optie zijn voor de aandrijving van voertuigen voor persoonlijk vervoer, zijn batterijen niet voldoende makkelijk schaalbaar voor de grootschalige energieopslag voor bijvoorbeeld industriële toepassingen. Als alternatief kan waterstof (H<sub>2</sub>) gebruikt worden als een chemische energiedrager om duurzame energie op te slaan en te transporteren, mits het waterstof via de elektrolyse van water kan worden geproduceerd. Brandstofcellen kunnen worden gebruikt om H<sub>2</sub> en O<sub>2</sub> om te zetten naar H<sub>2</sub>O. Hierbij wordt een elektrische stroom gegenereerd tussen de anode en kathode van de brandstofcel. Er zijn echter significante energieverliezen geassocieerd met de halfreactie die plaatsvindt aan de kathode, de reductie van O<sub>2</sub> naar H<sub>2</sub>O. Deze katalytische meerstapsreactie, waar vier protonen en vier elektronen mee gemoeid zijn, vindt plaats met een significante overpotentiaal. Zelfs de beste op platina gebaseerde katalysatoren zijn niet in staat deze reactie dichtbij de evenwichtspotentiaal van 1.23 V uit te voeren. Om de kosten en energie-efficiëntie van brandstofcellen te verbeteren is het ontwikkelen van alternatieve katalysatoren op basis van onedele metalen voor de efficiëntere reductie van zuurstof is daarom van groot belang.

In de natuur speelt koper een belangrijke rol in de actieve centra van veel redox-actieve enzymen die een rol spelen in de activatie en reductie van zuurstof. Geïnspireerd door deze natuurlijk systemen zijn er de afgelopen decennia veel moleculaire kopercomplexen onderzocht op hun vermogen om zuurstof te binden en te activeren. Bovendien is aangetoond dat het multikoperoxidase-enzym Laccase in staat is om de reductie van zuurstof naar water efficiënt te katalyseren. Elektrochemische studies aan Laccase hebben aangetoond dat de reductie van O<sub>2</sub> naar H<sub>2</sub>O dichtbij de O<sub>2</sub>/H<sub>2</sub>O evenwichtspotentiaal plaatsvindt, met een lagere overpotentiaal dan de op platina gebaseerde heterogene katalysatoren die momenteel gebruikt worden voor de zuurstofreductiereactie (ZRR) in waterstofcellen. Dit heeft geleid tot een grote interesse voor het gebruik van biomimetische moleculaire kopercomplexen als katalysatoren voor de elektrochemische ZRR. Het tris(2-pyridylmethyl)amine (tpma) kopercomplex Cu-tpma en gelijksoortige complexen zijn eerder bestudeerd voor de ZRR met behulp van stoichiometrische hoeveelheden

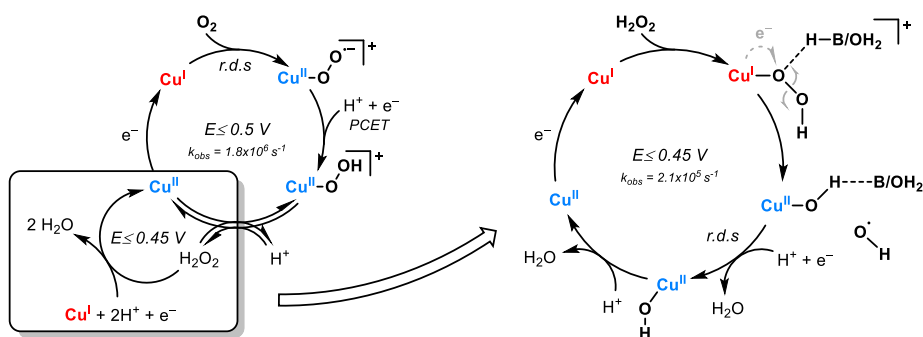
reductant. Initiële resultaten lieten zien dat er mogelijk een dinucleair deeltje gevormd wordt tijdens de katalytische reactie. Het mechanisme voor de ZRR door Cu-tmpa onder elektrochemische condities is echter nog niet volledig opgehelderd, noch is de reactiekinetiek van de elektrochemische ZRR onderzocht. Met het in dit proefschrift beschreven onderzoek hebben we een gedetailleerde mechanistische en kinetische analyse uitgevoerd van de elektrochemisch zuurstof- en waterstofperoxidoreductiereacties door Cu-tmpa, onder zowel waterige condities als in een organisch elektrolyt.

In Hoofdstuk 2 is de elektrochemische analyse van Cu-tmpa als homogene elektrokatalysator voor de ZRR beschreven. De elektrochemische metingen zijn uitgevoerd in een waterige pH 7 fosfaatgebufferde oplossing vanwege de gelimiteerde stabiliteit van Cu-tmpa onder zure condities en onze interesse in de katalytische prestaties onder neutrale condities. Vanwege de snelle liganduitwisseling van koper is eerst de stabiliteit van Cu-tmpa onder elektrochemische condities vastgesteld met behulp van in situ elektrochemische kwartskristal microbalans experimenten. De resultaten hiervan lieten zien dat er geen meetbare depositie van materiaal op de elektrode plaatsvond gedurende de ZRR, waarmee de homogene aard van de katalysator werd vastgesteld. Concentratiestudies van de katalysator lieten zien dat er een eerste-orde afhankelijkheid is van de katalysatorconcentratie op de katalytische stroom. Dit toont aan dat het katalytische mechanisme een enkel kopercentrum bevat, in tegenstelling tot het eerder voorgestelde koper-dimeer. Een ander belangrijk aspect van de ZRR is de aard van het reactieproduct en daarmee de hoeveelheid elektronen die betrokken zijn bij de katalytische reactie. Met behulp van roterende ringschijfelektrode en de resulterende Koutecky-Levich analyse werd een elektronenoverdrachtsgetal van bijna 4 bepaald. Hieruit blijkt dat  $\text{H}_2\text{O}$  het primaire product is in het potentiaalregime waar een limiterende stroom wordt behaald. In het potentiaalregime waar de limiterende stroom nog niet wordt behaald, werd er echter een kleine oxidatieve stroom waargenomen op de platina ring. Door de potentiaal van de Pt-ring te moduleren en de katalysatorconcentratie te variëren, werd vastgesteld dat de stroom gemeten op de Pt-ring door de oxidatie van  $\text{H}_2\text{O}_2$  werd veroorzaakt. Met behulp van chronoamperometrische metingen werd bevestigd dat  $\text{H}_2\text{O}_2$  preferentieel gevormd wordt bij potentialen dichtbij het aanvangspotentiaal van de katalytische reactie. Analyse van de Tafel-hellingen over het volledige potentiaalgebied toonde aan dat er inderdaad twee verschillende katalytische regimes zijn. Een katalytische eerste-orde snelheidsconstante van de partiele reductie van  $\text{O}_2$  naar  $\text{H}_2\text{O}_2$  werd bepaald met behulp van de *foot-of-the-wave* analyse (FOWA). Deze snelheidsconstante is één orde groter hoger is dan de snelheidsconstante geassocieerd met de volledige vier-elektronenreductie van  $\text{O}_2$  naar  $\text{H}_2\text{O}$ . Uit deze resultaten is gebleken dat er twee

verschillende katalytisch cycli plaatsvinden tijdens de ZRR, waarbij  $\text{H}_2\text{O}_2$  gemakkelijk wordt uitgewisseld in de coördinatiesfeer van het kopercentrum.

Het is duidelijk geworden dat waterstofperoxide een cruciale rol speelt in de elektrochemische reductie van zuurstof in de aanwezigheid van Cu-tmpa. Dit vertoont overeenkomsten met de Fenton-chemie die wordt waargenomen in verschillende koperhoudende enzymen, welke  $\text{O}_2$  activeren en reduceren. Ook kunnen deze enzymen onder bepaalde omstandigheden  $\text{H}_2\text{O}_2$  produceren of zelfs gebruiken als oxidant voor de oxidatiereacties die door deze enzymen worden uitgevoerd. Het inzichtelijk maken van de manier waarop waterstofperoxide wordt geactiveerd door deze koperenzymen en biomimetische kopercomplexen is van groot belang voor de ontwikkeling van nieuwe selectieve katalysatoren voor de reductie van  $\text{O}_2$ , of de elektrochemische productie van  $\text{H}_2\text{O}_2$ . Daarom hebben we de elektrochemische waterstofperoxidereductiereactie (WPRR) door Cu-tmpa in neutrale waterige oplossing onderzocht, zoals beschreven in Hoofdstuk 3. De elektrochemische WPRR bleek een eerste-orde afhankelijkheid te hebben in de katalysatorconcentratie, zoals ook het geval is voor de ZRR beschreven in Hoofdstuk 2. Kinetische studies toonden aan dat de reductie van waterstofperoxide significant langzamer is, met tenminste één orde grootte, dan de reductie van zuurstof. Door dezelfde elektrochemische analyse uit te voeren op de katalytische prestaties van Cu-tmpa in een fosfaatgebufferde  $\text{D}_2\text{O}$ -elektrolytoplossing, hebben we het kinetische isotoopeffect (KIE) van de WPRR kunnen bepalen. De toepassing van de FOWA en de bepaling van de snelheidsconstante door middel van de *current enhancement* ( $i_{\text{cat}}/i_{\text{p}}$ ) methode bij lage katalysatorconcentraties resulteerden beide in lagere katalytische snelheidsconstanten dan in een niet-gedeuteerde elektrolytoplossing. Dit vertaalde zich in een oplossings-KIE van 1.4 tot 1.7 voor de WPRR gekatalyseerd door de koperkatalysator. Dit betekent dat er een waterstof- of protonoverdracht betrokken moet zijn bij de snelheidsbepalende stap van de katalytische reactie. Naar aanleiding van deze resultaten hebben we een mechanisme voorgesteld dat vergelijkbaar is met mechanismes die zijn voorgesteld voor de actieve centra van koper monooxygenases. Hierbij worden zowel een  $\text{Cu}^{\text{II}}\text{-OH}$  deeltje en een vrij hydroxyl radicaal gevormd als reactie-intermediair. De algemene elektrokatalytische mechanismen voor de reductie van  $\text{O}_2$  en  $\text{H}_2\text{O}_2$  in aanwezigheid van Cu-tmpa op basis van Hoofdstuk 2 en 3 zijn weergegeven in Schema 1.

Hoewel we hebben aangetoond dat de reductie van zuurstof door Cu-tmpa een mononucleaire reactieroute volgt onder neutrale waterige condities, bleven er vragen over de aard van het katalytische mechanisme in organische oplosmiddelen. Het katalytische mechanisme kan immers aanzienlijk worden beïnvloed door de reactiecondities. Verschillende interacties tussen de oplosmiddelen en de katalytische deeltjes of reactieintermediaren, en verschillen in de aard van de protonenbron



**Schema 1.** De mechanistische cycli voor de ZRR en WPRR in aanwezigheid van Cu-tmpa, zoals voorgesteld op basis van Hoofdstuk 2 en 3.  $k_{\text{obs}}$  refereert hier naar de snelheidsconstanten die zijn verkregen via de FOWA.

kunnen ieder een grote rol spelen. In Hoofdstuk 4 is het onderzoek naar de ZRR en WPRR door Cu-tmpa in acetonitril beschreven, waarbij de katalytische reacties in verschillende zure en gebufferde elektrolytoplossingen werden geëvalueerd. Van de vier verschillende zuren die zijn onderzocht, resulteerden trifluoroazijnzuur (HTFA) en dimethylformamidium trifluoromethaansulfonaat (HDMF<sup>+</sup>) in instabiliteit van het Cu-tmpa complex. Hierdoor konden er geen reversibele redoxparen worden verkregen van het Cu-tmpa complex in aanwezigheid van deze twee sterke zuren. Wanneer de mildere zuren azijnzuur (HOAc) en triethylammonium (HNEt<sub>3</sub><sup>+</sup>) werden gebruikt, werden er echter wel reversibele redoxparen waargenomen. Nitrilen zoals EtCN en MeCN fungeren als sterke liganden voor de gereduceerde Cu<sup>I</sup>-tmpa deeltjes, waardoor er significante competitie plaatsvindt tussen de reversibele binding van O<sub>2</sub> en deze nitrilen aan Cu<sup>I</sup>. In het geval van EtCN is eerder aangetoond dat de evenwichtsconstante voor de vorming van [Cu<sup>II</sup>(O<sub>2</sub><sup>•-</sup>)(tmpa)]<sup>+</sup> slechts 0.38 M<sup>-1</sup> is bij kamertemperatuur als gevolg van competitie met de coördinatie van het oplosmiddel aan het kopercentrum. Dit leidt naar verwachting tot een significante afname van de snelheid van de katalytisch ZRR. Na het bestuderen van de reactiekinetiek van de elektrokatalytische ZRR in MeCN met behulp van de *current enhancement* methode bleek inderdaad dat de waargenomen snelheidsconstante  $k_{\text{obs}}$  met een factor 10<sup>5</sup> verminderd was ten opzichte van de ZRR in waterige oplossing. Ondanks de veel langzamere katalytische reactiesnelheid in MeCN, bleek de overpotentiaal geassocieerd met de ZRR meer dan 100 mV lager te zijn in de gebufferde MeCN-oplossing vergeleken met een neutrale waterige oplossing. Interessant genoeg zijn de katalytische snelheidsconstanten voor de WPRR hoger dan voor de ZRR. Het tegenovergestelde gedrag werd waargenomen in water. Deze studie heeft aangetoond dat het katalytische mechanisme voor de reductie van O<sub>2</sub> in acetonitril grotendeels vergelijkbaar is met wat we in water hebben waargenomen ondanks de aanzienlijke verlaging van de reactiekinetiek als gevolg van de competitieve



coördinatie van acetonitril.

In Hoofdstuk 5 is de synthese en elektrochemische analyse van drie verschillende pyridylalkylamine kopercomplexen beschreven. Hierbij werd de afstand tussen de centrale tertiaire amine en één van de pyridinearmen gevarieerd, waardoor de hoeveelheid deformatie in de coördinatiesfeer van het kopercomplex werd gevarieerd. Daarnaast werd er één ligand gesynthetiseerd als analoog aan bmpa (bmpa = bis(2-pyridylmethyl)amine), door middel van de introductie van een niet-coördinerende furanyl groep. In tegenstelling tot bmpa behoudt deze furanyl-verbinding de tertiaire amine functie, in plaats van de secundaire amine die aanwezig is in bmpa, en is daarmee beter vergelijkbaar met Cu-tmpa. De grootste toename van het redoxpotentiaal werd waargenomen voor Cu-bpmpa (bpmpa = bis[(2-pyridyl)methyl]-2-pyridylamine), met een +300 mV hogere redoxpotentiaal dan Cu-tmpa. Er werd een algemene trend waargenomen waarbij de toename van deformatie van de coördinatieomgeving rond het kopercentrum resulteerde in een hogere redoxpotentiaal. Er is een duidelijke lineaire *scaling relationship* vastgesteld tussen de redoxpotentiaal en de katalytische snelheidsconstanten voor de elektrochemische reductie van O<sub>2</sub> en H<sub>2</sub>O<sub>2</sub>. Hoe lager de redoxpotentiaal van het kopercomplex, hoe hoger de katalytische snelheidsconstanten. In het geval van Cu-bpmpa resulteert dit ook in een snellere WPRR dan ZRR, in tegenstelling tot de overige complexen. Dit toont aan dat de katalytische cycli van de ZRR en WPRR niet volledig aan elkaar zijn gerelateerd, wat bevestiging biedt aan het idee dat bij mononucleaire koperkatalysatoren twee afzonderlijke katalytische cycli plaatsvinden tijdens de ZRR.

## Toekomstperspectieven

We hebben Cu-tmpa geïdentificeerd als een uitstekende elektrokatalysator voor de ZRR, met een buitengewoon snelle kinetiek wat resulteerde in een katalysator die in staat is om zelfs bij uiterst lage katalysator concentraties maximaal te presteren. Echter is er een significante overpotentiaal (> 0.9 V) aanwezig voor de ZRR door Cu-tmpa. Pogingen om het overpotentiaal te verminderen door middel van ligandmodificaties die voor een deformatie in de coördinatiesfeer zorgden waren succesvol, maar resulteerden ook in een significante verlaging van de katalytische snelheidsconstante. Daarnaast hebben we ook kunnen aantonen dat het katalytische mechanisme voor de ZRR verloopt via een mononucleair deeltje. Dit resultaat is verkregen onder zowel neutrale waterige condities als in acetonitril in aanwezigheid van zwakke zuren. Hieruit blijkt dat het eerder voorgestelde  $[\{Cu^I(tmpa)\}_2(O_2)]^{2+}$  dimeer, dat onder niet-katalytische condities wordt gevormd en vanwaar de ZRR ook kan plaatsvinden, niet wordt gevormd onder volledige elektrokatalytische condities in het bijzijn van protonen. Dit onderstreept de noodzaak om het katalytisch mechanisme onder

elektrochemische condities te bestuderen als eerder gepubliceerde resultaten onder niet-elektrochemische condities zijn behaald, waarbij gebruik is gemaakt van stoichiometrische hoeveelheden reductant.

Bovendien toont de klaarblijkelijke stapsgewijze reductie van  $O_2$  naar  $H_2O$  via  $H_2O_2$  door mononucleaire koperkatalysatoren gebaseerd op structurele template van Cu-tmpa aan dat de standaardreductiepotentiaal van 1.23 V vs RHE waarschijnlijk niet de beperkende factor is bij het verlagen van het overpotential van dit soort katalysatoren. Het is juist de standaardreductiepotentiaal van 0.695 V vs RHE dat is geassocieerd met deze gedeeltelijke reductie van  $O_2$  naar  $H_2O_2$ . Dit heeft belangrijke implicaties voor het ontwerp van katalysatoren met lagere overpotentialen voor de 4-elektronreductie van  $O_2$ . Het wijst op de noodzaak van het ontwikkelen van multinucleaire koperkatalysatoren die de vorming van een hydroperoxo intermediair tijdens de katalytisch cyclus kunnen voorkomen en in plaats daarvan in staat zijn om de O-O binding direct te verbreken. In principe zou dit een katalysator vereisen waarin minimaal twee kopercentra op een optimale afstand van elkaar staan om  $O_2^{2-}$  via beide centra te kunnen binden, en met een rigide bruggend-ligand aan elkaar zijn verbonden. Dit kan de vorming van hydroperoxo deeltjes en dus de vorming van  $H_2O_2$  voorkomen. Daarnaast zal het redoxpotentiaal van dit kopercomplex ook veel dichterbij het  $O_2/H_2O$  evenwichtspotentiaal verschoven moeten worden om uiteindelijk betere katalytische prestaties te verkrijgen dan simpelere mononucleaire kopercomplexen die in staat zijn zowel  $O_2$  en  $H_2O_2$  dichtbij de  $O_2/H_2O$  evenwichtspotentiaal te reduceren.



# Curriculum Vitae

---

Michiel Langerman was born on the 30<sup>th</sup> of September 1991 in Maastricht, The Netherlands. In 2009, he obtained his VWO diploma from Het Baken Park Lyceum in the city of Almere. After graduating high school, Michiel studied Molecular Science & Technology, a joint bachelor program at the TU Delft and Leiden University. In 2013, he obtained his BSc degree after completing a minor in Advanced Chemistry. During this bachelor he wrote his thesis on photosubstitution reactions of fluorescent thioether ligands on ruthenium polypyridyl complexes. This research was performed in the Metals in Catalysis, Biomimetics & Inorganic Materials (MCBIM) research group at Leiden University under the supervision of Azadeh Bahreman and Prof.dr. Sylvestre Bonnet. Michiel then continued with a MSc degree in Research in Chemistry at Leiden University, with a focus on synthetic and biochemistry. In January 2014 he started his research project on the subject of the targeted drug delivery of photoactive ruthenium anticancer prodrugs, once again in the MCBIM research group, under the supervision of Dr. Bianka Siewert and Prof.dr. Sylvestre Bonnet. The research performed over the next 16 months contributed to two research publications. Michiel obtained his MSc degree in 2015.

In October 2015, Michiel started his PhD at Leiden University, under the guidance of Dr. Dennis Hetterscheid. The research activities took place in both the Metals in Catalysis, Biomimetics & Inorganic Materials (MCBIM) and Catalysis and Surface Chemistry (CASC) research groups. The project focused on the fundamental elucidation of the mechanism of the electrochemical ORR by mononuclear copper catalysts and the design principles of new molecular copper-based ORR catalysts. Results of the studies included in this thesis were presented at several (inter)national conferences, including an oral presentation at the Netherlands Catalysis and Chemistry Conference (NCCC) in 2018, and poster presentations at the HRSMC Symposium (2018), Reedijk Symposium (2019), NCCC (2016, 2017, 2018, 2019), CHAINS (2016, 2019), and the International Symposium on Homogeneous Catalysis (2018) conferences. Michiel completed several professional courses during his PhD, including *Catalysis: An Integrated Approach* organized by the Netherlands Institute for Catalysis Research (NIOK), *Physical Methods in Inorganic Chemistry* and *High Impact Writing* organized by the Holland Research School of Molecular Chemistry (HRSMC), and graduate courses organized by the Leiden University: *Effective Communication*, *Scientific Conduct*, and *Time Management*. Finally, Michiel has had the pleasure to contribute to the broader scientific community

as a referee for the Journal of Catalysis (Elsevier).

During his PhD, Michiel supervised a number of research students during their research projects; two Master, two Bachelor, one HBO Bachelor and two HRSMC short-term research students. Additionally, Michiel assisted in teaching several practical courses, “Basic Practical Skills” and “Organic Chemistry”, for undergraduate Molecular Science & Technology (MST) and Bio-Pharmaceutical Sciences (BFW) students. Additionally, he assisted in the “Chemistry 1”, “Organic Chemistry” and “Inorganic Chemistry” courses. In the summer of 2020, Michiel assisted in the planning of the 2020-2021 academic year for the Leiden Institute of Chemistry at Leiden University, and was responsible for the scheduling of the Life-Science & Technology BSc and MSc (practical) courses in accordance with COVID-19 safety and capacity restrictions.

# List of Publications

---

B. Siewert, M. Langerman, Y. Hontani, J. T. M. Kennis, V. H. S. van Rixel, B. Limburg, M. A. Siegler, V. Talens Saez, R. E. Kieltyka, S. Bonnet; Turning on the red phosphorescence of a [Ru(tpy)(bpy)(Cl)]Cl complex by amide substitution: self-aggregation, toxicity, and cellular localization of an emissive ruthenium-based amphiphile. *Chem. Commun.* **2017**, 53, 11126-11129.

B. Siewert, M. Langerman, A. Pannwitz, S. Bonnet; Synthesis and Avidin Binding of Ruthenium Complexes Functionalized with a Light-Cleavable Free Biotin Moiety. *Eur. J. Inorg. Chem.* **2018**, 4117-4124

M. Langerman, D. G. H. Hetterscheid; Fast Oxygen Reduction Catalyzed by a Copper(II) Tris(2-pyridylmethyl)amine Complex through a Stepwise Mechanism. *Angew. Chem. Int. Ed.* **2019**, 58, 12974-12978.

M. Langerman, D. G. H. Hetterscheid; Mechanistic study of the activation and the electrocatalytic reduction of hydrogen peroxide by Cu-tmpa in neutral aqueous solution. *ChemElectroChem* **2021**, 8, 2783.

M. Langerman, M. van Dorth, D. G. H. Hetterscheid; Dioxygen reduction in acetonitrile: the influence of acid strength on the catalytic reaction. *Manuscript in preparation*.

M. Langerman, H. van de Vijver, M. A. Siegler, and D. G. H. Hetterscheid; On the scaling relation between the reduction potential of copper catalysts and the turnover frequency for the oxygen and hydrogen peroxide reduction reactions. *Manuscript in preparation*.



# Acknowledgements

---

Many people have made a contribution in small or large ways to the establishment of this thesis, my personal growth, and my development as a researcher.

First of all, I want to thank Dr. Dennis Hetterscheid for offering me a position in his group and having confidence in my ability to pursue a different field of chemistry. I have always appreciated your willingness to discuss my ideas and hypotheses, and your perspective on presenting research has been invaluable. Both the independence and guidance you have provided me during these years have contributed tremendously to my scientific development. Secondly, I would like to thank Prof.dr. Lies Bouwman for welcoming me into the group many years ago and for carefully reading several of my theses over the years. For teaching me to always be critical of my results and interpretation, and for teaching me the ways of coordination chemistry. I would also like to thank Prof.dr. Marc Koper and the CASC research group for their unrelenting feedback and for always keeping me alert when it comes to electrochemistry. Additionally, a special thanks to Dr. Bianka Siewert, Dr. Samantha Hopkins, and Prof.dr. Sylvestre Bonnet who have been instrumental in my early development as a researcher and without whom I would have never started this journey.

It goes without saying that all my fellow “Minions” have made my PhD an enjoyable experience. Thank you very much Silvia, Konstantin, Koen, Martijn, Nicole, Bas, Shengxiang, Andrey, Daan, Kyra, Dana, Ross, Jan, Phebe, Sjoerd, Marleen, and Charlotte. The open and relaxed atmosphere within our group has been the perfect environment to freely discuss and explore scientific ideas without reservation. And perhaps most important of all; the combined efforts to run an extremely well-organized lab has made all the hard work possible. A warm thanks to the entire MCBIM group as well, especially Lucien, Hans, Michael, and Erik.

I would like to thank Dr. Maxime Siegler for X-ray crystallography (Chapter 5), Dr. Karthick Gupta and Fons Lefeber for any support that was required during NMR measurements. Dr. Bas van Dijk and Dr. Nicole Smits are thanked for their scientific input and the many discussions and brainstorm sessions. The efforts of all the students I’ve supervised have been an important part of the work and concepts contributing to this thesis, whether ultimately included or not. So thank you Sander, Renze, Hans (Chapter 5), Nicole, Lars, and Micha (Chapter 4) for your hard work.

Without the friends I’ve made along the way, life and this thesis would have been very different. So thanks for the many Thursdays and for the fun times Max, Roy,



Wessel, Elena, Aimee, Thom, Niek, Amedeo, Victorio, Velten, Willem, Liuba, Elena, Erjen, Luis, Luana, Dimitris, and many more. Thank you Lia and Elena, for always being there to celebrate the good times, and support me through the bad times.

Valeriia, thank you for being by my side during the last stretch of this journey and for always keeping me motivated. Finally, I would like to thank my parents Hans and Ellen for always fostering my curiosity from a young age, my family and hometown friends for their continuous support.